GENOTYPE-PHENOTYPE STUDIES IN INFANTILE NYSTAGMUS WITH EMPHASIS ON THE NOVEL *FRMD7* GENE
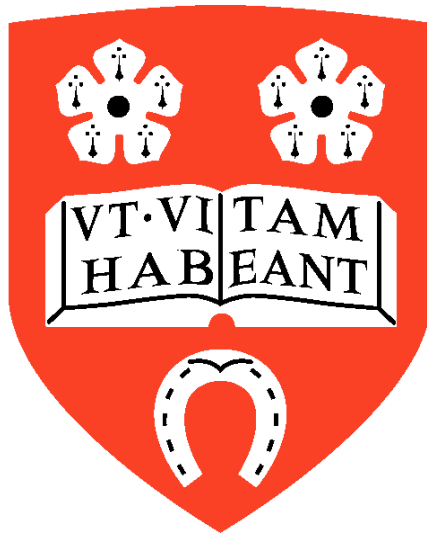
Thesis submitted for the degree of

Doctor of Philosophy

at the University of Leicester

by

Mervyn George Thomas BSc (Hons) (Leicester)

Ophthalmology Group

University of Leicester

December 2011

ABSTRACT

GENOTYPE-PHENOTYPE STUDIES IN INFANTILE NYSTAGMUS WITH EMPHASIS ON THE NOVEL *FRMD7* GENE

Mervyn George Thomas

FRMD7 mutations are a major cause of idiopathic infantile nystagmus (IIN). Infantile nystagmus can also be associated with albinism, *PAX6* mutations and achromatopsia; these disorders are associated with afferent visual anomalies which pose the question could this be a common aetiological factor for infantile nystagmus. The underlying neuroanatomical defects associated with *FRMD7* mutations are yet to be determined.

A large scale sequencing project was undertaken to genotypically characterize the causative mutations in IIN. The total number of *FRMD7* mutations identified was 37 of which 23 were novel. Penetrance of nystagmus in female carriers is related to mutation location rather than mutation type.

The genetic basis of idiopathic infantile periodic alternating nystagmus (II-PAN) was unknown. Sequence analysis in II-PAN patients showed that *FRMD7* mutations were causative of this disorder. In-situ hybridization results in human embryonic and foetal tissue suggested that the optokinetic reflex and vestibulo-ocular reflex arcs could be involved in the disease pathogenesis. Detailed spatiotemporal expression profiles in the retina suggested that *FRMD7* could have a significant role in retinal development. This formed the basis of performing optical coherence tomography (OCT) studies in patients with *FRMD7* mutations.

Retinal phenotyping studies in patients with *FRMD7* mutations showed foveal hypoplasia and abnormal optic nerve head morphology. These findings were also seen in patients with *PAX6* mutations and albinism. However in patients with achromatopsia, progressive retinal changes were observed at the fovea: outer nuclear layer thinning and disruption of the inner-outer segment junctions. Atypical foveal hypoplasia was also observed in patients with achromatopsia. The different retinal phenotypes observed with achromatopsia is linked to cone photoreceptor degeneration.

A structural grading system was developed for foveal hypoplasia; this takes into account the stage at which the retinal development was arrested. The grade of foveal hypoplasia was a strong predictor of visual acuity.

Therefore this thesis shows for the first time that arrested retinal development could be a common aetiological factor to the development of infantile nystagmus. The stage at which the retinal development was arrested is a strong indicator of visual acuity.

ACKNOWLEDGEMENTS

CONTENTS

LIST OF FIGURES

Chapter 3

Chapter 4

Chapter 5

Chapter 6

Chapter 7

Chapter 8

LIST OF TABLES

Chapter 7

Chapter 8

ABBREVIATIONS

AS-OCT	anterior segment optical coherence tomography
AZ	avascular zone
BCM	blue cone monochromatism
CDS	coding sequence
CMT	Central Macular Thickness
COST	cone outer segment tip
CS	carnegie stage
dpc	days post conception
dpf	days post fertilisation
dpo	days post ovulation
E10.5	embryonic day 10.5
ELM	external limiting membrane
ERG	electroretinography
ESE	exonic splicing enhancers
FD	foveal depth
GCL	ganglion cell layer
H&E	haematoxylin and eosin
HRZ	hyporeflective zone
IIN	idiopathic infantile nystagmus
II-PAN	idiopathic infantile periodic alternating nystagmus
ILM	internal limiting membrane
INBL	inner neuroblastic layer
INL	inner nuclear layer
INS	infantile nystagmus syndrome
IPL	inner plexiform layer
IS	inner segment
IS/OS	inner segment-outer segment junction
kb	kilobases
LCA	leber's congenital amaurosis
NPW	null point width
OA	ocular albinism
OCA	oculocutaneous albinism
OCT	optical coherence tomography
OD	optic disc
OKN	optokinetic nystagmus
OKR	optokinetic reflex
ONBL	outer neuroblastic layer
ONL	outer nuclear layer
ONS	optic nerve sheath
OPL	outer plexiform layer
OPS	optic stalk
OS	outer segment
P5	post natal day 5

QI	quality index
RGC	retinal ganglion cells
(R) NFL	(retinal) nerve fibre layer
RPE	retinal pigment epithelium
RT	retinal thickness
UHR	ultra high resolution
UTR	untranslated region
VEP	visual evoked potentials
VOR	vestibulo-ocular reflex
VZ	ventricular zone
wpc	weeks post conception

1. CHAPTER ONE: GENERAL INTRODUCTION

1.1 EYE MOVEMENTS AND RETINAL DEVELOPMENT

1.1.1 TELEOLOGY OF EYE MOVEMENTS

"*The muscles were of necessitie provided and given to the eye, that so it might move on every side: for if the eye stoode fast, and immoveable, we should be constrained to turn our head and necke (being all of one peece) for to see: but by these muscles it now moveth itself with such swiftness and nimbleness, without stirring of the head, as is almost incredible…*" (1)

In 1599 Andreas Laurentius commented on the importance of eye movements and how they play a crucial role in vision. There are four arguments that justify the *raison d'être* of ocular motility:

1.   Humans posses a region of maximal resolution in the retina, the fovea. The central portion of this pit like structure is the foveola (figure 1.1) where the cone photoreceptors are closely packed thus accounting for the high visual acuity (2).

2.   A perfectly stabilized image on the retina fades. In order to prevent perceptual fading miniature eye movements are necessary even during fixation (3).

3.   Retinal image velocity greater than 4°/s undergoes considerable motion blur because high spatial frequencies are filtered (4). Thus relative image stability is critical to maximal acuity.

4.   In humans, the two visual fields overlap. In order to avoid diplopia and visual confusion it is essential to align both primary visual axes simultaneously (5,6).

The efficiency of sampling a visual scene is dependent on a coordinated effort from the perceptual and oculomotor centres.
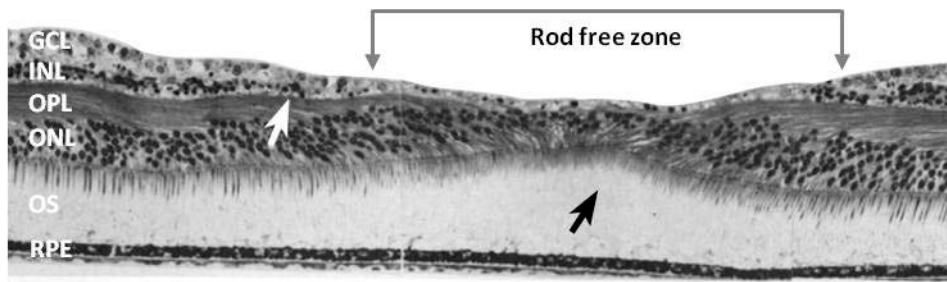
Figure 1.1: *Section through the centre of the fovea from a 72 year old individual. The width of the rod free foveola is indicated by the grey arrows. The white arrow indicates the most central cone synaptic pedicles. The black arrows show elongation and high density of the cone outer segments. The intra retinal layers are labeled.GCL = ganglion cell layer; INL = inner nuclear layer; OPL = outer plexiform layer; ONL = outer nuclear layer; OS = outer segment; RPE = retinal pigment epithelium. (Adapted with permission from: (7))*

1.1.2 TYPES OF EYE MOVEMENTS

There are six functional classes of eye movements (table 1.1).

Table 1.1: Functional classification of eye movements

Functional role	Class of eye movement
Stabilize gaze to keep images steady on the retina (for e.g. during head perturbations)	Vestibulo-ocular reflex (VOR)
	Optokinetic nystagmus (OKN)
Shift gaze towards an object of interest or to follow an object	Saccades
	Smooth pursuit
	Vergence
Prevent perceptual fading	Miniature eye movements

Both vestibulo-ocular reflex (VOR) and optokinetic nystagmus (OKN) are important in stabilizing the angle of gaze during head perturbations. There are three different types of VOR depending on the motion of the head. During brief or rapid head rotation the rotational VOR (r-VOR) stabilizes gaze. Translational VOR (t-VOR) compensates for translational or linear head movements. During lateral flexion of the neck or head tilt along the coronal

2

plane the third type of VOR, ocular counter-rolling response, stabilizes gaze. r-VOR is driven by the semicircular canals. However, t-VOR and the ocular counter-rolling response are driven by the otoliths in the lateral and medial portion of the utricle respectively (5,8).

The two main limitations of VOR are:

- During sustained rotation in the dark the system habituates
- The canals do not transduce very slow head movements well

The optokinetic system responds well to sustained and slow head rotation. OKN is a visually mediated reflex driven by the retinal slip velocity. The main limitation of this system is its longer latency of action, but this is not the case for the VOR which has a short latency (8). Thus, VOR and OKN form a symbiotic relationship vital for gaze holding.

Normally, saccades are fast, brief and accurate eye movements made in order to redirect the line of sight towards an object of interest. Smooth pursuit, as the name suggests, are eye movements responsible for smoothly tracking a moving object with a velocity closely matching that of the object. Vergence eye movements move the eyes in opposite directions in order to focus the object on each fovea. This movement is driven by two types of stimuli: image blur and image disparity (5).

1.1.3 THE RETINA

Although each gaze control system has its own specific function, they essentially ensure that the fovea is aligned with the object of interest. Thus the retina is an organ of paramount importance when considering gaze abnormalities. The retina is a specialised structure with photoreceptors, interneurons with a complex synaptic network.

During retinal development there is migration of cells in all three planes. In early retinal development the post mitotic retinal cells migrate from the scleral surface to the vitreal surface (z-axis) (figure 1.2), this is proposed to occur in one of three ways: (1) guided migration (9), (2) somal translocation (10) or (3) unconstrained migration (11). There are similarities to the development of the neurons destined for the cortical plate as well as migration of purkinje cells in the developing cerebellum. In the developing cortex the processes of the radial glia are used as guides to allow migration of new born neurons from the ventricular zone to the cortical plate (12). Similarly, in the retina the Muller glia form scaffolds to allow the post mitotic cells to migrate to the definitive positions (9). After the retinal cells have migrated to their respective cellular locations it results in a laminar structure (figure 1.1 and figure 1.3) which is evident both histologically and now can be visualised *in-vivo* and non-invasively using optical coherence tomography (OCT). Abnormalities of retinal cell migration or cell proliferation could lead to abnormal lamination or variation in laminar thickness patterns.

After a laminar structure is formed there is movement of cells (x- and y-axes) to form a highly specialised area with the retina, the *fovea* (Latin for "pit").

There is both centripetal migration of cones and centrifugal displacement of inner retinal cells (figure 1.3). This creates an area of high acuity or a pure cone area which is distinct on fundoscopy due to the lack of retinal vasculature and distinct pigmentation. Abnormalities of these processes would lead to foveal hypoplasia.
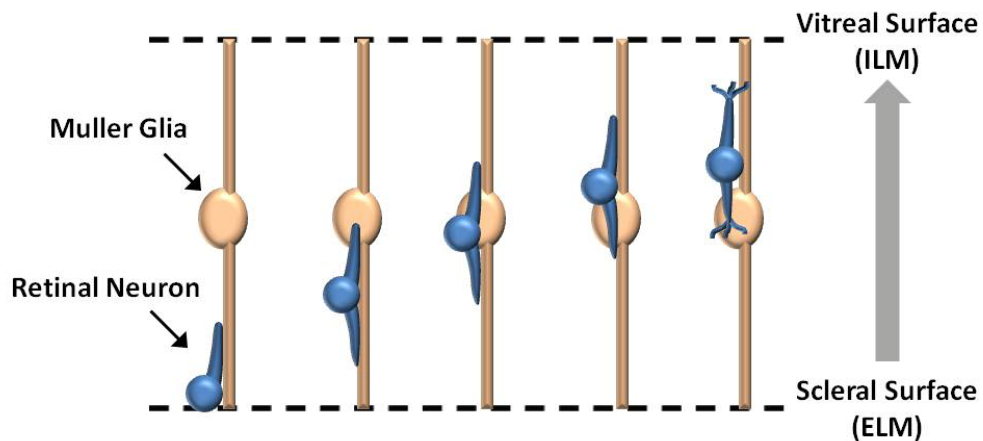
Figure 1.2: Glial guided migration of new born retinal neuron from the external limiting membrane (ELM) towards the internal limiting membrane (ILM).
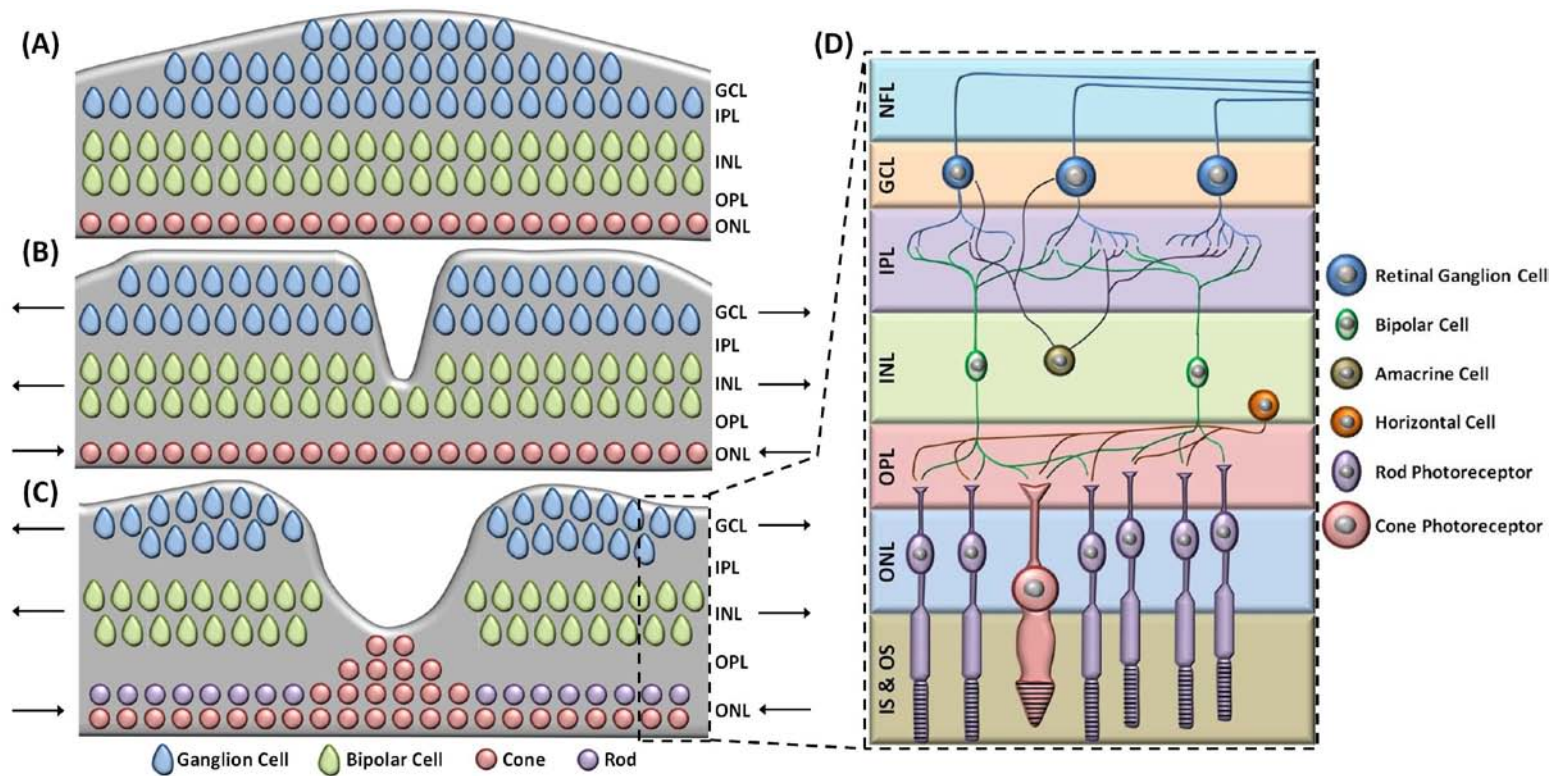
Figure 1.3: *Foveal pit formation and movement of retinal cells during formation of the area of high acuity. The laminar retinal structure prior to foveal pit formation is shown in (A). The inner retinal layers were displaced centrifugally (away from the future fovea) during foveal pit formation (B). The cone photoreceptors migrate centripetally (towards the fovea) and form the pure cone area (C). Arrows point in the direction of movement of the cellular layers. The magnified laminar structure with the different retinal cell types and the inner segment & outer segment (IS & OS) of the photoreceptors are shown in (D). NFL = Nerve Fibre Layer; GCL = ganglion cell layer; IPL = inner plexiform layer; INL = inner nuclear layer; OPL = outer plexiform layer; ONL = outer nuclear layer. (A, B, C are based on developmental theory proposed by Springer and Hendrickson)* (13)

1.2 NYSTAGMUS

"The diseases of the muscles of the eye, are principally three, the wrested or wrie eye, the shaking eye, and the astonished eye" (1)

1.2.1 DEFINITION AND ETYMOLOGY

Nystagmus is the rhythmic oscillation of the eyes which can be along horizontal, vertical, torsional axes or it can be multiplanar. For the pathological forms of nystagmus these oscillations are involuntary.

Nystagmus can present as a:

- Sign of an underlying disease (e.g. multiple sclerosis),

- Symptom (i.e. oscillating vision or oscillopsia),

- Disease entity (e.g. Idiopathic Infantile Nystagmus),

- Physiological entity (i.e. voluntary nystagmus – which can be produced at will by some individuals) (14).

The word nystagmus originates from the Greek words "nystagmos" meaning drowsiness and "nystazein" which means to nod (14). Certain forms of nystagmus have a slow drift phase followed by a quick phase. Sleepy individuals have head movements which resemble this form of eye movements which involves a slow downward drift followed by an upward jerking movement.

As noted in some of the works of Andreas Laurentius this condition, "shaking eyes", has been observed dating back to over 500 years, although it was erroneously considered to be a disorder of the extraocular muscles (1).

However, it was only in 1772 the term nystagmus was used by Sauvage in his nosology (15).

1.2.2 NYSTAGMUS CHARACTERISTICS

Based on the time of onset, nystagmus can be broadly classified into two groups: (1) infantile nystagmus (onset of nystagmus usually within the first 6 months of life) and (2) acquired nystagmus (16). This thesis is mainly concerned with infantile nystagmus although parallels to acquired nystagmus will be made. The terminology used to describe the characteristics of the nystagmus waveform is shown in table 1.2. The nystagmus waveform provides the clinician an objective measure of the disease state and it can be monitored for therapeutic response in drug trials (17).

Although the waveform communicates a considerable amount of information about the individual's condition, it is subject to variability (figure 1.4) based on gaze angle (18), level of attention (19), convergence (18,20), stress or anxiety, and visual stimuli (19,21-23). An example of how the nystagmus changes with gaze is shown in a video in the electronic appendix. A recent study has also shown that the nystagmus waveform is altered during reading tasks (24). In order to illustrate the effects of horizontal nystagmus on reading videos of a nystagmus patient reading and a control subject reading is also shown in the electronic appendix.
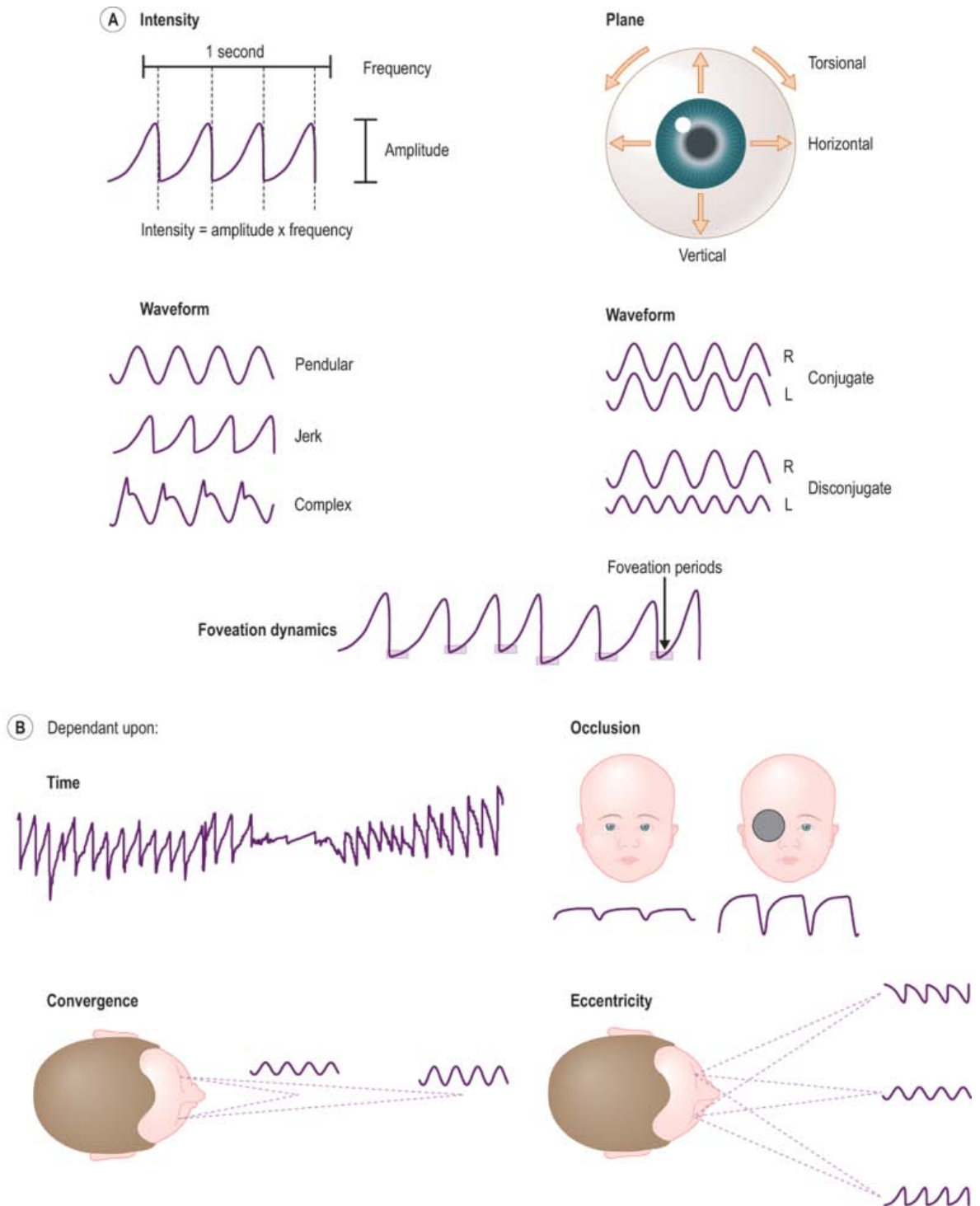
Figure 1.4: *Nystagmus characteristics. Nystagmus can be described using **(A)** eye movement intensity (amplitude x frequency), plane of oscillation, waveform, conjugacy between right (R) and left (L) eyes and duration and position of periods when the velocity of eye movements is slow enough to allow useful foveal vision (foveation). **(B)** Some of these characteristics can also vary with time, occlusion of one eye, convergence and eccentricity of eye position. (Reproduced with permission from:* (25)*)*

Table 1.2: Nystagmus waveform characteristics

Properties of the nystagmus waveform	Description
Frequency	Number of oscillations per second (Hz)
Amplitude	Distance traversed by the eye from peak to peak or the magnitude of the oscillation (degrees)
Intensity	A measure of the speed of the eye movement. It is the product of frequency (Hz) and amplitude (degrees), thus expressed in degrees/second
Foveation period	These are brief periods where the image is incident on or close to the fovea and corresponds to a time period where the eye velocity is relatively slow (26)
Direction	Nystagmus is described based on the direction of the quick phase. For example, if the fast movement is upwards, the nystagmus is referred to as "up-beating" (5,8,27)
Morphology of waveform	Nystagmus waveform is broadly split into pendular, jerk and dual jerk (18). See section 1.2.3 for more details.

1.2.3 CLASSIFICATION OF NYSTAGMUS

Classification systems provide a better understanding of both physiological as well as pathological processes. They may form the basis of predicting prognosis, determining further investigations and prescribing therapy. A diverse set of classification systems exist for nystagmus. A possible reason for this is due to the lack of consensus on the disease process or due to the limited applicability for each classification. Scientists from different backgrounds have worked in this field which has also contributed to the diversity of classifications.

One of the earliest classifications of nystagmus was broadly into two groups: (1) motor nystagmus and (2) sensory nystagmus. In motor nystagmus there is no detectable afferent visual defect. While in nystagmus patients where an underlying visual defect is present it has been termed as sensory nystagmus. These were based on early observations by David Cogan. He also suggested that there is a dual-cause for infantile nystagmus and the phenotypes observed were broadly classified into two: (1) jerk nystagmus and (2) pendular nystagmus (28).

Based on nystagmus waveforms derived from eye movement recordings in 65 subjects, Dell'Osso and Daroff created a comprehensive classification system for infantile nystagmus. They broadly classified nystagmus into three groups: pendular, jerk and dual. The jerk group was further divided into two groups depending on the direction of the quick phase (18). Figure 1.5 shows the 12 different waveforms described in congenital nystagmus. Subsequently, Dell'Osso and colleagues have disputed Cogan's classification suggesting that nystagmus waveforms arise from developmental instability of the ocular motor system and the waveforms are not pathgnomonic of a particular disorder (29).

I

II
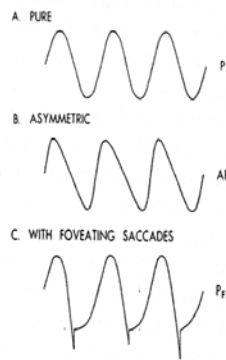
III
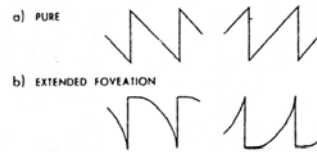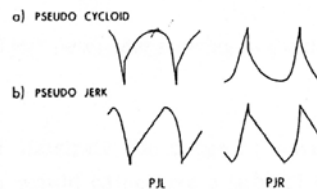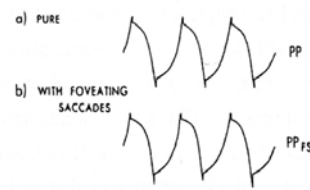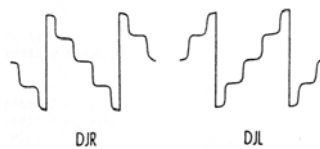
Figure 1.5: *The twelve waveforms described by Dell'Osso in 1975. They can be broadly classified into 3 groups: pendular, jerk and dual jerk nystagmus. Abbreviations used for different waveforms are indicated next to some of the waveforms. JR = Jerk Right and JL = Jerk Left. (Reproduced with permission from:* (18)*)*

The most recent classification of infantile nystagmus has been by a working group sponsored by the National Eye Institute (NEI). This group devised: A Classification of Eye Movement Abnormalities and Strabismus (CEMAS) (30). The CEMAS has divided infantile nystagmus into three categories:

(1) Infantile Nystagmus Syndrome (INS), (2) Fusion Maldevelopment

12

Nystagmus Syndrome (FMNS) and (3) Spasmus Nutans. The diagnostic criteria for INS, FMNS and Spasmus nutans are shown in table 1.3.

Table 1.3: CEMAS diagnostic criteria for various infantile nystagmus forms.

CEMAS Diagnosis	Criteria
Infantile Nystagmus Syndrome	1. Infantile onset 2. Accelerating slow phase (on eye movement recordings (EMR))
Fusion Maldevelopment Nystagmus Syndrome	1. Infantile onset 2. Associated with strabismus 3. Linear or decelerating slow phase (on EMR) 4. Jerk in direction of fixing eye
Spasmus Nutans	1. Infantile onset 2. Small amplitude, high frequency pendular oscillations with variable conjugacy (on EMR) 3. Head oscillations 4. Normal MRI/CT 5. Improves during childhood

INS is an umbrella term and it includes many disorders. Some examples of disorders that are grouped under INS are: idiopathic infantile nystagmus (IIN), albinism, aniridia, achromatopsia, blue cone monochromatism, congenital stationary night blindness, etc.

There also exists a clinical classification of infantile nystagmus described by Casteels et al. in 1992 (figure 1.6) (16). This is based on the clinical findings and subsequent clinical diagnosis and it is not always reliant on eye movement recordings. Therefore an individual with infantile nystagmus and no associated afferent defect would be classified as IIN (a diagnosis of exclusion). However if the patient had albinism, they would be classed as nystagmus associated with albinism. This classification makes no assumption

of causality, but provides the entire clinical picture, which may be necessary to treat any systemic manifestations of the disorder. For instance, albinism is associated with hypopigmentation and hence they are predisposed to skin cancer, therefore appropriate skin care is an essential part of the patients care plan.
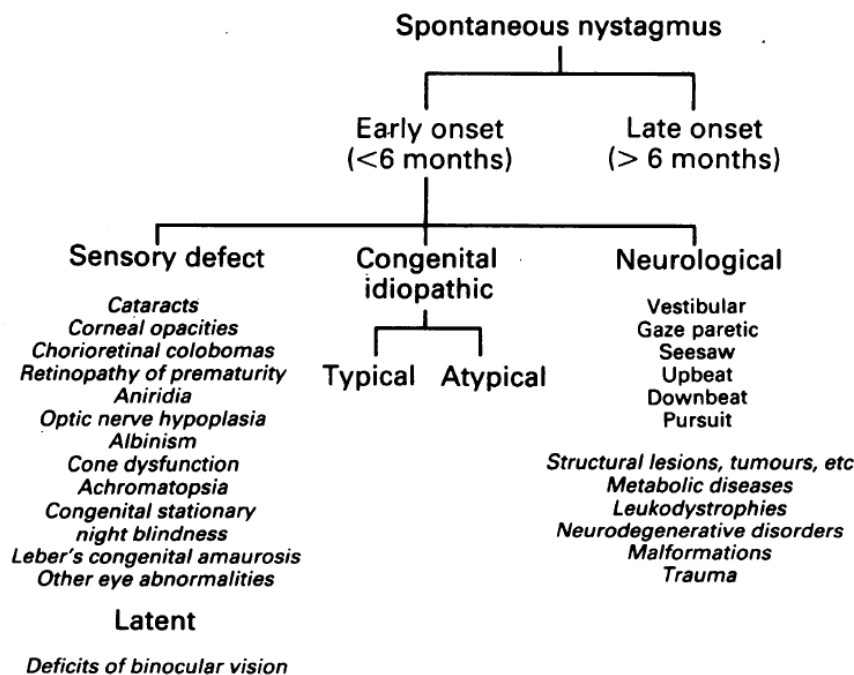
Figure 1.6: *Clinical classification of infantile nystagmus. A range of sensory defects can be associated with infantile nystagmus. If no sensory defects are detected it is classed as idiopathic. (Adapted with permission from Casteels et al. 1992)* (16)

Although the CEMAS classification has some potential benefits, it also has some problems which may influence patient management. Some of the problems associated with the INS classification are:

- Reduced accessibility in centres where there are no eye movement laboratories

- Clinically relevant information and possible aetiological factors are omitted

- Certain disorders may not fit into these broad groups (e.g. patients with aniridia have infantile onset nystagmus and can present with vertical nystagmus (31)).

Recently the CEMAS classification, in particular the INS classification has come under scrutiny (32). However Dell'Osso and colleagues have defended the basis of the classification since they suggest that the mechanism is the same for INS hence treatment and visual prognosis are not likely to be altered irrespective of the clinical diagnosis (33,34). Dell'Osso et al. argues that all INS is motor (i.e. a brain pathology) and that the link between afferent visual defects and occurrence of infantile nystagmus is unlikely to be an important factor in the pathogenesis of INS (33).

1.2.4 MECHANISMS OF INFANTILE NYSTAGMUS

There are a number of theories on causation of infantile nystagmus. Abnormalities in neural circuitries within different gaze holding centres have been implicated as the cause of infantile nystagmus. Jacobs and Dell'Osso suggest that excessive oscillations within the smooth pursuit subsystem are the mechanism of generations of the twelve waveforms observed in patients with infantile nystagmus (34). Optican and Zee suggest that the accelerating slow phase seen in infantile nystagmus arises from an unstable neural integrator (35). Barreiro has expanded on Optican and Zee's initial model and was able to generate all twelve nystagmus waveforms (36). Leigh and Khanna suggest that a congenital channelopathy could be responsible for

infantile nystagmus (37). An interesting yet old theory proposed in 1895 by Swanzy has received much attention since Harris and Berry had resurrected it (38). In 2006 Harris and Berry proposed that a failure of early sensorimotor integration could underlie the cause of infantile nystagmus. They suggest that retinal image motion is an adaptive mechanism in order to improve contrast sensitivity for low spatial frequencies. This maladaptive process leads to jerk nystagmus (39). The abundance of theories and lack of consensus suggests that the pathogenesis of infantile nystagmus still remains a mystery.

1.2.5 PREVALENCE AND SOCIAL FUNCTION

The Leicestershire Nystagmus Survey showed that the prevalence of nystagmus is estimated at 24 in 10,000. The prevalence on INS was 14 per 10,000. Among the infantile forms of nystagmus, IIN was the most common type in the Leicestershire Nystagmus Survey dataset (40). A breakdown of the different conditions associated with infantile nystagmus is shown in figure 1.7.
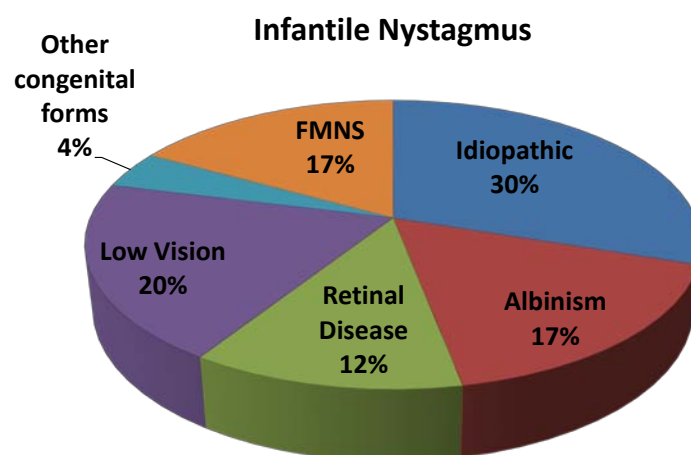
Figure 1.7: *A breakdown of the various disorders associated with infantile nystagmus. FMNS = Fusion Maldevelopment Nystagmus Syndrome.*

A study by Pilling *et al.* shows that poor visual function in nystagmus is associated with poor social functioning (41). Any chronic condition is associated with biographical disruption (42,43). This sociological concept has been described as a three step process as follows: "First, there is the disruption of taken-for-granted assumptions and behaviours; the breaching of common sense boundaries….Second, there are more profound disruptions in explanatory systems normally used by people, such that a fundamental re-thinking of the person's biography and self concept is involved. Third, there is the response to the disruption involving the mobilisation of resources, in facing an altered situation" (42).

Goffman describes 2 groups of stigmatised people – discredited and discreditable (44,45). Based on the presence of physically visible characteristics, patients with nystagmus would fit into the former category. It is therefore not uncommon for such patients to be stigmatised based on their "spoiled" identity and they would experience what is described as an enacted stigma (45). Whether these stereotypes lead to prejudice or discrimination has not been studied.

1.3 GENOTYPE-PHENOTYPE STUDIES IN INFANTILE NYSTAGMUS

This thesis will be focusing on IIN as a form of nystagmus where no sensory defect is known. In addition we will investigate the phenotypic heterogeneity in patients with albinism, *PAX6* mutations and achromatopsia. The latter three conditions are examples where sensory defects have been well documented.

1.3.1 IDIOPATHIC INFANTILE NYSTAGMUS

In the literature IIN has previously been referred to as congenital idiopathic nystagmus, motor nystagmus and also as part of the umbrella terms congenital nystagmus and infantile nystagmus syndrome (as discussed above).

1.3.1.1 THE NYSTAGMUS LOCI

IIN is a genetically heterogeneous disorder. In the literature three modes of inheritance have been reported: autosomal dominant, X-linked and autosomal recessive (46). Five nystagmus loci (NYS 1 – 5; NYS5 is further subdivided based on previous Online Mendilian Inheritance in Man (OMIM) records) have been described in literature (table 1.4). The nystagmus loci define regions of the human genome that are likely to be pathological in the presence of IIN. All of the nystagmus loci except NYS5a have been localized based on linkage analysis in affected kindred. NYS5a has been described and localized to the X-chromosome based on clinical features and an X-linked inheritance pattern. Refinement of the NYS1 region and further sequence analysis identified a novel gene, the *FRMD7* gene, mutations of which cause X-

linked IIN (47). There also exists an NYS6 locus (OMIM 300814), within which mutations of the *GPR143* gene cause ocular albinism. This will be discussed in the next section.

Table 1.4: The nystagmus loci

Locus and name	OMIM number	Gene identified	Inheritance	Key Publication
NYS 1 (Xq26.2)	310700	Yes (*FRMD7*)	X-linked	(47)
NYS 2 (6p12)	164100	No	Autosomal dominant	(48)
NYS 3 (7p11.2)	608345	No	Autosomal dominant	(49)
NYS 4 (13q31-33)	193003	No	Autosomal dominant	(50)
NYS 5 (Xp11.4-p11.3)	300589	No	X-linked	(51)
NYS 5a (X-chromosome)	300589*	No	X-linked	(52)

*Currently NYS5a does not exist based on the updated OMIM records

1.3.1.2 LOCI ON AUTOSOMES

Over the last century there have been numerous case reports of hereditary infantile nystagmus, however there is little cytogenetic data available in most of these reports (53-57). Thus prior to the 1990's no candidate regions were described to be pathologically affected. One of the first reports indicating possible loci that may be affected in autosomal dominant nystagmus was described in 1993 where a family spanning five generations reported horizontal nystagmus in the absence of other visual defects. Karyotyping revealed a balanced reciprocal translocation (non-Robertsonian) with breakpoints in 7p11.2 and 15q11.2 in two of the seven patients that were examined. The remaining five patients had a normal karyotype and no nystagmus (58).

The first mapping study in familial IIN was published in 1996 (48). This African-American family consisted of 28 affected patients with nystagmus and 30 unaffected individuals. Autosomal dominant inheritance was determined since there were affected individuals every generation with male to male transmission and unaffected members did not transmit the disease to their offspring. Abnormalities of both chromosome 7 and 15 were first excluded by karyotyping and linkage. However, six markers on 6p were linked ($\theta = 0$) and haplotype analysis localized the gene to an 18-cM region which spans over the 6p12 cytogenic band (48,59).

The 3 loci described above were investigated further in 1998, when a German family reported with infantile nystagmus with an autosomal dominant inheritance. Linkage analysis showed that regions 6p12 and 15q11 were unlikely to be the candidate regions and were excluded. However they were not able to exclude the 7p11.2 region in this family and it was suspected that the candidate gene(s) for this autosomal dominant nystagmus is harboured within this cytogenic band (49).

A similar approach was utilised by Ragge et. al. in a family presenting with autosomal dominant nystagmus. Firstly the two loci (6p12 and 7p11) were excluded since the disease did not link to the loci described. This disorder was linked to the interval 13q31-33 (50). However the phenotype associated with this family has been described as a vestibulocerebellar disorder (60), with the nystagmus in the vertical direction, which is distinct from the previously described infantile nystagmus forms (which were in the horizontal direction).

Autosomal recessive infantile nystagmus (OMIM 257400) is very rare and early reports by Waardenburg were based on simple pedigree observations (61,62). No linkage studies have been performed.

1.3.1.3 LOCI ON THE X-CHROMOSOME

Kerrison et. al. not only performed the first linkage study in the autosomal dominant IIN but also in X-linked IIN (63). Prior to this, numerous case reports have been described in the literature. A Swedish study also showed that the most common form of inheritance in familial nystagmus is X-linked (55,64). However on literature review there appears to be much confusion about whether the form of inheritance is dominant or recessive (54,65-67). Some studies described X-linked IIN inheritance as being "irregular dominant" (54-56,63).

Kerrison et al. identified 3 families with X-linked IIN showing incomplete penetrance in females. Initially the 3 loci on the X-chromosome known to be associated with nystagmus (*OA1*, *CSNB* and *BCM*) were excluded since the markers in their vicinity were not linked. An interval spanning ~7cM (corresponding to Xq26-q27) was shown to be linked in all three families. Two genes residing in this interval, *CDR1* and *SOX3*, were sequenced in affected members however no mutation was discovered (63). Subsequently Cabot et al. reported a new interval between Xp11.3-p11.4 in a large French family that was suspected to contain the gene, mutations of which would be responsible for X-linked IIN (51). Variable penetrance was seen among the female patients.

Soon the race to find the gene responsible for X-linked IIN was well underway with numerous groups reporting linkage to the same region described by Kerrison et al and Cabot et al. (68-73). The interval identified by Kerrison and colleagues was further narrowed to a 5cM region in 2001 (68). Furthermore, candidate genes *SLC25A14*, *SLC9A6* and *FGF13* within this interval were sequenced but no causative mutations were detected (68,72,74).

An additional locus (NYS5a) was described in 2005; this was based on a distinct phenotype, X-linked idiopathic infantile periodic alternating nystagmus (52). This was quite different to the previous phenotypes associated with the X-linked IIN.

The major breakthrough occurred in 2006 when Tarpey et al. refined the NYS1 locus and then carried out high throughput sequencing spanning over 80 genes within the interval of interest thus leading to the identification of the novel *FRMD7* gene, mutations of which cause X-linked IIN (47). The results were confirmed by other groups by linkage and sequence analysis in other families (75,76); followed by over 10 separate reports by other groups outlining various mutations of *FRMD7* (77-85).

1.3.1.4 *FRMD7* GENE, MRNA AND PROTEIN STRUCTURE

The *FRMD7* gene (previously known as LOC90167) located at Xq26.2 encodes for the FRMD7 protein (47). The FRMD7 protein has a role in neurite extension and branching (86).

The *FRMD7* gene is approximately 51 kb in length and consists of 12 exons (figure 1.8). The length of the mRNA transcript is approximately 3.2 kb (Accession number: NM_194277.2) and the normal gene product consists of 714 amino acids (Accession number: NP_919253.1) with a FERM domain at the N-terminus (figure 1.8).

Interestingly the region upstream to the 5'UTR (untranslated region) is highly similar to Pan Troglodytes to Rattus Norvegicus. This intergenic region appears to be a good candidate for the promoter of the *FRMD7* gene. Similarly the coding sequences (CDS) are also highly similar between the different species (figure 1.8).
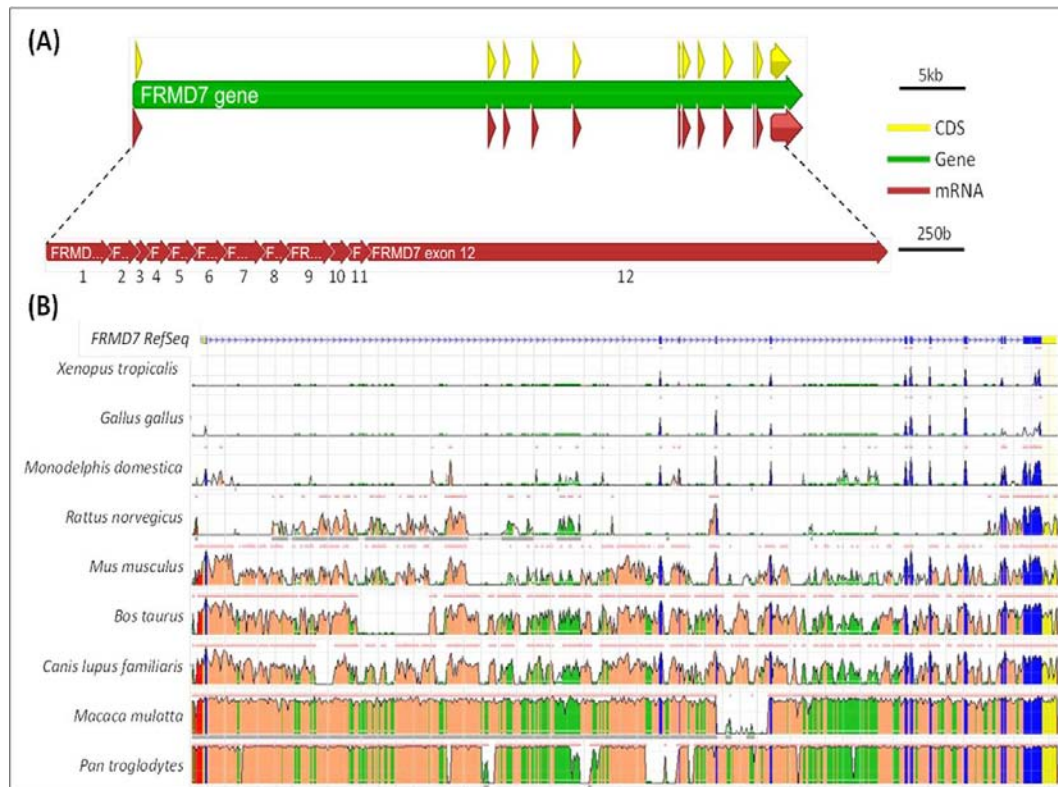
Figure 1.8*: Figure (A) depicts the FRMD7 gene structure. Scales are represented on the right. Figure (B) (from ECR browser) shows the similarity of residues between the different species. The height of the peaks indicates the degree of similarity to the Human FRMD7 sequence. The regions are colour coded with red representing intergenic regions, blue represents coding sequences, green represents simple repeats, yellow represents UTRs and salmon colour represents intronic regions. CDS = Coding sequence*

The FRMD7 protein has a significant homology with the FARP 1 and 2 proteins, with the homology concentrated at the N-terminus (figure 1.9). Based on the sequence homology it has been speculated that the function of the FRMD7 protein might be similar to the FARP proteins. FARP2 is also known to alter the length and degree of branching of neurites (87,88).
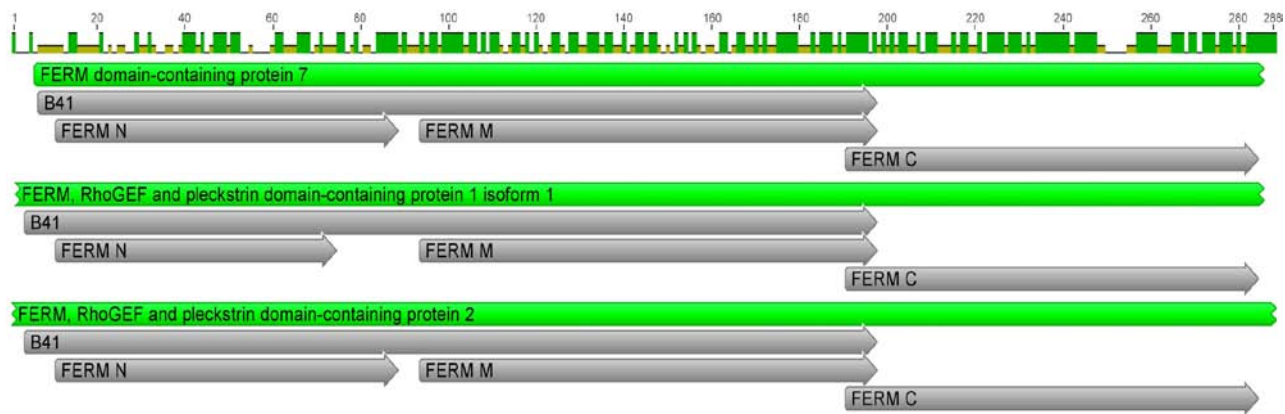
Figure 1.9: Alignment of FRMD7 with FARP1 and FARP2 proteins. Above the protein annotations the graph shows the degree of similarity between the sequences, the green sections of the graph indicated that the residues are identical. The homology is particularly concentrated within the FERM-C sub-domain.

1.3.1.5 PHENOTYPICAL CHARACTERISTICS

There is some evidence that the predominant nystagmus waveform changes over time in infantile nystagmus patients. At the onset, large-amplitude, low-frequency horizontal eye movements (described as triangular eye movements) are seen (89) (an example of this type of nystagmus is shown in the electronic appendix). This waveform pattern is followed by a smaller-amplitude pendular or jerk waveform and development of foveation (an example of this waveform in an adult IIN patient is shown in the electronic appendix). Another study reported that the predominant waveform during the first six months was asymmetric pendular and jerk with extended foveation (90).

The IIN group can be divided into two, patients with mutation of *FRMD7* (the FRMD7 group) and patients without a mutation (non-FRMD7 group). The penetrance of FRMD7-related infantile nystagmus in heterozygous carriers is

approximately 50%. There is a large overlap in the clinical findings between the two groups (FRMD7 & non-FRMD7), these include (46,91):

- Onset of nystagmus during infancy (within 6 months of life)

- Typically horizontal conjugate nystagmus

- Visual acuity (VA) is typically better than 0.3 logMAR

- The proportion of strabismus is between 7-10%

- Typically there is no latent nystagmus

- The frequency of nystagmus is normally between 3-4Hz

However there are certain clinical features that are different between the two groups (46,91):

- The female patients in the FRMD7 group tend to have better VA when compared to the males in the same group. This effect is not seen in the non-FRMD7 group

- The proportion of patients with stereopsis is greater in the FRMD7 group compared to the non-FRMD7 group

- The FRMD7 group has less anomalous head posture (typically <5°) compared to the non-FRMD7 group (an example of a patient with an anomalous head posture during reading is shown in the electronic appendix).

- The amplitude of nystagmus is reduced at primary position when compared to eccentric gaze positions (see example in electronic appendix). However, there are no significant gaze dependent changes in amplitude in the non-FRMD7 group.

The proportion of patients reported by Thomas et al. with strabismus was much lower compared to previous studies which suggested that stereovision is decreased in greater than 30% of patients due to associated strabismus (92) and retinal image motion (93). Brodsky and Fray also reported a higher percentage (17%) of IIN patients with strabismus (94) in comparison to the study by Thomas et al. in 2008 (91). Many IIN patients have a null zone, i.e. a range of eye positions where the intensity of nystagmus is least for that individual (95). It is not uncommon that this zone may lie eccentric to the primary position, in which case the patient may adopt a head turn or tilt to position their eyes where the nystagmus is minimal (96). It is interesting that there is a significant difference in anomalous head posture between the FRMD7 and non-FRMD7 group (figure 1.10). However there were no notable differences in VA between the two groups (91). The study by Stevens and Hertle found that IIN patients with an anomalous head posture (AHP) tend to have better VA than those without such a head posture (97) suggesting that VA is closely correlated to position of eyes in the orbit and duration of foveation (98,99). A plausible explanation for the lack of head turn amongst those with the mutated gene may lie with the fact that their null position is closer to the primary position of gaze (i.e. 0°). From figure 1.10 it is clear that the mean amplitude is significantly reduced at 0° when compared to ±15°, so there is no need for them to adopt an AHP (96).

OKN abnormalities have also been reported in patients with *FRMD7* mutations. Self et al. reported both low gain and absent OKN responses from patients with *FRMD7* mutations (79). Thomas et al. showed that unaffected

female carriers can have subclinical nystagmus and there is a bimodal

distribution of the OKN responses. Some carriers have good OKN responses

however poor gains were noted in some carriers (91) (figure 1.10).
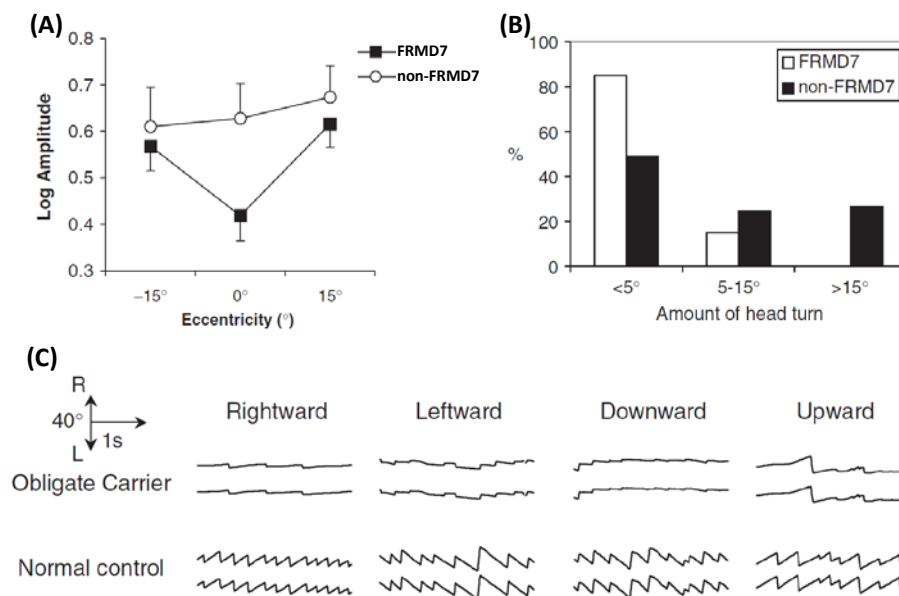
Figure 1.10: Phenotypical characteristics between FRMD7 and non-FRMD7 patients. FRMD7 patients have gaze-dependent changes in amplitude while non-FRMD7 patients do not have significant changes in amplitude with gaze (A). Non-FRMD7 group is associated with larger degrees of anomalous head posture when compared to the FRMD7 group (B). Some unaffected obligate carriers showed poor gain for OKN response in all directions (C). (Reproduced with permission from: (91))

1.3.1.6 INVESTIGATIONS

Most investigations in patients with IIN would yield negative findings.

However it is important to carry out these tests in order to rule out other

underlying disorders such as albinism, retinal dystrophies and structural

lesions in the brain. Previous studies have suggested that in families that

have nystagmus at least one affected individual should undergo

electrodiagnostic tests (this includes electroretinography (ERG) and visual

evoked potentials (VEP)) (47,91). It is recommended that singletons undergo

electrodiagnostic tests. A diagnosis of IIN is inferred if there are no significant abnormalities on electrodiagnostic testing.

Once a clinical diagnosis of IIN has been established sequence analysis should be used to confirm or rule out mutations of *FRMD7*. Previous studies have shown that sequence analysis of the exons and splice sites is associated with a higher frequency of mutation detection (between 83-94%) in X-linked families (46,47,75). On the other hand mutation scanning is associated with a lower mutation detection frequency (approximately 20%)(46,62,79).

1.3.2 ALBINISM

1.3.2.1 GENETICS

Albinism is subdivided into: Oculocutaneous Albinism (OCA) and Ocular Albinism (OA) (100). As a rough rule, in OCA there is both cutaneous and ocular involvement and in OA there is only ocular involvement. However, histopathological evidence suggests this terminology is not entirely accurate since in OA there could be some degree of cutaneous pigmentary dilution (101,102). Though there are many mutations associated with albinism, OCA is predominantly inherited as an autosomal recessive trait and OA is most commonly inherited as an X-linked disease (100,103-105). Mutation of the tyrosinase gene has been studied extensively and has been used to further sub classify OCA based on the tyrosinase hair bulb test (101). Mutations of five genes have been identified as the cause of albinism. Four genes are located on autosomes while one of the genes is located on the X-chromosome. A summary of genes involved in albinism are shown in table 1.5.

Table 1.5: The genes involved in albinism

Locus and name	OMIM number	Gene identified	Inheritance	Key Publication
OCA 1 (11q14-q21)	606933	Yes (*TYR*)	Autosomal recessive	(106)
OCA 2 (15q11.2-q12)	203200	Yes (*OCA 2*)	Autosomal recessive	(107)
OCA 3 (9p23)	203290	Yes (*TYRP1*)	Autosomal recessive	(108)
OCA 4 (5p13.3)	606574	Yes (*MATP*)	Autosomal recessive	(109)
OA 1 (Xp22.3)	300500	Yes (*GPR143*)	X-linked	(110)

1.3.2.2 PHENOTYPICAL CHARACTERISTICS

The word albinism originates from the Latin term *albus* which means 'white'; referring to the colour of the skin or hair of albinos due to hypomelanosis or amelanosis (14). Clinical features of OA are due to a reduction in the number of melanosomes. Interestingly, manifestations of OCA are due to reduced levels of melanin in each melanosome. Ocular pathologies associated with albinism are shown in table 1.6. Example of nystagmus associated with albinism is shown in the electronic appendix. One of the characteristic clinical features seen in albinism is transillumination defects of the iris (figure 1.11).

Increasing grades of iris transillumination associated with albinism
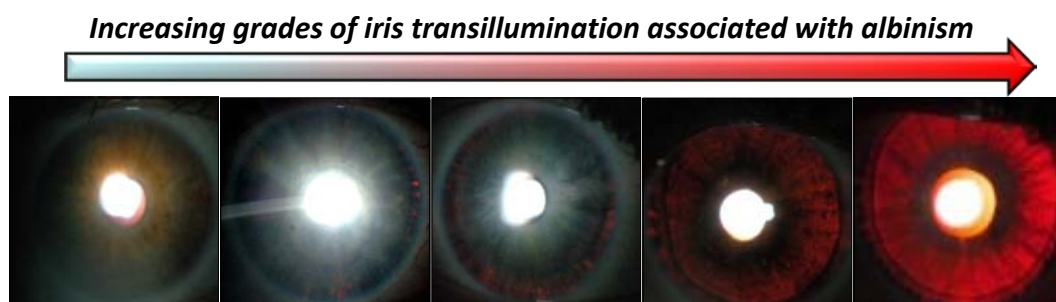
Figure 1.11: *Varying degrees of iris transillumination associated with albinism*

Table 1.6: Ocular pathologies associated with albinism

	Part of the visual system affected	Description
1.	**Eye movements**	• Nystagmus is present (111) • May have strabismus and anomalous head posture (5,101) • Nystagmus waveform is similar to that seen IIN
2.	**Iris**	• Diminution in size or number of melanin granules (101) • Clinically this is seen as a transillumination defect of the iris (6,12)
3.	**Retina**	• Foveal hypoplasia is almost always present. This causes decreased or absent foveal reflex and reduced vision (101) • Hypopigmented fundus • Some patients may complain of photophobia, since the retinal pigment epithelium melanin is reduced or absent. Melanin acts as a neutral density filter in scattering light (6,112). • Abnormal optic nerve has also been described (113)
4.	**Chiasm and visual cortex**	• Abnormal decussation of nerve fibres at the optic chiasm* (measured using VEP) • This may partly explain the degraded stereovision and abnormal representation of space in the central nervous system (114).

In healthy individuals, approximately 53% of the total fibres cross over at the optic chiasm. These fibres originate from the nasal hemi-retinae and join the fibres from contralateral temporal hemi-retinae (12,114). However in albinism the total number of fibres that cross over are much greater. The bulk of these fibres originate from the temporal hemi-retinae (figure 1.12).

These ocular pathologies are seen in both OCA and OA, thus suggesting that a reduction in melanin at focal sites is responsible for the pathologies rather than a pleiotropic effect of the responsible gene (101).
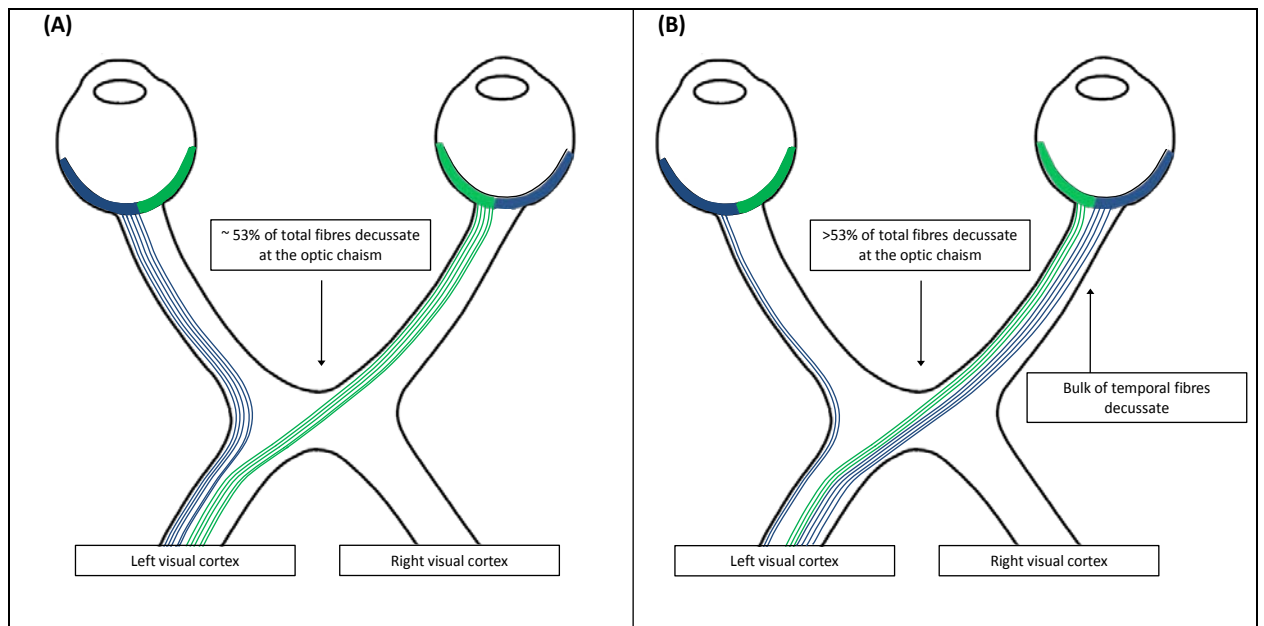
Figure 1.12: *Schematic representation of the decussation of nerve fibres at the optic chiasm in a normal subject (A) and an albino (B). Note in (B) the total number of fibres that cross over are much greater and a bulk of these fibres originate from the contralateral temporal hemi-retinae.*

1.3.2.3 INVESTIGATIONS

Apkarian et al. have shown that detecting asymmetric VEPs are the most

sensitive method for diagnosing albinism (figure 1.13) (115). In addition to

this other findings that would help support a diagnosis of albinism include

iris transillumination defects on slit lamp biomicroscopy (figure 1.11) and

foveal hypoplasia on fundoscopy and OCT.
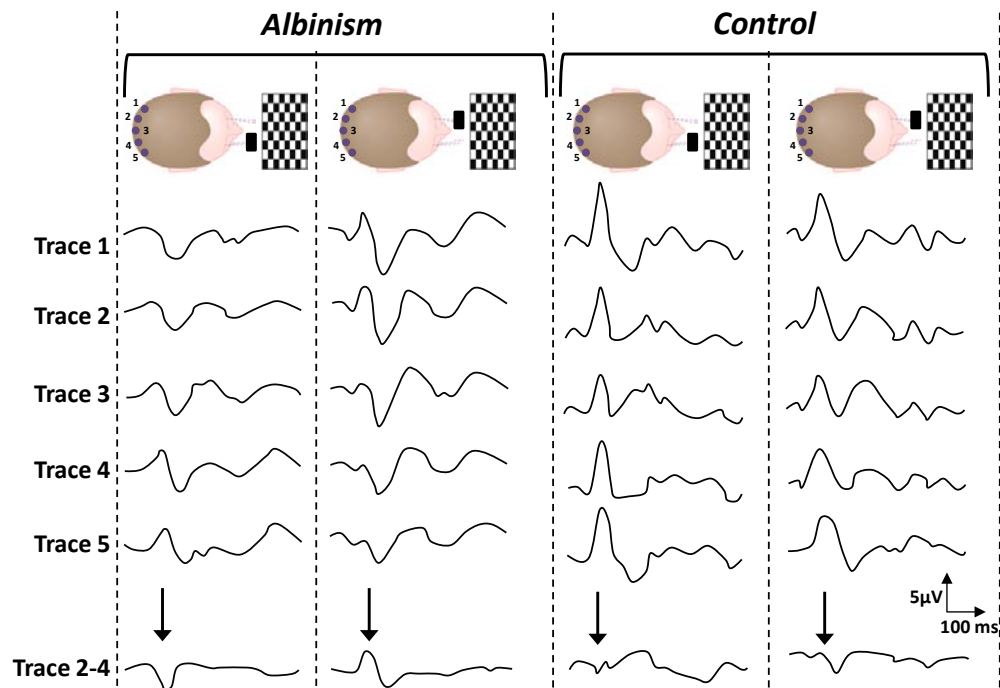
Figure 1.13: Albino patient demonstrating hemispheric VEP asymmetry to pattern onset responses. Control subject shows an absence of a VEP asymmetry. The electrodes are placed approximately equidistant from the central electrode (electrode 3). The electrodes 1 and 2 are placed on the left occiput while the electrodes 4 and 5 are placed on the right occiput. The respective electrical potentials from each electrode are represented by the traces 1-5. The difference in potential between the left and right sides during monocular stimulation are represented in the bottom trace. The arrows represent the polarity reversal seen with albinism, while with the controls there is no significant asymmetry. (Based on: (116)*)*

Approximately 85% of *TYR* mutations can be detected by sequence analysis of the CDS, splice junctions, the 5' promoter region and the 3' UTR (117). The remaining 15% of mutations are thought to be in regulatory sites thus affecting gene transcription (118). The testing strategy employed for *OCA2* mutations depends on the ethnicity of the individuals; for individuals from a sub-Saharan African origin the first step involves a targeted mutation analysis for a 2.7kb deletion. If the deletion is not present then sequence analysis of the CDS is performed (119). In individuals of non-African origin an approach similar to *TYR* mutation analysis is applied (100). Mutations of *TYRP1* are more common in southern Africa, however sequencing the CDS

and splice junctions should reveal most mutations (120). Mutations of the

MATP gene is one of the most common cause of oculocutaneous albinism in

Japan (121); although there are mutation hotspots sequence analysis is the

preferred method for mutation analysis. Mutations of *GPR143* are also

detected by sequence analysis, approximately 48% of reported mutations are

intragenic deletions and 43% are point mutations (122).

The total cost for sequencing one patient for all five genes is currently high

(for examples $2500 is required to test albinism panel of genes at the

University of Colorado, Denver Genetics Lab (123)). This approach is

expensive partly due to the number of genes needed to be tested and thus the

overall number of exons/amplicons would be considerably large.

1.3.3 ACHROMATOPSIA

1.3.3.1 GENETICS

Achromatopsia is an autosomal recessive disorder associated with mutations

of *CNGA3, CNGB3, GNAT2* and *PDE6C* genes (table 1.7). The protein products

from these genes are important in visual transduction and there is restricted

expression within the cone photoreceptors (124-127). Mutations of *CNGA3*

were identified to be causative of achromatopsia in 1998 by Kohl et al. They

showed that both homozygous and compound heterozygous mutations can

cause rod monochromacy (125). Previous reports have shown a high

prevalence of autosomal recessive achromatopsia in the Pingelapese

islanders in Micronesia. Sundin et al. identified that mutations of the *CNGB3*

gene were responsible for achromatopsia in the island of Pingelap.

Interestingly they identified a founder mutation resulting in the amino acid

variation S435F (124). It is suggested that the founder mutation may have arisen as a result of a typhoon in 1775 which left only 20 survivors (128). In 2002 Kohl et al. showed that mutations of *GNAT2* was the third gene responsible for achromatopsia, most mutations identified were null mutations and thus resulting in loss of function of the Guanine nucleotide-binding protein G(t) subunit alpha-2 (127). The fourth gene identified to be pathological in achromatopsia was *PDE6C.* Both homozygous and compound heterozygous mutations have been reported (129).

Kohl et al. showed that mutations of the *CNGB3* accounts for 50% of all cases of autosomal recessive achromatopsia. They also identified a mutation hotspot, c.1148delC, which was responsible for approximately 70% of all *CNBG3* mutant alleles (130). Approximately 25% of patients with achromatopsia have mutations of the *CNGA3* gene (126). Mutations of *GNAT2* and *PDE6C* account for approximately 2% of cases of achromatopsia (127,129).

Table 1.7: The genes involved in achromatopsia

Locus and name	OMIM number	Gene identified	Inheritance	Key Publication
ACHM 2 (2q11)	216900	Yes (*CNGA3*)	Autosomal recessive	(125)
ACHM 3 (8q21-q22)	262300	Yes (*CNGB3*)	Autosomal recessive	(124)
ACHM 4 (1p13)	139340	Yes (*GNAT2*)	Autosomal recessive	(127)
ACHM 5 (10q24)	600827	Yes (*PDE6C*)	Autosomal recessive	(129)

1.3.3.2 PHENOTYPICAL CHARACTERISTICS

Achromatopsia has been reported as a non-progressive cone photoreceptor disorder (131). Patients with achromatopsia present with infantile nystagmus, reduced visual acuity, photophobia, impaired colour discrimination and paradoxical pupils (124,125,127,132,133). The macular appearance is variable and the following findings have been previously reported: absent foveal reflex, pigmentary changes, bulls eye/atrophy (132).

Achromatopsia has been classified as complete and incomplete based on the severity of the phenotype (134). X-linked achromatopsia or blue cone monochromatism (BCM) has also been previously termed as incomplete achromatopsia (131). However, recent studies suggest that milder phenotypes (oligo cone trichromacy) are typically associated with splice mutations of *GNAT2* (135). Thiadens et al. showed that both complete and incomplete achromatopsia can arise from the same mutation, T383IfsX13-/- of the *CNGB3* gene (132,133). This suggests that there is much phenotypic variability associated with achromatopsia. The role of making a distinction between complete and incomplete achromatopsia is questionable since the genetic aetiology and phenotypic consequence is eventually the same.

The prevalence of achromatopsia is estimated at 1 in 30,000; however as mentioned above, in certain populations (for example in the Pingelap island the prevalence is estimated between 4-10%) and in regions where consanguinity is common the prevalence is higher (134).

1.3.3.3 INVESTIGATIONS

A clinical diagnosis of achromatopsia can be made based on the above
mentioned clinical findings and electrodiagnostic results. The
electroretinography typically show extinguished or severely reduced
photopic responses with normal scotopic responses (133) (figure 1.14).
However, it is difficult to distinguish between achromatopsia and BCM in
families where no females are affected (since BCM is X-linked recessive).
Some studies have used Berson's test in order to achieve this (136,137),
however it is not clear how sensitive the test is for screening BCM. In certain
specialized electrodiagnostic centres one can identify BCM by noting the peak
photopic luminosity function. In BCM this should be at 440nm which
corresponds to the S-cones peak sensitivity.
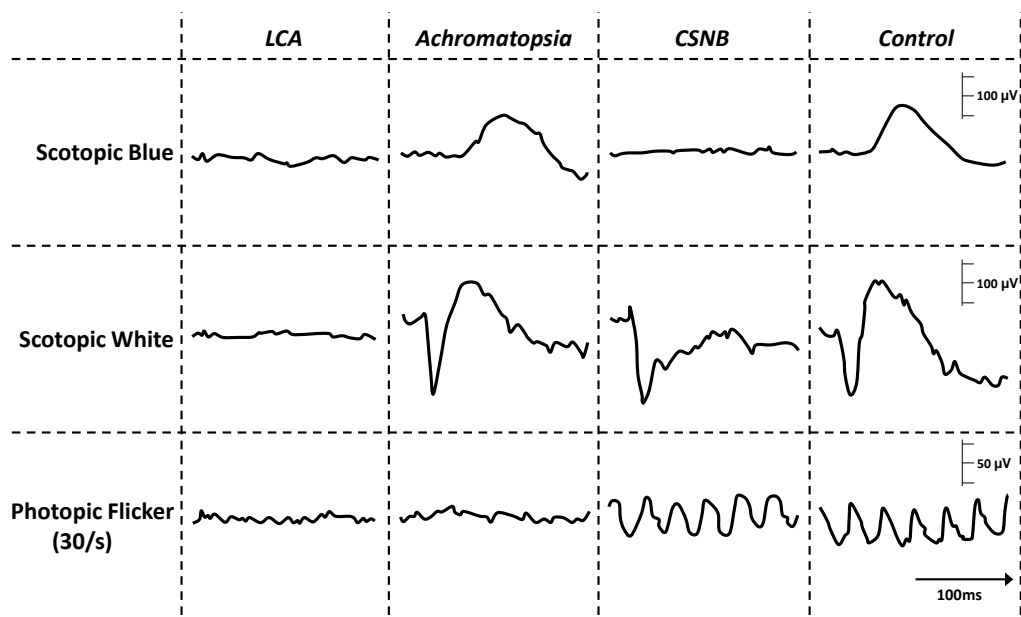
Figure 1.14: *Examples of typical electroretinography recordings from
patients with cone and/or rod dysfunction. An extinguished photopic response
is characteristic of achromatopsia. In Leber's Congenital Amaurosis (LCA)
both cones and rods are affected, while in Congenital Stationary Night
Blindness (CSNB) only the rods are affected. (Adapted with permission from:
(138))*

The total cost for sequencing all four genes implicated in achromatopsia is expensive (for example the achromatopsia genetic testing panel costs $2890 at the University of Colorado, Denver Genetics Lab) (123). Although the costs for sequencing are high; a testing strategy which employs a tiered approach by screening for the more prevalent mutations is more cost-effective. Thus a testing algorithm would consist of:

(1) Screening for the mutation hotspot c.1148delC in *CNGB3*

(2) Sequence analysis of *CNGA3*

(3) Sequence analysis of *CNGB3*

(4) Sequence analysis of *GNAT2*

(5) Sequence analysis of *PDE6C*

1.3.4 *PAX6*

1.3.4.1 GENETICS

One of the first cases that reported mutations of the *PAX6* gene was in sporadic cases with aniridia (139). In 1993, *PAX6* point mutations were identified in both sporadic and familial (autosomal dominant) cases (140). Soon it was clear that there was a high frequency of mutations of the *PAX6* gene and the main phenotype resulting from this is aniridia (141) (table 1.8).

PAX6 has an interesting expression pattern with restricted expression in neural and ocular tissue. However other sites that also show *PAX6* expression during development include the nasal and pancreatic tissue. *PAX6* has a role in organogenesis and it functions by altering the expression of other genes (142). In addition to the obvious ocular phenotypes, cerebral malformations

and olfactory dysfunction has also been reported (143). Thus the phenotypes

associated with *PAX6* mutations relate to the expression patterns seen.

Table 1.8: Details of aniridia locus

Locus and name	OMIM number	Gene identified	Inheritance	Key Publication
AN (11p13)	106210	Yes (*PAX6*)	Autosomal dominant	(139)

1.3.4.2 PHENOTYPICAL CHARACTERISTICS

The prevalence of aniridia is approximately 1/60,000 to 1/100,000 and thus

it is quite a rare disorder. However aniridia is not the only phenotype

associated with *PAX6* mutations. Other ocular phenotypes described with

PAX6 mutations included: congenital cataract, corneal dystrophy, foveal

hypoplasia, optic nerve hypoplasia, optic disc coloboma, strabismus and

nystagmus (140,141,144,145). The penetrance of this disorder is 100% in

both heterozygous males and females. In 95% of cases with *PAX6* mutations

nystagmus has been reported (146). Unlike IIN and albinism there is also a

significant vertical component associated with the nystagmus (see example

of video of vertical nystagmus in the electronic appendix).

Milder aniridia phenotypes have also been described to be associated with

PAX6 missense mutations. Similarly a classification from stromal hypoplasia

to complete aniridia has also been documented (147). Childhood or

adulthood glaucoma has also been associated with the aniridia phenotype

(148). Homozygotes and compound heterozygotes have also been reported

(144,149). It can be associated with still birth or with bilateral anophthalmia,

microcephaly and choanal atresia.

1.3.4.3 INVESTIGATIONS

A slit lamp examination would be able to detect cornea, iris and lens abnormalities. Examples or iris defects associated with *PAX6* mutations are shown in figure 1.15. Additional findings that could be detected on fundus examination include loss of the foveal reflex, and optic disc abnormalities. However since these phenotypes can occur in isolation, genetic testing is necessary to establish whether the phenotype is related to *PAX6* mutations if there is clinical suspicion.

| Circumpupillary Aplasia | Subtotal Aniridia | Complete Aniridia |

Figure 1.15: *Mutations of PAX6 can be associated with varying degrees of iris tissue loss ranging from circumpupillary aplasia to complete aniridia. (Adapted with permission from: (147))*

The mutation detection frequency is dependent on the type of test utilized. In simplex cases, sequence analysis of the CDS detects 55% of mutations and deletion testing detects 22% of mutations. In families with autosomal dominant inheritance of aniridia, sequence analysis of the CDS reveals 62.5% mutations while deletion testing detects 17% of mutations. It is speculated that the remaining mutations are located within control regions (150).

1.4 AIMS

1.4.1 OVERALL AIM

It is unclear whether there is a common aetiological factor that causes infantile nystagmus. Indeed, in albinism, achromatopsia and patients with *PAX6* mutations it is well known that there are retinal abnormalities, while in IIN (or *FRMD7*-related infantile nystagmus), to date, retinal abnormalities have not been described. Circumstantial evidence from disorders such as albinism, aniridia and achromatopsia suggest that an afferent defect in the visual system is the common link. However the presence of IIN, where to date no ocular abnormalities have been found, argues against an afferent defect. Thus it is presumed that a more central brain abnormality is likely to be the cause of nystagmus. Furthermore, the CEMAS classification and other studies (30,34,35) imply that the mechanism of causation, visual prognosis and treatment is the same and thus the umbrella term infantile nystagmus syndrome is used for all these disorders.

The overall aim is to genetically characterize a large cohort of IIN patients and subsequently perform detailed phenotyping experiments to assess whether an afferent defect could be present. The retinal phenotypical characteristics will also be compared to other infantile nystagmus forms with afferent defects.

In this thesis, patients with albinism, achromatopsia and *PAX6* mutations will be used as a representative group of nystagmus associated with afferent defects.

1.4.2 SPECIFIC AIMS

1.4.2.1 MOLECULAR GENETIC AIMS

- To characterize the mutational spectrum in families and singletons with IIN

- To determine whether the variability of penetrance in female carriers with *FRMD7* mutations is due to the mutation type or domain involved.

- To identify neural substrates that could be involved in *FRMD7* related infantile nystagmus. To characterize the spatial and temporal expression profile of *FRMD7* in developing human, murine, rat and zebrafish retina.

- To determine the molecular genetic basis of idiopathic infantile periodic alternating nystagmus

1.4.2.2 CLINICAL AIMS

- To investigate whether OCT measurements is a reliable method of phenotyping the retina in patients with infantile nystagmus.

- To identify whether there are retinal changes in patients with *FRMD7* mutations using OCT.

- To characterize and compare the retinal and optic nerve phenotype of patients with *PAX6* mutations, albinism and achromatopsia using OCT. To investigate in achromatopsia whether retinal changes are progressive.

- To compare and classify foveal hypoplasia in albinism, achromatopsia, patients with *PAX6* mutations and isolated cases and to investigate

whether morphological changes seen on OCT can help to predict

visual acuity in foveal hypoplasia.

2. CHAPTER TWO: METHODS

In this chapter the main methods relating to genotyping, cellular phenotyping and clinical phenotyping are described. The specific methods and patient cohorts relating to each experiment have been mentioned within each chapter.

2.1 METHODS RELATED TO GENOTYPING

The PCR design and optimisation was performed by the author. Subsequent high throughput sample preparations and sequencing were performed by Asper Biotech, Tartu, Estonia. Mutation analysis and interpretation of results was performed by the author.

2.1.1 SAMPLE COLLECTION

Ethical approval was obtained prior to the start of the study (Title of the study: "*Genetic studies of patients and their families with eye and eyelid movement disorders*"; UHL reference number: 9732). Prior to obtaining a saliva sample, the adult patients and/or family members were given an adult information leaflet (see electronic appendix) and appropriate consent forms (see electronic appendix). In children (less than 18 years of age) a child information leaflet and consent form was used (see electronic appendix). If the child was old enough they were also given the opportunity to give consent in addition to parents or guardians. After obtaining consent the saliva samples were collected using the Oragene® DNA sample collection kit (DNA Genotek Inc. Ontario, Canada). For DNA samples the OG-250 DNA disc format and OG-500 DNA tube format (figure 2.1 a&b) were used for collection of saliva. For mRNA samples the RE-100 Oragene RNA sample collection kit (figure 2.1c) was used. Buccal swabs (BuccalAmpTM, DNA

extraction kits- Epicentre Biotechnologies) were used if the child was unable to give a saliva sample. Saliva samples and buccal swabs were stored at 4°C.
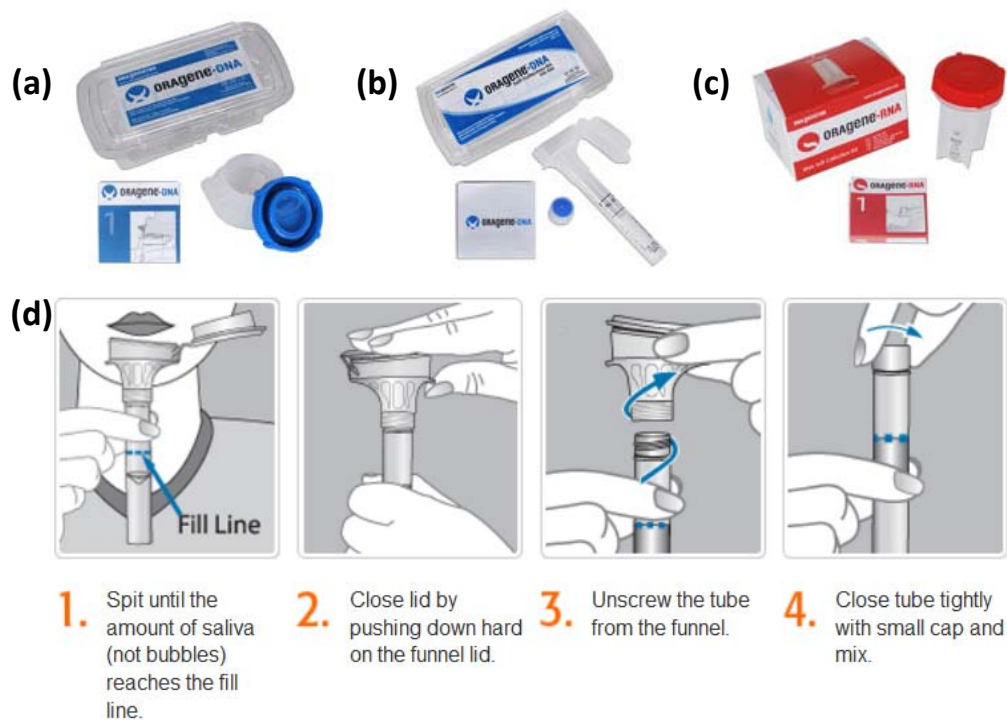
Figure 2.1: *DNA and RNA collection kits used for obtaining saliva samples. (a) OG-250 DNA disc format, (b) OG-500 DNA tube format, (c) RE-100 RNA collection kit, (d) instructions given to patients. (From: www.dnagenotek.com)*

2.1.2 NUCLEIC ACID EXTRACTION

2.1.2.1 DNA EXTRACTION

The OG-250 or OG-500 tubes were incubated at 50°C in a water bath for 1.5 hours. 500μL of the sample was then transferred into a 1.5mL microcentrifuge tube. 20μL of Oragene purifier (OG-L2P) was then added to the tube and then the sample was vortexed for 20 seconds. The samples were incubated on ice for 10 minutes and then centrifuged for 5 minutes at 13,000 rpm. The supernatant was transferred into a sterile and clean microcentrifuge tube. 500μL of 100% ethanol was added to the supernatant and inverted 20 times. In order to allow precipitation of the DNA, the samples

45

were kept at room temperature. The samples were centrifuged for 2 minutes at 13,000 rpm thus creating a DNA pellet. The supernatant was discarded. The pellet was washed with 250μL of 70% ethanol without disrupting the pellet. The pellet was either re-suspended in 100μL of TE buffer (Tris-HCL (10mM) and EDTA (1mM); pH =8.0) or dH$_2$O. The sample was vortexed to ensure that the pellet was completely dissolved. The sample was incubated at 50°C for 1 hour with vortexing at 15 minutes, 30 minutes and 45 minutes. The sample was stored at -20°C. For buccal swabs the Qiagen QIAamp DNA Mini Kit (Qiagen Ltd, UK) was used for DNA extraction.

2.1.2.2 RNA EXTRACTION

The RE-100 tubes were incubated at 50°C in a water bath for 1.5 hours. 500μL of the sample was then transferred into a 1.5mL micro-centrifuge tube. The samples were then incubated at 90°C for 15 minutes after which it was cooled to room temperature. 20μL of neutralizer solution was added to the sample and vortexed. In order to ensure precipitation of impurities the samples were incubated on ice for 10 minutes. The samples were centrifuged at 13,000rpm for 10 minutes. The supernatant was then transferred into a fresh tube. 1mL of 95% cold ethanol was added to the supernatant and the tube was vortexed. In order to ensure RNA precipitation the samples were incubated at -20°C for 30 minutes. The samples were then centrifuged for 3 minutes at 13,000rpm. The supernatant was removed ensuring that the pellet was not disrupted. The pellet was dissolved in 350μL RLT Buffer (RLT Buffer was obtained from QIAGEN RNeasy Micro Kit) by vortexing. 350μL of 70% ethanol was added to the sample and vortexed. The QIAGEN RNeasy

Micro Kit was used at the end of the RNA extraction protocol to clean up and elute RNA. The manufacturers' protocol for the RNeasy Micro Kit was used for the cleanup step.

2.1.3 QUALITY CONTROL AND QUANTIFICATION OF NUCLEIC ACIDS

The quality and quantity of DNA or RNA samples were assessed using a spectrophotometer. The NanoDrop® ND-1000 UV-Vis spectrophotometer (NanoDrop Technologies, Inc., Wilmington USA) was used to measure the sample concentration and purity. Prior to loading the sample the upper and lower pedestal of the sample retention system was cleaned using de-ionized water. The NanoDrop program was loaded on the PC connected to the machine and Nucleic Acid-DNA module is selected for quantification and determining the quality of DNA or RNA. Either the DNA-50 or RNA-40 feature is selected depending on whether the sample was DNA or RNA respectively.

A 1µL re-suspension buffer (either dH_2O or TE buffer) was placed on the lower measurement pedestal and the sampling arm was lowered into the down position. Subsequently the "blank" button is selected to calibrate the system. The sample is then loaded and the "measure" button is selected. The results screen gives the concentration in ng/µL and absorbance of the sample at 230nm (A230), 260nm (A260) and 280nm (A280). The A260:A280 ratio and A260:A230 ratios are assessed to determine the purity of the DNA/RNA. For DNA samples the ratio should be approximately 1.8 while for RNA samples the ratio should be approximately 2.0. The A260:A230 ratio is a secondary measure of nucleic acid purity and it should be higher than the A260:A280 ratio; typically in the range of 1.8-2.2. If the samples were too low

in concentration or had contaminants as reflected by poor (A260:A230) ratios the Zymo DNA Clean & Concentrator™ Kit (Zymo Research Corporation, Irvine, USA) was used to purify and concentrate the sample.

2.1.4 POLYMERASE CHAIN REACTION

The essential components required for polymerase chain reaction (PCR) include: (a) DNA template, (b) forward and reverse primers, (c) building blocks for the amplicons (dinucleotide triphosphates: dATP, dCTP, dGTP and dTTP), (d) enzyme to catalyse the reaction (Taq Polymerase) and (e) Co-factors such as $MgCl_2$. The PCR procedure consists of a series of temperature changes which is broadly classified into the following steps: (1) Initialisation step (95°C) to activate the DNA polymerase, (2) denaturation step (95°C) to separate the double stranded DNA, (3) annealing step (66°C) allowing the primers to anneal to the template, (4) extension step (72°C), the temperature is based on one which is optimal for the activity of DNA polymerase, (5) final extension step (72°C) and (6) final hold (4°C) for storage. Steps 2-4 were repeated for over 30 cycles before proceeding to step 5 and 6.

2.1.4.1 PRIMER DESIGN FOR *FRMD7* SEQUENCING

Primers were designed using Primer3 online primer design software (151) and then tested *in-silico* using GenomeTester v1.3 (152). The following principles were considered while designing the primers: (a) the size of the primers should be less than 20 bases (b) a GC clamp was used if possible to prevent primer-dimer formation (c) stretches of poly(A,T,G or C) repeats were avoided and (d) the melt temperatures (T_m) of the forward and reverse primers should match. The forward and reverse primers were designed to

48

amplify each exon and flanking sequences to include the splice site junctions.

The forward and reverse primers used are shown in table 2.1.

Table 2.1: Forward and reverse primer sequences, product sizes and melting temperature (Tm) used to amplify *FRMD7* exons.

Exon	Primers 5´- 3´	Product size	Tm (°C)
Exon 1	GGGCTGTTCACAAATGACAA	389 bp	59
	AAGAAGGCTAGAGGAAGTCCAG		58
Exon 2	AAACAAAGAGGGAGGACAAAAA	500 bp	57
	CCAAGGTGGTTTGTTATAAGGC		60
Exon 3	TCTCAAAGCCCTTTTCTCCC	500 bp	58
	TGGAGGGTTCAAATGTGGAG		58
Exon 4	CCCTTTGGATGATGAACACC	500 bp	58
	GAAAGAGGGGTGGGAGAACT		60
Exon 5	TCCCCTGTAAACCCTAACACAG	500 bp	62
	GCAGAAACCACCAGAGGATG		60
Exon 6	TGCCTCAAGAATGACATTTCC	396 bp	60
	GAGGCTTTGGACTGCATTG		59
Exon 7	ATCACCTTGGGAAAGGACAC	500 bp	58
	TCTGGCACAAACTCGGTACTT		59
Exon 8	GAGCTGCCCCATTTTCCTAT	500 bp	58
	GCCTTCTTTGACCACAGCTC		60
Exon 9	CTTAGGTAAGGTGCCCCCAT	500 bp	60
	TACAGGGAGCCAAGTGGAAA		58
Exon 10 + 11	TCAATTCATGGAAGCATTTGAA	500 bp	55
	TGCCTGGTCCTTGAATAAGTG		59
Exon 12A	GACAGGGTCCATATAAATAAAAGGG	474 bp	63
	TGTATACACTCAGAGTCTGGAAGTAGG		67
Exon 12B	CTTCATTGCAGTGGGCTCTA	500 bp	58
	ACCAAAATGTGAATGGAGTGC		57
Exon 12C	AGAACTGCTGGCAACTCCTG	481 bp	60
	CGGATGTGCCCTATATTCCT		58
Exon 12D	CCAATGAATATGTAGTAACCAAGAAAA	500 bp	61
	AGCAAACCCCTAAAAGGTCC		58
Exon 12E	CCTTCCTGAGGCTGTAGGAG	595 bp	59
	TGCTGAAGACAGGACTTCACTAAA		60
Exon 12F	CCTCCCTCCTTTTCCATGTT	591 bp	60
	TGACTGTGTTGATCTTTGTGCTC		60

2.1.4.2 STANDARD PCR METHODS

The standard thermocycling conditions and reagents used for PCR are shown

in table 2.2.

Table 2.2: Reagents for the PCR (A) and amplification protocol (B).

(A)

PCR reagents	Volume per 15µL (final concentration/quantity)
F+R primers (5µM)	3µL (1µM)
10x PCR reaction buffer	1.5µL (1x)
25mM MgCl$_2$	1.5µL (2.5mM)
2.5mM dNTP	1.5µL (0.25mM)
HotSmart DNA polymerase (10U/µl)	0.1µL (1U)
Template DNA (50ng/µL)	2µL (100ng)
MilliQ H$_2$O	Make upto 15µL

(B)

Step	Temperature (°C)	Time (minutes)
1	95	15.00
2	95	0.20
3	66	0.30
	(-1°C per cycle)	
4	72	0.35
5	Go to step 2	8 cycles
6	95	0.20
7	58	0.30
8	72	0.35
9	Go to step 6	16 cycles
10	95	0.20
11	56	0.30
12	72	0.35
13	Go to step 10	16 cycles
14	72	7.00
15	4	Storage

The PCR products were verified by loading 2 µl of the samples on a 1.5%

agarose gel (SeaKem® LE Agarose; BioAtlas Titan Sight) for gel

electrophoresis (figure 2.2).
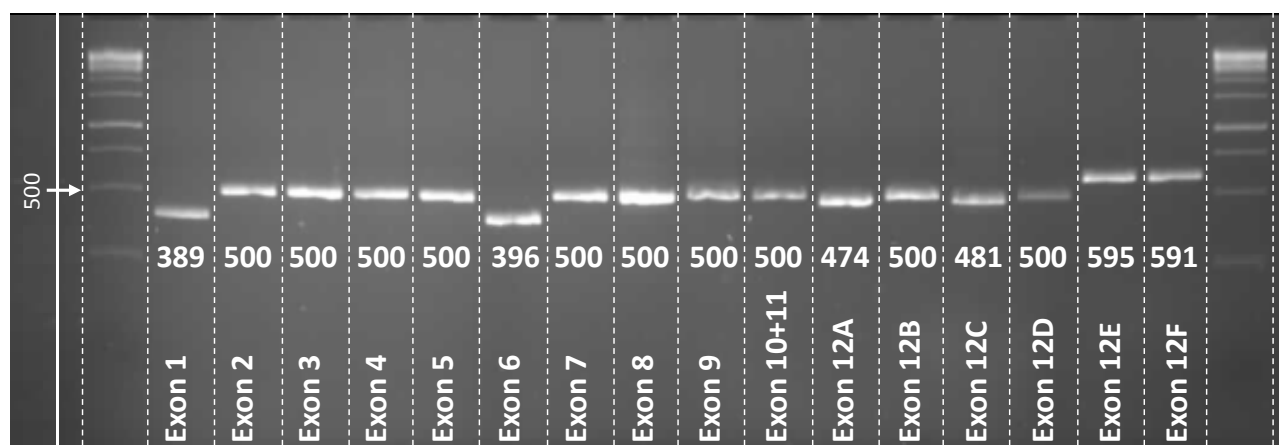
Figure 2.2: *PCR products on 2% agarose gel. Amplicon sizes and amplicon identity are shown below each band. The ladder is shown on the outer most lanes.*

2.1.5 SEQUENCING REACTION

After the amplicons were confirmed on a gel, the PCR products were cleaned up using Exonuclease I/Shrimp Alkaline Phosphatase (Fermentas). The PCR products were sequenced using the 3730xl DNA Analyzer (Applied Biosystems, Life Technologies Corporation, California, USA). The sequencing reactions were performed at the Estonian Biocentre, DNA Genotyping and Sequencing Core Laboratory. The output data was collected with 3730 Data Collection v3.0 and the analysis was done with Sequencing Analysis 5.3.1 using KB basecaller. This generated the ABI raw trace files.

2.1.6 MUTATION ANALYSIS

2.1.6.1 IDENTIFYING MUTATIONS AND POLYMORPHISMS IN *FRMD7*

The ABI trace files were analysed using two specialized software packages. Mutation analysis software SeqScape® version 2.1.1 (Applied Biosystems, Life Technologies Corporation, California, USA) and Mutation Surveyor® v3.30 (SoftGenetics, Pennsylvania, USA) were used for basecalling and alignment of the contigs. The Genbank file (Accession ID: NM_194277.2) was imported into SeqScape/Mutation Surveyor and used as the reference cDNA

sequence for contig alignment. Base position +1 corresponded to A of the translation initiation codon ATG. Intronic sequence changes were identified based on the *FRMD7* genomic sequence (Accession ID: NC_000023.10). Amino acid changes were identified based on the reference protein sequence (Accession ID: NP_919253.1). Allelic variations were assessed against the sequence data from 300 male controls (without nystagmus). The control dataset was kindly provided by Patrick Tarpey (Wellcome Trust Sanger Institute, UK).

2.1.6.2 MUTATION MODELLING

The polymorphisms detected on sequence analysis were analysed first against the control database. If the polymorphism was not present in the control dataset, *in-silico* predictions were used to model the mutation. The structural effects of these mutations were elucidated based on the known crystal structure of the closest orthologue (PDB Accession ID: 1GG3) and secondary structure prediction of the FRMD7 protein sequence using Emboss Garnier (153). Finally the stability of the mutant protein was assessed using I-Mutant (v2.0) (154) and Coot (v0.6) (155). The effect of splice site mutations and intronic base changes were analysed using Alternative Splice Site Predictor (ASSP) (156). All mutations and polymorphisms were reported according to the guidelines set out by the Human Genome Variation Society (HGVS) (157).

2.2 *IN-SITU* HYBRIDISATION IN HUMAN AND MURINE TISSUE

The experiments related to section 2.2 and 2.4.1 was performed by the author at the Centre for Life, MRC-Wellcome Human Developmental Biology Resource, Institute of Human Genetics, Newcastle, United Kingdom. The author was supervised by Professor Susan Lindsay and Mrs. Moira Crosier.

In-situ hybridisation is a molecular biology technique used to identify the mRNA of interest in tissues. This is achieved by using labelled probes which are complimentary to a unique part of the mRNA sequence. After the complimentary sequence hybridises to the mRNA an antibody is added which is conjugated with an enzyme (alkaline phosphatase). This is detected by chemiluminescence.

2.2.1 PROBE PREPARATION

The sense and antisense probes for in-situ hybridization experiments were generated as described in (47). This briefly consisted of using the *FRMD7* cDNA as the template for PCR amplification. A region between exon 9 and 12 (figure 2.3) was amplified using the standard PCR conditions. The primers used for this is shown in table 2.3. The amplimers were then subcloned into the pGEM-T Easy vector based on the manufacturer's guidelines. The FRMD7-pGEM-T Easy Vector was kindly provided by Mr. Steven Lisgo.

Table 2.3: List of primers used for generating probes for *in-situ* hybridisation experiments in humans, mice and zebrafish

Primer ID	Primer Sequence (5' – 3')	Product Size	mRNA of interest
FRMD7h_1F	AGGGTTCCAGTTTCCGCTAT	599	FRMD7 (X chromosome) Human*
FRMD7h_1R	CTGGGAGGCATAATACCAA		
FRMD7a_1F	CGACACCATAATGGCAGC	849	FRMD7 (Chr 1) Zebrafish
FRMD7a_1R	CGACTTGCAGTAACTTCTTTC		
FRMD7a_2F	AGAGACACGGTGGAGTTTTC	700	
FRMD7a_2R	TCTGATGGGTTTGAGGAAG		
FRMD7b_3F	TTGTGGACACCTTAAACTGG	787	FRMD7 (Chr 21) Zebrafish
FRMD7b_3R	GGAGTGATTTTTGCTTGCTC		
FRMD7b_4F	AATGTGCGCAAACTCAGC	828	
FRMD7b_4R	CCGCTGATAGTTTAAAATGC		

Due to the significant sequence homology between the human and murine mRNA sequence the same sense and antisense probes were used.

The relevant recognition sites used within the pGEM-T easy vector are:

- T7 promoter (sequence: 5'-TAATACGACTCACTATAGGG-3'; interval: 3000-2)
- SP6 promoter (sequence: 5'-TATTTAGGTGACACTATAG-3'; interval: 159-142)
- Cloned insert (interval: 60-61)
- Sal I restriction enzyme recognition site (sequence: 5'-GTCGAC-3'; interval: 91-96)
- Sac II restriction enzyme recognition site (sequence: 5'-CCGCGG-3'; interval: 46-51)

Two sets of linearised vector were created using Sal I and Sac II. These were subsequently used for the *in-vitro* transcription reaction.
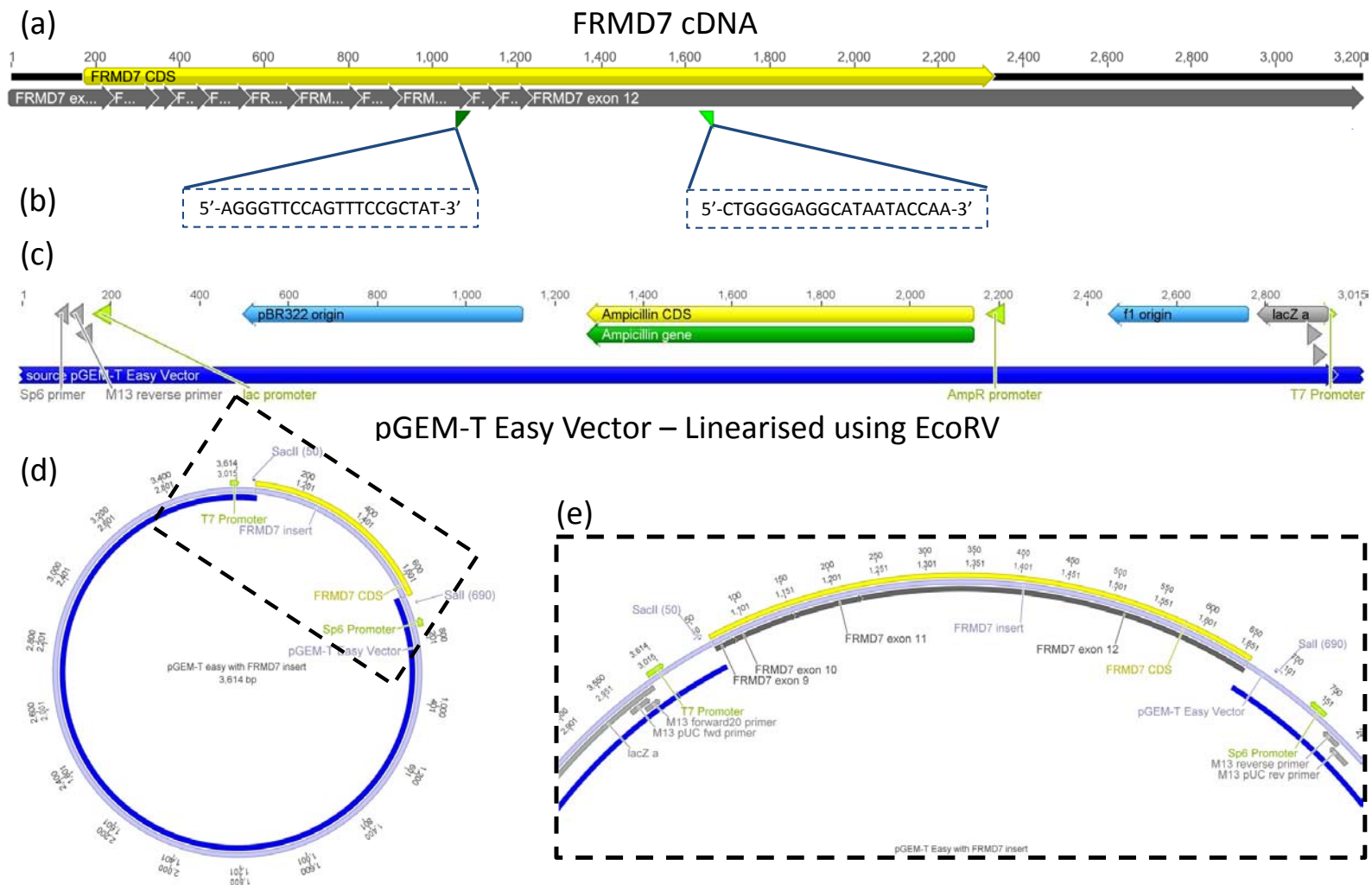
Figure 2.3: *The FRMD7-pGEM-T Easy Vector. A region between exon 9-12 of the FRMD7 cDNA (a) was amplified using the primers (b). The amplicon was inserted into the linearised vector (c) within the multiple cloning site (d). A magnified image of the multiple cloning site (e) shows the flanking T7 and SP6 promoters which were used to generate the anti-sense and sense probes respectively.*

2.2.2 *IN-VITRO* TRANSCRIPTION REACTION

A 20µL reaction mixture was prepared using the following elements:

1. 1µg of linearised DNA

2. 2µL of 10x Transcription buffer

3. 2µL DIG RNA Labelling mix

4. 1µL of RNAsin

5. 2µL of RNA polymerase

The transcription buffer, DIG RNA labelling mix, RNAsin and the RNA polymerases were obtained from Roche (Roche Diagnostics GmbH, Germany). The reaction mixture was made up to 20µL using ddH$_2$O. This was incubated at 37°C for 2 hours. After 2 hours, 2µL of DNase 1 was added to the reaction mixture; this was gently mixed and incubated at 37°C for 15 minutes. The reaction mixture was made up to 50µL by adding 0.1% v/v diethylpyrocarbonate (DEPC) treated H$_2$O and vortexing. In order to remove the unincorporated nucleotides from the labelling reaction the illustra™ ProbeQuant™ G-50 Micro Columns was used as per the manufacturer's guidelines. The concentration of the probes was determined using Nanodrop (as described in section 2.1.3 using the RNA-40 module).

Two sets of reactions were performed. The only elements that changed were the linearised DNA and the RNA polymerase. In the first reaction; T7 RNA polymerase was used with a vector that was linearised using Sal I restriction enzyme. In the second reaction: SP6 RNA polymerase was used with the vector that was linearised using Sac II restriction enzyme. The first reaction

would create the antisense probes (probe ID: 476) which are complimentary to part of the *FRMD7* mRNA sequence. The second reaction would create the sense probes (probe ID: 477), these represent the control probes which are anti-complimentary to the *FRMD7* mRNA sequence. In order to confirm the products of the in-vitro transcription reaction, the products were run on an RNA formamide gel (figure 2.4). After confirming the product sizes the samples were stored at -80°C.
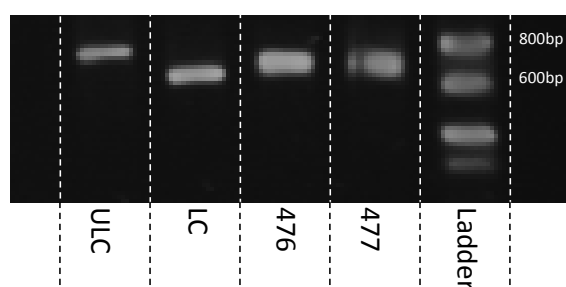
Figure 2.4: *RNA gel run to confirm products of in-vitro transcription reaction. Both probes 476 (antisense) and 477 (sense) were approximately 680 bases. Control RNA was also used this was either labelled (LC) or unlabelled (ULC) with digoxigenin.*

2.2.3 PREPARING AN RNA AGAROSE GEL

In order to perform an RNA gel run, an RNase free environment is essential hence baked glass ware and DEPC treated H_2O was used. 36mL of DEPC-H_2O was mixed with 5mL of 10x MOPS buffer and 1g of agarose. The mixture was microwaved for 1 minute. The mixture was then made up to 41mL using DEPC-H_2O. Subsequently 9mL of 37% formamide was added to make the solution up to 50mL. The gel was then poured and allowed to set while the samples and base pair ladder were prepared. The samples consisted of a mixture of: (a) 5µL DEPC-H_2O, (b) 6µL dye and (c) 1µL sample. The ladder consisted of a mixture of: (a) 3µL DEPC-H_2O, (b) 6µL dye and (c) 3µL ladder (Fermentas SM1831 Ribo Ruler RNA Ladder). Prior to loading, the samples

were heated at 70°C for 10 minutes and then cooled on ice for 2 minutes. The gel tank was filled with 1x MOPS-EDTA buffer and the electrophoresis was performed at 30 volts for 2 hours. After the run was complete the gel was stained in a solution of SYBR® Green II (Molecular Probes Inc., USA) for 15 minutes with gentle agitation and covered with foil. The results for the FRMD7 sense and antisense probes are shown in figure 2.4.

2.2.4 EMBRYO EMBEDDING AND SECTIONING

Human embryonic and foetal tissues were obtained from the MRC-Wellcome Trust Human Developmental Biology Resource (158) (www.hdbr.org) Institute of Human Genetics, Newcastle University. The samples were collected with appropriate maternal consents and ethical approval by the Newcastle and North Tyneside Research Ethics Committee.

2.2.4.1 EMBRYO PROCESSING

Depending on the size of the specimen an appropriate plastic cage was chosen. If the sections were too large they were dissected ensuring that the region of interest was preserved. The cage was cleaned using 0.1% DEPC in ethanol. The cage was labelled with the embryo number (a unique ID given to each embryo) and the age of the embryo at the time of termination. This was either in the form of Carnegie Stage of the embryo or the number of week post conception. 70% ethanol was poured over the cage with the embryo and then placed immediately into the Shandon Pathcentre Tissue Processor (Thermo Electron Corporation, UK). The specimens were dehydrated in a series of ethanol concentrations and subsequently embedded in wax

(Pastillated Fibrowax was used for paraffin embedding). A typical overnight

processing schedule is shown in table 2.4.

Table 2.4: An example of the embryo processing schedule used in the
Shandon Pathcenter Tissue Processor

Program	Duration
70% Ethanol	15 minutes
100% Ethanol	45 minutes
100% Ethanol	1 hour
100% Ethanol	1 hour
Xylene	45 minutes
Xylene	1 hour
Xylene	1 hour
Wax	1 hour 30 minutes
Wax	1 hour 30 minutes
Wax	1 hour 45 minutes
Wax	1 hour 45 minutes

2.2.4.2 EMBRYO EMBEDDING

After the embryo processing the plastic cages were removed from the

processor and transferred to the molten wax holding tank in the embedding

machine. Using metal moulds the embryos were embedded typically with the

embryo in the lateral position with the rostral part on the left while the

caudal end on the right (figure 2.5).

Once the embryo was placed in the correct orientation, they were allowed to

set on a cold plate at 4°C for 20 minutes. The wax block was then stored at

4°C in a foil wrapping which was treated with DEPC-ethanol.
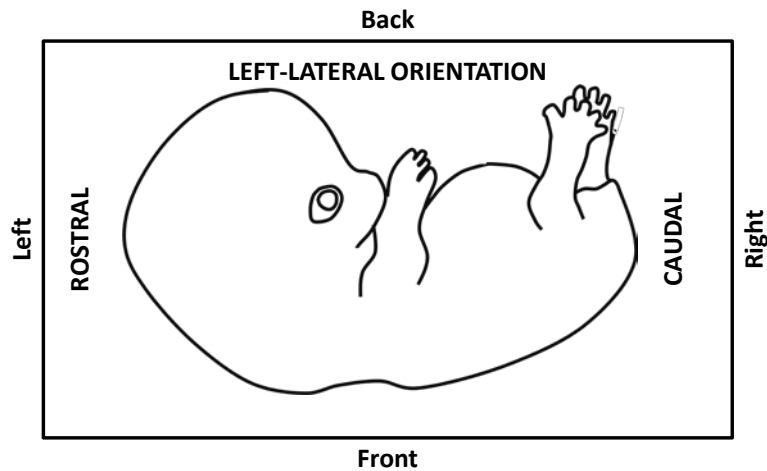
Figure 2.5: *View of the orientation of the embryo from above during embedding. The rostral part of the embryo is adjacent to the left face of the metal mould, while the right face of the metal mould is adjacent to the caudal part of the embryo.*

2.2.5 SECTIONING PARAFFIN WAX BLOCKS

The appropriate embryo (embedded in a paraffin wax block) was selected and trimmed using a razor blade to a size that would fit on the metal adapter. Using a dry heat air blower the bottom of the wax block was melted and subsequently it was mounted on a heated metal adapter. During this process it was ensured that the embryo was orientated correctly for the relevant plane of sectioning. The specimen was left with the metal adapter to set at 4°C for 30 minutes. The adapter was then attached to the microtome and sectioned with a thickness of 7-8μm. The ribbons of sections produced were placed in a tray (treated with DEPC-ethanol to ensure it was RNase free). The ribbon was cut using a scalpel and a series of reference sections were also produced for haematoxylin and eosin staining. An example of how the reference sections are determined is shown in figure 2.6. The sections were mounted on to Superfrost slides (BDH, Poole, UK). The slides with the sections were incubated in an oven at 37°C overnight. After air drying the

slides those labelled H&E staining were stained the next day. The remaining

unstained slides were stored at 4°C until required for *in-situ* hybridisation

experiments.
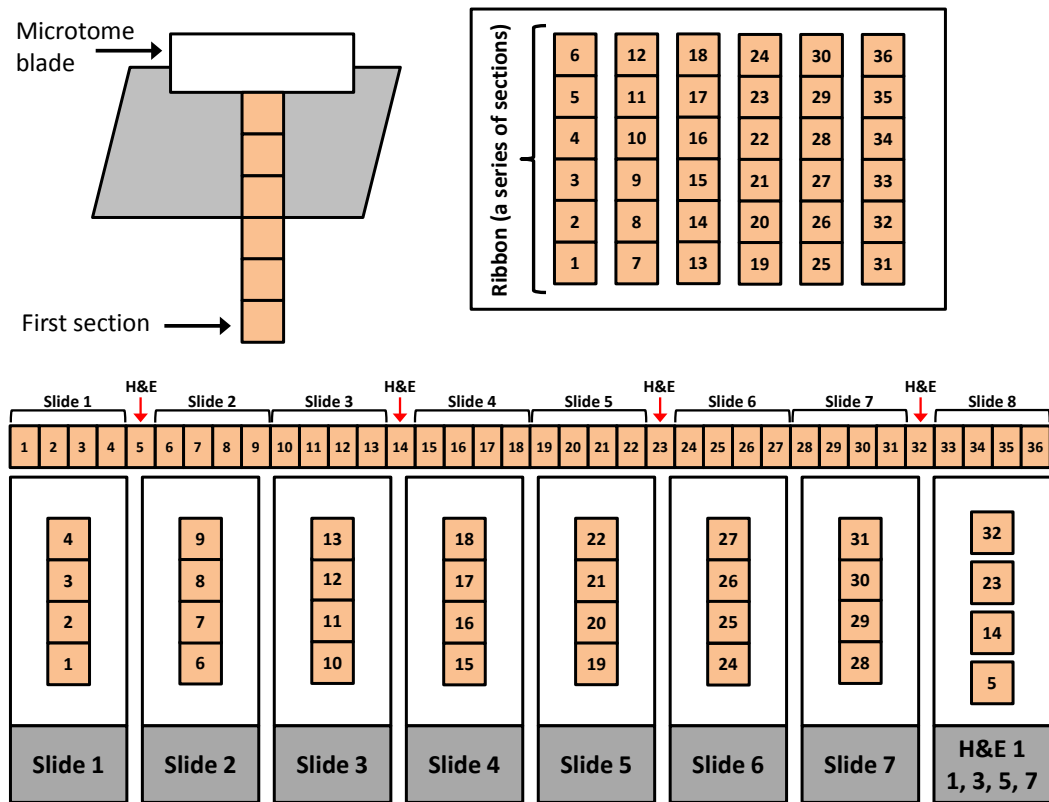
Figure 2.6: *Sectioning and preparing the reference slides. Sectioning using a rotary microtome produces ribbons (series of sections). The ribbons are divided ensuring approximately 4 sections are mounted per slide. The reference slide (H&E 1) is made of sections between slide 1 and 2; 3 and 4; 5 and 6 etc.*

2.2.6 NON-RADIOACTIVE TISSUE *IN-SITU* HYBRIDISATION

Prior to performing the in-situ hybridisation experiments the following solutions were made:

- 20x SSC:
    - 3M NaCl
    - 0.3M Na-Citrate (pH = 7.2)
- Buffer 1:
    - 0.1 M Tris (pH = 7.6)
    - 0.15M NaCl
- Buffer 2:
    - 0.1M Tris (pH = 9.5)
    - 0.1 NaCl

 Buffers 1 and 2 were made up to 1 litre using DEPC-H_2O. All PBS used in the experiments were treated with DEPC 0.1%v/v.

2.2.6.1 SLIDE SELECTION

The reference slides were assessed using light microscopy to determine the anatomical location of adjacent slides. If the region of interest was observed on the reference slides, the corresponding slide numbers and adjacent slides were noted and used for hybridisation with the sense and antisense probes respectively. Using figure 2.6 as an illustration, if the region of interest (e.g. developing neural retina) was noted on section 14 on the H&E slide; the slides 3 and 4 were chosen for the in-situ experiments one for hybridisation with the sense probes, while the other slide for hybridisation with the antisense probes. An additional slide, typically containing the spinal cord,

was also chosen for hybridisation with antisense probes generated against the Sonic Hedge Hog mRNA. This was the internal control for the experiment.

2.2.6.2 PRE-HYBRIDISATION

All glassware used was baked at 180°C for 4 hours before the pre-hybridisation experiment. Sections were dewaxed and gradually rehydrated by stepwise xylene and ethanol changes. This was achieved by immersing the metal rack of slides in the following order: 5 minutes in xylene (3 changes), 5 minutes in 1:1 xylene:ethanol, 3 minutes in 100% ethanol (2 changes), 3 minutes each for 90%, 70% and 50% ethanol. After rehydration the slides were washed twice in PBS (DEPC treated PBS) for 2 minutes each. The sections were then treated for 8 minutes in Proteinase K (20µg/ml) in PBS at 37°C. Using DEPC-PBS the sections were rinsed for 30 seconds. The sections were fixed in 4% paraformaldehyde in PBS for 20 minutes. After fixation the slides were washed twice for 2 minutes in DEPC-PBS. The sections were treated with 0.1M Triethanolamine (pH = 8.0), 0.25% Acetic anhydride for 10 minutes. The slides were again washed twice for 2 minutes in DEPC-PBS. The sections were subsequently dehydrated using increasing concentrations of ethanol (in the following order): 50%, 70%, 90%, and 100% (twice). The slides were immersed in the aforementioned ethanol concentration series for 2 minutes each. The sections were air dried by placing in a filtered air stream for 1 hour.

2.2.6.3 HYBRIDISATION

The previously described probes (section 2.2.1 and 2.2.2) were mixed with the hybridisation solution (DIG Easy Hyb, Roche). The hybridisation mix was

made up for both sense (ID: 477) and antisense probes (ID: 476) in the following proportions: 300ng of labelled probe per 100µL DIG Easy Hyb. Approximately 100µL of hybridisation mixture (probe with hybridisation solution) was required to cover one slide. Therefore sufficient quantities of the hybridisation mixture were made depending on the number of slides. The slides were placed within the hybridisation chamber and the hybridisation mixture was added to each slide and a cover slip was placed on each slide. The hybridisation chamber was moistened using 50% formamide/2x SSC. The chamber was placed in an oven overnight at 68°C.

2.2.6.4 POST-HYBRIDISATION TREATMENT

The cover slips were removed by rinsing slides in 5x SSC (pre warmed to 60°C). The slides were washed in the following solutions for 10 minutes each: 5x SSC (60°C), 5x SSC (60°C), 2x SSC (60°C) and 2x SSC (room temperature). The slides were washed in buffer 1 twice at room temperature for 10 minutes each. The sections were blocked with 10% foetal calf serum (FCS)/buffer 1 for 1 hour (Note: The FCS was previously heat inactivated at 58°C for 30 minutes). After the blocking step, the slides were covered with anti-DIG mix (Anti-Digoxigenin-AP, Fab fragments (Roche), diluted 1:1000 in 2%FCS/buffer1). The slides were placed in a tray that was moistened with buffer 1 and kept at 4°C overnight. The next day the sections were washed three times in buffer 1 for 10 minutes each. The sections were washed three times in buffer 2 for 5 minutes each. During the washes the NBT/BCIP (Roche) (20µg/ml) was prepared in buffer 2; the falcon tubes were foil wrapped since the mixtures are light sensitive. Approximately 100µL were

added onto each slide. The slides were developed in the dark at room temperature. The sections were periodically checked under a light microscope to prevent over staining. The staining was stopped by washing the slides in buffer 2 and then several times in distilled H_2O. Sections were mounted using Aquamount and analyzed using a Zeiss Axioplan 2 microscope. Images were captured with a Zeiss Axiovision 4 imaging system.

2.3 WHOLE MOUNT *IN-SITU* HYBRIDISATION IN ZEBRA FISH

The experiments related to section 2.3 was performed by the author at the Department of Neurobiology, Institute of Molecular Life Sciences, University of Zurich, Switzerland. The author was supervised by Dr. Matthias Gesemann and Professor Stephan Neuhauss.

Unlike the human genome which has only one *FRMD7* gene, in the zebra fish (Danio rerio) genome there are two *FRMD7* paralogs. Thus it was required to design two sets of sense and antisense probes to investigate whether there were any differences in the spatial and temporal expression profiles of these genes. The two paralogs are located on chromosome 1 and 21. The ensemble ID's for these genes are: ENSDARG00000070495 and ENSDARG00000068958. For simplicity in this thesis these paralogs will be referred to as *FRMD7*a and *FRMD7*b respectively.

2.3.1 PROBE PREPARATION

The overall principle for probe preparation is approximately the same as that described above for the humans. However the methodology for whole mount *in-situ* is different. The PCR primers used to amplify *FRMD7*a and *FRMD7*b are shown in table 2.3. The location of the primers in relation to the CDS of the

respective genes is shown in figure 2.7. The FRMD7-pCR II Topo vectors were

provided by Dr. Matthias Gesemann.
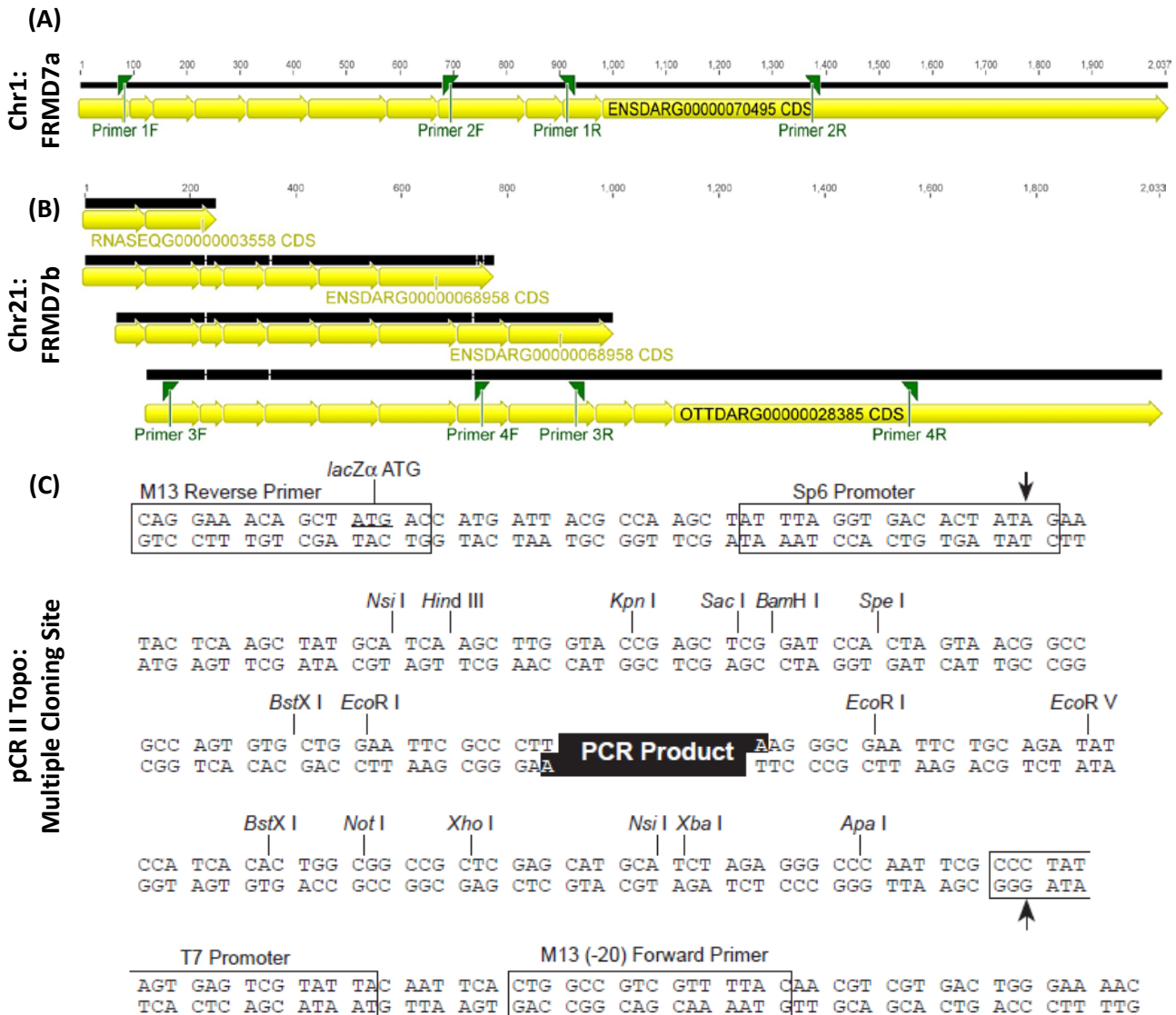
Figure 2.7: The location of the primers relative to the zebrafish (A) FRMD7a
and (B) FRMD7b cDNA. The sequence of the multiple cloning site with the
restriction digest sites for pCR II Topo is shown in (C). One transcript is
produced for FRMD7a, whereas four transcripts were produced for FRMD7b.

2.3.2 CONTROL DIGESTION

In order to confirm the *FRMD7* insert within the pCR II Topo a control digest

was performed with EcoR I and the FRMD7 insert was sequenced using SP6

and T7 polymerase (figure 2.8). The sequencing was performed by the

66

Sequencing facility at the Institute of Molecular Biology at the University of Zurich. The EcoR I restriction enzyme was chosen since it digests the vector on both sides of the insert (figure 2.7). The upper band in the gel represents the supercoiled plasmid and the lower band represents the FRMD7 insert. The FRMD7b insert is larger compared to the FRMD7a insert (table 2.3) and this is seen in the gel.
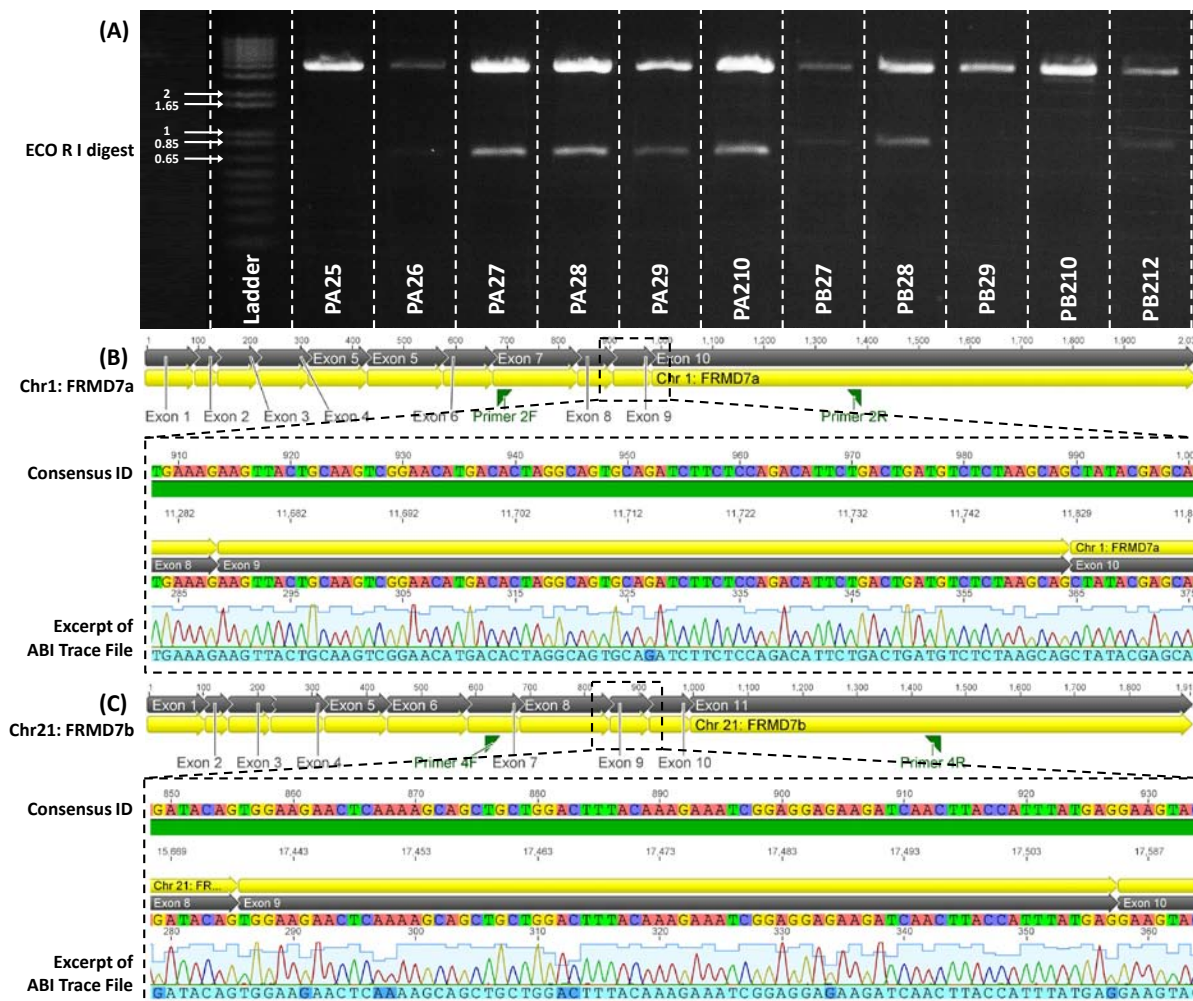
Figure 2.8: *Gel electrophoresis of ECO RI digest (A). Excerpts of the sequence trace file for FRMD7a and FRMD7b (B) and (C) respectively. Ladder size is shown kilobases.*

PA25, FRMD7a insert amplified using primer set 2 for FRMD7a (2F and 2R) the plasmids were obtained from colony 5.

PB27, FRMD7b insert amplified using primer set 2 for FRMD7b (4F and 4R) the plasmids were obtained from colony 7.

2.3.3 *IN-VITRO* TRANSCRIPTION REACTION

The *in-vitro* transcription reaction was performed as previously described in section 2.2.2. Two sets of reactions were performed. In the first reaction; T7 RNA polymerase was used with vector that was linearised using Sac I restriction enzyme. In the second reaction: SP6 RNA polymerase was used with the vector that was linearised using Not I restriction enzyme. The linearised plasmids were run on a 1% agarose gel run, the results of which are shown in figure 2.9. The sense and antisense probes were stored at -80°C.
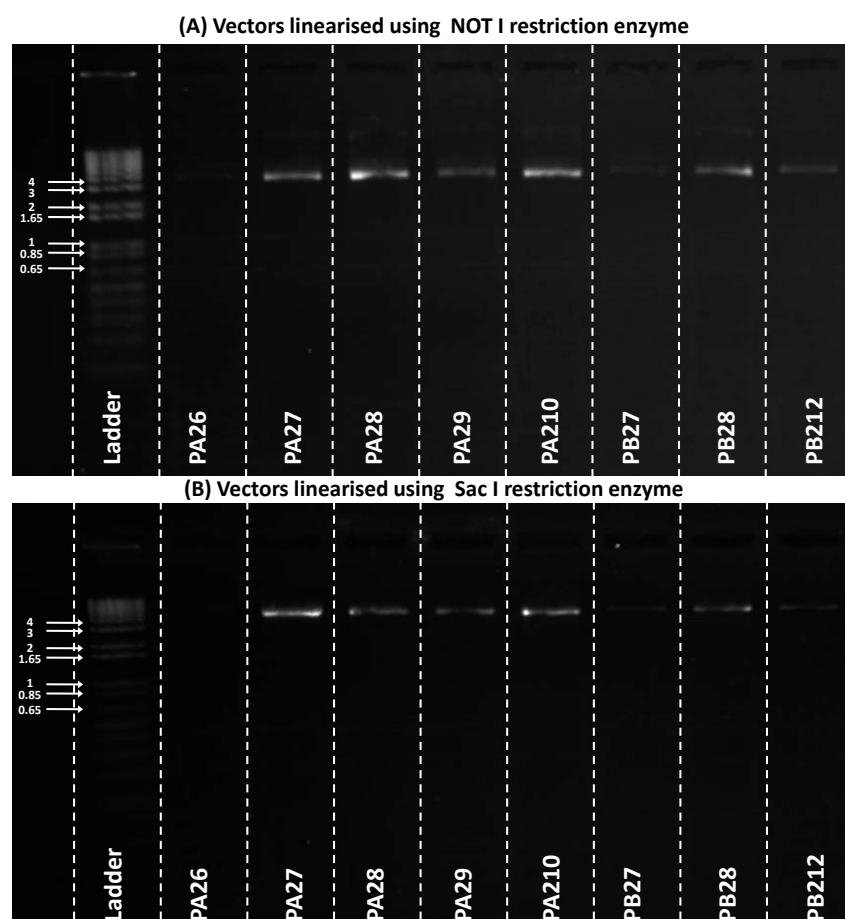
Figure 2.9: *1% agarose gel confirming products of linearization using NOT I (A) and Sac I (B) restriction enzyme. The faint upper band seen in (A) represents supercoiled plasmid while the stronger band represents the linearised vector for FRMD7a insert it is approximately 4.6kb while the vector with the FRMD7b insert is approximately 4.8kb. Ladder sizes represented on the left are in kilobases.*

68

2.3.4 *IN-SITU* HYBRIDISATION PROTOCOL

2.3.4.1 PREPARATION OF EMBRYOS

The zebrafish embryos were fixed in 4% paraformaldehyde for 1 hour at room temperature. The embryos were washed twice in PBST (Phosphate Buffered Saline with 0.1% Tween 20) for 5 minutes each. The embryos were then dehydrated in PBST/Methanol solutions (made up in the following proportions; 3:1, 1:1, 1:3) for 5 minutes each. Finally the embryos were washed twice in 100% methanol for 10 minutes each and stored at -20°C in methanol for at least 1 hour.

All solutions made were treated to ensure they were RNase free. All glassware and magnetic stir bars used for the experiments were either autoclaved or baked in the oven overnight.

2.3.4.2 WHOLE MOUNT *IN-SITU* MACHINE

An automated liquid handling platform, BioLane™ HTI (Hölle & Hüttner AG, Tübingen, Germany), was programmed for in-situ experiments. This allowed for automation of the *in-situ* protocol. The *in-situ* robot was controlled by a user PC using a program called HTI BioLane. The *in-situ* robot allows the user to control the temperature, source of solution (over 9 positions/different solutions can be used), direction of flow (i.e. draining or pumping into the machine) and incubation time.

Prior to starting the machine the pre-hybridisation solutions were made and installed in the appropriate position (table 2.5).

Table 2.5: Solutions used in the HTI BioLane loading positions 1-8 prior to hybridisation

Position	Solution
1 & 2	Proteinase K (5µg/ml)
3	100% methanol
4	1x PBS (with 0.1% Tween20)
5	Empty
6	4% paraformaldehyde
7	Prehyb- buffer: • 50% Formamide • 5x SSC
8	Hyb+ buffer: • 50% Formamide • 1x SSC • Hering Sperm (125µg/ml) • Torula RNA (5mg/ml) • Heparin (50µg/ml)

Both the Prehyb- and hyb+ buffers were made to an appropriate volume using DEPC-H_2O. The template program used prior to the hybridisation reaction is shown in figure 2.10.

Pre-hybridisation protocol

Nr.	Name	Source	Drain	Pump Vol. Mode	Agitation Mode	Tray Temp. [°C]	Incubation Time
1	MeOH-IN	No Pumping In	Waste	4	3	22	0:00:01:00
2	75% MeOH	Pos 3/	No Pumping Out	3	3	22	0:00:00:01
3	25% PBST	Pos 4/	Waste	1	3	22	0:00:10:00
4	drain	No Pumping In	Waste	4	3	22	0:00:00:01
5	50% MeOH	Pos 3/	No Pumping Out	2	3	22	0:00:00:01
6	50% PBST	Pos 4/	Waste	2	3	22	0:00:10:00
7	drain	No Pumping In	Waste	4	3	22	0:00:00:01
8	25% MeOH	Pos 3/	No Pumping Out	1	3	22	0:00:00:01
9	75% PBST	Pos 4/	Waste	3	3	22	0:00:10:00
10	drain	No Pumping In	Waste	4	3	22	0:00:00:01
11	PBST-1	Pos 4/	Waste	4	3	22	0:00:10:00
12	PBST-2	Pos 4/	Waste	4	3	22	0:00:10:00
13	PBST-3	Pos 4/	Waste	4	3	22	0:00:10:00
14	Prot K	Pos 1/Cooled pos. Sys.1/Cooled pos. Sys.2	No Pumping Out	4	3	22	0:00:00:01
15	Prot K	Pos 2/Cooled pos. Sys.1/Cooled pos. Sys.2	Waste	4	3	22	0:00:50:00
16	drain	No Pumping In	Waste	4	3	22	0:00:00:01
17	PBST-1	Pos 4/	Waste	4	3	22	0:00:10:00
18	PBST-2	Pos 4/	Waste	4	3	22	0:00:10:00
19	PBST-3	Pos 4/	Waste	4	3	22	0:00:10:00
20	PFA	Pos 6/	Waste	4	3	22	0:00:20:00
21	PBST-1	Pos 4/	Waste	4	3	22	0:00:10:00
22	PBST-2	Pos 4/	Waste	4	3	22	0:00:10:00
23	PBST-3	Pos 4/	Waste	4	3	22	0:00:10:00
24	PBST-4	Pos 4/	Waste	4	3	22	0:00:10:00
25	Pre Hyb-	Pos 7/	Waste	4	3	57	0:00:20:00
26	Pre Hyb+	Pos 8/	No Pumping Out	4	3	57	0:06:00:00

Figure 2.10: *The pre-hybridisation protocol used in the HTI BioLane program*

2.3.4.3 HYBRIDISATION

The hybridisation reaction was performed outside of the BioLane HTI machine. A 24-well plate was prepared with the sense and antisense probes in adjacent wells. The plates were placed in the incubator at 56°C for 10 minutes this would help unfold the RNA secondary structure. The baskets with the embryos were transferred into the 24-well plate and left overnight in the incubator at 56°C.

2.3.4.4 POST-HYBRIDISATION WASHES

Post-hybridisation blocking, antibody incubation and washes were performed in the BioLane HTI machine. The embryos with the baskets were removed from the 24-well plate and loaded into the machine. A few micro litres of Hyb+ mixture was put in to the baskets while loading the machine. The solutions were made and placed in appropriate loading positions (table 2.6). The blocking solution was made up in MABT solution and the antibody was diluted in the blocking solution. The program used for post hybridisation is shown in figure 2.11.

71

Table 2.6: Solutions used in the HTI BioLane loading positions after the hybridisation reaction

Position	Solution
1 & 2	Antibody • Anti DIG-Antibody (1:4000)
3	NTMT • Tris 100mM (pH = 9.5) • NaCl 100mM • $MgCl_2$ 50mM • Levamisol 1mM • Tween 0.1%
4	Blocking solution • Blocking powder (20mg/ml)
5	MABT (pH = 7.4) • 1x Maleic acid • Tween 0.1%
6	1x PBST
7	0.2x SSC
8	Hyb+ mixture: • 50% Formamide • 1x SSC • Hering Sperm (125μg/ml) • Torula RNA (5mg/ml) • Heparin (50μg/ml)
9	2x SSC

Post-hybridisation protocol

Nr.	Name	Source	Drain	Pump Vol. Mode	Agitation Mode	Tray Temp. [°C]	Incubation Time
1	preheat	No Pumping In	Waste	4	0	57	0:00:01:00
2	25% SSC	Pos 9/	No Pumping Out	1	3	57	0:00:00:01
3	75% Hyb	Pos 8/	Waste	3	3	57	0:00:15:00
4	Drain	No Pumping In	Waste	4	1	57	0:00:00:01
5	50% Hyb	Pos 8/	No Pumping Out	2	3	57	0:00:00:01
6	50% SSC	Pos 9/	Waste	2	3	57	0:00:15:00
7	Drain	No Pumping In	Waste	4	1	57	0:00:00:01
8	25% Hyb	Pos 8/	No Pumping Out	1	3	57	0:00:00:01
9	75% SSC	Pos 9/	Waste	3	3	57	0:00:15:00
10	Drain	No Pumping In	Waste	4	1	57	0:00:00:01
11	0.2xSSC	Pos 7/	Waste	4	3	57	0:00:30:00
12	0.2xSSC	Pos 7/	Waste	4	3	57	0:00:30:00
13	75% SSC	Pos 7/	No Pumping Out	3	3	22	0:00:00:01
14	25% PBST	Pos 6/	Waste	1	3	22	0:00:10:00
15	Drain	No Pumping In	Waste	4	1	22	0:00:00:01
16	50% SSC	Pos 7/	No Pumping Out	2	3	22	0:00:00:01
17	50% PBST	Pos 6/	Waste	2	3	22	0:00:10:00
18	Drain	No Pumping In	Waste	4	1	22	0:00:00:01
19	25% SSC	Pos 7/	No Pumping Out	1	3	22	0:00:00:01
20	75% PBST	Pos 6/	Waste	3	3	22	0:00:10:00
21	Drain	No Pumping In	Waste	4	1	22	0:00:00:01
22	PBST	Pos 6/	Waste	3	3	22	0:00:10:00
23	MA-1	Pos 5/	Waste	4	3	22	0:00:10:00
24	MA-2	Pos 5/	Waste	4	3	22	0:00:10:00
25	Blocking	Pos 4/	Waste	4	3	22	0:03:30:00
26	antibody	Pos 1/Cooled pos. Sys.1/Cooled pos. Sys.2	No Pumping Out	4	3	4	0:00:00:01
27	antibody	Pos 2/Cooled pos. Sys.1/Cooled pos. Sys.2	Waste	4	3	4	0:14:00:00
28	Drain	No Pumping In	Waste	4	1	22	0:00:00:01
29	MA+bb-1	Pos 4/	Waste	4	3	22	0:00:15:00
30	MA+bb-2	Pos 4/	Waste	4	3	22	0:00:15:00
31	MA+bb-3	Pos 4/	Waste	4	3	22	0:00:20:00
32	NTMT1	Pos 3/	Waste	4	3	20	0:00:20:00
33	NTMT2	Pos 3/	Waste	4	3	20	0:00:20:00
34	NTMT3	Pos 3/	Waste	4	3	20	0:03:00:00
35	NTMT4	Pos 3/	Waste	4	3	20	0:01:00:00

Figure 2.11: *Post-hybridisation protocol used in the HTI BioLane program*

2.3.4.5 STAINING PROCEDURE

For the 24-well plate, 45μL of NBT was mixed with 35μL of BCIP and the solution was made up to 10mL in the NTMT buffer. Approximately 500μL of staining buffer was used per well and the plates were placed in darkness with periodic checking under a light microscope. When appropriate staining was observed the staining buffer was replaced with PBS to stop the reaction. After this the wells were washed twice for 10 minutes each in PBS. The embryos were then fixed in 4% paraformaldehyde for 20 minutes in room temperature. The embryos were washed again twice for 10 minutes in PBS. The embryos were subsequently dehydrated in 50% methanol (in PBS) and then 100% methanol 5 minutes each. The embryos were treated in a gradient of methanol/glycerol (1:1) and then 100% glycerol. Finally the embryos were stored in 100% glycerol at 4°C for microscopy in order to determine expression patterns.

2.4 IMMUNOHISTOCHEMISTRY

2.4.1 PARAFFIN EMBEDDED TISSUE

The sections (murine and rat samples) were dewaxed in two changes of xylene and dehydrated in two changes of 100% ethanol. Endogenous peroxidase was blocked using a methanol peroxide solution for 10 minutes at room temperature. The slides were rinsed in running water. The antigen retrieval step consisted of placing slides in a solution of 0.01M Citrate Buffer (pH = 6.0) and microwaved for 5 minutes. The slides were microwaved for a further 5 minutes and topped up with additional buffer. The slides were allowed to cool and then rinsed in TBS (100ml 1M Tris-HCl (pH=7.5), 30ml 5M NaCl, 870ml H_2O) for 5 minutes. The sections were incubated with 10% normal serum (species in which secondary antibody was raised) in TBS for 10 minutes at room temperature. Excess serum was removed and the sections were incubated with the anti-FRMD7 antibody (Prestige Antibodies®, Sigma-Aldrich) in normal serum/TBS (dilution of primary antibody 1:400). The sections were incubated for 2 hours at room temperature. Following this the sections were washed twice in TBS for five minutes each. The sections were incubated with the secondary antibody, polyclonal goat anti-rabbit immunoglobulin biotinylated (Dako, Glostrup, Denmark) in normal serum/TBS for 30 minutes (dilution of secondary antibody was 1:500). After incubation the sections were washed as described above for the primary antibody. The sections were then incubated with avidin-biotin-peroxidase complex (ABComplex, HRP; Dako) in TBS at room temperature for 30 minutes. After incubation the sections were washed as

described above for the primary antibody. The sections were developed

using a mixture of diaminobenze (Sigma D-4293) and urea hydrogen

peroxide for 10 minutes at room temperature. The slides were washed in

H_2O to get rid of excess reaction mixture. The slides were dehydrated and

mounted for imaging.

2.4.2 FROZEN TISSUE

Fixed tissue (rat samples) was embedded in Optimal Cutting Temperature™

medium at -80°C. The samples were stored at -25°C. The samples were

sectioned using a cryostat microtome. The sections were air dried at 40°C for

one hour. The sections were washed three times in PBS for five minutes each.

The sections were then washed four times in PBSTx (PBS with 0.04% Triton-

X) for 10 minutes each. The sections were blocked for one hour using a

blocking solution (PBS with 0.02% Triton-X and 2% Foetal Bovine Serum).

The sections were incubated in the primary antibody (dilution 1:1000)

overnight at 4°C. The following day the sections were then washed four times

in PBSTx (PBS with 0.04% Triton-X) for 10 minutes each. After the washes

the sections were incubated for two hours at 30°C with the secondary

antibody (Alexa 488 anti-rabbit IgG, dilution 1:400). After further washes in

PBSTx and PBS the sections were mounted and ready for microscopy.

2.5 PRIMARY CELL CULTURE AND IMMUNOCYTOCHEMISTRY

The experiments related to section 2.4.2 and 2.5 was performed by the author at the Department of Developmental Neurobiology, Nara Womens University, Japan. The author was supervised by Professor Masasuke Araki.

2.5.1 MICRODISSECTION OF NEURAL RETINA AND CEREBELLUM

All animal experiments performed were approved by the Nara Womens University (NWU) committee for animal research.

Neonatal Wistar rats (Wistar rat strain was supplied by Japan SLC Co. Ltd) were anaesthetised in ether and killed by decapitation. For retinal cell culture the rats were obtained within 24 hours of birth. All dissection equipment was cleaned using 70% ethanol. The lines of incision used for dissecting are shown in figure 2.12. The superficial tissue was reflected laterally to access the orbit. The globe was dissected out of the orbit and an incision was made in the anterior half of the globe (figure 2.12). The neural retina was separated from other ocular tissue using forceps under a dissecting microscope. The neural retina was then treated with 0.05% EDTA for 20 minutes at room temperature followed by incubation in 0.25% trypsin (Difco, 1:250) for 25 minutes at 37°C. Approximately 5×10^6 cells (derived from one eyeball) were seeded into a 35 mm culture dish pre-coated with collagen. The culture medium used was Dulbecco's modified Eagle MEM supplemented with 6% foetal calf serum (Hyclone, Utah), 55 mg/ml sodium pyruvate and 0.6% glucose.

Cerebellar tissues were removed from Wistar rats at postnatal 2-4 day. During microdissection of the cerebellum it is important to separate the

piamater and the blood vessels. The dorsal part of the tissues (the future

cerebellar cortex) was isolated and treated with EDTA and trypsin for

dissociation as described above for the neural retina.
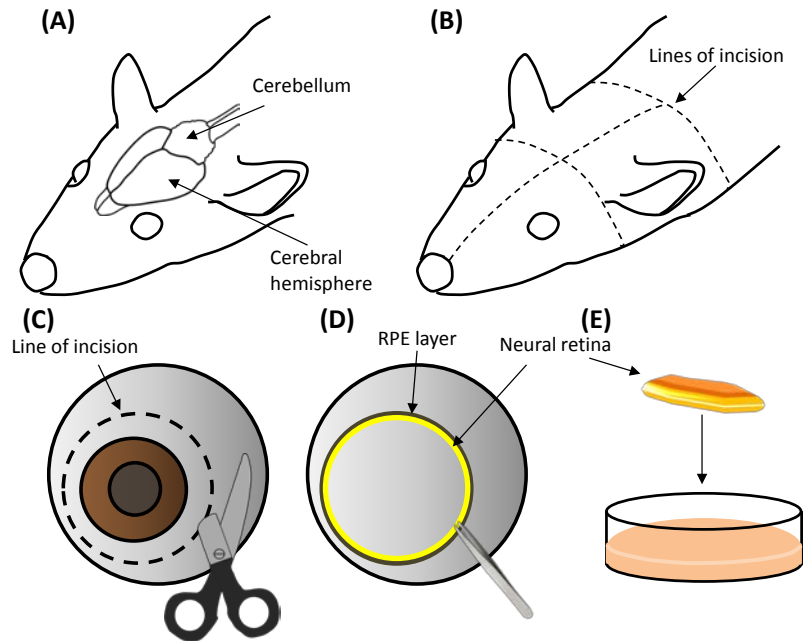
Figure 2.12: Microdissection of neural retina and cerebellum from rat. (A) shows the anatomical relations of the brain to surface landmarks in rat. The lines of incision made are shown in (B). The scalp was reflected laterally and the eye and cerebellum was microdissected. An incision was made posterior to the iris and using scissors the incision was extending along the circumference to reveal the neural retina (C). The neural retina was peeled away from the retinal pigment epithelium (RPE) using forceps (D). The neural retina was dissociated in trypsin and cultured in a petri dish (E).

2.5.2 IMMUNOCYTOCHEMISTRY

The cells were allowed to grow *in-vitro* for 5-6 days until the petri dish was

confluent (figure 2.13). The cultured cells were fixed in 2%

paraformaldehyde and washed in PBS for 5 minutes. The cells were

subsequently washed three times in PBSTx (PBS with 0.2% Triton-X) for 5

minutes each. The cells were incubated in a blocking solution (PBSTx and 2%

foetal bovine serum) at room temperature for one hour. The cells were

incubated overnight at 4°C with the primary antibody (Anti-FRMD7) in a dilution of 1:1000. The antibody was diluted in the blocking solution. The next day the cells were washed four times in PBSTx for five minutes each. The cells were incubated at 30°C for 2 hours with the secondary antibody (Alexa 488 Anti-Rabbit IgG, dilution of 1:400). Finally the cells were washed in PBSTx four times for 5 minutes each and then mounted for microscopy.

Day 4   **Day 6**

Neural retina
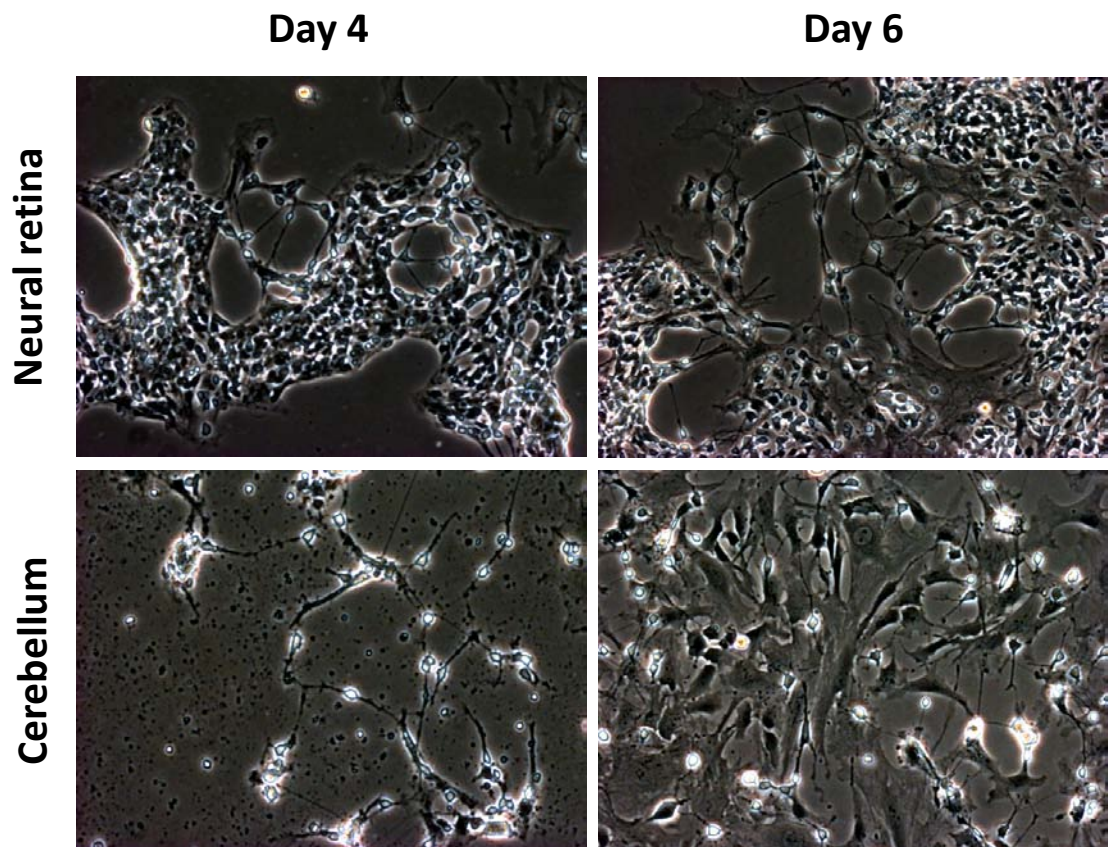
Cerebellum

Figure 2.13: Phase contrast microscopy images of primary cultures of neural retina and cerebellum after 4 and 6 days of in-vitro growth. The broad cells with large nuclei represent the glial cells, while the slender cells with smaller nuclei represent the neuroblasts.

2.6 CLINICAL INVESTIGATIONS

Prior to experimentation each test was explained to the volunteers, parents or guardians in conjunction with the patient information leaflet (electronic appendix). Opportunity to ask questions and sufficient time to make an informed decision about whether or not to participate in the study was given. Only volunteers where consent forms were signed were included in this study. The study was performed in accordance with the tenets of the Declaration of Helsinki and was approved by the local ethical committee.

The clinical investigations consisted of detailed ophthalmic examinations which were performed by an experienced ophthalmologist. Patients also underwent electrodiagnostic testing according to ISCEV standards (159) at the Medical Physics Unit based at the Leicester Royal Infirmary. The phenotypes of patients were characterised using eye movement recordings and optical coherence tomography. As stated previously in this study we use patients with albinism, achromatopsia and *PAX6* mutations as examples of "sensory forms of nystagmus". Patients with idiopathic infantile nystagmus (IIN), which included patients with and without *FRMD7* mutations, were used as examples of patients with "motor forms of nystagmus". In this section we will describe how the diagnoses for the aforementioned conditions were established.

The patient cohorts and phenotyping specific for each experiment is elaborated within each chapter.

2.6.1 HISTORY

A detailed history was obtained from each patient. In addition to the basic medical history, a more focussed history was also taken. Specific questions were asked to determine the following:

1. Time of onset of nystagmus
2. Presence of oscillopsia
3. Family history of nystagmus, hypopigmentation or poor vision
4. Light sensitivity and whether visual function is better during day or night

The first two questions help in determining whether the nystagmus is infantile or acquired. Determining the pattern of inheritance of nystagmus was a crucial part of this study. For instance, the phenotype associated with *PAX6* mutations is inherited in an autosomal dominant manner, phenotypes associated with achromatopsia and oculocutaneous albinism is inherited in an autosomal recessive manner, while phenotypes associated with *FRMD7* mutations and ocular albinism is inherited in an X-linked manner. A history of light sensitivity is relevant since cone dysfunction syndromes are associated with photophobia. The pedigrees and clinical data were managed using Genetic Pedigree Software Progeny v7 (Progeny Software, LLC, Florida, USA).

2.6.2 OPHTHALMIC EXAMINATION

The presence of an anomalous or alternating head posture was noted. The best corrected visual acuity was determined without correcting for the

torticollis to ensure that the visual acuity reflects the real-life acuity. Clinically detectable features of the nystagmus were noted; this included the plane of oscillation, conjugacy, estimate of the amplitude/frequency and convergence induced dampening. Colour vision defects were screened for using Ishihara plates and Farnsworth D-15. Gross stereopsis was assessed using the Lang test; if positive the level of stereopsis was determined using Frisby test. Cover test was used to determine whether the patient had strabismus.

The anterior segment was assessed using slit-lamp biomicroscopy and the presence and location of trans-illumination defects of the iris was noted (see figure 1.11). Fundoscopy was used to examine the retina. Abnormalities such as hypopigmentation, absent foveal reflex, optic disc abnormalities were noted.

2.6.3 ELECTRODIAGNOSTIC TESTING

All singletons with nystagmus underwent electrodiagnostic testing which consisted of electroretinography (ERG) and visual evoked potentials (VEP). In families with nystagmus at least one family member with nystagmus underwent electrodiagnostic testing.

ERG and VEP testing provide an indication of the functional status of the photoreceptors and optic chiasm respectively. Extinguished photopic response with a normal scotopic response indicates that the rods are functioning normally while there is no functional response detectable from the cones, thus the differential diagnosis is likely to be a cone dysfunction

syndrome, which may include blue cone monochromatism or achromatopsia (figure 1.11). The hallmark feature in albinism is the misrouting of axonal fibres of the optic nerve at the optic chiasm. Thus the most sensitive diagnostic modality for albinism is VEP, which will show an asymmetric response (figure 1.13). In idiopathic infantile nystagmus (IIN) all electrodiagnostic tests will be normal.

2.6.4 ESTABLISHING A DIAGNOSIS

2.6.4.1 ALBINISM

The diagnostic criteria used in this study for patients with albinism were: (1) asymmetric VEPs and (2) trans-illumination defects of the iris. Additional clinical findings that aided a diagnosis of albinism were foveal hypoplasia, fundus and skin hypopigmentation, autosomal recessive or X-linked inheritance. Sequencing was not performed in patients with albinism since it is associated with mutations of five possible genes and thus would be a costly undertaking as described in section 1.3.2.3.

2.6.4.2 ACHROMATOPSIA

The diagnostic criteria used in this study for patients with achromatopsia were: (1) impaired colour discrimination and (2) extinguished or markedly diminished photopic ERG with normal scotopic ERG. Additional clinical findings that aided a diagnosis of achromatopsia were increased light sensitivity, pigment mottling on fundoscopy and an autosomal recessive inheritance pattern. Since blue cone monochromatism (BCM) is phenotypically similar and also fulfils the diagnostic criteria additional genetic testing was performed in selected families. If females were affected in

a family we were able to exclude BCM (since BCM is X-linked and non-penetrant in females). However in families/singletons where only males were affected a tiered mutation analysis approach was used for excluding BCM and confirming achromatopsia. The tiered approach included targeted mutation analysis of the most common mutation 1148delC in *CNGB3*. Subsequently sequence analysis of the entire coding sequence was performed in the following order: *CNGA3*, *CNGB3*, *GNAT2* and *PDE6C*. This approach was used the more commonly mutated genes are screened first and this would be a more cost effective approach. The sequence analysis of the achromatopsia genes were performed by Professor Susanne Kohl at the University of Tuebingen, Germany.

2.6.4.3 *PAX6*

Previous studies have shown that the phenotypes associated with *PAX6* mutations is highly heterogeneous and mutation dependent (146). Hence it was difficult to set common diagnostic criteria for this group. Although aniridia is a common presentation associated with *PAX6* mutations, the Ophthalmology clinics at the Leicester Royal Infirmary receives patients with a wide range of atypical presentations where the diagnosis is unclear.

However some of the findings (which could occur in combination or isolation) that prompted a genetic test were: (1) aniridia or iris hypoplasia (2) foveal hypoplasia, (3) optic nerve hypoplasia and (4) corneal or lens opacities (5) autosomal dominant inheritance. The genetic testing for *PAX6* mutations was either performed at the Regional Genetics Centre on the National Health Service or in collaboration with the Professor Elizabeth Engle

at the Engle Lab, Children's Hospital Boston, USA. The structural effects and classification of pathogenic/non-pathogenic polymorphisms were performed by the author.

2.6.4.3 IDIOPATHIC INFANTILE NYSTAGMUS

IIN is a diagnosis of exclusion, thus other disorders such as albinism and other afferent defects associated with nystagmus were excluded prior to establishing a diagnosis of IIN. Hence all patients in this group had a normal VEP and ERG. Subsequently these patients underwent sequence analysis for mutations of the *FRMD7* gene.

2.6.5 OCULAR MOTILITY RECORDINGS

2.6.5.1 EYE TRACKER

In order to characterise the features of the nystagmus we used an infra red video pupil tracker, EyeLink II (SR Research, Ontario, Canada). The eye tracker consists of three miniature cameras (figure 2.14). Two of these track the eyes with a sampling rate of 500Hz. The third camera tracks four infra red markers mounted on the display (figure 2.14) for head motion compensation and true gaze position. The miniature eye cameras detect the pupil, based on eye illumination and threshold levels set by the operator. Eye illumination is achieved by two illuminators (figure 2.14) which emit IR rays at a wavelength of 950nm. The resolution of the eye tracker is 0.005° with a gaze tracking range of ±40° horizontally and ±36° vertically. The cameras are placed lateral to the nose and inferior to the eyes ensuring that the visual field of the subject is not obstructed by the cameras.
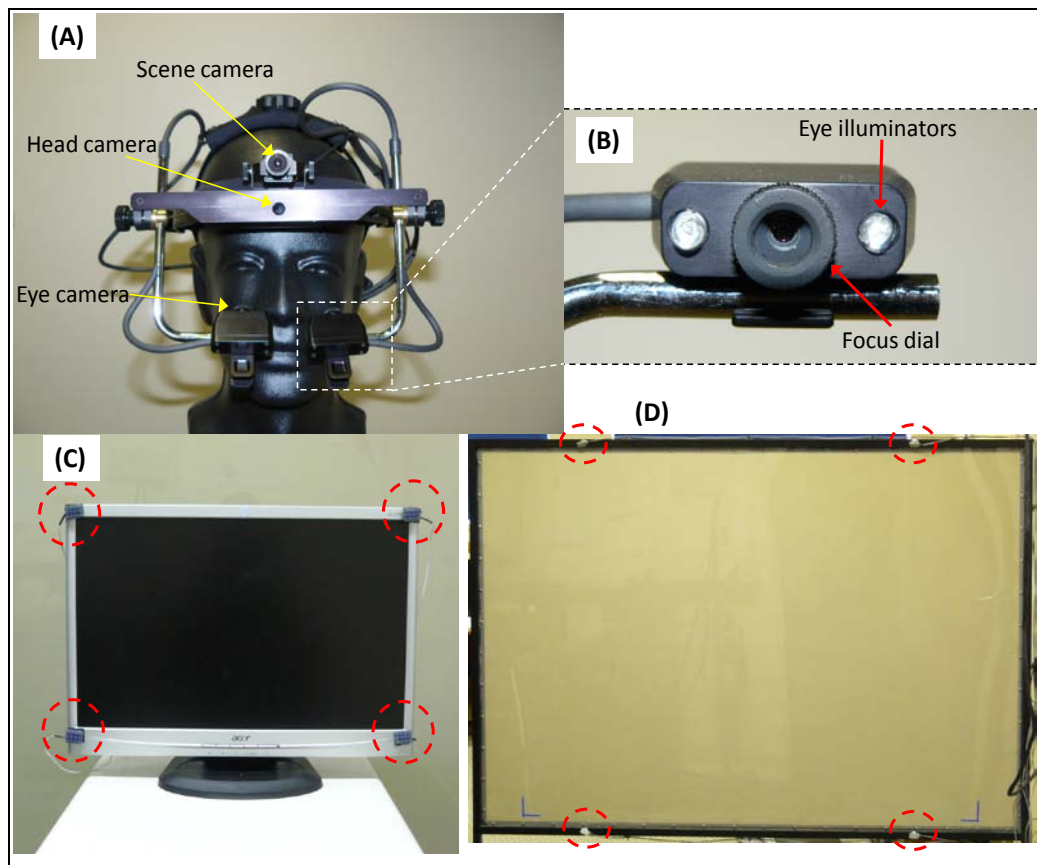
Figure 2.14: *Apparatus used for eye and head tracking. Eye and head movements were recorded using EyeLink (A). EyeLink consists of 3 cameras for tracking, two for tracking the eyes and one for tracking head movements. Gaze data can be overlayed on the scene, which can be recorded using the scene camera. (B) shows a magnified image of one of the eye cameras. Pupil detection relied on eye illumination using the IR illuminators and focusing the image using the focus dial. The IR markers (red dashed circles) used for head tracking were mounted on the rear projection screen (D) for distance tasks. For the fixational task at near the IR markers were mounted on the high resolution monitor (C).*

2.6.5.2 EXPERIMENTAL PROCEDURE

The fixational and optokinetic nystagmus (OKN) tasks were created using the SR Research Experiment Builder Software v1.4. The stimulus consisted of a dark filled circle subtending a visual angle with a diameter of 1°. This was projected onto a rear projection screen (1.8m wide and 1.2m high) using a video projector (Epson EMP-1715). In order to maintain the head position during the experiment a chin rest and cheek supports (figure 2.15) were used. The experimental setup is shown in figure 2.16.

Figure 2.15: *Chin rest (A) and cheek supports (B) used for head stabilisation. The handle on the chin rest (red arrow) enabled the patient to adjust the height of the chin rest to a level comfortable for the subject. The cheek supports were designed and partly made by the author and Dr. Proudlock, the material at the end of the cheek support (blue arrow) was made using Rolyan® Aquaplast®. Once this material is immersed in hot water it becomes transparent and soft, it is then moulded into the desired shape and allowed to cool. The remainder structures were made by the engineers at the medical physics workshop. The ball joint (black arrow) allowed control over the cheek supports to accommodate different facial contours. The final picture (C) shows the cheek supports mounted on the chin rest.*

Prior to the start of the experiments an online calibration was performed using nine fixation points in a 3x3 grid. The first task was called "manual calibration" this consisted of projecting a series of fixation dots in a random order in a 3x3 grid. This was done during monocular viewing and binocular viewing. The first task allowed us to perform offline calibrations by selecting the foveations and calibrating it to the target position. It also provides an opportunity to analyse for the presence of manifest latent nystagmus. The next task consisted of an extended central fixation to determine if the patients have periodic alternating nystagmus (PAN). The task is setup for continuous recording for 5 minutes; however if the patient exhibited a PAN

cycle greater than 5 minutes, a longer recording of 10 minutes was performed. In addition OKN was tested in all affected patients with PAN. The OKN stimulus consisted of square wave contrast gratings of 2.2° cycle size and Michelson contrast 0.88 cd/m². OKN was tested at 20°/s velocity in both horizontal (stimulus direction: rightwards and leftwards) and vertical directions (upwards and downwards). For further details of the experimental setup see Thomas et al. (91).

Finally a null point width task was performed, which consisted of presenting the circle in the horizontal direction from -30° to +30° with 3° steps. If vertical nystagmus component was present the same task was done in the vertical plane. The target was displayed at each position for 5 seconds.
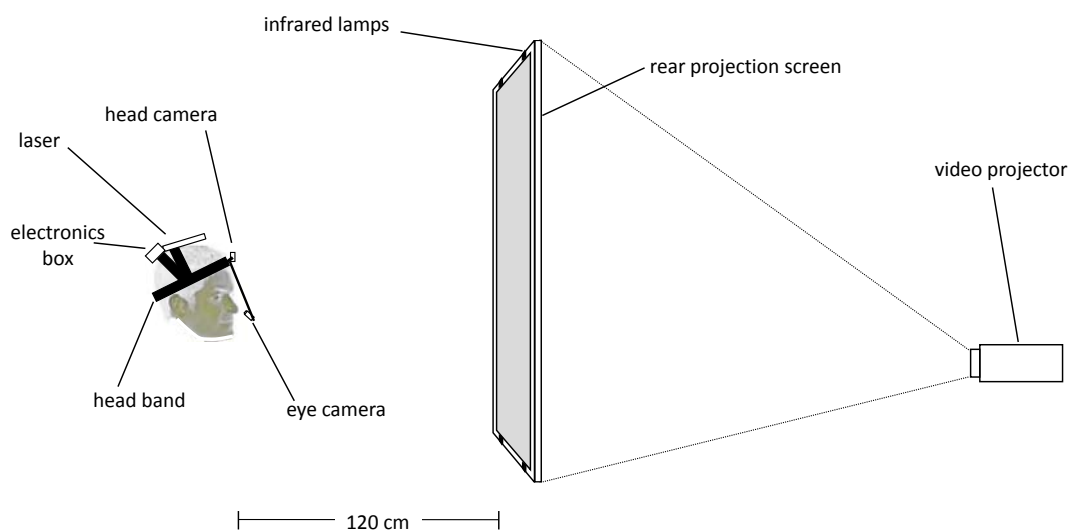
Figure 2.16: The experimental setup for eye movement recordings

2.6.5.3 DATA ANALYSIS

The data from the three cameras are recorded as an EDF file onto the hard disk of the host PC and it is sent to the display PC via an ethernet link. The EDF file stores multichannel data such as eye position, HREF position, gaze position, pupil size and data from response buttons (triggers) coded as ASCII characters.

The display PC keeps a record of the name, date and start time all the trials (stimuli used) and this is stored in the form of a LOG file. The EDF file is then integrated with the stimuli data and converted into an SMR file (Spike2 data file). The SMR files were analysed using a neuro-physiological software Spike2 (v6.14, Cambridge Electronic Design, UK).

2.6.6 OPTICAL COHERENCE TOMOGRAPHY

2.6.6.1 SOCT COPERNICUS HR

In order to characterise the structural features of the retina we used an Ultrahigh resolution spectral-domain OCT (SOCT Copernicus HR; OPTOPOL Technology S.A., Zawiercie, Poland) (figure 2.17). This OCT uses a super-luminescent light emitting diode at a central wavelength of 850 nm. The OCT achieves an axial resolution of 3μm and a transverse resolution of 12-18μm. The scanning speed of the OCT is 52,000 A-scans/second. The OCT has a chin rest which is adjustable to ensure that the objective lens is aligned with the eyes. During the scanning process the OCT enters the view finder mode and the operator aligns the scanning window to the centre of the pupil. As the measurement head moves closer to the eye the OCT enters a retina mode and the system focuses on the retina. The operator can alter the fixation control

to either fovea mode or optic disc mode which places the fovea or optic disc to the centre of the scanning window. Subsequently the scans were obtained.

For anterior segment imaging the anterior chamber adapter (figure 2.17) was installed on the objective lens and subsequently by altering the location of the measurement head the desired position of the anterior chamber (cornea, iris, lens and iridiocorneal angle) was imaged.

2.6.6.2 DATA ANALYSIS

The data obtained from the OCT was visualised and managed using the SOCT Copernicus HR software (v4.1). It was not clear whether reliable and reproducible measurements can be achieved using this OCT in the presence of nystagmus. Hence we tested the reproducibility of OCT measurements and optimised the methodology used for OCT image analysis. These questions and issues associated with methodology optimisation are addressed in chapter 6.
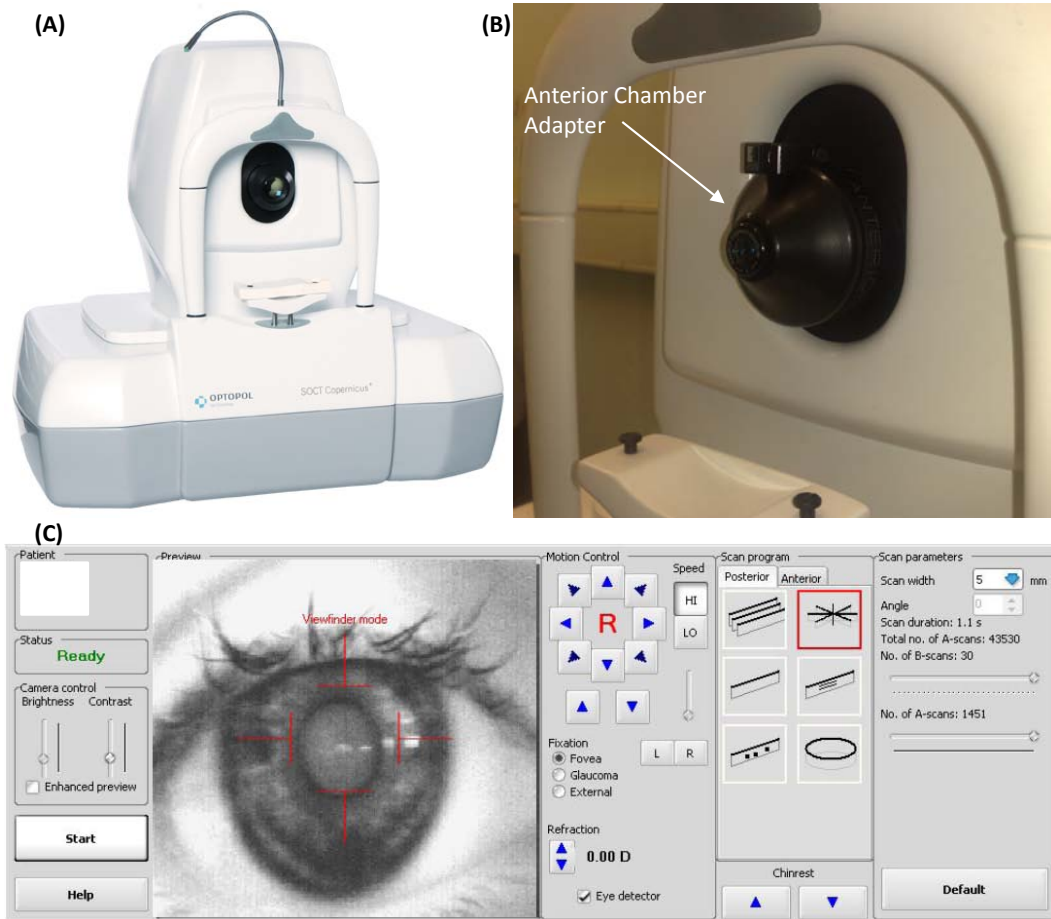
Figure 2.17: *SOCT Copernicus HR was used to obtain ultra high resolution images of the retina (A). The anterior chamber adapter was used to image the anterior segment (B). The SOCT software controls the SOCT instrument, it can be used to control the position of the lens, chin rest, scan program and scan parameters (C).*

3. CHAPTER THREE: MUTATION SPECTRUM AND VARIABLE PENETRANCE IN *FRMD7* RELATED INFANTILE NYSTAGMUS

This chapter addresses the aims:

- To characterize the mutational spectrum in families and singletons with idiopathic infantile nystagmus
- To determine whether the variability of penetrance in female carriers with *FRMD7* mutations is due to the mutation type or domain involved.

3.1 INTRODUCTION

Mutations of the *FRMD7* gene are a major cause of X-linked idiopathic infantile nystagmus (IIN) (47). The frequency of mutations in IIN families and singletons from different studies are variable. In families where linkage was performed the mutation frequency of the *FRMD7* gene was between 83-94% (47,75,80). Tarpey et al. reported that in families where no linkage data was present but at least two family members were affected with IIN the mutation frequency was 57% (47). Similarly Tarpey et al. reported a mutation frequency of 7% among singletons. However Self et al. reported a mutation frequency of 3.6% and 20% for singletons and familial cases respectively (79). Thus they suggested that majority cases of familial IIN and singletons were not due to mutations of the *FRMD7* gene. Numerous other reports in smaller cohort have also reported many mutations of the *FRMD7* gene. However no mutation hot spots or alternate testing strategy have been identified although most mutations are clustered with the FERM domain.

In hemizygous males the disorder is fully penetrant, however in heterozygous females variable rates of penetrance have been reported. Tarpey et al. reported an overall penetrance of 50%, while Schorderet et al. reported a penetrance of 35% (47,75). Using pedigree data from three previous studies (47,75,79) Self et al. performed a logistic regression model (n=21 families) to assess the effect of mutation type on the penetrance. They reported that truncating mutations were associated with a lower penetrance (32%) while non-truncating mutations were associated with higher penetrance (64%) (62).

3.2 METHODS

3.2.1 PILOT STUDY

A pilot study was performed using 10 samples which were previously investigated by Tarpey et al. (47). The samples consisted of 7 families and 3 controls:

- Five families with *FRMD7* mutations (Family IDs as reported in Tarpey et al.: N1, N5, N9, N10 and F31).

- One family (Family ID: N8) with linkage to Xq26-27 but no mutation of the *FRMD7* gene.

- One family (Family ID: F10) with IIN but with no linkage data and no mutations of the *FRMD7* coding sequence.

Since family N8 had linkage within the Xq26-27 region it is likely that they harbour a mutation within a regulatory site which was missed previously on sequencing. Similarly family F10 had a phenotype which was consistent with

FRMD7 mutation. The pilot study would allow us to identify whether family N8 and F10 has a mutation within 5' or 3' un-translated regions (UTRs), or intronic sequences that were not sequenced previously in the study performed by Tarpey et al (47). In addition to this the pilot study was used to optimise the PCR, sequencing and mutation analysis protocols. The families N1 (splice mutation), N5 (silent mutation), N9 (splice mutation), N10 (nonsense mutation) and F31 (deletion) were chosen since there is a variety of different types of mutation which affect different regions of the *FRMD7* gene. It would also give an opportunity to identify the suitable analysis package for subsequent high throughput analysis of cases. The two analysis packages used were: Seqscape version 2.1 (Applied Biosystems, USA) and Mutation Surveyor version 3.30 (SoftGenetics, Pennsylvania, USA).

3.2.2 NEW FAMILIES AND SINGLETONS

We identified a total of 44 families and 56 singletons with IIN. The protocol for diagnosis of IIN has been outlined in section 2.6.4.3. All singletons and at least one affected member in the family underwent sequence analysis for *FRMD7* mutations (see section 2.1.4 for details about PCR and sequencing methodology). Mutations were classified based on which domain was disrupted (FERM-N, M, C, FA and C-terminal), the effect on the FRMD7 protein (truncating, non-truncating) and the effect on the alternate *FRMD7* transcript.

To corroborate the findings by Self et al. (62) we performed a logistic regression model using our dataset as well as data previously reported in the literature to identify whether the mutation type (truncating versus non-

truncating) has a significant effect on the penetrance in females. The logistic

regression model was performed using software Stata version 11.1 (Stata

Corp LP, Texas, USA).

3.3 RESULTS

3.3.1 PILOT STUDY

Pedigrees of families sequenced in the pilot study are shown in figure 3.1.

Mutations identified and respective electropherograms are shown in figure

3.2. Mutations were identified in families N1, N5, N9, N10 and F31 as

expected, however no mutations were identified in family N8 and F10. The

control samples did not have any mutations of the *FRMD7* gene.
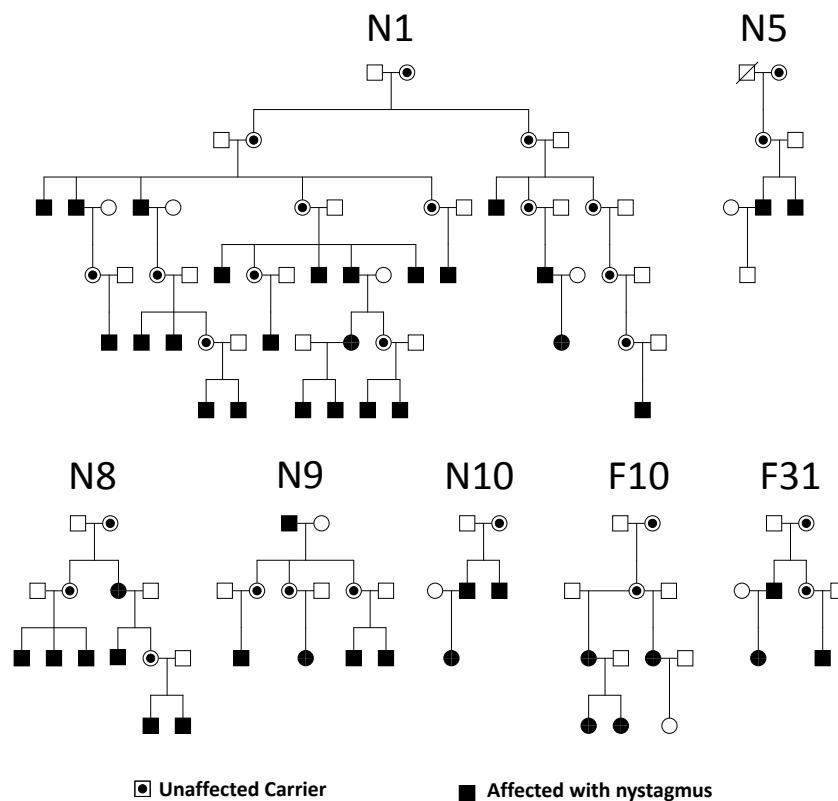
Figure 3.1: *Pedigree of families sequenced for the pilot study.*
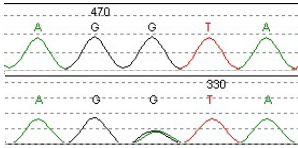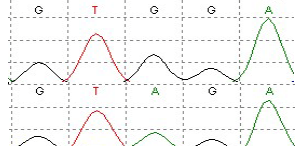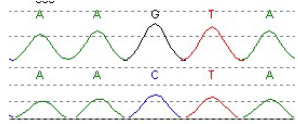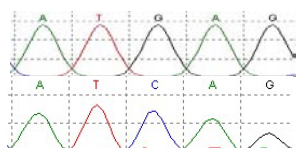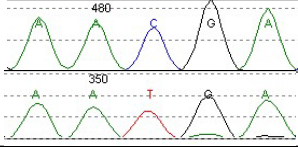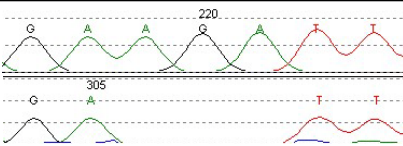
Family ID	Mutation	Amino acid change	Electropherogram (WA/MA)	Country of Origin
N1	c.[284+1G>A] (splice)	-		England
N5	c.[252G>A] (silent)	(p.=)		England
N8	None	-	-	Germany
N9	c.[1050+1G>C] (splice)	-		Germany
N9	c.[1371G>C] (missense)	p.M457I		Germany
N10	c.[1003C>T] (nonsense)	p.R335X		England
F10	None	-	-	England
F31	c.41_43delAGA (deletion)	p.K14del		England

Figure 3.2: *Mutations identified in the pilot study. The cDNA change and the amino acid changes are shown. The eletropherogram for the wildtype allele (WA) is shown above the mutant allele (MA). In family N1, the electropherogram shows a heterozygous mutation.*

Using both Seqscape and Mutation Surveyor we were able to validate the

mutations in families N1, N5 and N10. No mutations were detected in

families N8 and F10.

In family N9 two mutations were detected at the DNA level c.1050+1G>C and c.1371G>C. The missense mutation c.1371G>C is novel and results in the substitution of methionine for isoleucine at amino acid position 457 (p. M457I). The splice mutation c.1050+1G>C is pathological since it results in exon skipping (exon 11).

In family F31 the mutation c.41_43delAGA was detected. This was the same as what was previously reported in the Tarpey et al. study. The predicted amino acid change reported in the Tarpey et al. study was deletion of Isoleucine at amino acid position 14 (p.I14del). On re-evaluation of the mutation it was evident that the protein effect was deletion of lysine at amino acid position 14 (p.K14del) (figure 3.3).
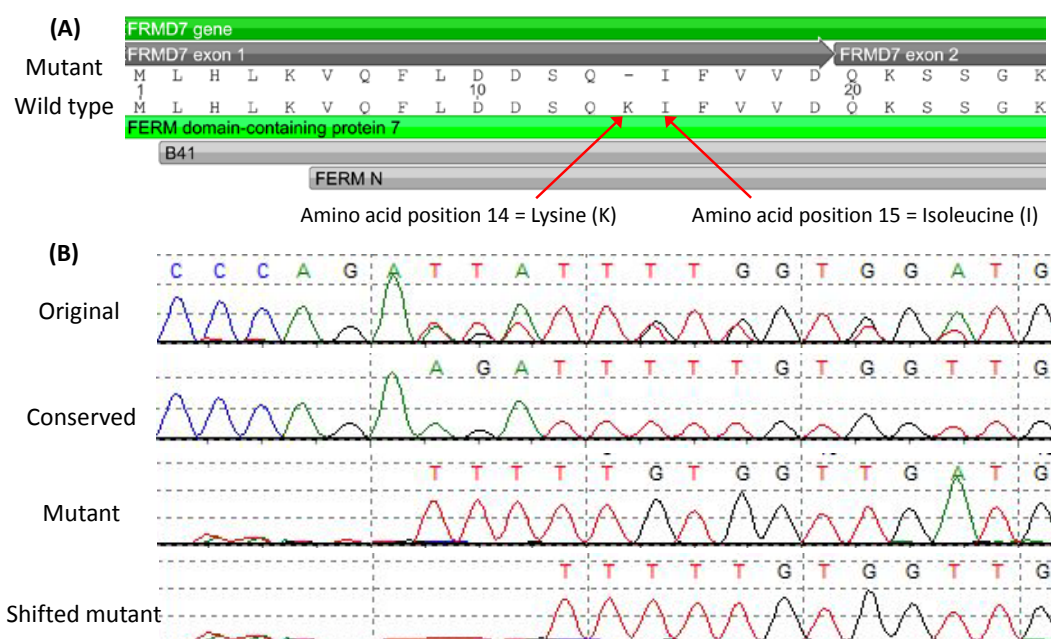
Figure 3.3: *Deletion of Lysine resulting from c.41_43delAGA. Previously family F31 was predicted to have I14del, however the mutation results in deletion of lysine rather than isoleucine (A). Electropherograms from mutation surveyor from individual I:2 in family F31 (B). Mutation surveyor uses a deconvolution algorithm which is able to identify both alleles (i.e. the normal/conserved allele and the mutant allele) in a patient with heterozygous deletion. Seqscape only produced the original sequence, thus resulting in ambiguous basecalling downstream to the heterozygous deletion.*

Both the mutation detection software's identified the substitutions and hemizygous indels with ease. Mutation surveyor was more effective at basecalling in the presence of a heterozygous indel due to its unique deconvolution algorithm (see figure 3.3). Seqscape's basecalling was ambiguous in the presence of a heterozygous indel, appearing as an impure product. Furthermore, downstream basecalling for the remaining amplicon was also ambiguous.

Therefore mutation surveyor was the preferred analysis package for detecting heterozygous indels however it was associated with erroneous annotation of amino acid variation within trinucleotide repeat regions as seen in family F31.

3.3.2 MUTATION SPECTRUM

We identified mutations of the *FRMD7* gene in 29/44 (66%) families and 8/56 (14%) singletons. Among these 23 were novel mutations.

3.3.2.1 MISSENSE MUTATIONS

Fifteen families and one singleton had missense mutations of the *FRMD7* gene. The pedigrees of families with missense mutations are shown in figure 3.4. The details of the mutation are outlined in table 3.1. Ten of the missense mutations were novel changes and predicted to be pathological.
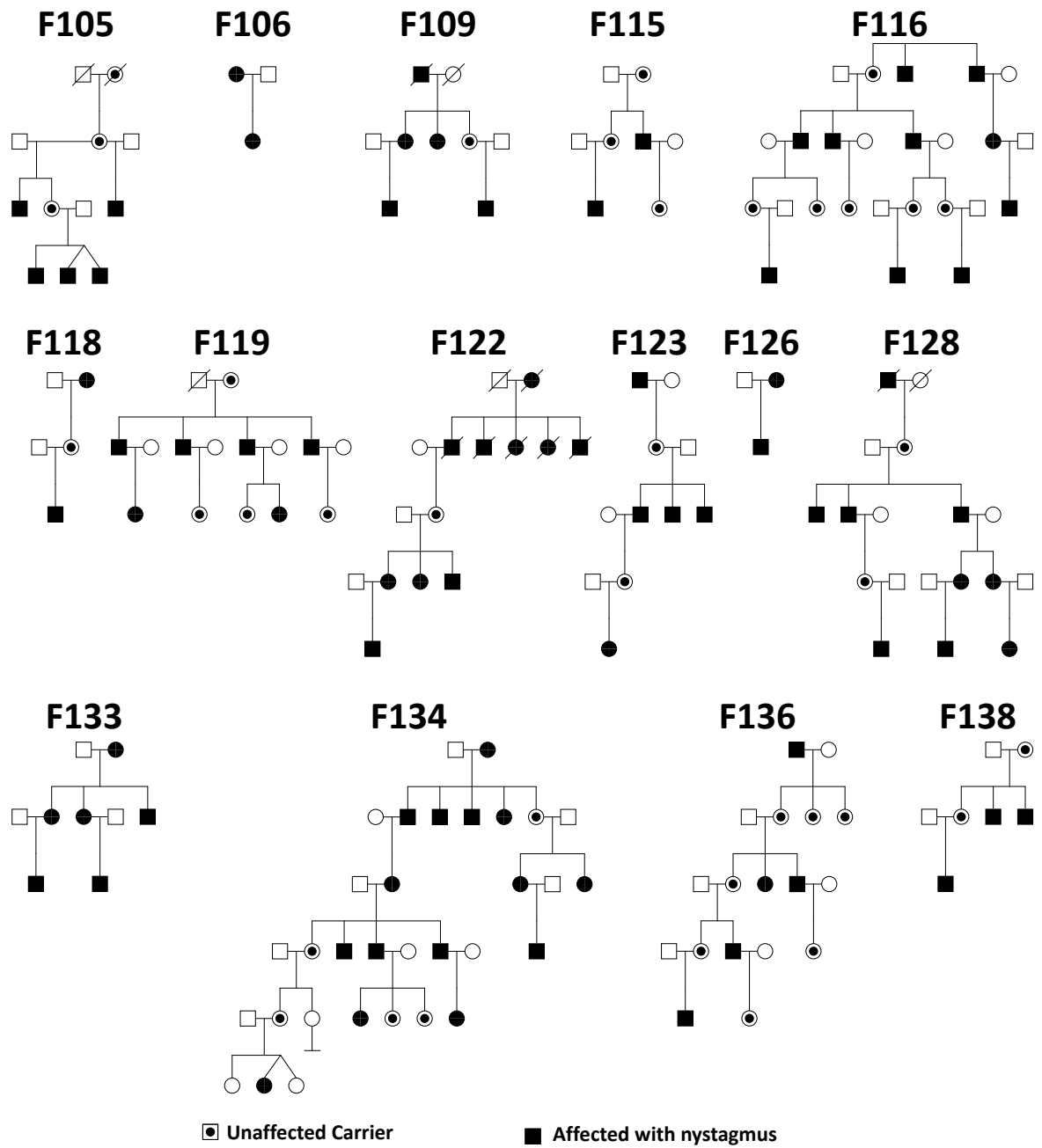
Figure 3.4: *Pedigrees of families with missense mutations.*

Table 3.1: Missense mutations of the *FRMD7* gene

Sample ID	DNA variation	Amino acid variation	Novel Mutation	Domain affected	Country of Origin
F105	c.[713T>C]	p.F238S	Yes	FERM-C	England
F106	c.[983A>G]	p.Y328C	Yes	FA	England
F109	c.[47T>C]	p.F16S	Yes	FERM-N	England
F115	c.[796G>C]	p.A266P	No	FERM-C	England
F116	c.[425T>C]	p.L142P	Yes	FERM-M	Denmark
F118	c.[796G>C]	p.A266P	No	FERM-C	England
F119	c.[673T>C]	p.W225R	Yes	FERM-C	England
F122	c.[782G>A]	p.R261Q	No	FERM-C	England
F123	c.[796G>C]	p.A266P	No	FERM-C	England
F126	c.[290T>C]	p.L97P	Yes	FERM-M	England
F128	c.[824A>G]	p.H275R	Yes	FERM-C	England
F133	c.[886G>C]	p.G296R	No	FA	Australia
F134	c.[796G>C]	p.A266P	No	FERM-C	Australia
F136	c.[670A>G]	p.N224D	Yes	FERM-C	England
F138	c.[389T>C]	p.L130P	Yes	FERM-M	India
S121	c.[811T>A]	p.C271S	Yes	FERM-C	England

Sample IDs with a prefix F represents families while a prefix S represents

singletons.

3.3.2.2 NONSENSE MUTATIONS

Five families had nonsense mutations of the *FRMD7* gene. The pedigrees of families with nonsense mutations are shown in figure 3.5. The details of the mutation are outlined in table 3.2. We identified two novel mutations (c.1225C>T and c.154G>T) within these families. The mutation c.1003C>T has been previously reported in a singleton, an Indian family, English family and Chinese family (47,77). The mutations c.910C>T has previously been reported in a Chinese family (80); however previously this mutation was inaccurately predicted to result in a change of arginine to a stop codon at amino acid position 303 (p.R303X).
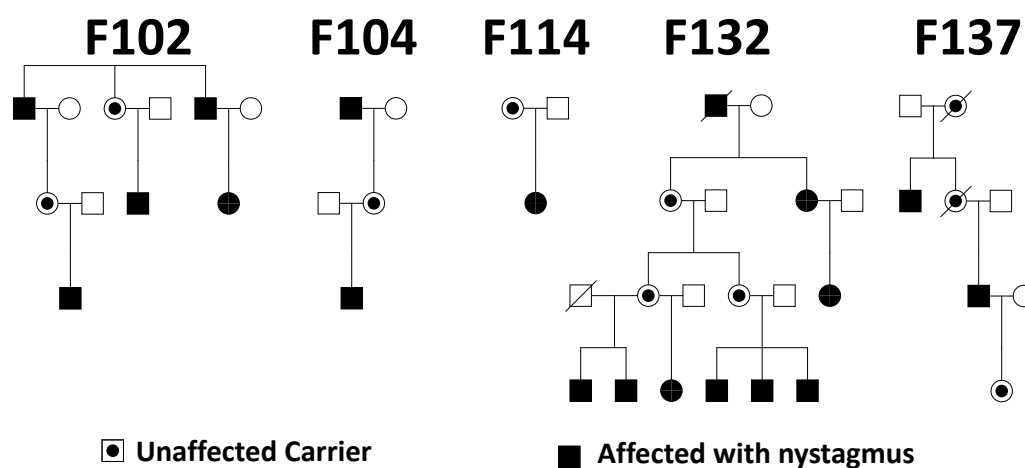
Figure 3.5: *Pedigrees of families with nonsense mutations.*

Table 3.2: Nonsense mutations of the *FRMD7* gene

Sample ID	DNA variation	Amino acid variation	Novel Mutation	Domain affected	Country of Origin
F102	c.[1225C>T]	p.Q409X	Yes	C-terminal	England
F104	c.[1003C>T]	p.R335X	No	FA	India
F114	c.[910C>T]	p.R304X	No	FA	Belgium
F132	c.[910C>T]	p.R304X	No	FA	Australia
F137	c.[154G>T]	p.G52X	Yes	FERM-N	England

3.3.2.3 SPLICE MUTATIONS

Three families had splice mutations of the *FRMD7* gene. The pedigrees of families with splice site mutations are shown in figure 3.6. The details of the mutation are outlined in table 3.3. Families F101 and F121 harboured novel mutations.
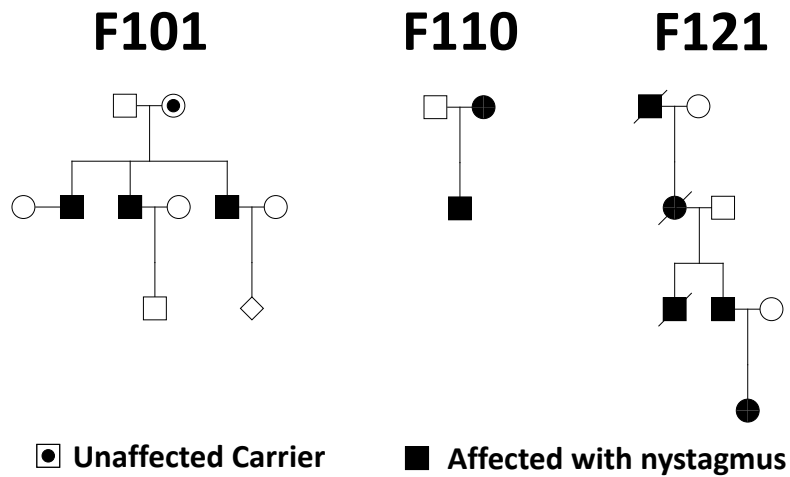
Figure 3.6: Pedigrees of families with splice mutations.

Table 3.3: Splice site mutations of the *FRMD7* gene

Sample ID	DNA variation	Novel Mutation	Domain affected	Country of Origin
F102	c.[58-1G>A]	Yes	FERM-N	England
F110	c.[162+5G>A]	No	FERM-N	England
F121	c.[206-5T>A]	Yes	FERM-N	England

3.3.2.4 FRAMESHIFT, SILENT AND INTRONIC MUTATIONS

We identified two novel frameshift mutations, seven novel intronic mutations and one novel silent mutation. The pedigrees of families within this group of mutations are shown in figure 3.7. The details of the mutation are outlined in table 3.4

■ Unaffected Carrier   ■ Affected with nystagmus
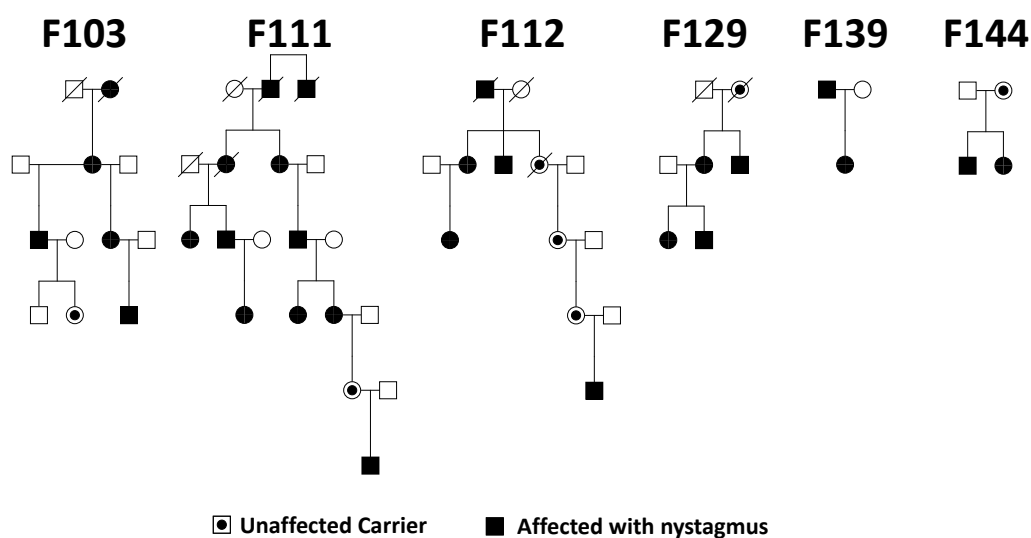
Figure 3.7: *Pedigrees of families with frameshift, silent and intronic mutations.*

Table 3.4: Frameshift, silent and intronic mutations of the *FRMD7* gene

Sample ID	DNA variation	Mutation type	Novel Mutation	Country of Origin
F103	c.[285-118C>T]	Intronic	Yes	England
F111	c.660delC	Frameshift	Yes	Belgium
F112	c.660delC	Frameshift	Yes	Belgium
F129	c.[382+7_382+8 insT]	Intronic	Yes	England
F139	c.[285-118C>T]	Intronic	Yes	England
F144	c.[741+14T>C]	Intronic	Yes	England
S113	c.[383-48T>A]	Intronic	Yes	England
S119	c.[579C>T]	Silent	Yes	Belgium
S127	c.[383-48T>A]	Intronic	Yes	England
S129	c.[645+40G>A]	Intronic	Yes	Germany
S133	c.[646-56C>T]	Intronic	Yes	Germany
S141	c.[19delC]	Frameshift	Yes	Germany
S151	c.[285-118C>T]	Intronic	Yes	England

3.3.3 PREDICTED STUCTURAL EFFECTS

3.3.3.1 MISSENSE MUTATIONS

The residues at amino acid position 16, 97, 130, 142, 224, 225, 238, 261, 266, 271, 275, 296 and 328 are identical between the species *Macaca mulatta, Callithrix jaachus, Equus caballus, Mus musculus, Rattus norvegicus and Gallus gallus* (see figure 3.8). Residues at all the above mentioned positions except for 328 are identical for *Xenopus tropicalis.* Furthermore, residues at position

16, 97 and 142 are identical in *Danio rerio*. Most amino acid variations occurred within highly invariant blocks of amino acid between species. This suggests that the amino acids at these positions are critical for correct protein function. All missense mutations were predicted using i-Mutant 2.0 (154) and Polyphen-2 (160) to result in a decrease in free energy and hence destabilise the protein.

Currently the crystal structure of the FRMD7 protein is not known hence the structural effects of missense mutations was determined by mapping the mutations on the three dimensional structure of the core domain of the cytoskeletal protein 4.1 (PDB ID: 1GG3). This is the closest ortholog with a known crystal structure. The crystal structure extends from 1-279 residues hence all mutations in table 3.1 can be mapped except G296R and Y328C. Disruption of the α-helix within the FERM-C domain was the most common mechanism of destabilising the FRMD7 protein. Other FERM domain changes included disruption α-helical domain with the FERM-M and disruption of the β-sheets within the FERM-N and FERM-C domains (figure 3.9).

The structural effects of the G296R and Y328C mutations were modelled using European Molecular Biology Open Software Suite (EMBOSS). EMBOSS tools can predict RNA folding and the garnier toolkit allows prediction of secondary structure of the FRMD7 protein and subsequently the effects of the amino acid variation can be modelled. Both mutations result in abnormal RNA folding when compared to the wild type sequence (figure 3.10). Both mutations were modelled and shown to disrupt the secondary structure of the FRMD7 protein (figure 3.11). The G296R variation results in disruption of

the β-strand and coil structure within the FA domain. The Y328C variation

also results in disruption of a β-strand within the FA domain.
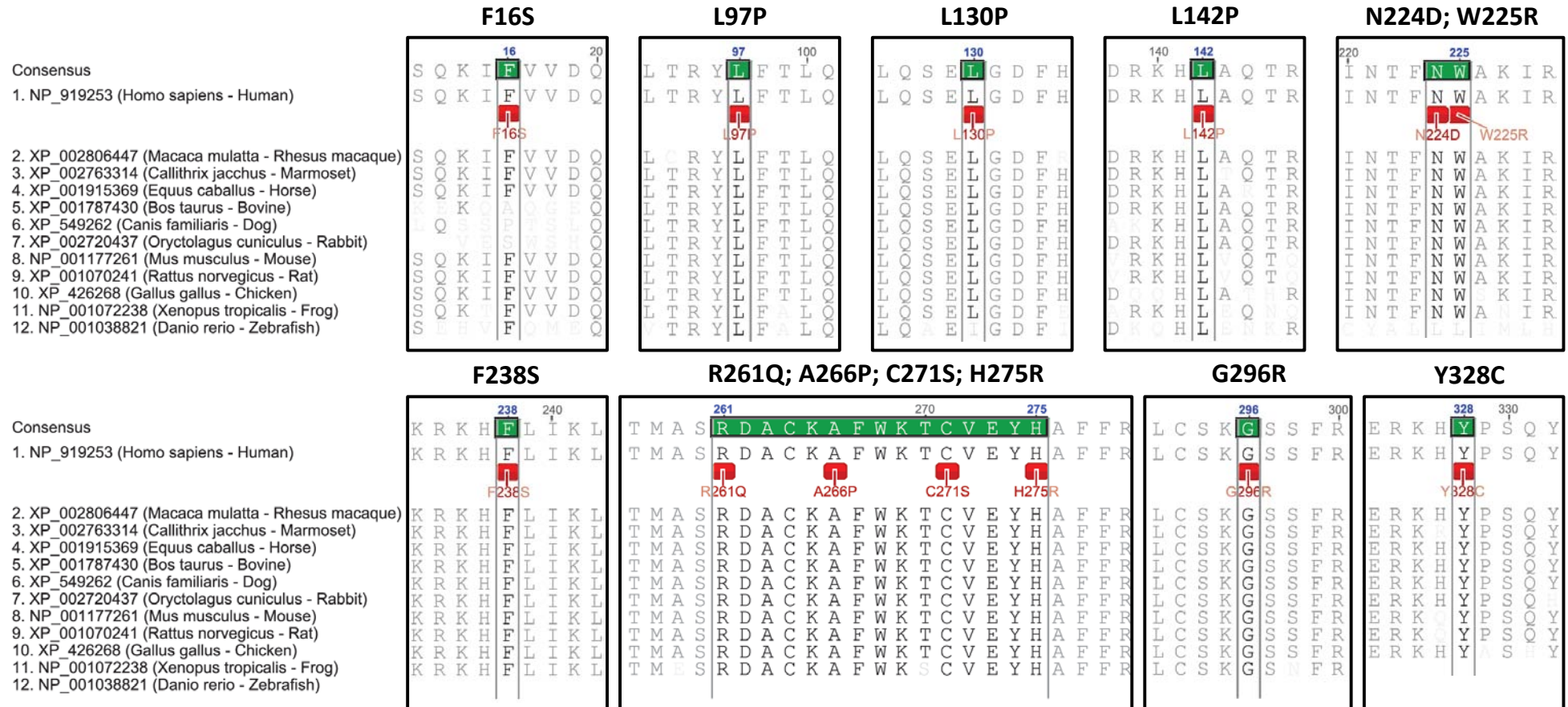
Figure 3.8: *Alignment of FRMD7 amino acid sequences between different species. The sequences are identical between most species at location of missense mutations.*
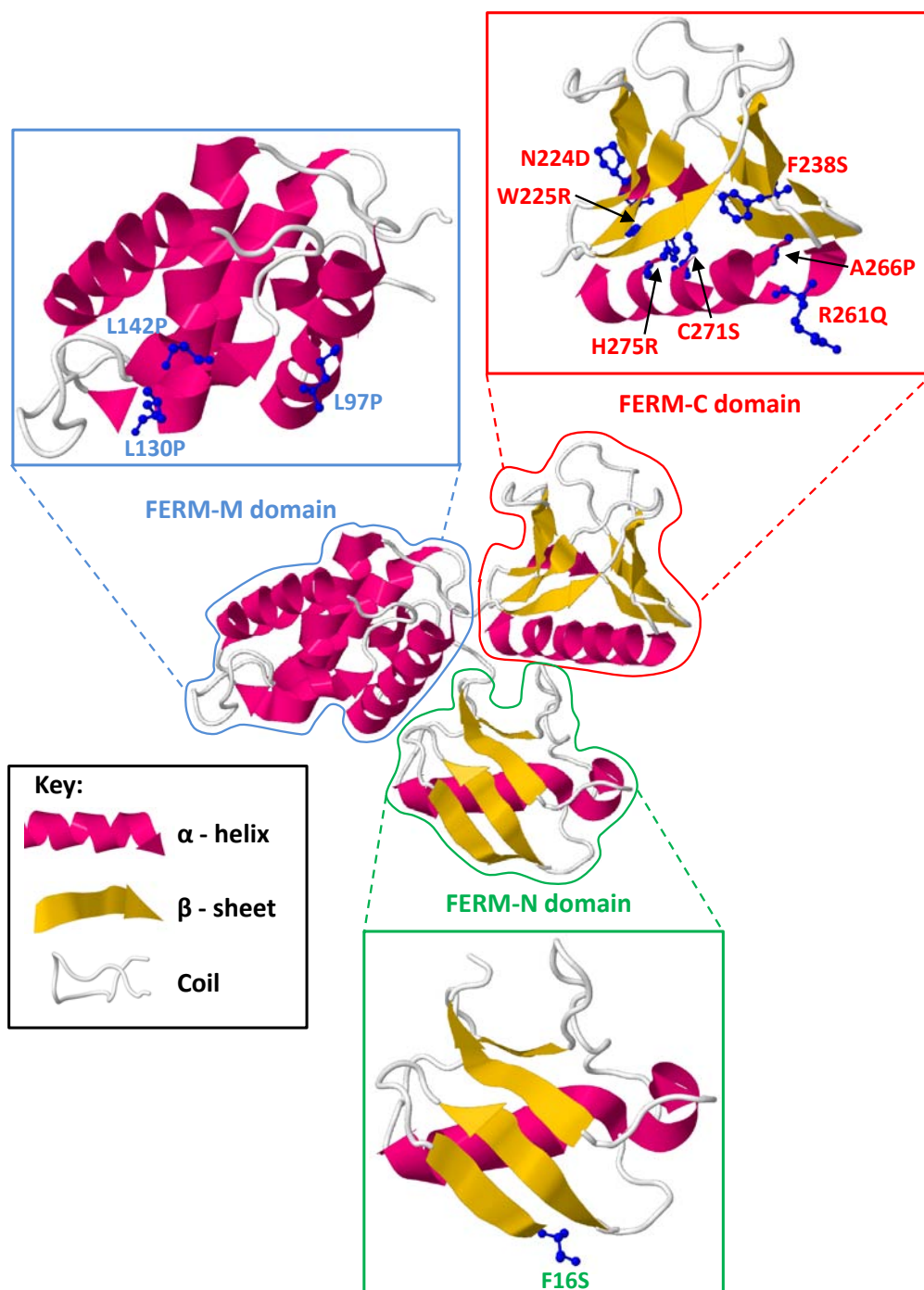
Figure 3.9: *Three dimensional model of the FERM domain based on band 4.1 cytoskeletal protein. Missense mutations have been modelled and structural effects predicted based on this 3-D model. Disruption of the α-helix within the FERM-C domain was one of the common mechanisms of destabilising the FRMD7 protein.*

Normal FRMD7 mRNA structure

983A

886G

Translation start site

FRMD7 mRNA structure due to 886C>G mutation

886G>C

Translation start site

FRMD7 mRNA structure due to 983A>G mutation

983A>G

Translation start site
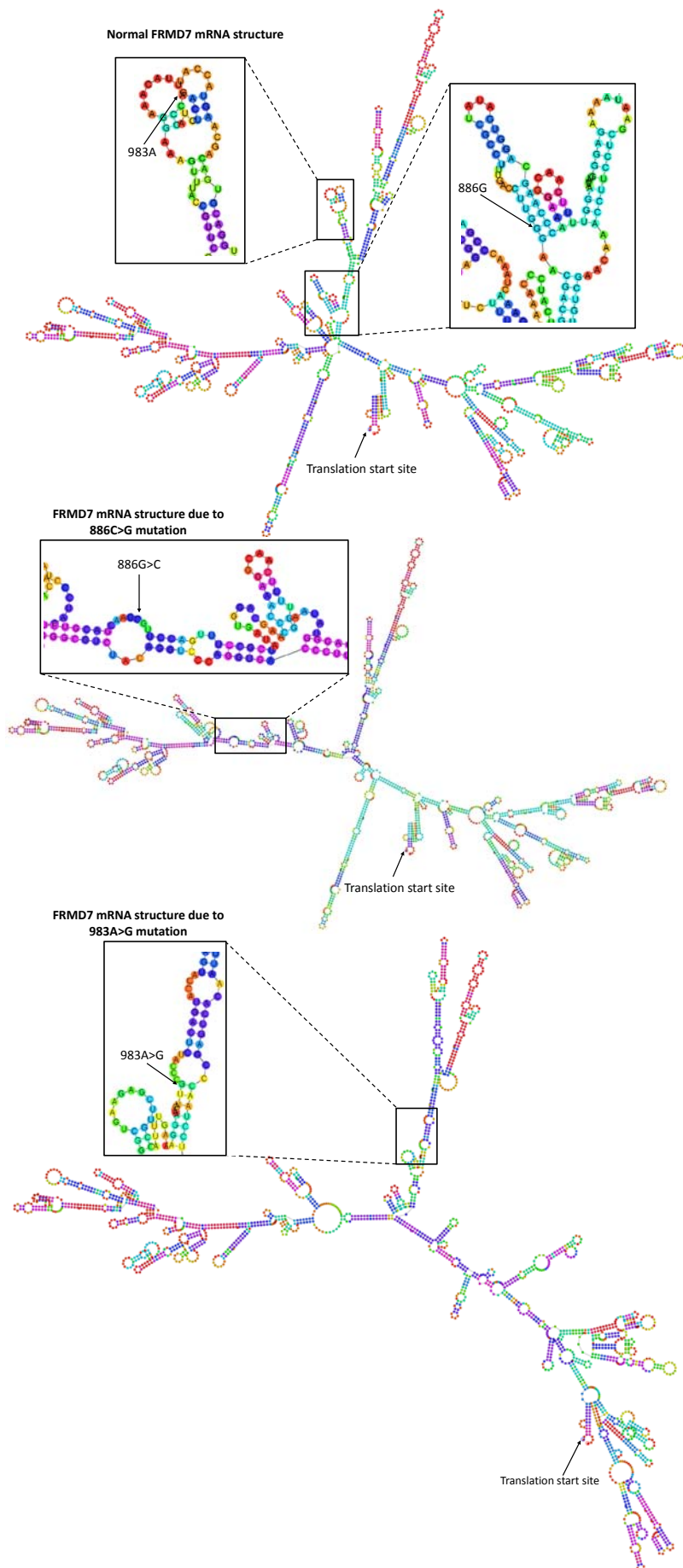
Figure 3.10: The normal FRMD7 mRNA structure and the abnormal RNA folding resulting from c. 886G>C and c.983A>G
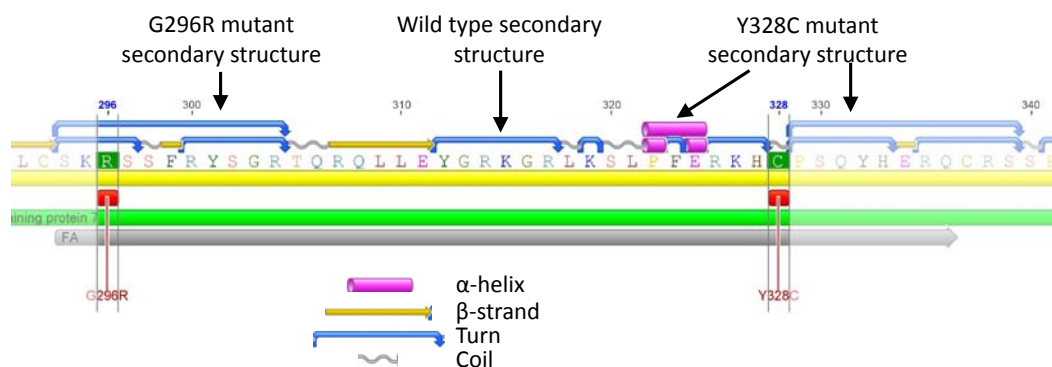
Figure 3.11: Predicted secondary structure alteration as a result of G296R and Y328C mutations. The mutant secondary structure is shown above the wild type structure.

3.3.3.2 NONSENSE AND FRAMESHIFT MUTATIONS

The nonsense mutations (c. 154G>T, c. 910C>T, c. 1003C>T and c. 1225C>T)

and frameshift mutations (c. 19delC and c. 660delC) result in a truncated

protein due to a premature stop codon. The expected protein sizes are shown

in table 3.5 and figure 3.12.

Table 3.5: Structural effects of nonsense and frameshift mutations on the FRMD7 protein

Amino acid variation	Mutation Type	Expected protein size (amino acids)	Percent of protein "intact"
p.Q7SfsX24	Frameshift	31	4.3%
p.G52X	Nonsense	52	7.3%
p.I220IfsX12	Frameshift	232	32.5%
p.R304X	Nonsense	304	42.6%
p.R335X	Nonsense	335	46.9%
p.Q409X	Nonsense	409	57.3%
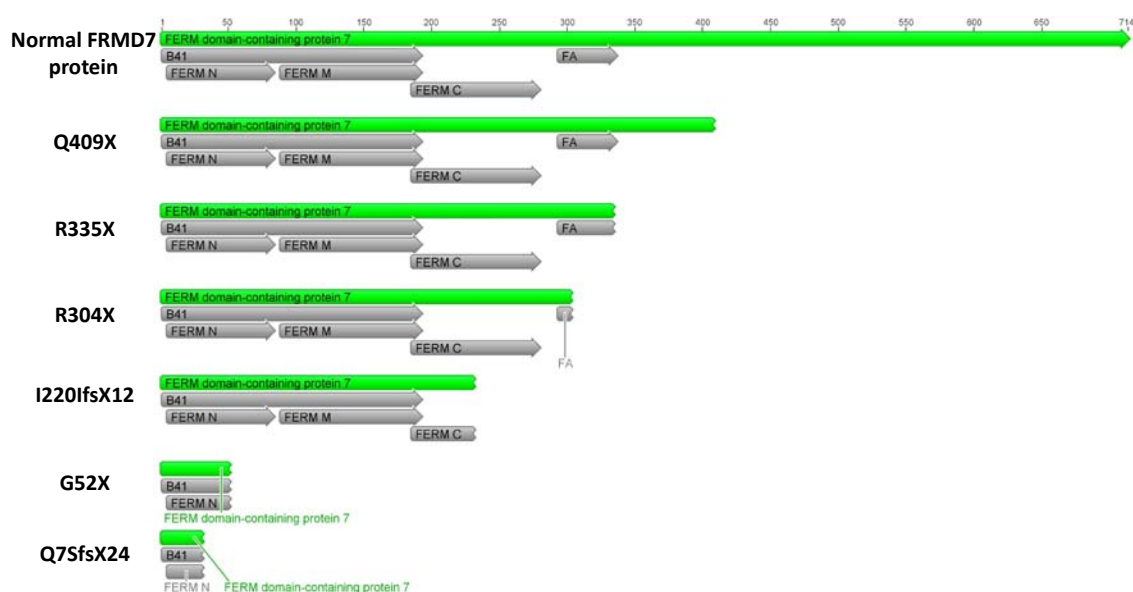
Figure 3.12: Illustration of truncated proteins in relation to domain affected in comparison to the normal FRMD7 protein

3.3.3.3 SPLICE MUTATIONS

The c. 58-1G>A and c.162+5G>A mutations result in obliteration of the splice

acceptor and donor site within intron 1 and intron 2 respectively. This

results in loss of exon 2, however since it is in-frame it results shorter

polypeptide with 689 amino acids. c. 206-5T>A mutation results in

obliteration of the splice acceptor site in intron 3. This causes exon skipping

(exon 4), however since this shifts the reading frame it results in a premature

stop codon within exon 5. Thus the translated product is shorter with 75

amino acids. Furthermore the translational products are likely to be subject

to nonsense mediated decay (161). The protein products resulting from these

splice mutations are illustrated in figure 3.13.
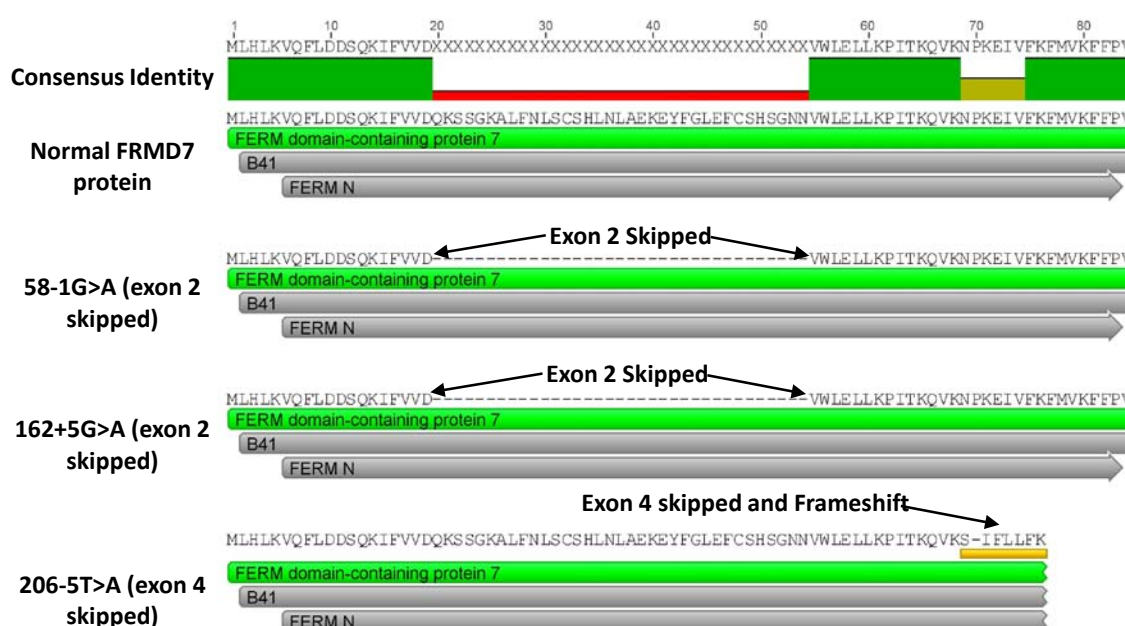
Figure 3.13: *Illustration of effect of splice mutations on the FRMD7 protein.*

3.3.3.4 SILENT AND INTRONIC MUTATIONS

All the intronic mutations and the silent mutation reported in section 3.3.2.4 were considered pathological since these sequence variants were not seen among the normal variants reported in:

- 300 male controls sequenced for the FRMD7 control dataset

- SNPs reported in the HapMap dataset

- SNPs reported in the 1000 genomes dataset

Furthermore the in-silico effects of these mutations were predicted to results in an abnormal protein structure thus rendering it non-functional. These effects are detailed below.

The c.579C>T mutation creates a splice acceptor site adjacent to the mutation location within exon 7 (figure 3.14). Normally the intron exon boundaries are enhanced by certain elements called exonic splicing enhancers (ESE), these include serine rich proteins such as SRp40 which binds to the following motif 5'-TCACCCC-3'. The mutation alters this site to: 5'-TCACCCT-3' thus the binding site for the ESE is abolished. This may result in loss of part of exon 7.

The c.285-118C>T and c.382+7_382+8insT mutation activates a cryptic splice donor within intron 4 and intron 5 respectively (figure 3.14). Similarly the c.645+40G>A creates a splice acceptor site 30 bases downstream from the exon-intron (exon7-intron7) junction. The mutations c.383-48T>A, c.646-56C>T and c.741+14T>C results in mutations affecting branch point motifs thus predicted to alter the splicing mechanism which could either result in exon skipping or intron retention.
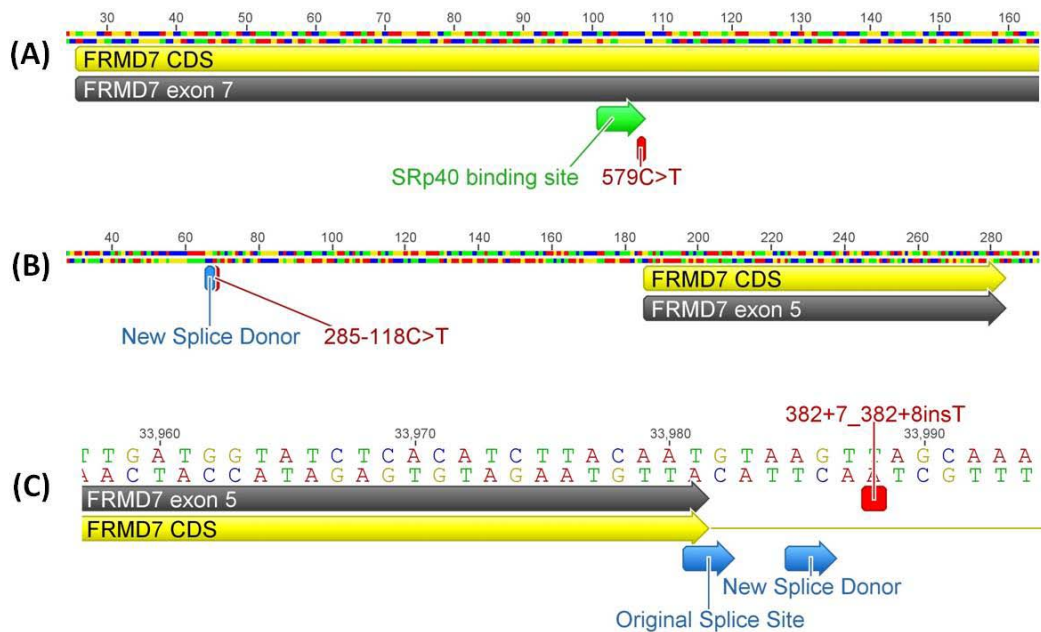
Figure 3.14: *Predicted effects of mutations: 579C>T (A), 285-118C>T (B) and 382+7_382+8insT (C). The mutation 579C>T results in the obliteration of the exonic splicing enhancer binding site (SRp40). The mutation 285-118C>T and mutation 382+7_382+8insT activates a cryptic splice donor within intron 4 and intron 5 respectively*

3.3.4 MUTATION HOTSPOTS

Using data from this study along with previous reports of *FRMD7* mutations allows us to characterise mutation hotspots and possibly identify a targeted mutation analysis strategy. The frequency of mutations based on the location on the coding sequence is shown in figure 3.15. Although mutations are spread throughout the *FRMD7* gene, there are some interesting trends in the distribution and clustering of mutations. The most frequently encountered mutation is the missense mutation c.796G>C resulting in substitution of amino acid alanine for proline at position 266. The most frequently encountered nonsense mutation is c.1003C>T which results in a premature stop codon at amino acid position 335, this mutation was also the second most common mutation overall. Among the splice mutations the most

commonly reported mutation is 284+1G>A which is considered pathological

due to exon skipping and subsequent nonsense mediated decay.
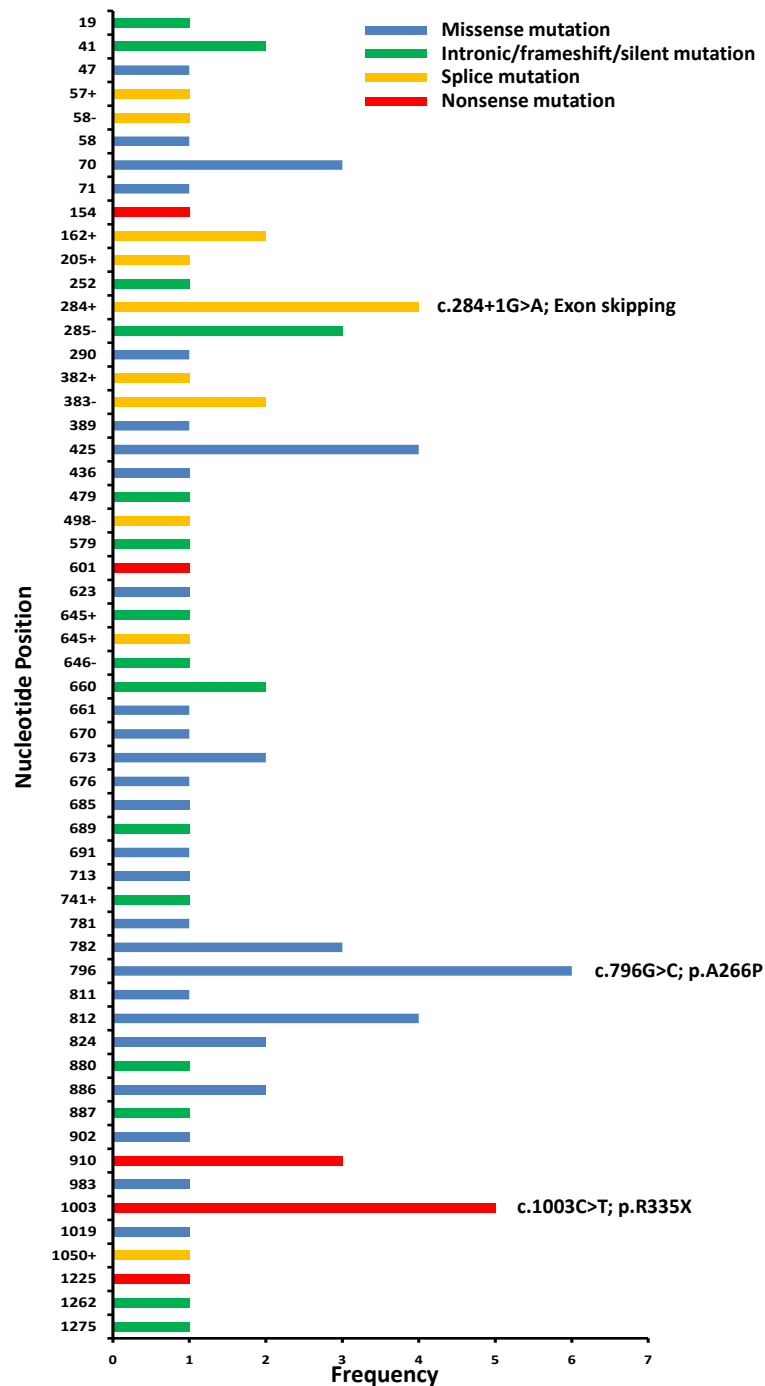
Figure 3.15: *Distribution of mutations based on location of nucleotide variation. The mutation type is colour coded and the nucleotide positions with suffix +/- indicate variation in introns.*

A frequency plot of mutations that disrupt each domain is shown in figure 3.16. The FERM-C domain has the highest frequency of mutations while the unstructured C-terminal region has the least number of reported mutations. Truncating mutations most commonly affect the FERM-N domain while non-truncating mutations most commonly affect the FERM-C domain.

Figure 3.16 shows the frequency of mutations based on the mutation class and whether familial/singleton cases were reported. The most common type of mutation is the missense mutation followed by the nonsense and splice mutations. These three types of mutations are mostly responsible for the familial cases of *FRMD7*-related infantile infantile nystagmus. The intronic group consists of intronic changes upstream and downstream of the splice donor and splice acceptor sites respectively. Mutations of nucleotides within the canonical positions (-2, -1, +1 and +2) and up to 5 base pairs of intronic sequence flanking the splice site were classed as splice mutations. The remaining intronic changes were grouped in the "intronic" mutation group. Interestingly there are a higher proportion of intronic mutations within the singletons group when compared to the familial group with intronic mutations as well as the number of singletons with the other three mutation classes.
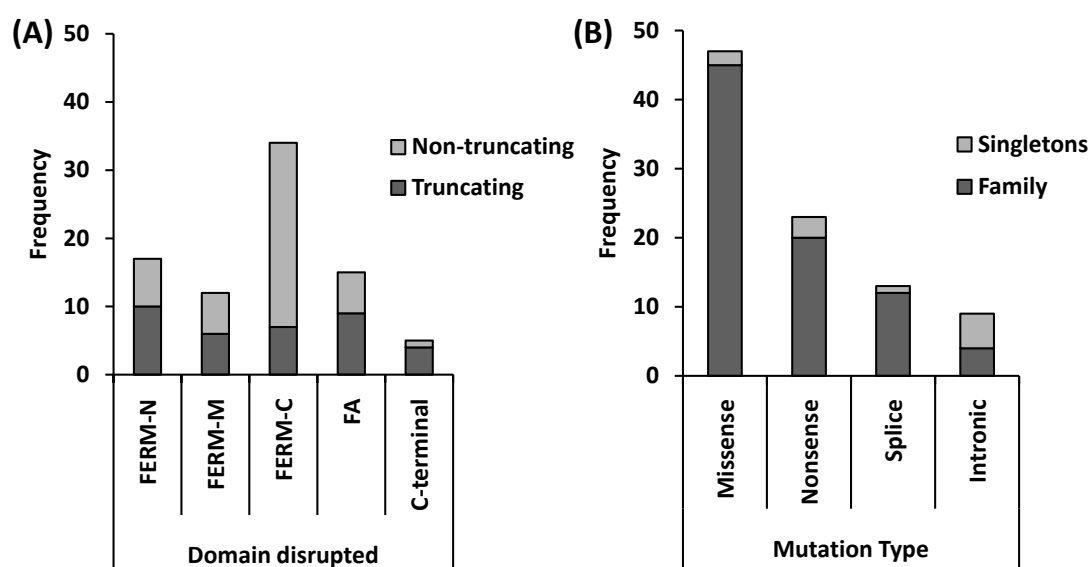
Figure 3.16: *The distribution of mutations based on domain disrupted (A) and the type of mutation (B).*

3.3.4 VARIABLE PENETRANCE

We assessed whether the following factors had an effect on the penetrance in female carriers:

1. Mutation type/effect (missense (non-truncating), nonsense (truncating), splice)
2. Domain disrupted (FERM-N, M, C, FA and C-terminal)
3. Alternate transcript disruption (Ensemble protein ID: ENSP00000359916)

The families were weighted in the logistic regression model based on the number of carrier females, thus accounting for the differences in family structure.

From a total of 83 FRMD7 families (includes families reported in the literature and this study) 75 FRMD7 family pedigrees were analysed. Eight reports were excluded due to: (1) lack of pedigree data (for instance, Zhang

et al. reported mutation of the *FRMD7* gene however no pedigree data was provided (162)) or (2) mutations affecting regulatory sites and thus its effect on the FRMD7 protein maybe varied. The number of families from previous studies used for the logistic regression model is shown in table 3.6. The mutation locations and proportion of mutations that disrupt various regions of the FRMD7 protein are shown in figure 3.17.

Table 3.6: Pedigree data from previous studies used for logistic regression model

Study (Reference)	Missense mutations	Nonsense mutations	Splice mutations	Number of families
Tarpey et al. (47)	11	6	6	23
Schorderet et al. (75)	2	1	2	5
Zhang et al. (76)	4	0	0	4
Self et al. (79)	0	1	1	2
Zhang et al. (77)	2	1	0	3
Kaplan et al. (81)	1	0	0	1
Shiels et al. (78)	2	0	0	2
He et al. (82)	1	0	0	1
Li et al. (80)	5	1	0	6
He et al. (85)	0	1	0	1
Fingert et al. (84)	0	1	0	1
Li et al. (83)	1	0	0	1
Total	29	12	9	50
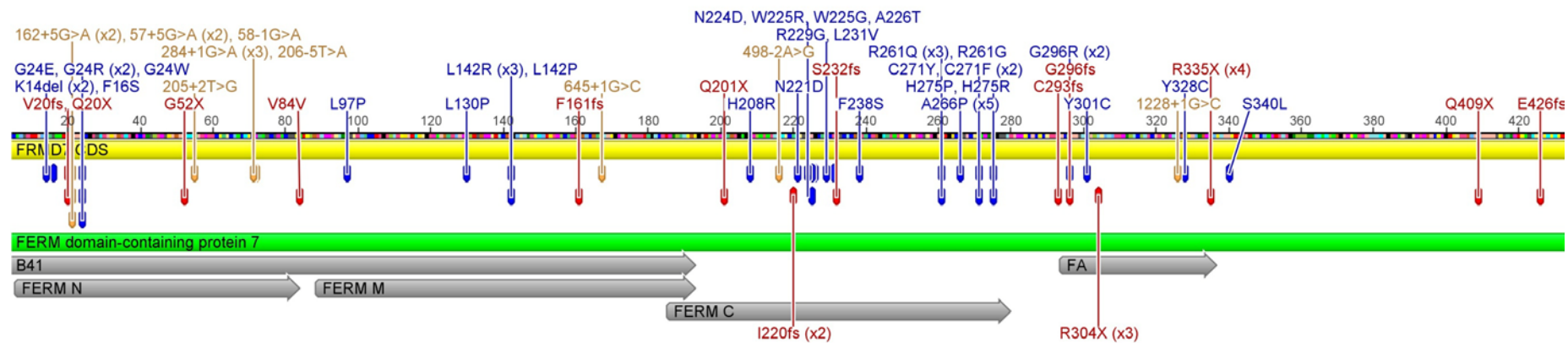
Figure 3.17: *(A) Summary of mutations analysed for variability of penetrance. The missense mutations are in blue while nonsense and splice mutations are shown in red and orange respectively.*

The type of mutation did not have a significant effect ($p>0.05$) on the penetrance among carrier females (figure 3.18). However the model predicts that the mutations within the FERM-C and FA domain were associated with significantly higher levels of penetrance (49% and 60% respectively) compared to the FERM-N (33%), FERM-M (26%) and C-terminal domains (37%) (figure 3.19). Similarly mutations affecting the alternate transcript are associated with a significantly higher penetrance (49%) compared to mutations that do not disrupt the alternate transcript (27%). Using the logistic regression model, the estimated odds ratio of penetrance with a mutation disrupting the alternate transcript rather than a mutation unlikely to disrupt the alternate transcript is 2.2 (95% confidence interval 1.2 to 4.3, $p=0.017$).

In large families there is also some evidence that the variability of penetrance are likely to be due to mutation specific effects. For instance in two separate families with amino acid variation C271F penetrance levels were approximately similar (see example in figure 3.20).
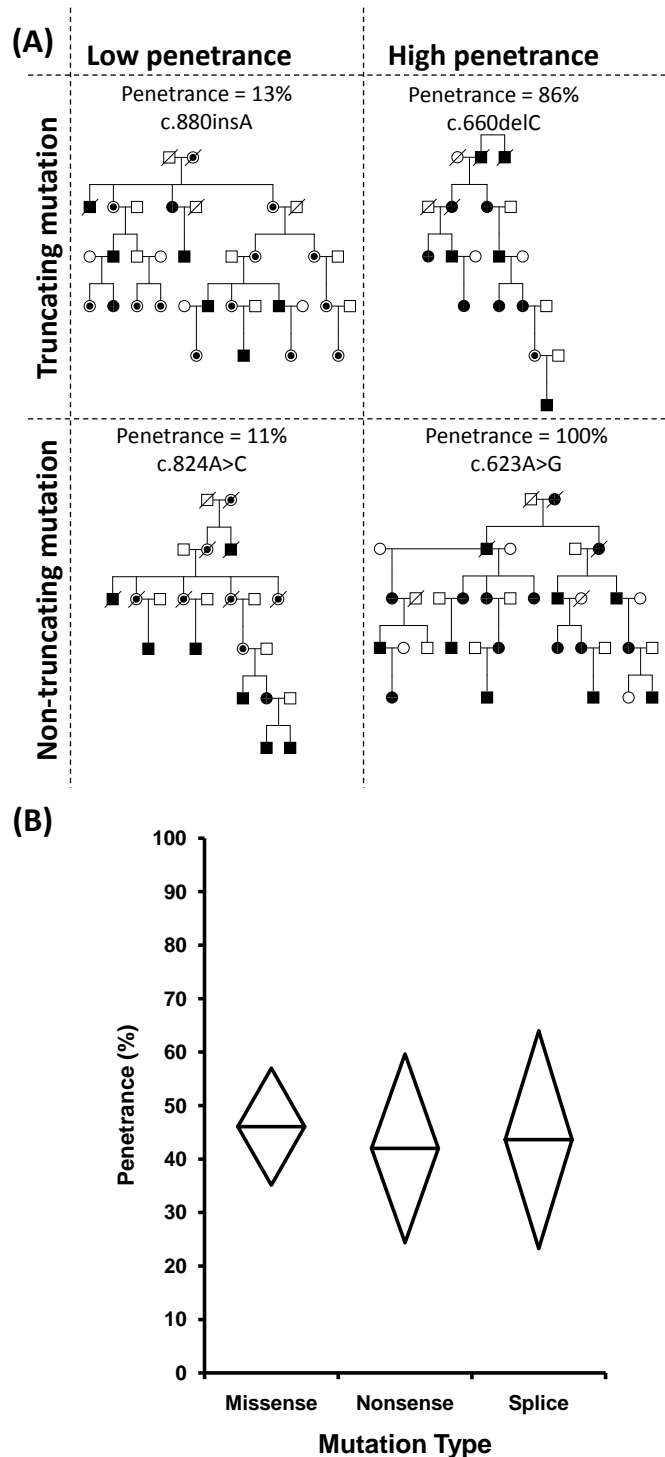
Figure 3.18: *(A) Example of families with truncating and non-truncating mutations with low and high penetrance in female carriers. The mutations c.880insA was reported by Self et al. while c.824A>C and c.623A>G were reported by Schorderet et al and Li N et al. The mutation c.660delC is from family F111 as described in section 3.3.2.4. (B) Diamond plots showing confidence intervals at the ends of the diamond bisected by the means showing no significant difference in penetrance based on mutation type.*

120
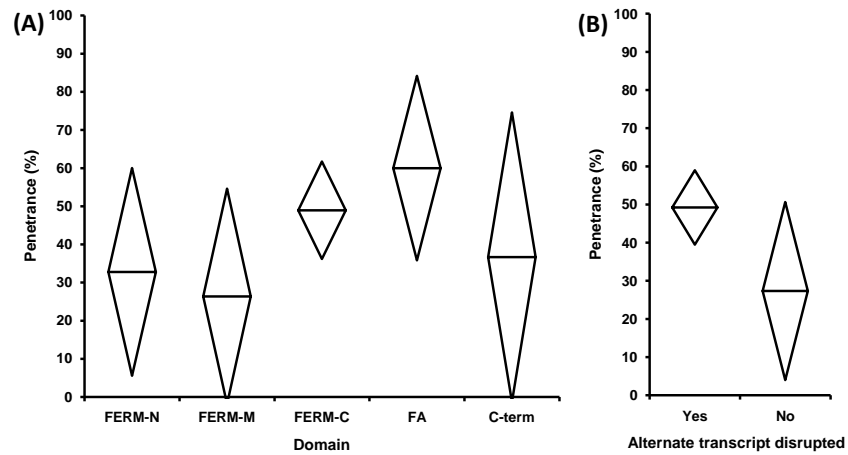
Figure 3.19: *Diamond plots showing the variability of penetrance based in the domain disrupted (A) and whether the alternate transcript is disrupted (B). The ends of the diamond represent the 95% confidence interval and the line bisecting the diamond represents the mean.*

Mutation: 812G>T
Amino acid variation: C271F
Penetrance: 52%

Mutation: 812G>T
Amino acid variation: C271F
Penetrance: 57%
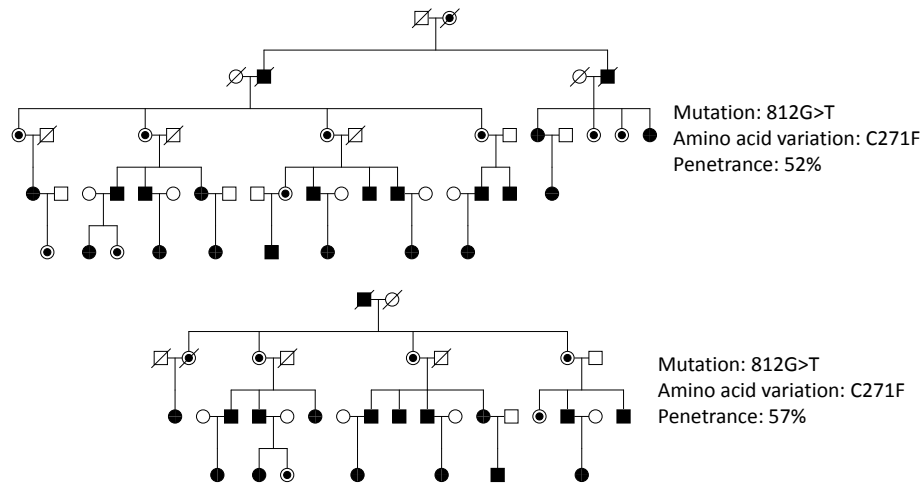
Figure 3.20: *Identical mutations in two separate families showing similar levels of penetrance. Family on the top of the figure was reported by He et al.* (82) *while the family in the bottom part of the figure was reported by Li et al.*(80)*.*

3.4 DISCUSSION

In this chapter we present the results of the largest sequencing project undertaken for *FRMD7* mutations. We identified that 66% of familial IIN and 14% of singleton cases were due to an *FRMD7* mutation. This is higher than previous reports which ranged from 20-57% in families and 3.6-7% in singletons. The difference in detection rate is likely to be due to the following factors: (a) different strategies for mutation detection (b) variation in sample sizes (c) lack of consensus on the diagnosis of IIN. In the study reported by Self et al. they first performed single-strand confirmation polymorphism to screen for mutations. Although this method is cheaper than sequencing all familial IIN cases, this approach has a lower mutation detection rate when compared to direct sequencing (79). Similarly smaller sample sizes were used in previous studies. The study performed by Tarpey et al. had comparable sample numbers however the detection rate in families and singletons were lower compared to this study. This could be since sequencing was confined to only the coding sequence and we find that among singletons and some families there are mutations within intronic elements and splicing elements which could be potentially missed if the sequencing coverage is limited to the coding sequence. For instance the mutation 285-118C>T would have been missed since it lies deep within the intronic sequences. We find this occurring in two separate families F103 and F139 from England. In addition to the deep intronic changes in families we report for the first time mutations that potentially affecting the branch point motifs in singletons and families. The branch site is an important element for recognition of the U2 small nuclear RNA (part of the spliceosome complex), the branch site is located upstream from the splice

acceptor site and acts as a signal for the spliceosome to recognise the splice acceptor site (163,164). Therefore mutations within these sequences can result in abnormal pre-mRNA splicing. Mutations involving branch point sequences are rare and have been identified in disorders such as xeroderma pigmentosa, congenital contractural arachnodactyly, fish-eye disease and neurofibromatosis 2 (165-169).

One of the main limitations in identifying novel mutations was problems associated with annotation from previous studies. Although all reports have been based on HGVS nomenclature standards there were numerous errors. For instance, initially the amino acid variation (R304X) in families F114 and F132 and amino acid variation (R261Q) in family F122 were considered novel since it had not been previously reported. The amino acid variation R303X and R260Q had been previously reported by Li et al in 2008 (80). Close inspection of these regions show that both previous reports were inaccurately annotated since the amino acid at position 303 is Glycine (G) rather than Arginine (R) and amino acid at position 260 is Serine (S) rather than Arginine (R). Similar errors in annotation at the cDNA level include report of 283+1G>A (from He et al. (85)), 676-2A>G (from Schorderet et al. (75)), 686C>G (from Kaplan et al. ((81)), 990G>T (from Li et al. (170)), and 1274-1275delTG (from He et al. (85)); these should be 284+1G>A, 498-2A>G, 685C>G, 812G>T and 1275-1276delTG respectively. These errors are further perpetuated by reviews where they remain uncorrected (62,85). The possible reasons for numerous errors in mutation reporting could be due to: (1) lack of specialised mutation detection software, (2) errors associated with manual

annotation, (3) incorrect annotation of transcription start site hence incorrect use of HGVS recommended nomenclature.

The identification of the mutation hotspots provides useful information for establishing a tiered testing strategy which could potentially be more cost effective. For instance a useful first step could be for identification of the 796G>C DNA change. This can be done using restriction fragment length polymorphism (RFLP). This region harbours the recognition site for the BglI enzyme (5'-GCCNNNN^NGGC-3') a mutation would alter this site to (5'-GCCNNNN^NGCC-3'), therefore results in obliteration of this recognition site. Similarly since mutations affecting the FERM-N and FERM-C domain represent approximately 57% of all mutations (52/92 mutations) it would be more cost effective to sequence these two regions prior to sequencing the remaining regions. The identification of mutations deep within intronic sequences also suggests that further high throughput sequencing studies encompassing the entire genomic sequence and flanking sequences are needed to identify the rarer allelic variants which could be responsible for mutations within singletons and some families.

In 2007 Self et al. showed that truncating mutations were associated with significantly lower levels of penetrance (27%) compared to non-truncating mutations (64%) (n=21 families) (62). Contrary to the previous report we did not find that the mutation type had a significant effect on the penetrance in carrier females (n=75 families). Although we noticed that in some families with truncating mutations the penetrance was lower this was not consistently observed in all families (see examples in figure 3.18). We also investigated whether penetrance was dependent on the mutation location. Mutations were also divided based on

whether they disrupted different FERM domains and whether it disrupted the alternate transcript. Interestingly we found that mutations within the FERM-C and FA domain were associated with a higher level of penetrance, similarly mutations that disrupted the alternate transcript were also associated with a higher level of penetrance. The alternate transcript encodes for a shorter peptide extending from amino acid position 171-714. This region also overlaps with the FERM-C and FA domains. A possible explanation for the difference in penetrance observed based on domains affected could be that mutations affecting FERM-N and FERM-M domains are associated with a more deleterious cellular phenotype and subsequent skewed X-inactivation and clonal selection would result in these observed differences. Similar examples of highly skewed X-inactivation and clonal selection have been reported with X-linked agammaglobulinemia (OMIM 300300) (171,172).

From a genetic counselling perspective one could move towards providing information based on each mutation. For instance the amino acid variation C271F is associated with a penetrance of 52-57% which has been seen in two separate large families. Similarly amino acid variations L142R in larger families are associated with penetrance levels between 50-66%. This provides some evidence of variation in penetrance based on specific mutation, which could be used as a rough guide for genetic counselling. However it would be necessary to identify further large families with identical mutations to determine whether the variability of penetrance in carrier females is due to genetic or environmental factors.

A major limitation associated with determining penetrance for the phenotype of nystagmus is that some carrier's exhibit subclinical nystagmus (which can be detected only on eye movement recordings). Since all genetic testing centres do not have access to eye movement recordings it is clear that all obligate carriers were not screened for subclinical nystagmus. This could also be the reason why some families with the same mutation could be presenting with different levels of penetrance.

With the evolution of massive parallel sequencing technologies and decreasing cost for sequencing, performing whole genome sequencing would help identify further candidate genes likely to be involved in IIN. Similarly the variability in penetrance could be addressed within the next few years as whole transcritome sequencing and expression analysis become more accessible.

In summary, we present the results of the largest FRMD7 sequencing project. The total number of FRMD7 mutations identified was 37 of which 23 were novel. For the first time we show the mutation hotspots and deep intronic mutations associated with FRMD7-related infantile nystagmus. We also show that penetrance of nystagmus in female carriers is related to the mutation location rather than mutation type.

4. CHAPTER FOUR: THE CLINICAL AND MOLECULAR GENETIC FEATURES OF IDIOPATHIC INFANTILE PERIODIC ALTERNATING NYSTAGMUS

This chapter addresses the aims:

- To determine the molecular genetic basis of idiopathic infantile periodic alternating nystagmus

- To identify neural substrates that could be involved in *FRMD7* related infantile nystagmus.

4.1 INTRODUCTION

In idiopathic infantile periodic alternating nystagmus (II-PAN), the direction of the quick phase and slow phase alternates periodically with time. This phenotype of nystagmus is distinct from other nystagmus forms due to the periodic time component. Acquired forms of PAN are also reported and arise due to instability of the vestibulo-optokinetic systems (173). Animal and mathematical models for acquired PAN have demonstrated how instability of the velocity storage mechanism for vestibular eye movements and an adaptive mechanism for this instability can results in a periodicity of oscillations of 4 minutes (37,174). It has also been shown that patients with acquired PAN have abnormalities of optokinetic nystagmus (OKN), with some patients having no OKN response and the PAN cycle continues through the OKN stimuli (175). The acquired form of PAN often responds well to specific drugs such as baclofen (176).

II-PAN is considered to be a subtype of IIN; however its diagnosis has different implications for pharmacological and surgical treatment (177). The first report of

familial II-PAN was by Huygen and colleagues where both mother and daughter were reported to have PAN since birth (66). Shallo-Hoffmann et al. reported a case of II-PAN with an X-linked history of nystagmus (178,179). Hertle et al. described another family spanning three generations, with a phenotype of PAN in all four patients examined with eye movement recordings. Based on an X-linked mode of inheritance and the distinct phenotype consistently seen in all generations it was assumed that a unique locus for II-PAN was present on the X-chromosome (52). However no molecular genetic studies were performed in these families to substantiate that a separate locus is present for II-PAN. There is some evidence for an additional locus for IIN on the X-chromosome (51). Cabot et al. reported a four generations French family with X-linked IIN; linkage analysis showed mapping to Xp11.4-11.3 (between the polymorphic markers DXS8015 and DXS1003) (51). However the type of nystagmus in this family has not been described.

In this chapter we present evidence showing that mutations of the *FRMD7* gene can be associated with PAN. We report ten mutations of the *FRMD7* gene associated with PAN. Furthermore, we highlight the spectrum of variable phenotypes associated with *FRMD7* mutations and that expression of *FRMD7* correlates to neuronal circuits which have been associated with acquired PAN.

4.2 METHODS

Using eye movement recordings we examined a cohort of 31 X-linked IIN families and 14 singletons (total of 70 patients). Fifteen of the families were previously described to have *FRMD7* mutations (47); four families did not have *FRMD7* mutations. The remaining 12 families and 11 singletons with IIN were sequenced as part of the cohort described in chapter 3. Within this cohort we identified 10 families (figure 4.1) and one singleton with II-PAN (total of 21 patients). In our study population, II-PAN occurred in 18 males and in three females.

A central fixation task was used for diagnosing PAN. All patients with PAN underwent OKN testing. The setup for eye movement recordings and the details of the tasks are described in section 2.6.5.

Bidirectional sequence analysis and *in-situ* hybridisation experiments were performed as described in sections 2.1 and 2.2. Tissue sections from 8 samples were analysed from Carnegie Stage (CS) 16 (~37 days post conception (dpc); n=1); CS19 (~47 dpc; n=3); CS22 (~54 dpc; n=2) and CS23 (~56 dpc; n=2). All human embryos selected for sectioning had a normal karyotype and morphology. The stage of embryonic development was determined by Professor Susan Lindsay by assessment of external morphology as described in (180,181).

4.3 RESULTS

4.3.1 CLINICAL CHARACTERISTICS

The pedigrees with patients diagnosed with II-PAN are shown in figure 4.1. Among the 10 families we were able to perform eye movement recordings in 26 of the affected patients, of which 20 patients had II-PAN (figure 4.1). The phenotypes in affected members of family 2 have previously been described by Hertle, et al. 2005 (52).
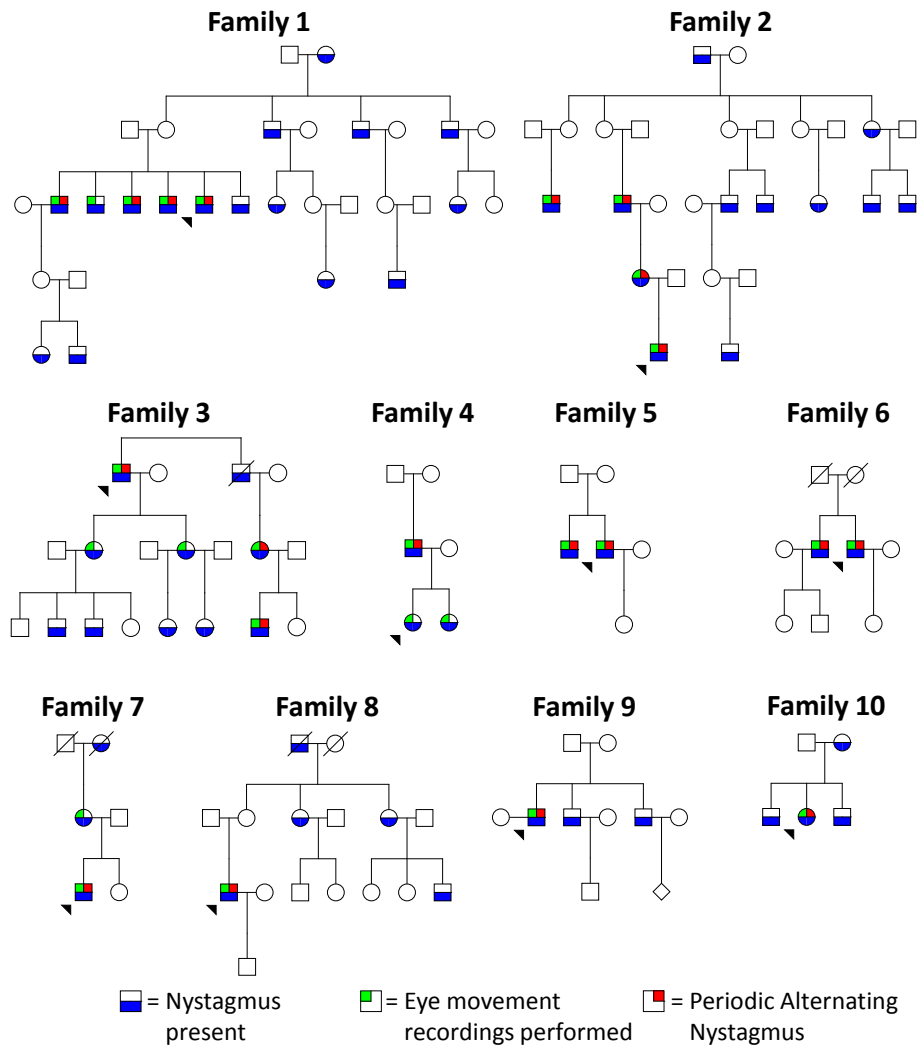
Figure 4.1: *Families with idiopathic infantile periodic alternating nystagmus. In families 1-4 eye movement recording were performed in three or more affected individuals, while in families 4-7 eye movement recordings were obtained in two or more affected individuals. In families 8-10 eye movement recordings were only performed in one affected individual.*

The best-corrected visual acuity in our cohort of patients with PAN ranged from 0.0 LogMAR to 0.54 LogMAR with a median of 0.2 LogMAR. Three patients with II-PAN had a slight anomalous head posture between 5-10 degrees. However, only in one patient the head posture was noticed to occur alternating to the right or left on two different examination days. None of the II-PAN patients had strabismus. All had some degree of stereopsis; the range of stereoacuity was 85 – 550'' with a median stereoacuity of 150''.

Sequence analysis showed that all ten of the II-PAN families and the singleton had mutations of the *FRMD7* gene. A summary of the mutations and domains affected are shown in figure 4.2.

Family F8 had a missense mutation (c.47T>C) in exon 1, resulting in the substitution of phenylalanine by serine at position 16 (p.F16S). Sequence analysis of the proband in family F9 revealed a splice site mutation (c.58-1G>A) at the 3' end of intron 1. This results in the loss of the conserved splice acceptor residue. The effects of the mutation were predicted using the alternative splice site predictor (156), and considered pathological due to exon skipping resulting in an mRNA transcript with exon 2 missing. The singleton S1, had a missense mutation (c.811T>A) in exon 9 resulting in a substitution of cysteine to serine at position 271 (p.C271S). Both missense mutations at amino acid positions 16 and 271 were considered pathological as they involved residues that were identical within invariant blocks in the species *Mus, Gallus, Xenopus* and *Tetraodon*. The amino acid change C271S would disrupt a large alpha helical domain in the wild-type structure. Similarly, the amino acid change F16S is likely to disrupt adjacent secondary structure. Consequently, both missense mutations, F16S and C271S, decrease the stability of the mutant protein (due to a decrease in the free energy value).

Six of the eight remaining families (F1, 2, 3, 4, 7 and 10) all revealed missense mutations of the *FRMD7* gene. These mutations have been previously reported and their translational effects have been described (47). Family F5 and F6 were the only families which had a nonsense mutation (c. 1003C>T) resulting in a

premature stop codon at amino acid position 335 (p. R335X). F2 was the family previously reported by Hertle et al. with an II-PAN phenotype and an X-linked inheritance (52). Sequence analysis of this family revealed a missense mutation (c.70G>A) resulting in hemizygous replacement of glycine with arginine at position 24 (p. G24R). The amino acid changes as a result of the missense mutations in families F1 (L231V), F2 (G24R), F3 (C271Y), F4 (A266P), F7 (A226T) and F10 (S340L) are associated with a decrease in the free energy value thus likely to destabilise the mutant protein.

ID	Country of origin	Mutation	Electropherogram (WA/MA)	Mutation type	Domain affected
F1	Ireland & Germany	c.691T>G; p.L231V		Missense	FERM-C
F2	Ireland	c.70G>A; p.G24R		Missense	FERM-N
F3	England	c.812G>A; p.C271Y		Missense	FERM-C
F4	England	c.796G>C; p.A266P		Missense	FERM-C
F5	England	c.1003C>T; p.R335*		Nonsense	FA
F6	India				
F7	England	c.676G>A; p.A226T		Missense	FERM-C
F8	England	c.47T>C; p.F16S		Missense	FERM-N
F9	England	c.58-1G>A		Splice	FERM-N
F10	Romania	c.1019C>T; p.S340L		Missense	C-terminal
S1	England	c. 811T>A; p.C271S		Missense	FERM-C

Figure 4.2: Country of origin, mutations of the FRMD7 gene in the families (F1-10) and singleton (S1) with II-PAN are shown in (A). The electropherograms from the respective families and singleton are shown with the wild type allele (WA) represented on top of the mutant allele (MA). All mutant electropherograms show hemizygous mutations of the FRMD7 gene except for the female probands in families F4 and F10 where a heterozygous mutation is shown. The type of mutation and domain affected is shown in (B). Missense mutations were the most common and changes to amino acid at positions 271 and 335 occurred in two families (271: F3 and S1; 335: F5 and F6). F1 = Family 1; S1 = Singleton 1; B41 = Band 4.1; FA = FERM adjacent domain.

4.3.3 NYSTAGMUS WAVEFORM CHARACTERISTICS

The II-PAN was not diagnosed clinically in any of the families or the singletons. However the use of eye movement recordings during a prolonged duration of fixation (5 minutes) aided the diagnosis of II-PAN. An example of original eye movement recordings from family F3 is shown in figure 4.3. In families F1, F3, F4 and F7 we observed phenotypic heterogeneity as not all the examined patients had II-PAN (figure 4.3). Among the families with II-PAN, 6 of 26 subjects in which eye movements were performed did not have PAN. Overall, the time period for the II-PAN cycle varied between 90s and 260s and the singleton had a periodicity of 280s. All family (F1-F10) members with II-PAN had a jerk-related or dual jerk nystagmus. In family members without II-PAN (F1, III:3; F3, II:2 and 4; F4, III:1 and 2; F7, II:1;) the predominant nystagmus waveform was pendular.
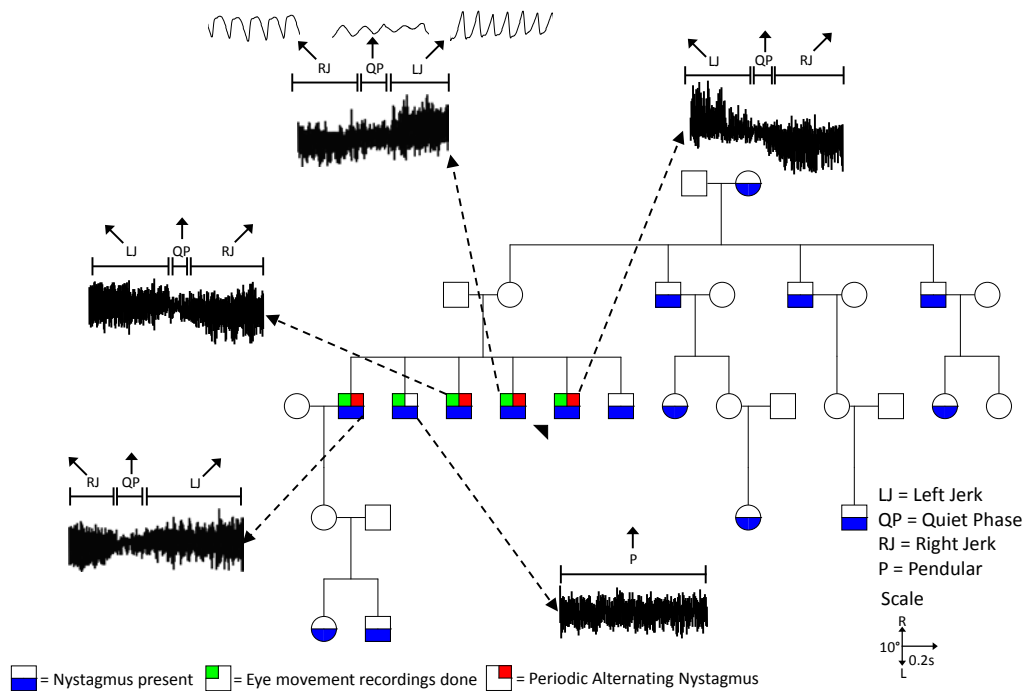
Figure 4.3: *Original eye movement recordings from family F1. Overviews of the three phases of the PAN cycle and excerpts from within each phase of the cycle are shown in this figure. A typical PAN cycle which consists of three phases: i) left jerk (LJ), where the quick phase is directed to the left, ii) a quiet phase (QP), where the intensity of the nystagmus is minimal and iii) a right jerk (RJ), where the quick phase is directed to the right. One of the examined family member (III:3) did not have PAN, but a pendular (P) nystagmus. Scale for the excerpts are shown in the bottom right with waveform deflection upwards and downwards representing horizontal eye movements to the right and left respectively.*

None of the patients with II-PAN showed an optokinetic response for both horizontal stimulus directions (rightwards and leftwards). The PAN cycle continued through the OKN testing and was not changed by the OKN stimuli (figure 4.4). Vertical OKN was seen in all patients in both directions (upwards and downwards).
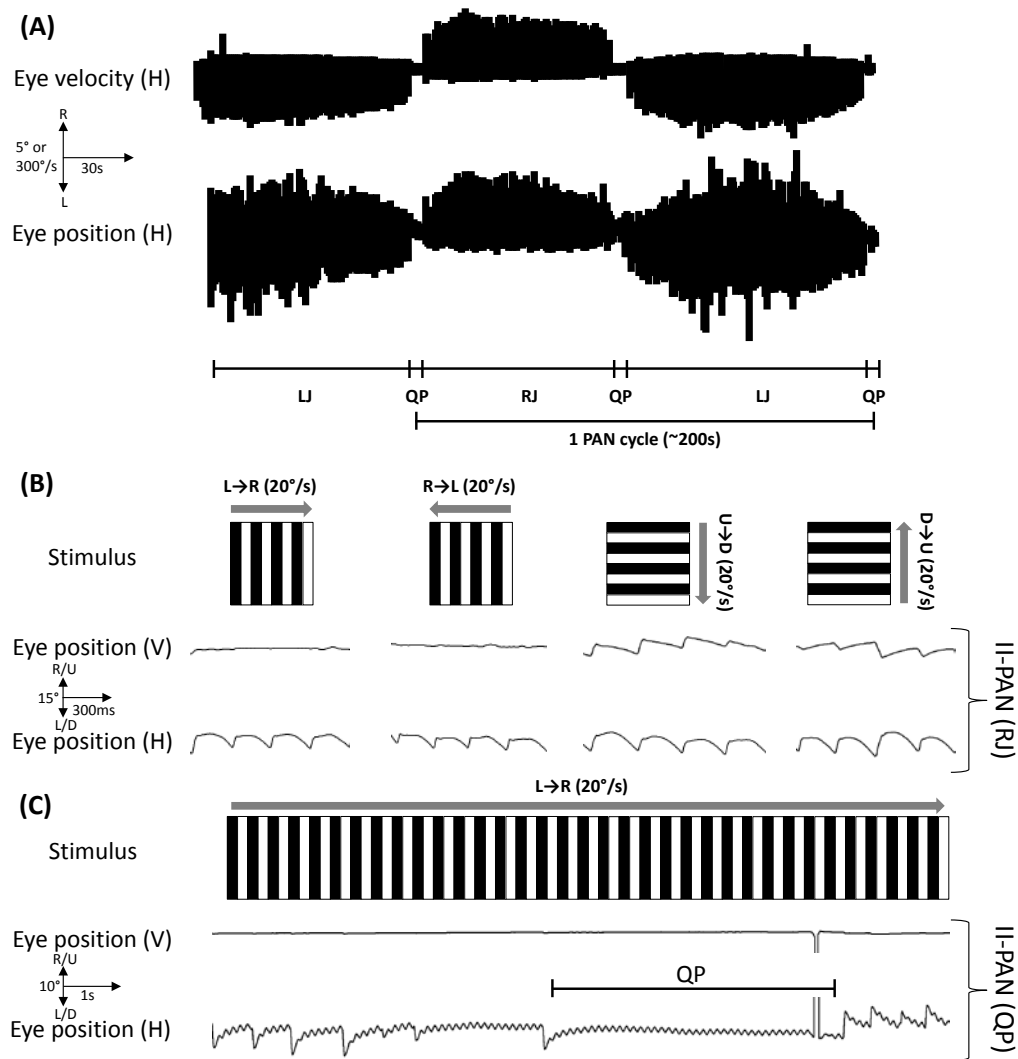
Figure 4.4: *Compressed eye movement recordings showing an overview of the various phases of the PAN cycle (A). In the above example 1 cycle consists of right jerk (RJ) followed by a quiet phase (QP), left jerk phase (LJ) and another quiet phase (QP). Upward deflection of the horizontal (H) position and velocity trace represents right beating nystagmus and downward deflection represents left beating nystagmus. The optokinetic response was measured for OKN stimuli (B) moving in the horizontal (rightwards (L→R) and leftwards (R→L)) and in the vertical direction (downwards (U→D) and upwards (D→U)). The patient (II-PAN) shows no horizontal optokinetic response to the stimulus; the nystagmus is unchanged in the right jerk phase during OKN testing. However for the vertical OKN stimuli, a vertical optokinetic response is seen in the vertical trace (V) for the patient. The II-PAN cycle was not changed by the horizontal OKN stimuli as shown in (C). The transition (QP) between left jerk and right jerk is seen during an extended horizontal OKN task.*

137

4.3.4 EXPRESSION OF *FRMD7*

In-situ hybridisation experiments showed strong hybridisation signals from the structures involved in setting up the vestibulo-ocular reflex (VOR) and optokinetic reflex (OKR) arc, this included the developing cerebellum, vestibular apparatus and developing neural retina (figure 4.5A-E). Expression is detected in the ventricular zone (VZ) of the neural retina and optic stalk (figure 4.5B). In structures of the VOR, *FRMD7* is expressed in the otic vesicle and vestibulocochlear ganglion (figure 4.5C). The vestibular nuclei, which arise partly from the VZ of rhombomeres 2, 3 and 4, form the horizontal neural integrator which is an important structure in the VOR and OKR arcs. *FRMD7* expression is seen in the VZ of rhombomeres 2, 3 and 4 (figure 4.5D) as well as in the developing cerebellum (figure 4.5E). The cerebellum arises entirely from rhombomere 1 and its VZ gives rise to neuroblasts which migrate on radial glia to develop into the cerebellar nuclei and purkinje cells in the cerebellar cortex. *FRMD7* is expressed in differentiating and migrating neurons as well as in the VZ, for example in the cerebellum and rhombomeres 3 and 4 in the hindbrain (e.g. figure 4.5D and E).

(A) Low magnification view

Rh1

Rh2

os

nr

Rh3/4

Rh1

vc/ov

po/os

ov

CS16   CS19   CS22   CS23   CS23

(B) Developing OKR arc   **(C) Developing VOR arc**   **(D) Developing neural integrator**   **(E) Developing cerebellum**

Antisense images

nr   os   po   os   ov   vc   ov   Rh4 Rh3   Rh2   Rh1   Rh1

Sense images

| Neural retina (nr) CS16 | Optic stalk (os) CS16 | Preoptic area (po) CS23 | Otic vesicle (ov) CS23 | Vestibulo-cochlear ganglion(vc) CS23 | Rhombomere 3/4 (Rh3/Rh4) CS16 | Rhombomere 2 (Rh2) CS19 | Rhombomere 1 (Rh1) CS19 | Rhombomere 1 (Rh1) CS22 |

(F) Overview of VOR and OKR arcs

Cerebellum

Feedback loop

VOR arc   SCC   CN VIII   VN   Oculomotor nerves   EOM

OKR arc   Retina   CN II

139

Figure 4.5: *FRMD7 expression in developing human brain. Panel A shows low magnification views of the sections from which higher magnification views are shown in Panels B to E. Panel F gives a simplified overview of the VOR and OKR arcs indicating the afferent arm of the reflex arc starting at the semicircular canals (SCC) and retina followed by the cranial nerves (CN) involved in the respective arcs. The neural signal is integrated at the vestibular nucleus (VN) which is subject to the feedback loop through the cerebellum. The efferent arm of the reflex consists of the oculomotor nerves innervating the effector organ i.e. the extraocular muscles (EOM). Panel A, shows the following images from left to right: CS16 section through forebrain and hindbrain, CS19 whole embryo sagittal section, CS22 section through midbrain and hind brain, CS23 section through midbrain, hindbrain and forebrain, CS23 head sagittal section. In panels C to F images of sections hybridized with antisense probes (signal detected as purple stain) are shown above corresponding sections hybridized to sense control probes (no signal detected). Abbreviations: nr – neural retina; os – optic stalk; po – preoptic area; ov – otic vesicle; vc – vestibulocochlear ganglion; Rh1-4 – rhombomere 1 – 4. Scale bar for the low magnification images (A) represents 1 mm for all images except the CS16 image where the scale bar is 0.5mm. For all high magnification images (B-E) the scale bar represents 0.3mm except the preoptic image (CS23) where it represents 0.6mm.*

4.4 DISCUSSION

In this study we show for the first time that II-PAN can be associated with mutations of the *FRMD7* gene. II-PAN was only detected using eye movement recordings and most patients had relatively good visual acuity (median: 0.2 LogMAR) and stereoacuity (median: 150''). The PAN cycle length varied from 90-280s and none of the II-PAN patients had a horizontal optokinetic reflex. We show that *FRMD7* is expressed within developing VOR and OKR arcs, which identifies the likely neural substrates involved in II-PAN and in *FRMD7*-related infantile nystagmus. We identified eleven mutations in ten families and one singleton and describe both the phenotypic and translational effects of these mutations. In our cohort of families, the predominant class of mutation associated with this phenotype were missense mutations (8/11) though both truncating (2/11) and splice site (1/11) mutations are also seen. Ten of the eleven mutations resulted in amino acid changes within functionally significant domains (FERM-N, FERM-C and FA).

From a clinical point of view PAN is typically under-diagnosed (95,182,183) as it often can only be identified on eye movement recordings during an extended fixation task to demonstrate the periodicity of the nystagmus and its three phases. A recent study estimated that approximately 15% of all infantile nystagmus syndrome patients have PAN (184). In contrast, Shallo-Hoffmann et al. showed that a higher proportion of approximately 39% of congenital nystagmus patients have PAN (178). Interestingly, in the II-PAN incidence study by Shallo-Hoffmann, et al. a family with X-linked PAN has been described, though no genetic diagnosis was provided (178,179). We

141

noticed the occurrence of II-PAN, using eye movement recordings, in at least one family member with an *FRMD7* mutation in 10/31 (32%) families and 1/14 (7%) singletons. This suggests that most II-PAN patients are likely to have a family history of nystagmus and it is important to screen for *FRMD7* mutations. Diagnosing PAN is important since it has different therapeutic implications compared to other forms of infantile nystagmus. The Kestenbaum procedure is used in IIN to correct anomalous head posture if it is constantly directed towards one side. However it is inappropriate in patients with PAN since it does not correct anomalous head posture which can alternate to both sides as in II-PAN or may even accentuate the head position to one side (183). Abadi and Bjerre showed that among the cohort of patients with PAN only 18% were IIN and the remaining 82% were associated with albinism (95). The incidence of PAN with both albinism and *FRMD7* mutations suggests that there may be a common mechanism in the occurrence of PAN in these two disorders.

The FRMD7 protein is homologous to the FARP1 and FARP2 proteins; this homology is concentrated at the N-terminus. Previous studies have shown that FARP1 and FARP2 are involved in neurite outgrowth and branching (88,185). Recently it has been demonstrated that knockdown of *FRMD7* in Neuro-2A cells results in shorter neurites, suggesting a role in axonogenesis or dendritogenesis (86). We found expression of *FRMD7* within the developing VOR and OKR arcs. In this study we observed that all patients with PAN and *FRMD7* mutations had no OKN response. Previous phenotypic studies in *FRMD7* related infantile nystagmus have shown that the OKN gain

is lower in affected individuals with *FRMD7* mutations or no OKN response was detected (79). There are also reports of reversal of OKN in patients with congenital nystagmus (176), albino rabbits (186) and achiasmatic fish (187); which are suggested to arise due to miswiring within the OKN arcs. In unaffected carriers of *FRMD7* mutation a subnormal OKN gain has been reported (91). This suggests that the optokinetic system is involved in this disorder and we have now provided substantial evidence from the expression studies that *FRMD7* is expressed within the neural substrates in the developing OKN and VOR arcs. However the expression is not restricted to these tissues (for example expression is also detected in the midbrain [figure 4.5A]). This provides general evidence of the neuronal networks involved in *FRMD7* related infantile nystagmus. Based on the in-vitro assays in FRMD7 and studies from homologous proteins (FARP1 and FARP2) there may be miswiring of the developing OKN and VOR systems thus predisposing to the phenotypes of PAN and *FRMD7* related infantile nystagmus. Phenotypic data (not confined to PAN) from patients with albinism also suggest that VOR and OKN systems are affected (188,189). The higher prevalence of PAN in patients with albinism (as suggested by Abadi and Bjerre 2002) may be due to the misrouting of the retinogeniculate fibres which may predispose to instability within the OKR arc. Therefore the PAN phenotype may represent a part of the spectrum of infantile nystagmus forms depending on the degree of instability of the vestibulo-optokinetic systems. However, the presence of sibship clustering (seen in the larger families F1, F2 and F3) and familial involvement of the PAN phenotype may suggest that

certain mutations of the *FRMD7* gene predispose to the PAN phenotype. For example the R335X mutation was seen in two families of different descent, similarly mutations at amino acid position 271(F3: C271Y and singleton C271S) in one family and the singleton resulted both in II-PAN phenotype. The differences in phenotype between patients could possibly be due to variable expressivity which could arise as a result of involvement of disease modifying genes and environmental influence that may affect the post-natal development of the oculomotor system. We have previously also reported intra-familial variability in the type of nystagmus (91)

The aetiology of acquired PAN has been associated with dysfunction of the cerebellum, including cerebellar degenerations, cerebellar tumours, multiple sclerosis and other mass lesions involving the cerebellum (173,190-192). Leigh et al. hypothesize that acquired PAN arises as a result of instability within the optokinetic-vestibular system (173). Phenotypic data from patients with acquired PAN also suggest that the patients had no optokinetic function and the OKN stimuli did not perturb the PAN cycle (173,175). The time period for one PAN cycle in acquired forms varies from 200-240 seconds, (173,175,190) in this study we observed that the time period for II-PAN varies from 90 -280s. Only one of our patients had a time period of 90 seconds, while the remaining had a time period greater than 190 seconds. Thus there is some similarity in the periodicity of the II-PAN cycle when compared to the acquired PAN. The neuronal substrates implicated in acquired PAN and phenotypic data from patients with acquired PAN are closely related to the phenotypic and expression results highlighted in this

144

study. This also suggests some similarity in the aetiological mechanisms between infantile and acquired PAN.

Acquired forms of PAN have been treated successfully using baclofen (a GABA agonist). Baclofen suppresses the velocity-storage mechanism possibly by reinforcing the action of the inhibitory GABAergic purkinje cells from the nodulus to the vestibular nuclei. Some congenital forms respond occasionally to baclofen (193,194). It would therefore be interesting to see whether these subsets of a phenotypically homogenous population have a different therapeutic response compared to the other phenotypes encountered with both *FRMD7* patients and non-*FRMD7* patients (91).

In conclusion, we have shown that mutations in the FRMD7 gene form the genetic basis of idiopathic infantile periodic alternating nystagmus. Expression and phenotypic data suggest that II-PAN arises from instability of the optokinetic-vestibular systems.

5. CHAPTER FIVE: RETINAL EXPRESSION OF *FRMD7*

This chapter addresses the aim:

- To characterize the spatial and temporal expression profile of *FRMD7* in developing human, murine, rat and zebrafish retina.

5.1 INTRODUCTION

In 2006 Tarpey et al. showed that *FRMD7* is expressed at 56 days post ovulation (dpo) in the developing midbrain, hindbrain and neural retina (47). Due to its sequence homology to the FARP1 and FARP2 proteins it was speculated that the FRMD7 protein could also have a similar function to these proteins. Overexpression assays for FARP2 have shown an increase in the number of lateral growth cones from neurites (88) hence it was suggested that FRMD7could be involved in determining neurite length and branching. In 2009, Self et al. suggested that FRMD7 could be involved in synapse formation and axon growth (195). In 2010, Betts-Henderson et al. showed, in a Neuro-2A assay, that knockdown of *FRMD7* resulted in an overall decrease in neurite length but with an increased number of cells (figure 5.1). Therefore Betts-Henderson et al. provided the substantial evidence that FRMD7 has a role in neuronal development (86).

The rationale to perform spatiotemporal expression studies in the developing retina arises as a result of two studies: (1) In chapter 4, while investigating the global expression patterns we observed strong hybridisation signals within the developing OKR arc in particular the neural

retina; (2) Tarpey et al. also observed at one developmental stage (56 dpo) strong hybridisation signals within the neural retina (47).

Therefore these preliminary findings warranted further investigations to systematically assess *FRMD7* expression profile in the retina. This could provide insights into if there are any specific cell types that could be involved in *FRMD7*-related infantile nystagmus. Previous studies have been limited to mRNA expression and it is unclear if FRMD7 protein expression is also observed in these tissues. Using different species would help establish the trends in the expression pattern. The differences in cell distribution in different species are helpful in identifying cell types that may or may not be affected. For instance rat and mice are rod dominated retinas hence to compare the outer nuclear layer staining patterns with humans and zebra fish would be useful. Post natal expression profiles in humans are difficult to determine due to limited accessibility of post natal tissue samples. Hence murine/rat tissue samples would be required for postnatal expression profiles. Therefore in this chapter we will focus on the retinal spatial and temporal expression of *FRMD7* in developing human, murine, rat and zebra fish tissue.
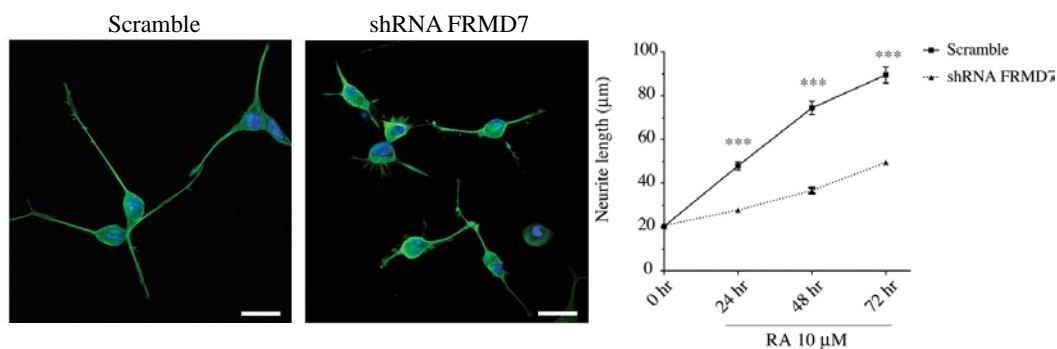
Figure 5.1: *Knockdown of FRMD7 in Neuro-2A cells using shRNA FRMD7 shows an increase in the degree of branching but an overall decrease in the length of the neurites compared to cells transfected with a non-silencing sequence (scramble). The graph on the right shows that cells transfected with shRNA-FRMD7 show a significantly decreased overall neurite length compared to cells transfected with the scramble sequence. (Reproduced with permission from:* (86)*)*

5.2 METHODS

The embryos were prepared as described in chapter 2. The specific methods related to *in-situ* hybridisation, immunohistochemistry, primary culture and immunocytochemistry are outlined in sections 2.2-2.5. The developmental stages investigated are shown in table 5.1.

Table 5.1: Developmental stages used for investigating FRMD7 mRNA and protein expression

Species	Developmental Stage
Human	1. Carnegie Stage 15 (35 dpc*) 2. Carnegie Stage 16 (37 dpc) 3. Carnegie Stage 19 (47 dpc) 4. Carnegie Stage 22 (54 dpc) 5. Carnegie Stage 23 (56 dpc) 6. 9 weeks post conception
Mouse/Rat	1. Embryonic day 10.5 (E10.5) 2. Embryonic day 16.5 (E16.5) 3. Post natal day 5 (P5) 4. Post natal day 6 (P6) 5. Post natal day 16 (P16) 6. Post natal day 18 (P18)
Zebrafish	1. 3 days post fertilisation (3dpf) 2. 5 days post fertilisation (5dpf)

*dpc = days post conception

5.3 RESULTS

5.3.1 EXPRESSION IN DEVELOPING HUMAN RETINA

A migratory expression pattern was seen in the developing neural retina. At CS15 the optic cup consists of an inner wall which will form the sensory retina and an outer wall which will form the retinal pigment epithelium (RPE). The inner wall is further subdivided into the inner and outer neuroblastic layers. At this stage restricted expression of *FRMD7* was seen within the outer neuroblastic layer (figure 5.2). The development of the retinal ventricular zone (VZ) is similar to the cortical VZ development. The postmitotic cells from the VZ migrate to the future cell layer (ganglion cell layer and inner nuclear layers). The postmitotic neurons are closely apposed to the radial glia and have processes extending up to the vitreal surface (see illustration in figure 1.2). Expression was also seen in the developing RPE.

At CS16 *FRMD7* expression is seen within the inner neuroblastic layer. These are likely to represent the first group of post mitotic retinal neurons (ganglion cells) which have undergone radial migration to the future ganglion cell layer. By this stage melanogenesis has begun and melanin shows up as a false positive and hence staining of the RPE is also seen in the sense images. Differentiation of the retina begins centrally (at the optic disc) and then gradually extends peripherally towards the rim. Thus a different staining pattern is seen between the central and peripheral retina at stages CS16 and CS19. At CS23 a bi-laminar expression pattern begins to emerge which is clearly evident by 9 weeks post conception (wpc). We also see

expression in the optic stalk at stages CS15, CS16 and CS19, while at 9wpc the expression was confined to the optic nerve sheath.
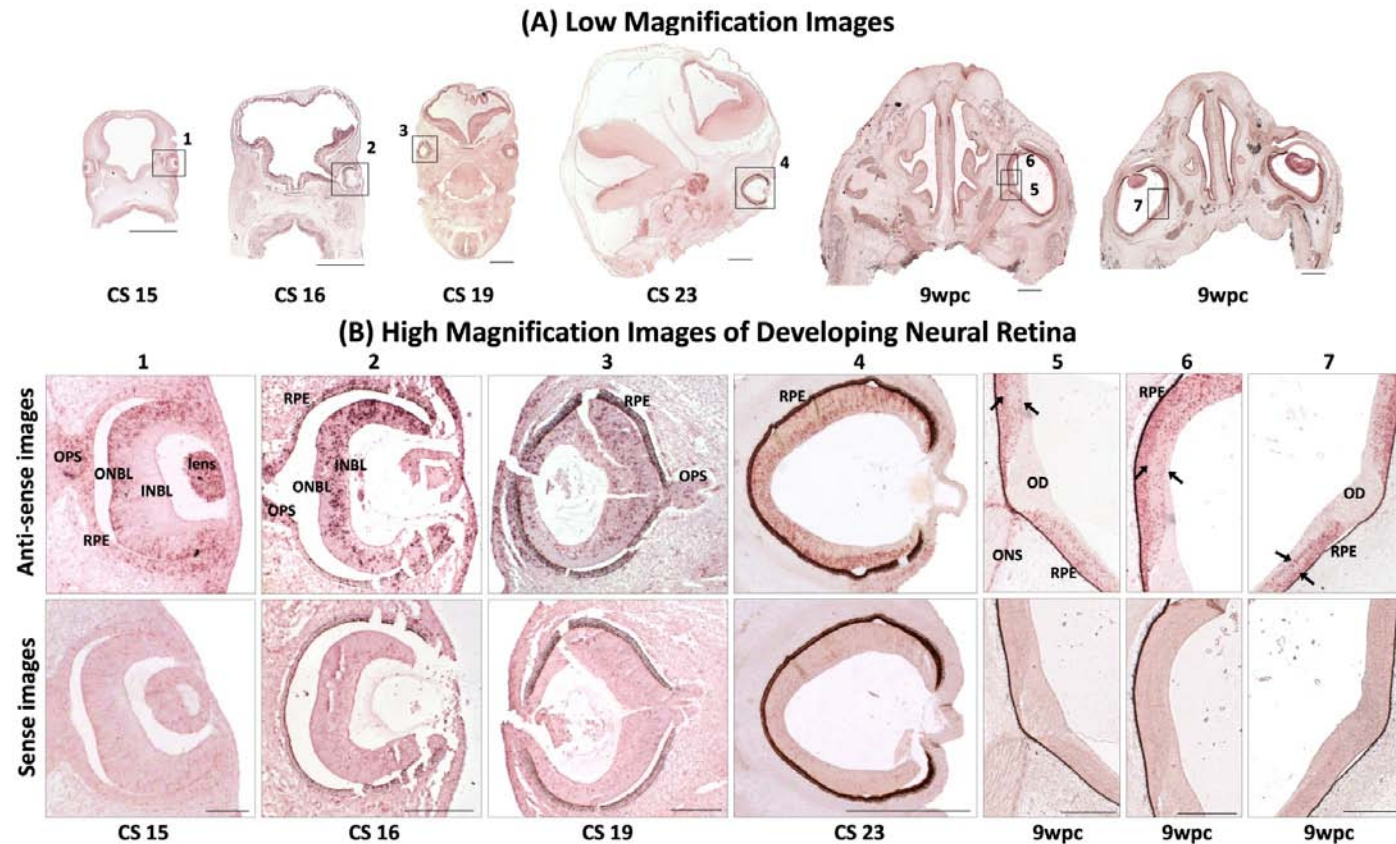
Figure 5.2: *Spatial and temporal FRMD7 mRNA expression profile in the developing human neural retina. (A) shows the low magnification image of the embryos from Carnegie Stages (CS) 15, 16, 19, 23 and 9 weeks post conception (wpc). (B) A migratory expression pattern was seen with initially expression confined to the outer neuroblastic layer (ONBL) at CS15, subsequently expression is seen within the inner neuroblastic layer (INBL). At 9 wpc a bilaminar expression pattern was seen (see arrows). In CS15, CS16 and CS19 expression was seen within the developing optic stalk (OPS). Expression was restricted to the optic nerve sheath (ONS) and was not seen in the developing optic disc (OD) at 9wpc. The peripheral neural retina is the last to differentiate and laminate hence a difference in the expression pattern between the central and peripheral neural retina is seen. This is most evident at stages CS16 and CS19. The sense images are shown below the antisense images and once pigmentation occurs the retinal pigment epithelium (RPE) shows up as a false positive for expression at stage CS16 onwards. The scales in the low magnification images represent 500μm while the scale bar in the high magnification images represents 200μm.*

151

5.3.2 EXPRESSION IN MOUSE AND RAT

In-situ hybridisation studies in mouse retina at embryonic day 10.5 (E10.5) show expression of *FRMD7* initially in the outer neurobalstic layer and the optic stalk (figure 5.3). However at E16.5 a different expression pattern develops and a distinction between central and peripheral retina expression is clearly visible. At E16.5 staining is predominantly observed within the inner retinal layers at the periphery, while in the central retina a bi-laminar expression profile is developing similar to what is observed in humans at 9wpc.
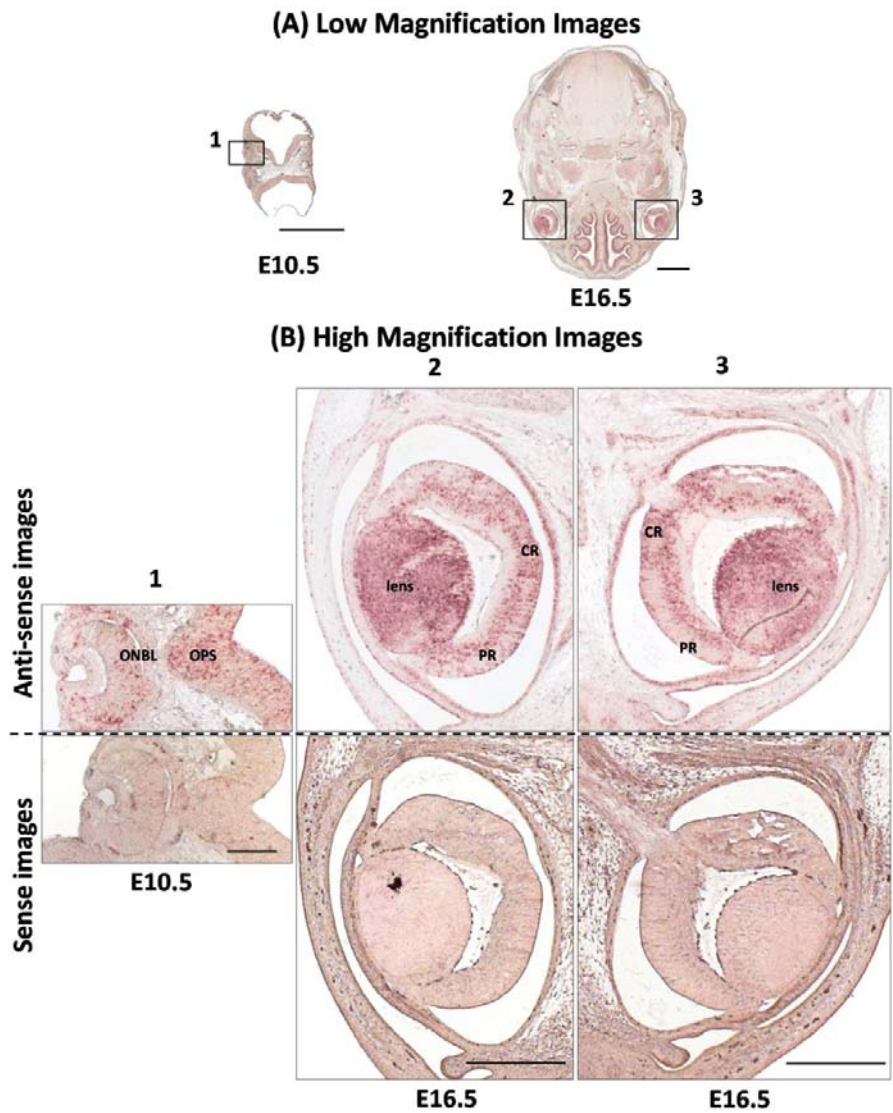
Figure 5.3: *FRMD7 mRNA expression in the developing murine retina. (A) shows the low magnification images of mouse embryo sections at embryonic day 10.5 (E10.5) and embryonic day 16.5 (E16.5). (B) shows the higher magnification images with expression in the optic stalk (OPS) and outer neuroblastic layer (ONBL) at E10.5, while at E16.5 there is a distinct difference between the central retinal (CR) and peripheral retina (PR) expression. Expression was also seen in the lens at E16.5. Scale bars in (A) and (B) represents 500µm and 200µm respectively.*

Immunohistochemistry studies show expression of FRMD7 protein within the VZ at E10.5. Subsequently at E16.5 protein expression is mainly seen within the developing nerve fibre layer and the ganglion cell layer. This same pattern persists even at post natal day 5 (P5) (figure 5.4). The inner

plexiform layer is formed by this stage and shows some protein expression too. However the ONBL shows no expression. The outer plexiform layer begins forming and we also see expression within this region at P16 and P18. The ONL however shows no expression of the FRMD7 protein although some expression is also seen in the developing inner and outer segments of the photoreceptors (figure 5.4).

Immunocytochemistry studies in primary culture of retinal and cerebellar neurons show expression of FRMD7 protein in the progenitor neuroblastic cells however no expression is seen in the surrounding glial cell as shown in figure 5.5. The glial cells can be morphologically identified due to the relatively larger nuclei compared to the neuroblasts. In the retinal culture protein expression is seen along the primary extensions of the axons which tend to be long. The progenitor neurons in the cerebellar culture tend to have shorter neurites and also show protein expression along the axonal processes.
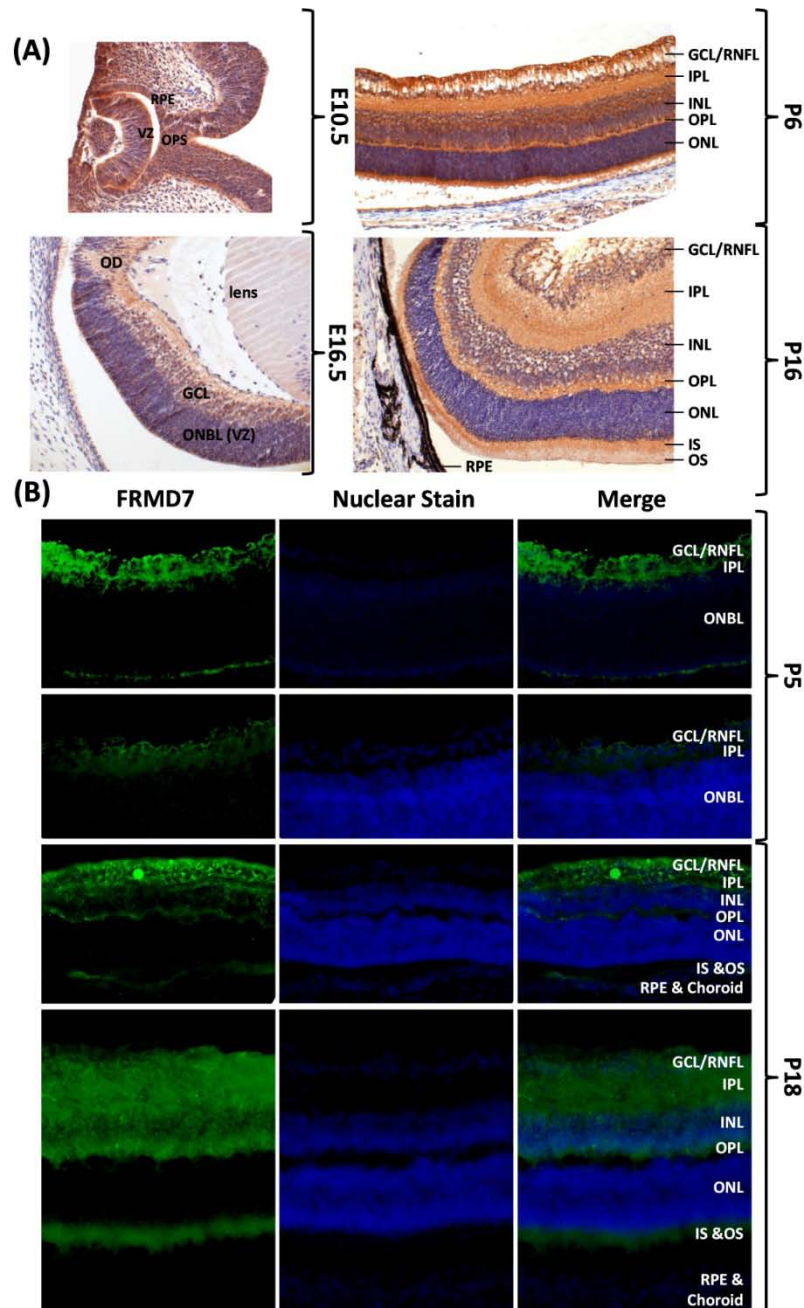
Figure 5.4: *FRMD7 protein expression in the developing mouse (A) and rat retina (B). At embryonic day (E) 10.5, staining was seen in the neural retina in the ventricular zone (VZ) as well as the optic stalk (OPS). At E16.5 staining was seen in the ganglion cell layer (GCL), retinal nerve fibre layer (RFNL) and optic disc (OD) region; however no staining was seen in the outer neuroblastic layer (ONBL). At day 5 and 6 post partum (P5 and P6) expression was seen in most retinal layers except the outer nuclear layer (ONL)/outer neuroblastic layer (ONBL). A similar pattern was seen at P16 and P18 as well. Expression within the inner and outer segment (IS & OS) of the developing photoreceptors was seen at P16 and P18. At stages P6, P16 and P18 the staining in the inner nuclear layer (INL) was relatively weak. IPL = Inner Plexiform Layer; OPL = Outer Plexiform Layer; OPS = Optic Stalk; RPE = Retinal Pigment Epithelium.*

FRMD7	Nuclear Stain	Merge	
(A)			Retinal
(B)			Cerebellar
(C)			
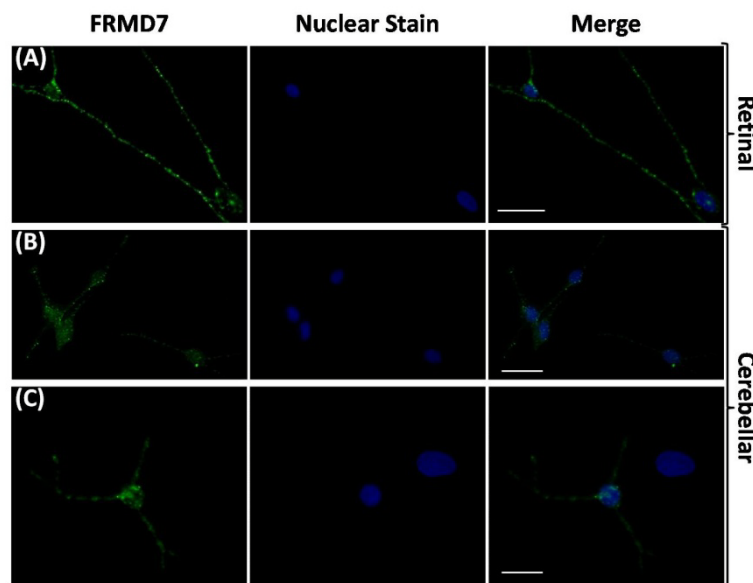
Figure 5.5: Subcellular localisation of FRMD7 protein detected on immunofluorescence. Primary culture of retinal (A) and cerebellar (B and C) progenitor cells shows FRMD7 protein expression within the primary extensions of neurites. No expression was seen in the glial cells which can be distinguished from neuroblasts based on the size of the nucleus (C). Scale bars = 10μm.

5.3.3 EXPRESSION IN ZEBRAFISH

Whole mount *in-situ* hybridisation studies in zebrafish larvae (3dpf and 5dpf) showed restricted expression of *FRMD7a* and *FRMD7b* within the optic tectum, cerebellum, inner ear and neural retina (figure 5. 6). We did not find any differences in the expression patterns between both *FRMD7* paralogs (*FRMD7a* and *FRMD7b*) in the two larval stages investigated.

High resolution images obtained from the retina showed that expression was restricted to the inner retinal layers and no expression was seen in the outer nuclear layer, a similar pattern to what was described in the other species. Interestingly, within the inner nuclear layer the expression was mainly confined to the inner part. Sections were also obtained from 5dpf larva after overstaining which showed higher resolution images of expression within the tectum and cerebellum (figure 5.6 D&E). The expression patterns were

interpreted using reference images from developmental atlases from the

Zebrafish Virtual Atlas (http://zfatlas.psu.edu/index.php) and The Zebrafish

Model Organism Database (http://zfin.org/zf_info/dbase/db.html)

(196,197).
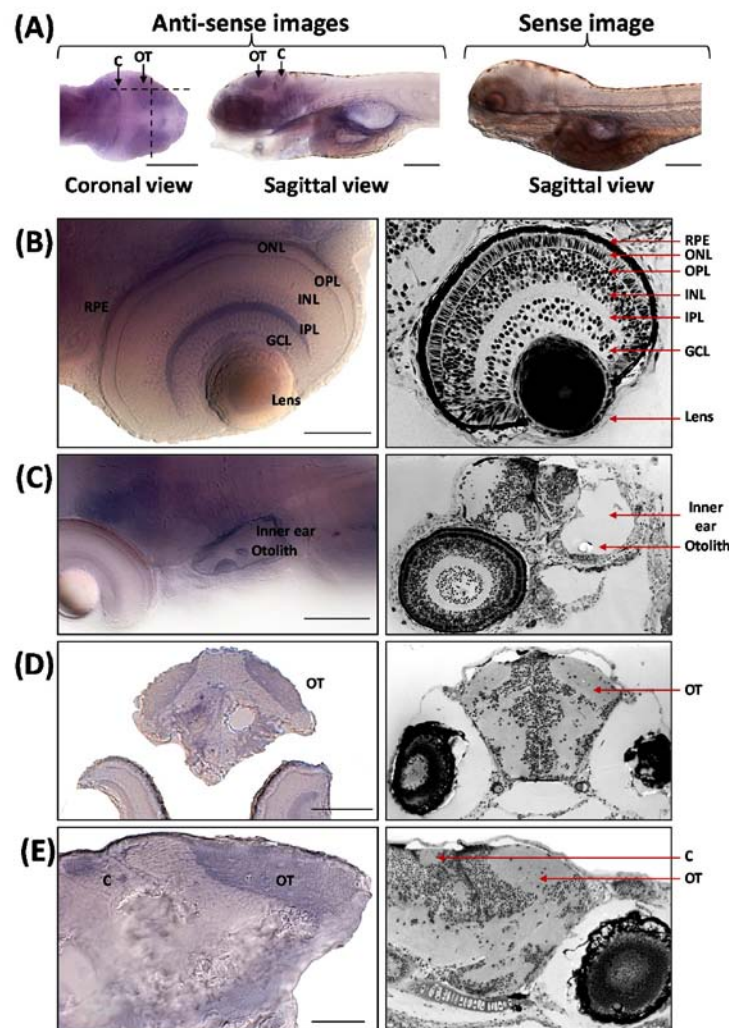
Figure 5.6: *Results from the in-situ hybridisation experiments in whole mount zebrafish. (A) shows an overview of the sense and anti-sense images showing expression in the optic tectum and cerebellum. The dashed lines show the approximate locations where sections were made for figure D and E. High magnification images show expression within the retina (B), inner ear (C) optic tectum (D and E) and cerebellum (E). Reference images are shown on the right of the antisense images in (B to E). Reference images were obtained to interpret anatomical locations. Scale bars represent: (A) 200μm, (B) 50μm, (C) 100μm, (D) 100μm and (E) 50μm. Abbreviations: optic tectum (OT), cerebellum (C), retinal pigment epithelium (RPE), outer nuclear layer (ONL), outer plexiform layer (OPL), inner nuclear layer (INL), inner plexiform layer (IPL), ganglion cell layer (GCL).*

5.4 DISCUSSION

In this chapter we report the detailed spatial and temporal retinal expression profile of *FRMD7*. Preliminary data from Tarpey et al. and from chapter 4 showed that there was *FRMD7* mRNA expression in the retina (47). Self et al. used qPCR to determine the relative temporal expression profiles within the developing murine brain (195). Based on the expression pattern described by Self et al. they suggested that *FRMD7* could have a role in: (1) carbohydrate, lipid and amino acid metabolism, (2) cell adhesion and recognition and (3) synapse formation and function (195). However the definitive role of FRMD7 in neurite outgrowth and branching comes from the study from Betts-Hendersen et al. (86).

The main disadvantage of using the qPCR approach is that the whole brain including the retina is homogenised, thus it would be difficult to determine which anatomical structures were contributing to the differential expression. Thus the spatial localisation of the *FRMD7* mRNA would remain unclear with such an approach. Although the *in-situ* hybridisation technique is more labour intensive in comparison to the qPCR approach, it is a more sensitive approach to determine the spatiotemporal expression profile. Therefore in this study we used an *in-situ* hybridisation technique as opposed to the qPCR approach. Identifying neural substrates involved in *FRMD7*-related infantile nystagmus provide the foundation to identify potential therapeutic targets which could be applicable to other infantile nystagmus forms as well. Similar approaches have been used to identify subtle phenotypic abnormalities in patients with *PAX6* mutations. For instance, the most obvious phenotype

associated with *PAX6* mutations is aniridia, this is because it is easily detected and the most obvious complaint a patient would present with (i.e. vision related problems) (140). However *PAX6* expression studies showed that it is not only restricted to the anterior segment but also the developing optic stalk and retina (139). This is consistent with retinal and optic nerve head abnormalities associated with *PAX6* mutations (198,199). Using the *in-situ* hybridisation technique in 1997 Mastick et al. identified that *PAX6* is also expressed within the developing murine forebrain (200). Therefore this raised an interesting question whether patients with *PAX6* mutations had subtle brain changes which were previously not described. In 2001, Sisodiya et al. addressed this question and performed an MRI study which revealed that *PAX6* haploinsufficiency leads to cerebral malformations. Thus this is an example of how expression studies were able to reveal cryptic phenotypes.

In both human and mouse retina we observe a migratory expression pattern which is initially confined to the outer neuroblastic layer and later expression is observed within the inner neuroblastic layer. Further evidence for this expression pattern is seen in the mouse retina which shows a difference between the central and peripheral retina (figure 5.3), since they differentiate at different rates (i.e. the peripheral retina differentiates at a slower rate in comparison to the central retina) (201). In early development the outer neuroblastic layer represents a proliferative zone which gives rise to the various retinal cell types. The first set of cells to become post mitotic is the retinal ganglion cells. In the mouse retina retinal ganglion cell birth begins at approximately E11 and by E16.5 there is a large population of

159

retinal ganglion cells (202). In the mouse retina there is a strong FRMD7 expression within the GCL just prior to birth (E16.5). We followed the expression within this layer and found that it continues to express FRMD7 in both post natal murine (P5 and P16) and rat retinal tissues (P5 and P18). Primary culture also shows that there is strong expression within the retinal progenitor cells along the primary extensions which are likely to represent the precursors to the retinal ganglion cells. Interestingly expression is also seen in the other developing retinal layers including the developing inner and outer segments.

Although there is widespread retinal expression in humans, mice and rat retina there are some notable differences between the different species. The main difference in the expression pattern between human and rat retina is that in human's expression is observed within the outer retinal layer at 9 wpc however at P5 and P18 we do not see any expression of FRMD7 within the outer retinal layer. This might be because the human retina contains both cones and rods while the rat retina is rod dominated. Therefore in the outer nuclear layer *FRMD7* expression could be restricted to cone photoreceptors and not rod photoreceptors.

In humans CS15, CS16 and CS19 *FRMD7* expression is seen within the developing optic stalk and by 9wpc the expression was confined to the optic nerve sheath. Murine samples also had a similar expression pattern (at stages E10.5 and E16.5), showing both FRMD7 mRNA and protein being expressed in the optic stalk and the optic disc. *PAX2* has been shown to be expressed within the developing optic stalk and has been implicated to be an essential

protein for optic stalk development. *PAX2* knockout mice are associated with a failure of optic fissure to close which results in a coloboma (203). Although it is unlikely *FRMD7* mutation is associated with a severe phenotype such as coloboma (since it would have been described on fundoscopic examination), it would be interesting to investigate whether there are any subtle optic nerve head abnormalities which have not been previously described.

Expression patterns observed in zebrafish larvae were consistent with findings described in humans, mouse and rat neural tissues. This provides additional evidence regarding the neural substrates implicated in *FRMD7*-related infantile nystagmus. Expression was seen in the developing inner ear, retina, optic tectum and cerebellum. This is similar to the global expression pattern (VOR, OKN arcs and cerebellum) described in the previous chapter. Within the retina we find strong hybridisation signals from the inner retinal layers. Primary culture of rat cerebellar neurons also shows expression within the primary extensions and *FRMD7* expression was confined to the cells with smaller nuclei which are presumably developing purkinje cells (rather the cells with the larger nuclei, i.e. the glial cells). However further studies with co-immunostaining for specific cell markers would be needed to confirm whether FRMD7 expression is confined to a particular cell lineage. fMRI studies in a family with IIN showed abnormal activation of the cerebellum (204). Similarly, recent tractography studies in the same family shows loss of fibres in the pons and cerebellum (205).

To date there have been no reports of retinal abnormalities in patients with *FRMD7* mutations. Moreover, the criteria to diagnose IIN (prior to

161

performing sequence analysis for *FRMD7* mutations) include a normal visual evoked potential and electroretinography, which suggests that both these investigative modalities were not able to detect any afferent abnormalities. However the expression studies presented in this chapter which are extensive and not only restricted to humans but also other species poses an interesting question; Could there be afferent defects associated with *FRMD7* mutations which have not been previously identified?

This question will be addressed by performing ultra high resolution optical coherence tomography studies in patients with *FRMD7* mutations.

In summary, this is the first study showing a migratory FRMD7 expression pattern in the developing retina. This suggests that FRMD7 could have an important role in retinal development.

6. CHAPTER SIX: REPRODUCIBILITY OF OPTICAL COHERENCE TOMOGRAPHY MEASUREMENTS IN INFANTILE NYSTAGMUS

This chapter addresses the aim:

- To investigate whether OCT measurements is a reliable method of

  phenotyping the retina in patients with infantile nystagmus

6.1 INTRODUCTION

The invention of Optical Coherence Tomography (OCT) has revolutionized

the field of Ophthalmology. Although it has wide range of applicability in the

fields of cardiology, dermatology, orthopaedics, gastroenterology and animal

research, it is most commonly used in phenotyping the retina. Over the last

20 years there has been a dramatic increase in the number of publications

arising from using this imaging modality (figure 6.1A). However the number

of publications related to phenotyping patients with nystagmus using OCT is

relatively limited (figure 6.1B). This is likely to change in the coming years

since OCT technology is a rapidly advancing with significant improvements in

scanning speeds, axial resolution and eye tracking. For instance the time

domain OCT's have a scanning speed of approximately 400 A-scans/second

with an axial resolution of 10μm . With the advent of fourier domain OCT the

scanning speeds and axial resolution have improved significantly. For

example, most commercially available FDA approved Spectral Domain OCTs

have an approximate scanning speed of 20,000 A-scans/second and an axial

resolution of 6μm (206). Only a handful of fourier domain instruments are

able to achieve the ultrahigh resolution (UHR) (3μm) and high-speeds

(>50,000 A-scans/second). Examples of retinal OCT scans obtained from different instruments are shown in figure 6.2. The pioneers in the field of OCT technology, such as Wolfgang Drexler and James Fujimoto have reported axial resolution of 1µm and scanning speeds over 100,000 A-scans/second in some of their prototype instruments. Thus they are able to resolve features of the outer retina such as the cone outer segment tips and subcomponents of the inner segments of the photoreceptors (207,208).
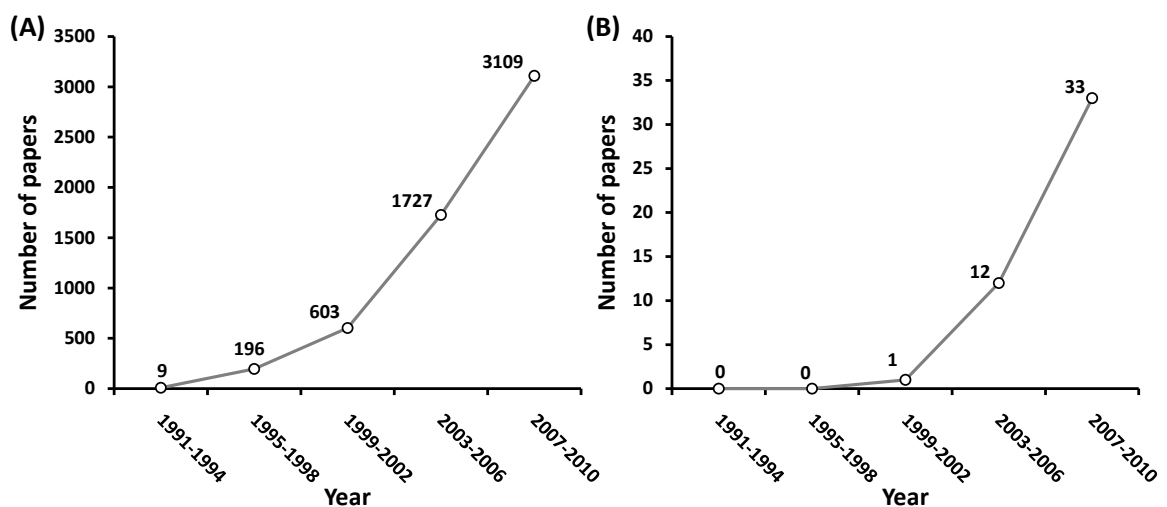
Figure 6.1: *Number of papers published from 1991-2010 based on optical coherence tomography and nystagmus. (A) shows the number of papers published on optical coherence tomography alone; (B) represents the number of papers published on optical coherence tomography and nystagmus. These results were obtained using the SCOPUS search engine (www.scopus.com).*

In routine ophthalmology clinics OCT is widely used for diagnosing and monitoring therapeutic improvements for retinal disorders such as age related macular degeneration. Using Bland-Altman tests it has been shown that OCT measurements (retinal thickness and retinal nerve fibre layer thickness) are reproducible in normal subjects and patients with glaucoma (209,210). Because of possible motion artefacts the reliability of OCT in nystagmus is unknown especially using older generation instruments with

slower scanning speeds. Hence capturing a scan of the fovea can be

challenging (113,211). For example recent gene therapy trials for LCA have

used OCT to identify gross morphological features such as complications of

intra-retinal injections (212). However because of associated nystagmus

longitudinal intra-retinal thickness measurements to chart therapeutic

improvements were not performed possibly due to slower scanning speeds.
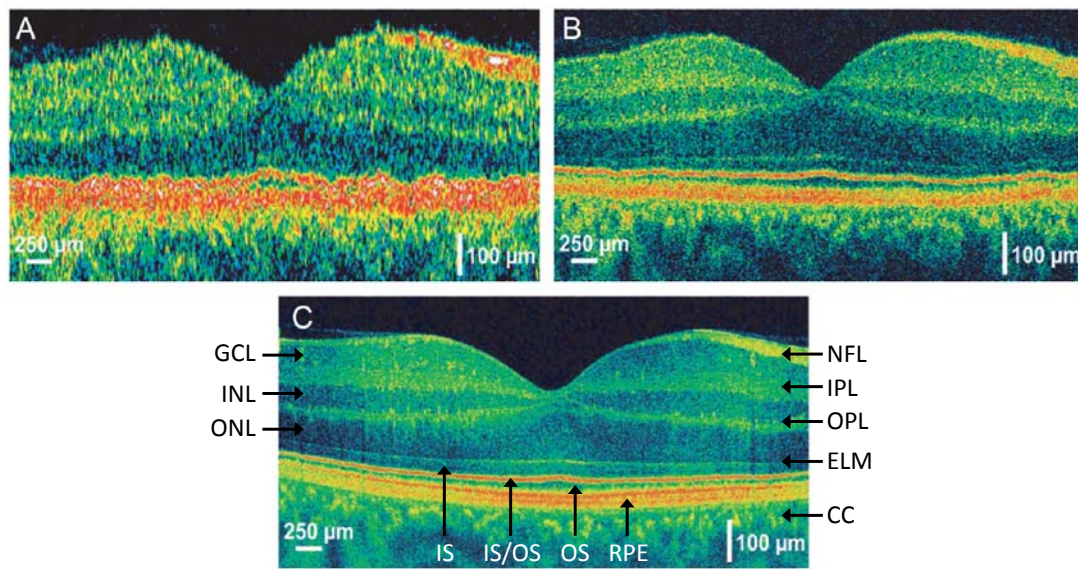
Figure 6.2: OCT images of a normal fovea obtained from a standard time domain (A), ultrahigh resolution time domain (B) and an ultrahigh resolution fourier domain (C) instruments. The axial resolution of images A, B and C are 10μm, 3μm and 3μm respectively. The scanning speeds were 400 A-scans/second (A), 150 A-scans/second (B) and 25,600 A-scans/second (C). Note the enhanced representation of the retinal laminar structure associated with the fourier domain instrument. NFL = Nerve Fibre Layer, GCL = ganglion cell layer, IPL = inner plexiform layer; INL = inner nuclear layer, OPL = outer plexiform layer, ONL = outer nuclear layer, ELM = external limiting membrane, IS = inner segment, OS = outer segment, IS/OS = inner-outer segment junction, RPE = retinal pigment epithelium and CC = choriocapillaries. (Reproduced with permission from: (207))

Since infantile nystagmus can be associated with retinal pathologies it has the

potential to become an excellent tool for diagnosis and monitoring

therapeutic changes in the form of morphological features and intra-retinal

thickness measurements. Most manufacturers of OCT machines also provide

software which performs automated segmentation; however this is limited to measurements such as retinal nerve fibre layer (RFNL) thickness and retinal thickness (RT) (206). Therefore segmentation of the other intra-retinal layers at the fovea and parafovea can be challenging. One simple yet robust method of segmentation is using reflectivity profiles (137,213,214). This method has previously been used for segmentation in patients with achromatopsia and it has been suggested that absolute reflectivity values can be used to differentiate between disorders such as blue cone monochromatism and achromatopsia (137). However, it is unclear to what extent these results can be used for diagnosis as it is not known whether the presence of nystagmus allows reproducible high-resolution OCT measurements of both thickness and reflectivity.

Using a high-speed and ultrahigh resolution OCT we aimed to determine whether: (1) there was a significant difference in the scan quality (determined by signal to noise ratio quality index (QI)) between the groups, (2) RT measurements were reproducible using two different segmentation methods (SOCT software vs ImageJ) and (3) the intra-retinal thickness measurements (FD, ONL, IS, OS, RPE and RT) and reflectivity measurements (ELM and IS/OS) were reproducible between separate examinations.

6.2 METHODS

6.2.1 PATIENTS AND CONTROLS

The study population consisted of nystagmus volunteers (n=23; IIN=13 and albinism=10) and control volunteers (n=20) without any ocular pathology. Control volunteers were only included if they had a normal examination and visual acuity better than or equal to 0.0 LogMAR. The mean ages in the nystagmus and control group were 27.3 years (range = 8-60 years; SD=14.2) and 33.4 years (range = 9-55 years; SD = 12.0), respectively. The intensity of nystagmus ranged between 8°/s and 60°/s with a median intensity of 12°/s.

6.2.2 OCT ACQUISITION AND ANALYSIS

The OCT specifications and scanning protocol has been described in section 2.6.6. The 3-D scan program (743x75) consisting of 75 B-scans and 743 A-scans per B-scan line was used to capture the foveal and parafoveal regions. The scanning widow covered a 7x7mm retinal area centred at the fovea. Using the above protocol maximises the number of B-scans within the slow phase and typically only 4 B-scans (for e.g. in a patient with intensity of 12°/s) coincide with the quick phase of the nystagmus (figure 6.3).

Range of movement within timeframe of one B-scan

Foveation period	Slow phase	Quick phase
• Min = 0.00°	• Min = 0.03°	• Min = 1.60°
• Max = 0.01°	• Max = 0.16°	• Max = 2.00°

0.5°
0.1s

B-scan frequency

26.4%   68.1%   5.5% → % of B-scans within each phase

Time for one cycle ≈ 360ms

Foveation period (~20/75 B-scans)
Slow phase (~51/75 B-scans)
Quick phase (~4/75 B-scans)
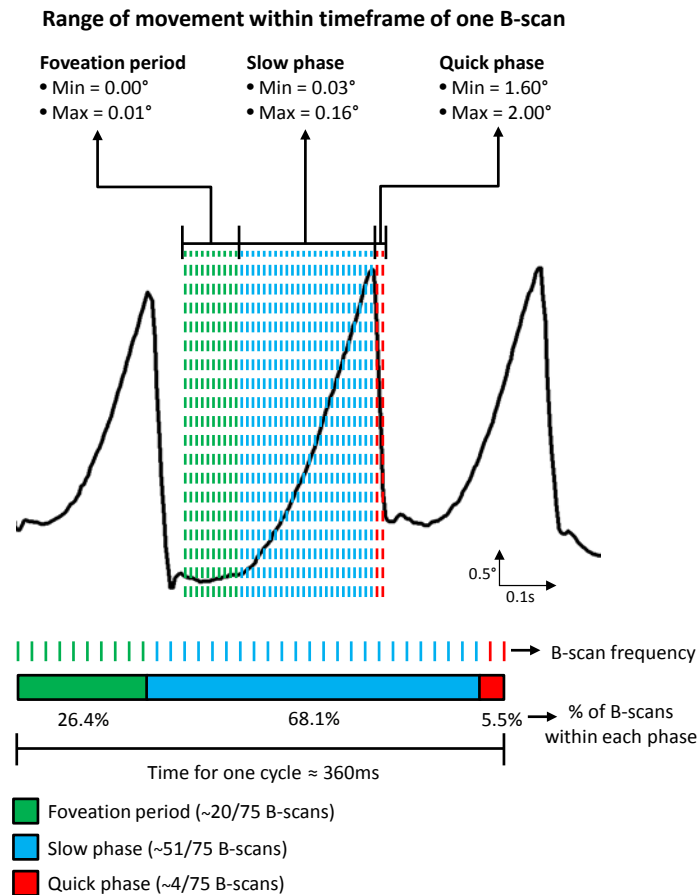
Figure 6.3: Example of nystagmus waveform illustrating the degree of horizontal rotation within the timeframe of one B-scan. The degree of rotation is variable and dependent on the phase of the nystagmus cycle. Degree of rotation is minimal during foveation period and maximum rotation occurs during the quick phase. The overall majority of the nystagmus cycle, in terms of time, is made of the slow phase and the foveation period. This also means that most of the B-scans would occur during the foveation period and slow phase. The scale for the nystagmus waveform is shown with upward deflection representing eye rotation to the right. The visual angle subtended by a 7 mm B-scan is approximately 31°.

Scanning was performed at least three times for each eye in each subject. All scans were performed on the same day. The eye with the highest quality index (QI) was subsequently chosen for further analysis. In the set of examinations for the chosen eye the two foveal scans with the highest QI were selected. The QI was also documented. The QI is based on a signal to noise ratio which takes into account the distance of the image from the zero delay line. The foveal scan was identified based on the following unique

morphological features: (1) deepest foveal pit, (2) widening of the outer nuclear layer and (3) lengthening of the cone outer segment (215,216). If a mirror artefact was present scans were excluded and examinations repeated. Similarly if the image was wrongly segmented this was noted and manually corrected.

6.2.3 EXPERIMENT 1

The OCT images were segmented using the software provided by the manufacturer (SOCT software version 4.1) (figure 6.4); this creates a retinal thickness (RT) map. The RT map is divided into 9 quadrants, the fovea is located within quadrant A1. The software allows the user to calculate the A1 minimum which corresponds to the central macular thickness (CMT).
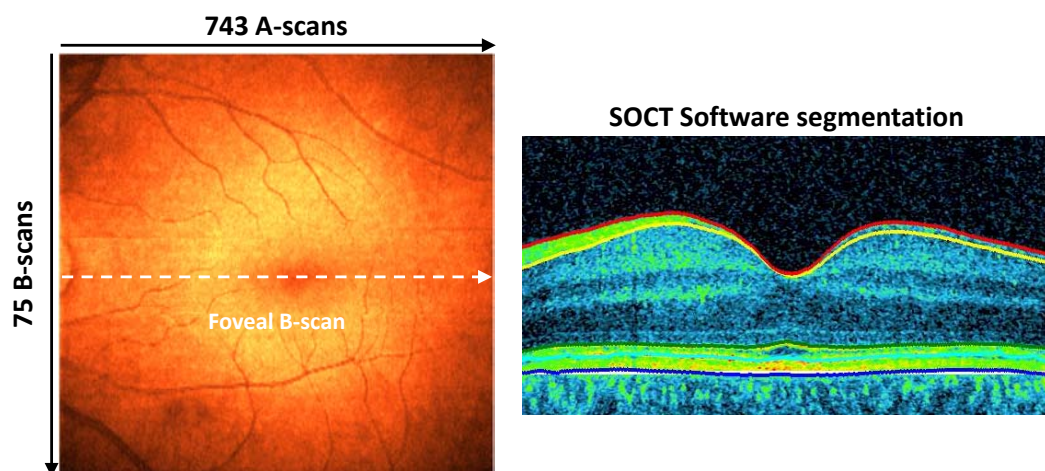
Figure 6.4: *Fundus image representing the scan dimensions in a 7x7 mm window centred at the fovea and segmentation of the foveal B-scan using the SOCT software.*

The same foveal scan was also analysed using ImageJ which is an image analysis software developed at the National Institute of Health (available at: http://rsbweb.nih.gov/ij/). In ImageJ we used a sampling window with a width of 10 pixels (this corresponds to 100μm in the transverse direction),

169

which was centred at the foveola to obtain a longitudinal reflectance profile (figure 6.5). Spike2 (v.6.12, Cambridge Electronic Design Ltd, Cambridge) was used to analyse the reflectivity profiles. The reflectivity profile not only allows the user to calculate the CMT but it also segments the other intra retinal layers and provides reflectance values for each region.

In this experiment CMT measurements at the fovea from images segmented using the SOCT and ImageJ software were compared. Segmentation using both methods was also performed on the second scan from each patient to compare the degree of variability between separate examinations for both methods.
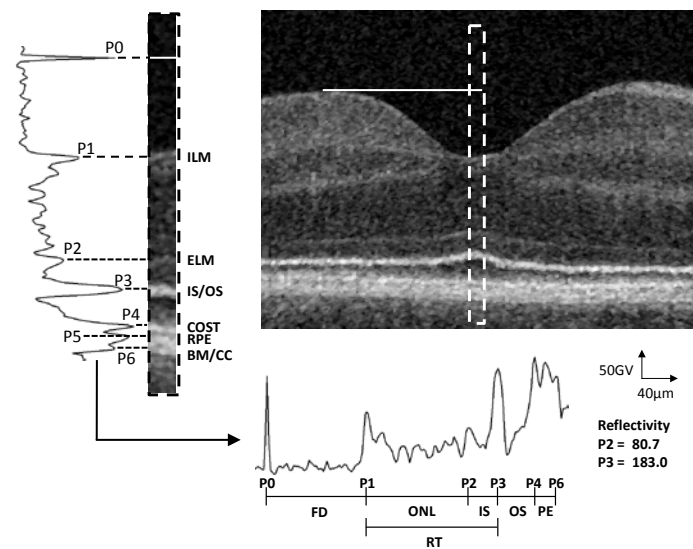
Figure 6.5: Optical coherence tomogram of a control subject at the fovea. The white dashed rectangle represents the sampling window and its enlarged image is shown in the left. The reflectivity profile shows six peaks: P1, internal limiting membrane (ILM); P2, external limiting membrane (ELM); P3, inner-outer segment junction (IS/OS); P4, cone outer segment tip (COST); P5, retinal pigment epithelium (RPE) and P6, Bruch's membrane and choriocapillary complex (BM/CC). An additional peak P0 was used to annotate the outer limit of the parafovea. Using the reflectance profile and the distance between the peaks the following measurements were derived: foveal depth (FD) (P0-P1), outer nuclear layer (ONL) thickness (P1-P2), inner segment (IS) thickness (P2-P3), outer segment (OS) thickness (P3-P4), pigment epithelial (PE) thickness (P4-P6) and retinal thickness (RT) (P1-P3). The reflectivity, in terms of pixel gray value (GV), was determined for peaks P2 and P3.

6.2.4 EXPERIMENT 2

Assessment of reproducibility of OCT measurements for all other intra-retinal layers was done by comparing thicknesses derived between two separate examinations. Each foveal scan was segmented using reflectivity profiles. In the control subjects, at the foveola, the reflectance profile generated 6 peaks (figure 6.5). P1 corresponds to the internal limiting membrane (ILM), P2 is the external limiting membrane (ELM), P3 is the IS/OS junction, P4 represents the cone outer segment tips (COST), P5 is the retinal pigment epithelium (RPE), and P6 is the Bruch's membrane/choriocapillary complex. An additional peak (P0) was used to annotate the outer limit of parafovea thus enabling to derive the foveal depth (FD).

The intra retinal thickness measurements derived were: FD (P0 – P1), outer nuclear layer (ONL) (P1 – P2), inner segment of the photoreceptor (IS) (P2 – P3), outer segment of the photoreceptors (OS) (P3 – P4) and RPE thickness (P4 – P6). The absolute reflectivity values for peaks representing ELM (P2) and IS/OS junction (P3) were also calculated. A summary of the scan acquisition and analysis is shown in figure 6.6.
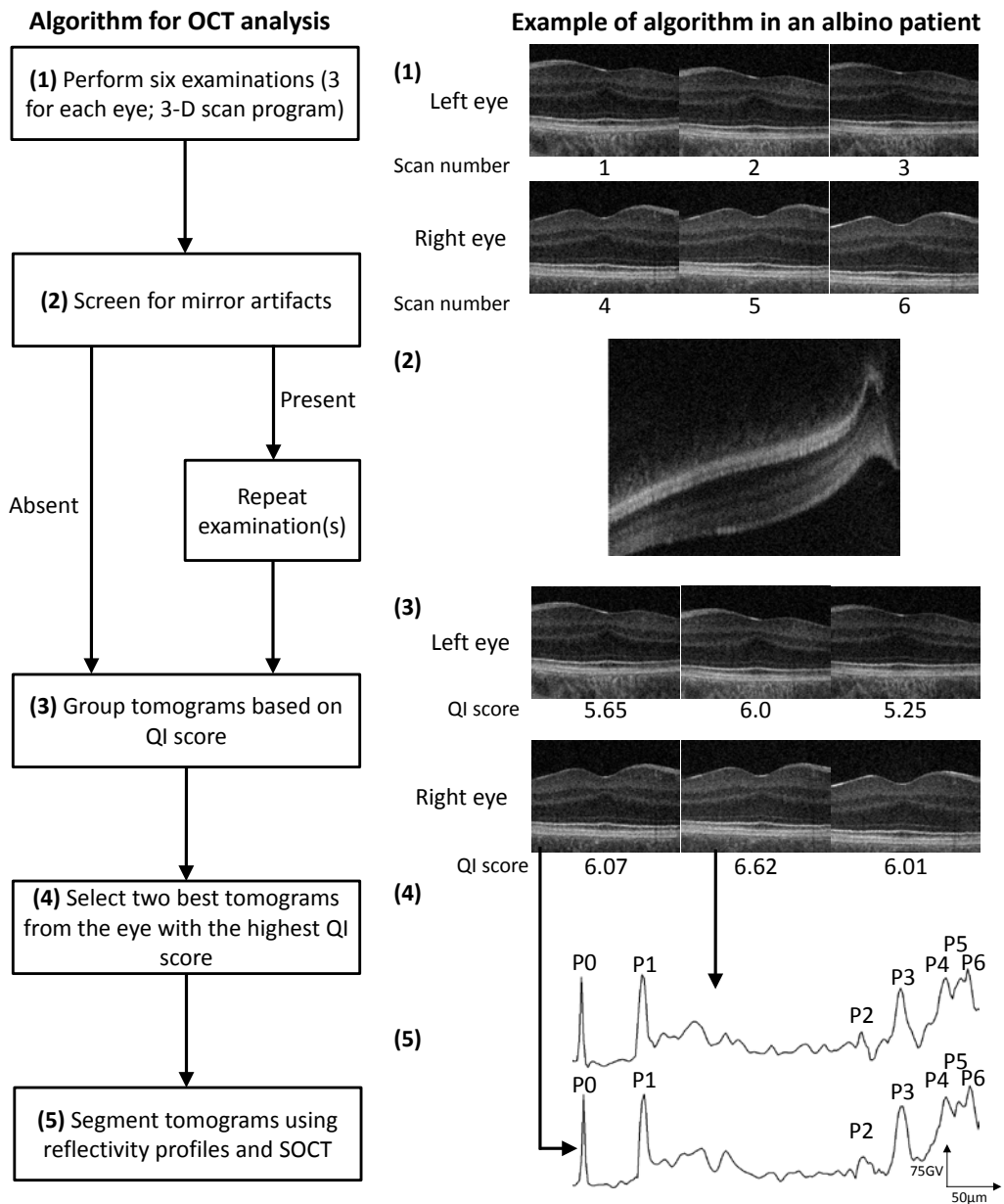
Figure 6.6: *Algorithm used for optical coherence tomography image acquisition and analysis used in experiment 2. An example from an albino subject is shown alongside the flow chart. If mirror artefacts were detected, as shown in 2, the examination was repeated to obtain a scan where the quality index (QI) was higher and the image in the right orientation. The two best scans were chosen from the eye with the highest QI for subsequent segmentation and reflectivity and thickness measurements.*

6.2.5 STATISTICAL METHODS

One-way ANOVA was used to compare the difference in quality index between the three groups (controls, IIN and albinism). In experiment 1, the Bland-Altman test was used to determine agreement between the measurements from the SOCT and ImageJ software. The intraclass correlation coefficient (ICC) was used to compare the degree of variability for each method between two separate examinations. This approach has been previously reported in a study by Ho et al. (217).

In experiment 2, the Bland-Altman test was used to determine agreement for the thickness and reflectivity measurements between the two examinations for which two groups of tomograms were defined either using QI's or order of acquisition (218). For thickness measurements, the groups were defined based on the QI, with the higher quality tomograms assigned to group 1 and the other tomograms to group 2. Since absolute reflectivity measurements are dependent on the QI (i.e. the higher the QI the higher the reflectivity measurements), for the absolute reflectivity measurements, the groups were defined based on order of tomogram acquisition, with the tomograms acquired first assigned to group 1 and the other tomograms to group 2. The bias (average difference between the measurements) and 95% limits of agreement were calculated for experiment 1 and 2. The null hypothesis was that the bias is equal to zero and the significance level was set at $p<0.05$.

173

6.3 RESULTS

6.3.1 EXAMPLES OF ORIGINAL DATA

Examples of an OCT from an albino and IIN subject along with the respective

reflectivity profiles are shown in figure 6.7. In all OCTs of patients with

albinism there was foveal hypoplasia which is indicated by the continuation

of the inner (IPL) and outer plexiform layers (OPL) at the foveola. Therefore,

in patients with albinism the width of the ONL was determined by the

distance between trough representing the end of OPL (T1a) and the peak

representing the ELM (P2) was used (figure 6.7). An example of the

reproducibility of the OCT tomograms and the reflectivity profiles are shown

in figure 6.6.

Diagnosis	OCT Tomogram	Reflectivity Profile	Nystagmus Waveform	Nystagmus Characteristics
IIN				Amplitude = 6.2° Frequency = 2.4 Hz Intensity = 14.9°/s
Albinism				Amplitude = 4.0° Frequency = 3.2 Hz Intensity = 12.8°/s
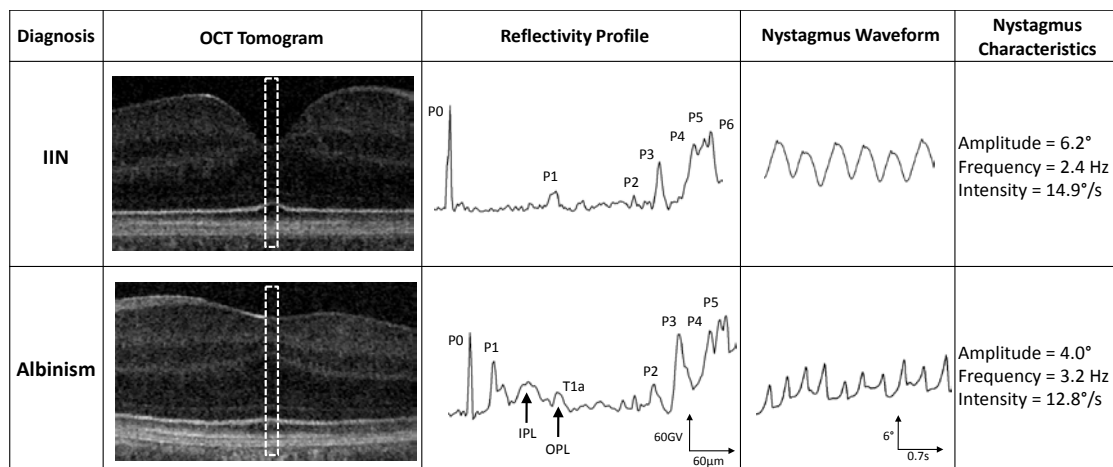
Figure 6.7: An example of an OCT from patient with idiopathic infantile nystagmus (IIN) and patient with albinism. The reflectance profile from each sampling windows are depicted on the right. In the albino OCT there is continuation of the inner and outer plexiform layers (IPL and OPL), this is a sign of foveal hypoplasia. In order to determine outer nuclear layer thickness in these patients, measurements were made from the trough representing the end of the OPL (T1a) to P2. The nystagmus waveforms from both the IIN and albino patient are shown with a mean intensity at primary position of 14.9 and 12.8°/s, respectively. The scale bars shown are for the reflectance profiles with pixel gray values (GV) on the y-axis and depth on the x-axis. Similarly scale bars for the nystagmus waveform show degree of rotation on the y-axis and time on the x-axis. An upward deflection of the nystagmus waveform represents rotation to the right.

174

6.3.2 COMPARISON OF QUALITY INDEX

Although the nystagmus groups had a lower mean QI (mean QI for: IIN=5.4, SD=1.4; albino=5.6, SD=1.0; and control=6.2, SD=1.1) compared to the controls, there was no significant difference in the quality index for the tomograms between the IIN, albinos and controls (p=0.13). A common segmentation error associated with SOCT software was that ELM was annotated instead of the IS/OS. This occured only in the nystagmus group where 7/92 (7.6%) foveal scans were wrongly segmented which typically occured if the quick phase of nystagmus coincided with the occurence of the foveal B-scan (figure 6.8). This would result in an underestimation of the central macular thickness however manual correction of the segmentation boundary rectifies this problem.
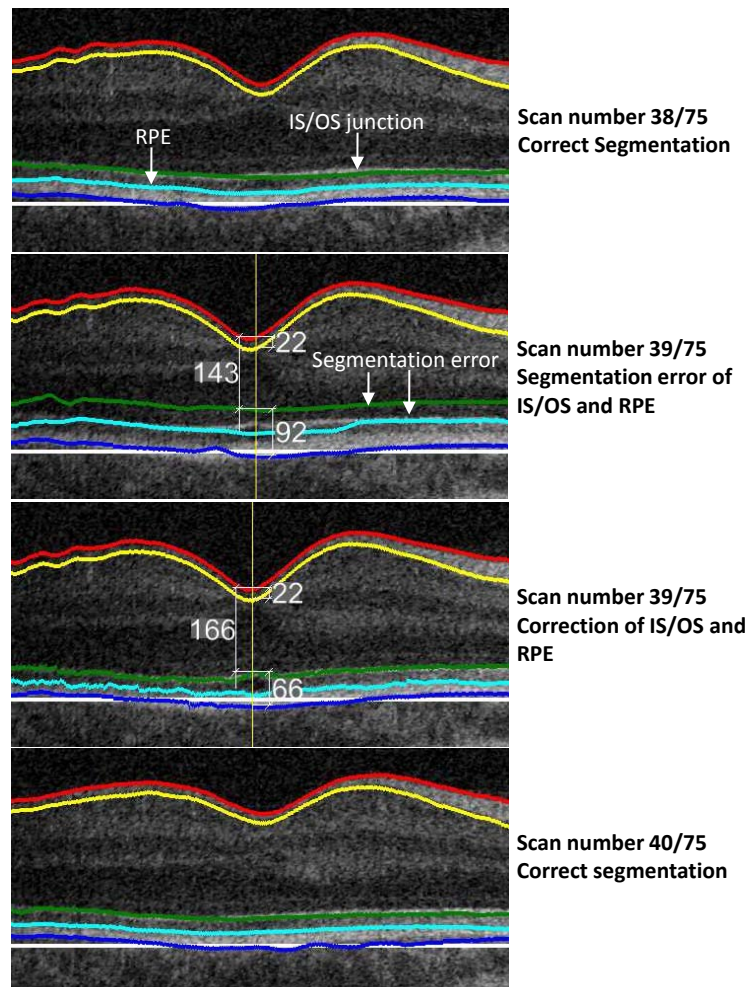
Figure 6.8: *Scan 39 in this example coincided with the quick phase of the nystagmus and was associated with segmentation error of the inner segment-outer segment junction (IS/OS) and retinal pigment epithelium (RPE). This is also associated with an underestimation of the central macular thickness (see image of before and after segmentation correction). The adjacent (scan 38 and 40) scans show correct segmentation.*

6.3.3 REPRODUCIBILITY BETWEEN DIFFERENT SEGMENTATION METHODS

The Bland-Altman plots showed good agreement in all three groups for central macular thickness measurements derived from the SOCT software and ImageJ. The agreement plots with the 95% agreement limits are summarised in figure 6.8 and table 6.1.
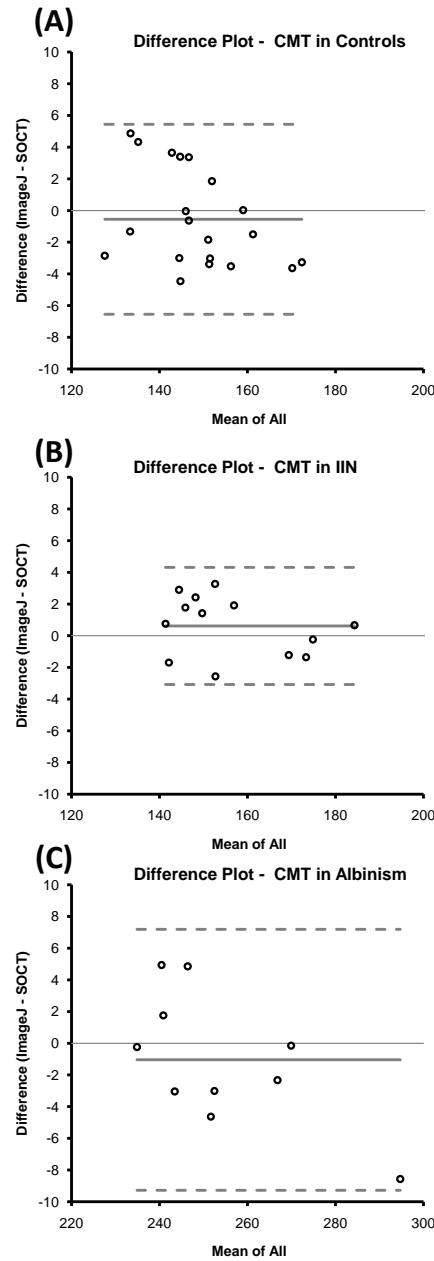
Figure 6.9: *Bland-Altman plots showing agreement between the two different methods of segmentation. The bias (solid grey line) and the 95% limits of agreement (dashed grey line) are also shown in the figure.*

The bias is not significantly different from zero in all three groups.

Furthermore the 95% limits of agreement include zero in all three groups.

The albino group had larger 95% limits of agreement compared to the IIN

and control groups. Both methodologies showed good degree of

177

reproducibility between two examinations with ICC greater than 0.95 and the

lower limits of the 95% confidence interval greater than 0.90 (table 6.2).

Table 6.1: Bland-Altman plot summary for retinal thickness derived
from different segmentation methods

Diagnosis	Mean ImageJ CMT (µm)	Mean SOCT CMT (µm)	Bias	*p*-value	95% Limits of agreement
Control	148.25	148.80	-0.55	0.43	-6.5 - +5.4
IIN	156.92	156.31	0.62	0.26	-0.5 - +1.8
Albinism	253.66	254.70	-1.04	0.45	-9.3 - +7.2

Comparison of central macular thickness (CMT, in micrometers) in SOCT
software vs reflectivity based segmentation within each group.

Table 6.2: Reproducibility of First- to Second-Scan Central Macular
Thickness Measurements using SOCT software and ImageJ

Diagnosis	Intraclass Correlation Coefficient		95% Confidence Interval	
	SOCT	ImageJ	SOCT	ImageJ
Control	0.98	0.97	0.96-0.99	0.93-0.99
IIN	0.97	0.97	0.92-0.99	0.91-0.99
Albinism	0.98	0.98	0.94-0.99	0.93-0.99

6.3.4 REPRODUCIBILITY OF INTRARETINAL THICKNESS AND REFLECTIVITY
MEASUREMENTS

Table 6.3 summarises the bias, *p*-values and the 95% limits of agreement for

the thickness measurements: FD, ONL, IS, OS and RPE. An example of the

Bland-Altman plot for ONL thickness and reflectivity of IS/OS junction is

shown in figure 6.9. The bias was not significantly different from zero in all

three groups for all intra-retinal thickness measurements as well as

reflectivity measurements. Similarly the 95% limits of agreement cross zero

in all three groups for all measurements. The thickness measurements were associated with smaller 95% limits of agreements however the reflectivity measurements had comparatively larger 95% limits of agreement.
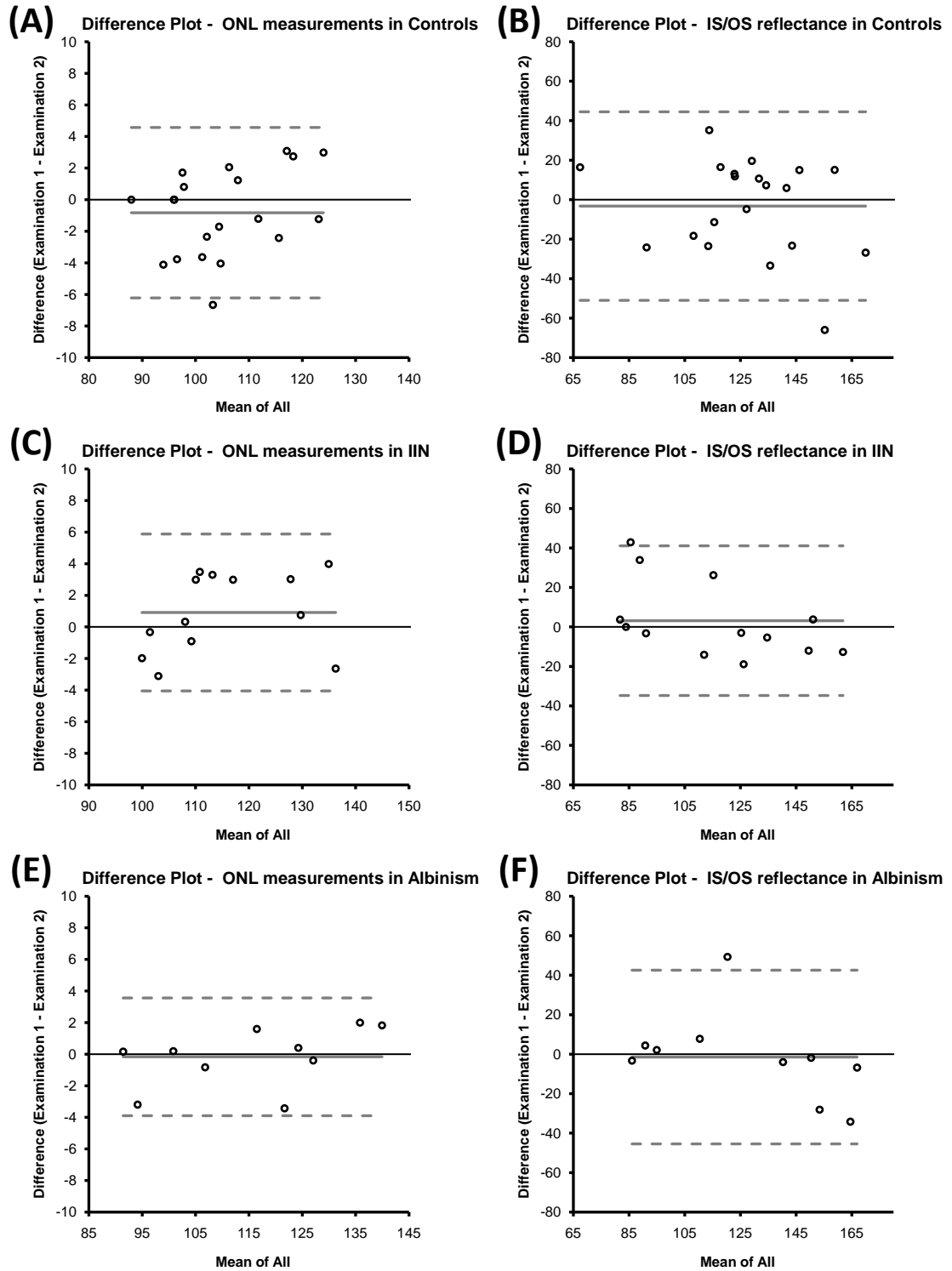
Figure 6.10: *Examples of Bland-Altman plots showing reproducibility for outer nuclear layer (ONL) thickness measurements (A, C, E) and reflectance measurements for inner segment –outer segment junction (IS/OS) (B, D, F). The solid grey line represents the bias and the dashed grey lines represent the upper and lower 95% limits of agreement and the solid black line represents identity.*

180

Table 6.3: Bland-Altman plot summary for intra-retinal thickness measurements

Thickness measurement	Control			IIN			Albinism		
	Mean (SD)	Bias (*p*-value)	95% Limits of agreement	Mean (SD)	Bias (*p*-value)	95% Limits of agreement	Mean (SD)	Bias (*p*-value)	95% Limits of agreement
Foveal Depth	132.4 (20.3)	0.47 (0.39)	-4.2 - +5.2	116.3 (29.2)	0.75 (0.41)	-5.5 - +7.0	22.4 (21.9)	-0.63 (0.43)	-5.4 - +4.1
Outer Nuclear Layer	105.9 (9.9)	-0.82 (0.20)	-6.2 - +4.6	113.6 (12.3)	0.91 (0.21)	-4.1 - +5.9	118.9 (16.1)	-0.17 (0.79)	-3.9 - +3.6
Inner Segment	33.2 (2.2)	0.60 (0.18)	-3.2 - +4.4	33.0 (1.9)	0.31 (0.43)	-2.4 - +3.0	33.3 (1.9)	-0.49 (0.49)	-4.7 - +3.7
Outer Segment	45.8 (2.4)	0.36 (0.48)	-4.0 - +4.7	42.7 (2.4)	0.71 (0.34)	-4.3 - +5.8	36.6 (5.1)	0.55 (0.42)	-3.5 - +4.6
Retinal Pigment Epithelium	20.8 (3.6)	-0.23 (0.77)	-7.0 - +6.6	23.2 (2.8)	-0.47 (0.48)	-5.0 - +4.1	21.6 (2.3)	0.27 (0.73)	-4.5 - +5.0

Table 6.4: Bland-Altman plot summary for absolute reflectivity measurements

Reflectivity measurement	Control			IIN			Albinism		
	Mean (SD)	Bias (*p*-value)	95% Limits of agreement	Mean (SD)	Bias (*p*-value)	95% Limits of agreement	Mean (SD)	Bias (*p*-value)	95% Limits of agreement
External Limiting Membrane	68.9 (19.0)	0.44 (0.87)	-23.2 - +24.0	48.2 (25.4)	1.18 (0.75)	-24.2 - +26.5	53.9 (26.7)	-1.74 (0.76)	-36.7 - +33.2
Inner-Outer Segment Junction	129.0 (29.0)	-3.26 (0.56)	-51.0 - +44.5	114.3 (34.2)	3.2 (0.57)	-34.7 - +41.1	128.5 (37.7)	-1.46 (0.84)	-45.4 - +42.5

6.4 DISCUSSION

This is the first study to systematically investigate the reproducibility of retinal thickness and reflectivity measurements using UHR-OCT in patients with nystagmus. In this study we found that there was good agreement between both methods of segmentation for CMT measurements. Furthermore we show that using ImageJ we can derive consistently reproducbile thickness measurements for separate examinations in all three cohorts for FD, ONL, IS, OS and RPE.

We used high speed (52,000 A-scans/second) spectral domain OCT to acquire images in patients with nystagmus; the fast scan acquisition time ensures that the overall examination time is short and each B-scan is acquired sufficiently quickly to minimize an associated motion artifact. Based on our proposed scan acquisition algorithm each B-scan takes approximately 14 ms. Majority of the B-scans acquired fall during the foveation period and the phase which are associated with minimal motion during the time frame of a B-scan (maximum rotation is approximately 0.16°) (figure 6.3), which is almost comparable to the degree of fixational eye movements in control subjects (3). Motion during the quick phase is considerably more, but represents only a small proportion of the 3-D scans (in a patient with a nystagmus intensity of 12°/s, approximately 4/75 B-scans occur during quick phase). The probability of this distorting the foveal image is small, however repeating the scan decreases the likelihood that the quick phase will coincide with the foveal B-scan.

Using a reflectivity based segmentation algorithm we were able to measure thickness of the different retinal layers at the fovea. This method has been

previously used for segmentation and to describe the layers at the macula (214,219). Barthelmes *et al.* showed that reflectivity of the IS/OS junction in patients with blue cone monochromatism was significantly less compared to controls (137), though reproducibility of these findings were not investigated. Here we show that the reflectivity of peaks representing ELM (P2) and IS/OS junction (P3) are reproducible (table 6.4). However this must be interpreted with caution since the 95% limits of agreement are quite large. The reason for the larger variability in the reflectivity measurements is unlikely to be due to the nystagmus since the control cohort also had large 95% limits of agreement. This variability could be due to the inherent problem associated with spectral domain OCT, which is associated with depth dependent sensitivity (207) (see examples in figure 6.11). The sensitivity roll off, i.e. the decrease in reflectivity values as the image moves away from the zero delay line, seen with spectral domain OCT (217) could explain why there is increased variability in the absolute reflectivity values. Occasionally this can also lead to mirror artefacts, since spectral domain instruments cannot distinguish between postive and negative echo delays (figure 6.6). However we excluded all scans with a mirror artifact and we used the QI's provided by the software to closely match the scans. Using these quality control step we were able to closely match the scans based on the distance from the zero delay line, which could explain the reproducible results for reflectivity.
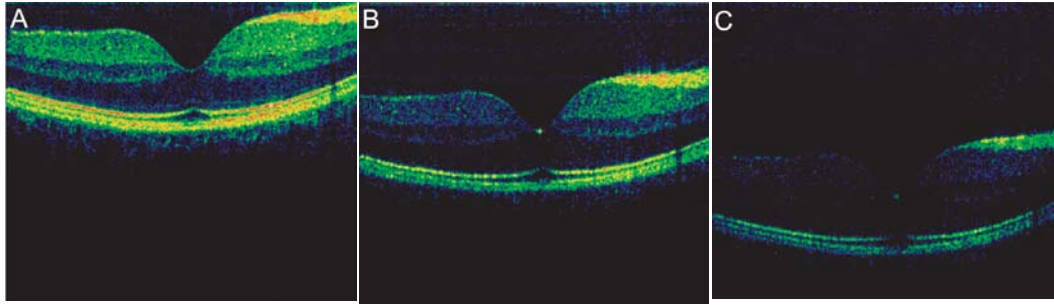
Figure 6.11: *One of the fundamental limitations of the fourier domain detection system is depth dependent sensitivity which is demonstrated in images (A-C). Image A shows stronger signals including the external limiting membrane (ELM) and inner-outer segment junction. While the ELM signal is not discernable in image C. (Reproduced with permission from:* (207)*).*

The ability to use OCT reliably is likely to have an important role in diagnosing and predicting visual prognosis in not only afferent retinal disorders associated with nystagmus such as albinism or achromatopsia (215,216,220) but also acquired forms of nystagmus such as mutliple sclerosis. Gene therapy has been successfully implemented in mouse models (221) for example in achromatopsia hence it is imminent in humans. Establishing longitudinal OCT measurements to chart structural improvements would provide an improtant objective measure of therapeutic response in future gene therapy trials in patients with nystagmus.

In summary, we show that quantitative OCT measurements can be reliably derived from patients with nystagmus.

7. CHAPTER SEVEN: OCULAR PHENOTYPES IN INFANTILE NYSTAGMUS

This chapter addresses the aims:

- To identify whether there are retinal changes in patients with *FRMD7* mutations using OCT.

- To characterize and compare the retinal and optic nerve phenotype of patients with *PAX6* mutations, albinism and achromatopsia using OCT. To investigate in achromatopsia whether retinal changes are progressive.

7.1 INTRODUCTION

To date there have been no OCT studies in patients with *FRMD7* mutations, however there have been a number of OCT studies investigating the foveal morphology in patients with albinism (113,211,216,222-227). Two interesting studies in albinism have shown that the outer segment at the fovea is significantly decreased in length in patients with albinism when compared to controls (216,224). Surprisingly there have been limited numbers of OCT studies in patients with *PAX6* mutations (146,228). Bredrup et al. reported absence of a foveal pit in patients (n=5) with c.383G>C mutation of *PAX6* (228). Holmstrom et al. reported foveal hypoplasia in patients with aniridia (n=3) but genetic analysis was not performed (226).

There have been no studies investigating the intra-retinal thickness within the parafoveal regions for patients with *PAX6* mutations. However there is some evidence suggesting that there are parafoveal abnormalities in patients with albinism. A recent study in albino children (n=13) showed some evidence that the

parafoveal retinal thickness is decreased in comparison to controls, although the reason for this is unclear (226). An interesting findings described within the parafovea of patients with albinism is the decreased retinal nerve fibre layer thickness and ganglion cell layer thickness (229). Thus the decrease in parafoveal retinal thickness described could be due to decrease in the inner retinal layers.

There have been no OCT studies investigating the optic disc morphology in patients with *PAX6* mutations. Interestingly Chong et al. reported an incidental finding related to optic nerve head morphology. Although the study was designed to determine foveal morphology, they noted an elevated optic disc in six patients with albinism. The reason for this remains unclear (113). Mohammad et al. identified that the optic cup was shallower in patients with albinism; however the disc diameter was not significantly different when compared to controls (229). There have been no studies to date looking at the peripapillary nerve fibre layer thickness in patients with *PAX6* mutations or albinism.

OCT has been previously used in two studies to characterise macular changes in patients with achromatopsia (137,230). In both studies a time domain OCT (10µm, axial resolution) was used to acquire macular images. The main findings from these studies showed structural changes at the foveola, which included the absence of the inner segment/outer segment (IS/OS) boundary and lack of widening of the photoreceptor outer segment (137,230). Varsanyi et al. showed that the retina was significantly thinner in achromats compared to controls (230). However Barthelmes et al. did not find any significant differences in retinal thickness (137). Therefore it still remains unclear whether there are significant detectable retinal changes in patients with achromatopsia on OCT.

There is some evidence that suggests that achromatopsia could represent a progressive disorder (133). However to date there have been no longitudinal OCT studies documenting whether there are retinal changes which get worse with time. Hence we first performed a cross sectional study to document the retinal changes associated with achromatopsia and subsequently we used a longitudinal study in a subset of patients to identify whether there were any progressive retinal changes. There is no evidence to suggest that there are progressive retinal changes in patients with *FRMD7* mutations, *PAX6* mutations and albinism hence a cross sectional study design was used.

In chapter 5 we observed extensive expression of *FRMD7* within the developing neural retina. This suggests that *FRMD7* could have a role in development and formation of neural retinal circuitry. Therefore in this chapter ultra high resolution optical coherence tomography (UHR-OCT) has been used to characterise and compare the ocular phenotypes (fovea, parafovea and optic disc) in four groups of patients. These include patients with: (1) *FRMD7* mutations, (2) *PAX6* mutations, (3) albinism and (4) achromatopsia.

7.2 METHODS

7.2.1 PATIENTS

OCT was obtained from patients with *FRMD7* mutations (n=45; mean age = 34.7 years, SD = 17.4, range = 7-79 years), *PAX6* mutations (n=15; mean age = 32.3 years, SD = 19.6, range = 7-72 years), albinism (n=34; mean age = 27.6 years, SD = 13.8, range = 7-60 years) and achromatopsia (n=14; mean age = 25.0 years, SD = 21.7, range 4-64 years). OCTs were also obtained from controls (n=80; mean age = 35.0 years, SD = 13.8, range = 5-62 years) of similar ages. The sample size was determined based on a pilot study. The main outcome measure for the pilot study was the average retinal nerve fibre layer thickness (SD = 2.75μm; significance level, p = 0.01; power = 90%; effect size = 2.4μm).

The sample size calculations, pilot study details and power curves are presented in detail in the electronic appendix. The scanning and foveal analysis protocols were described in chapter 6.

In order to investigate whether there were progressive retinal changes in achromatopsia patients OCT scans were performed in a subset of 8 patients during a follow up visit. The mean follow up time was 16 months (range: 11-25 months).

7.2.2 PARAFOVEAL ANALYSIS

To enable performing parafoveal segmentation and analysis, the OCT tomograms were smoothed, compounded and median filtered as described elsewhere (231). Prior to carrying out intra-retinal thickness measurements the OCT images (B-scans) were flattened by adjusting the A-scans in the z-direction.

Image smoothing was performed using the manufacturer's software SOCT (version 4.1). For image compounding the images were registered in Matlab (R2010a, The MathWorks, Natick, MA, USA) based on point mapping, and if necessary manual correction was also applied. The process of image compounding and median filtering ensures there is a decrease in the speckle noise (figure 7.1) and also improves the signal to noise ratio for subsequent parafoveal segmentation which was carried out using custom scripts written in ImageJ and Matlab. After image segmentation was performed all intra-retinal thickness measurements were derived (figure 7.2). The average parafoveal thickness was calculated as the overall average thickness across the retina excluding the central macular 2mm region. Similarly the nasal and temporal parafoveal thickness measurements represent the average measurements between 1mm to 3mm on either side of the fovea. In order to assess the asymmetry between the nasal and temporal retinal thicknesses a naso-temporal ratio (NT ratio) was used. The GCL-IPL boundary was not always clearly demarcated due to the speckle noise hence we used a measurement of GCL+IPL complex which would provide a more robust measurement due to the clear boundary between the IPL-INL interfaces. All thickness measurements presented in this chapter are in the horizontal direction.
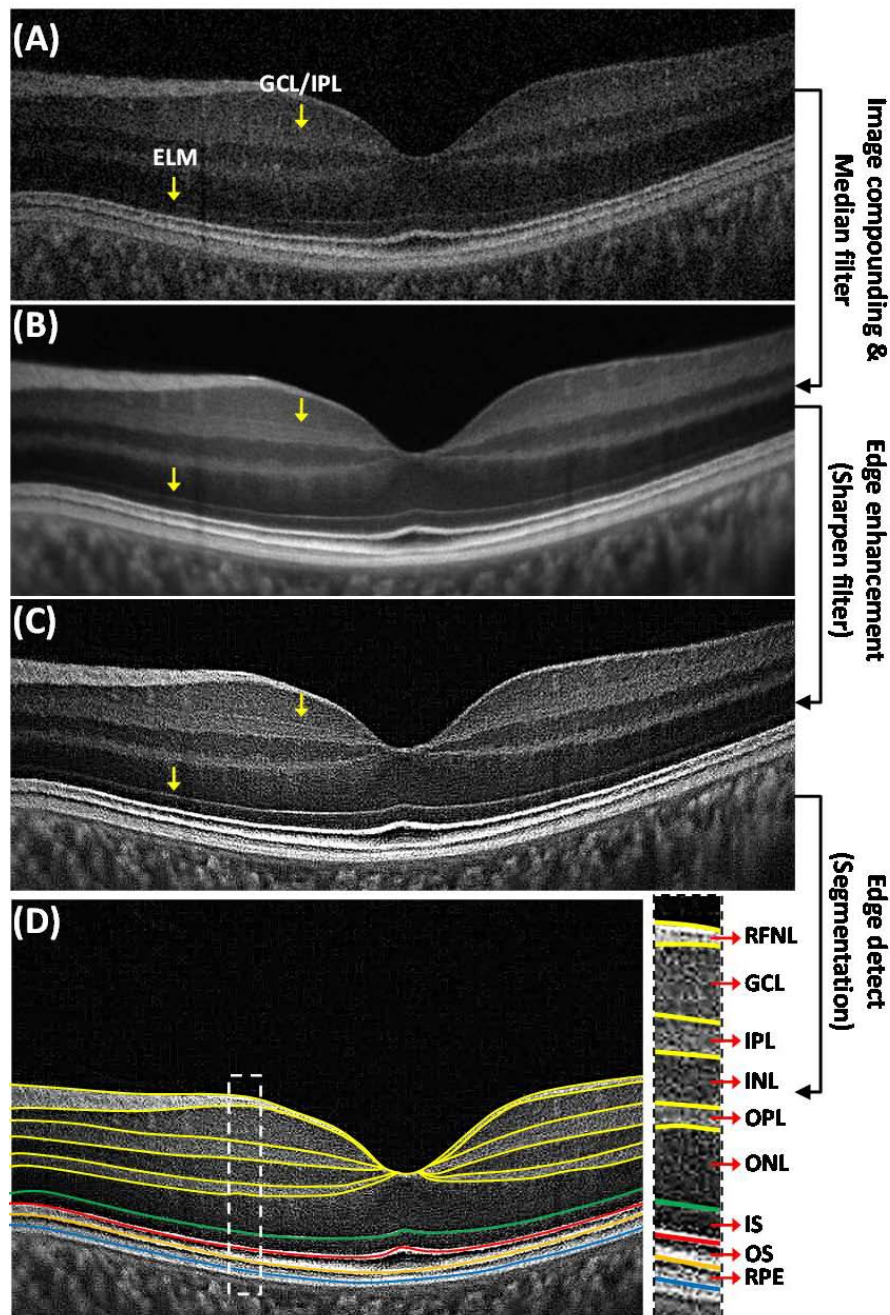
Figure 7.1: *OCT compounding and segmentation. (A) The original OCT image has significant noise resulting in loss of parafoveal ELM and GCL/IPL interface signals (yellow arrows). Image compounding and median filtering results in reduction of the speckle noise and improves parafoveal signals (yellow arrows) (B). Edge enhancement algorithm provides better definition of the boundaries between hyporeflective nuclear layers and hyper-reflective plexiform layers (C). Edge detection and fitting a non-uniform B-spline to the interfaces creates a segmented image (D). The intra-retinal layer thickness (high magnification panel in D) can be derived from the segmented image. Abbreviations: ELM = external limiting membrane; GCL/IPL = ganglion cell layer/inner plexiform layer interface; RFNL = retinal nerve fibre layer; INL = inner nuclear layer; OPL = outer plexiform layer; ONL = outer nuclear layer; IS = inner segment; OS = outer segment; RPE = retinal pigment epithelium.*
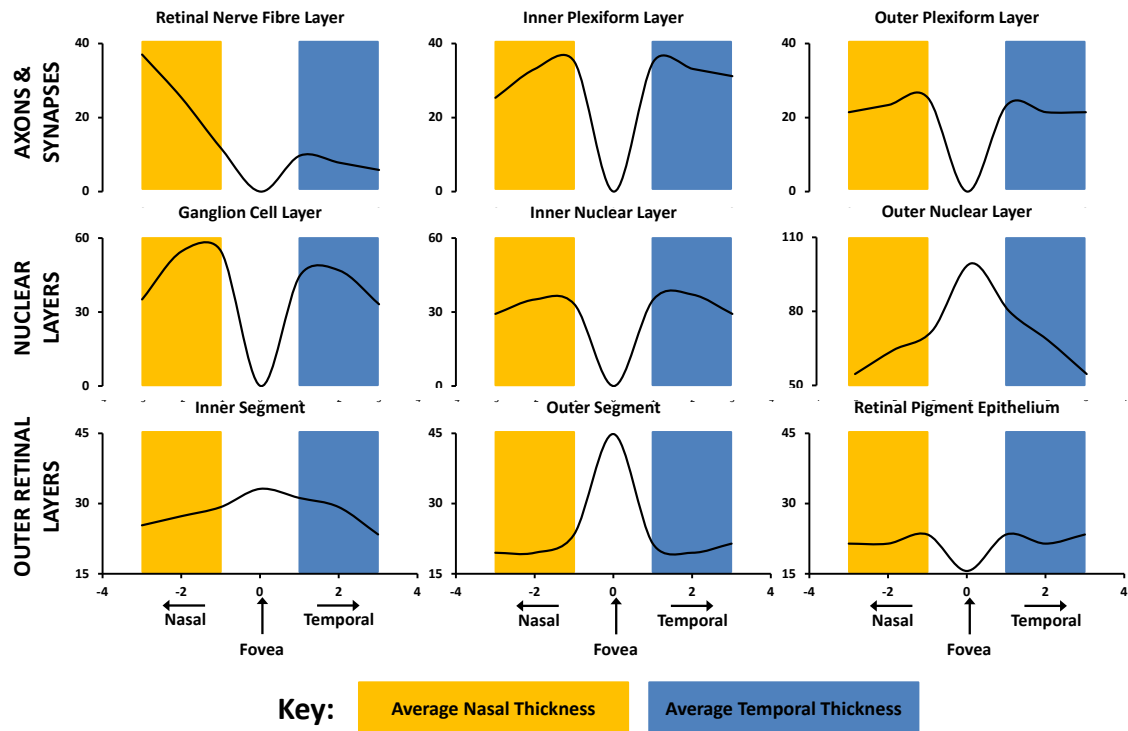
Figure 7.2: *An example of the intra-retinal retinal layer thicknesses derived from the segmented OCT image from a normal subject. The X-axis represents the distance from the fovea in the nasal and temporal directions (in mm). The Y-axis represents the layer thickness in microns.*

7.2.3 OPTIC NERVE HEAD ANALYSIS

The peripapillary nerve fibre layer was segmented in a similar manner as described in the previous section. The disc and cup diameter were calculated from B-scans as shown in figure 7.3. The terminations of the RPE were used to indicate the boundaries of the optic disc, the cup diameter was calculated using an anterior offset of 150 microns as previously described (232,233). The average retinal nerve fibre layer thickness around the optic disc was also calculated for a 2mm region around the optic disc (figure 7.3). The average cup depth was also calculated by averaging the nasal and temporal cup depth (figure 7.3). This was only calculated for the horizontal B-scan. Therefore the results presented in this chapter represent the horizontal thickness measurements.

191

In order to achieve the above image processing and analysis tasks (parafoveal and optic nerve head) a dedicated computer workstation was utilised (8 Core, Intel® Core i7® processor 2.9GHz, 8GB RAM, 512 MB nVidia graphics card). In addition a dual monitor was utilised for multi-tasking and to achieve high throughput.
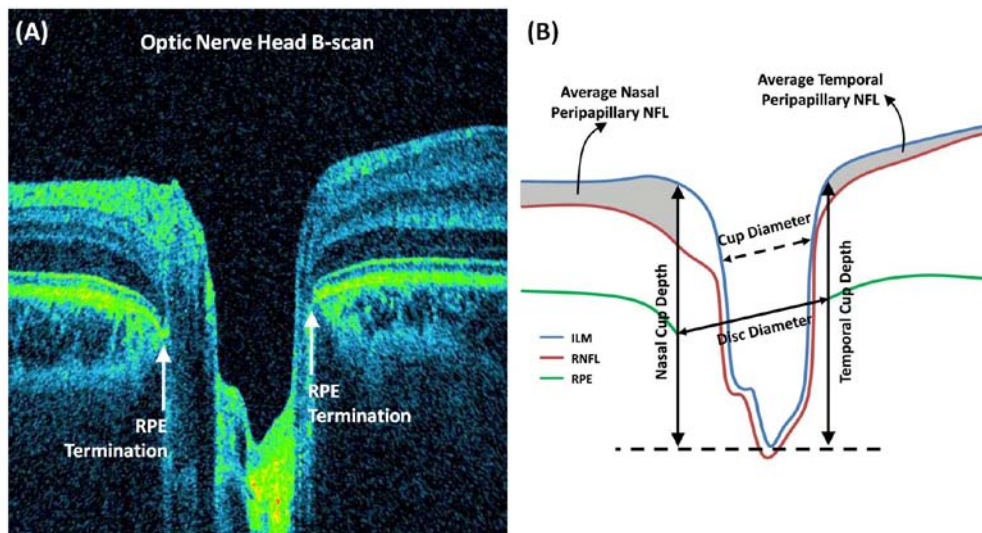
Figure 7.3: *Examples of OCT B-scans showing the optic nerve head (A). The segmented optic disc image allowed calculating disc diameter (from the terminations of the retinal pigment epithelium (RPE)). Similarly the average retinal nerve fibre layer (RNFL) nasal and temporal to the optic disc was calculated. The cup diameter was determined by an offset from the terminations of the RPE. The cup depth was calculated from the inflexion of the inner limiting membrane (ILM) to the deepest part of the cup (B).*

7.2.4 STATISTICAL METHODS

Each set of thickness measurement was assessed for normality and homogeneity of variances. Parametric tests (t-test/1-way ANOVA) were chosen based on the normal distribution and equal variance of the data. If the data was not normally distributed, the data was Log transformed to achieve normality (see section 7.3.6).

7.3 RESULTS

7.3.1 *FRMD7* MUTATIONS

7.3.2.1 OVERVIEW OF FAMILIES AND SINGLETONS WITH *FRMD7* MUTATIONS RECRUITED FOR THE OCT STUDY

We recruited families and singletons with *FRMD7* mutations identified in chapter 3 and the Tarpey et al. study. A total of 23 families and 3 singletons with *FRMD7* mutations were recruited for the OCT study. This consisted of a total of 11 families and 1 singleton with truncating mutations and 12 families and 2 singletons with non-truncating mutations. The detailed effects of the mutations have been discussed in chapter 3.

The details of the mutations, amino acid variation, structural effects and domains affected are shown in table 7.1. The pedigree ID shown in table 7.1 refers to the family/singleton ID from chapter 3 or from the Tarpey et al. study. The pedigrees with the prefix N refer to families that linkage analysis was performed as part of the Tarpey et al. study (47).

Table 7.1: The families and singletons with *FRMD7* mutations recruited for the OCT study. The pedigree ID refers to ID's designated in chapter 3 and Tarpey et al. study.

OCT ID	Mutation	Amino acid variation	Mutation Type	Structural Effect	Domain Affected	Pedigree ID
1	c.205+2 T>G		Splice	Truncating	FERM-N	N4
2	c.252G>A	p.V84V	Nonsense	Truncating	FERM-M	N5
3	c.796G>C	p.A266P	Missense	Non-truncating	FERM-C	N6
4	c.162+5 G>A		Splice	Truncating	FERM-N	N7
5	c.1003C>T	p.R335X	Nonsense	Truncating	FA	N10
6	c.812G>A	p.C271Y	Missense	Non-truncating	FERM-C	N11
7	c.661A>G	p.N221D	Missense	Non-truncating	FERM-C	F15
8	c.1019C>T	p.S340L	Missense	Non-truncating	C-terminal	F20
9	c.71G>A	p.G24E	Missense	Non-truncating	FERM-N	F21
10	c.1003C>T	p.R335X	Nonsense	Truncating	FA	F24
11	c.796G>C	p.A266P	Missense	Non-truncating	FERM-C	SF21
12	c.58-1G>A		Splice	Truncating	FERM-N	F102
13	c.983A>G	p.Y328C	Missense	Non-truncating	FA	F106
14	c.47T>C	p.F16S	Missense	Non-truncating	FERM-N	F109
15	c.660delC	p.I220IfsX12	Nonsense	Truncating	FERM-C	F111
16	c.910C>T	p.R304RX	Nonsense	Truncating	FA	F114
17	c.796G>C	p.A266P	Missense	Non-truncating	FERM-C	F112
18	c.796G>C	p.A266P	Missense	Non-truncating	FERM-C	F115
19	c.673T>C	p.W225R	Missense	Non-truncating	FERM-C	F116
20	c.206-5T>A		Splice	Truncating	FERM-N	F118
21	c.285-118C>T		Intronic	Truncating	FERM-M	S151
22	c.285-118C>T		Intronic	Truncating	FERM-M	F137
23	c.782G>A	p.R261Q	Missense	Non-truncating	FERM-C	F119
24	c.824A>G	p.H275R	Missense	Non-truncating	FERM-C	F125
25	c.154G>T	p.G52X	Nonsense	Truncating	FERM-N	F134
26	c.811T>A	p.C271S	Missense	Non-truncating	FERM-C	SM101

7.3.1.1 FOVEAL ABNORMALITIES ASSOCIATED WITH *FRMD7* MUTATIONS

Foveal hypoplasia (defined as the continuation of the inner retinal layers posterior to the foveola) was identified in 12/45 patients (26.7%) with *FRMD7* mutations. The *FRMD7* mutations associated with foveal hypoplasia were: c.205+2T>G (n=1), c.206-5T>A (n=2), c.285-118C>T (n=2), c.796G>C (n=2), c.812G>A (n=3), c.1003C>T (n=2). All the patients with foveal hypoplasia had a rudimentary foveal pit and there were no cases of fovea plana. Examples of OCTs from patients with foveal hypoplasia are shown in figure 7.4. Patients with *FRMD7* mutations had significantly: (1) shallower foveal pit, (2) thinner IS and OS, (3) thicker ONL, (4) thicker RPE and (5) increased CMT in comparison to controls. These results are summarised in table 7.2 and figure 7.5. The diamond plots are shown in section 7.3.5.

Figure 7.4: The morphological abnormalities associated with foveal hypoplasia and FRMD7 mutations are shown in (A). All patients had a rudimentary pit, continuation of the inner retinal layer posterior to the foveola and shorter outer segments (A & B). Examples of foveal hypoplasia associated with each mutation are shown in (B). The mutations are shown above the tomograms. The amino acid changes and the locations in relation to the FRMD7 protein are also shown (C). The number of patients with each mutation and foveal hypoplasia are shown in parenthesis. The missense mutations are shown in blue while the nonsense mutation in red and splice mutations in orange (C).

196

Table 7.2: Summary of foveal measurements in patients with *FRMD7* mutations in comparison to controls

Thickness measurement (μm)	Control group mean (μm)	*FRMD7* group mean (μm)	Difference (μm)	*P*-value
Foveal Depth	133.8	108.6	25.2	<0.0001
Outer Nuclear Layer	102.9	113.4	-10.5	0.0006
Inner Segment	33.5	32.1	1.4	0.0056
Outer Segment	50.2	41.9	8.3	<0.0001
Retinal Pigment Epithelium	18.2	20.1	-1.9	0.0013
Central Macular Thickness	190.8	202.9	-12.1	0.0014

7.3.1.2 PARAFOVEAL ABNORMALITIES ASSOCIATED WITH *FRMD7* MUTATIONS

The average parafoveal NFL, OPL and RPE thicknesses were significantly decreased in *FRMD7* patients compared to controls. The parafoveal GCL+IPL complex and INL were significantly thicker within the *FRMD7* group in comparison to controls. These findings have been summarised in table 7.3 and figure 7.5. The average parafoveal ONL, OS and RT were not significantly different ($p > 0.05$) between the *FRMD7* group and controls. The diamond plots are shown in section 7.3.5.

Figure 7.5: *Intra-retinal thickness measurements in patients with FRMD7 mutations in comparison to controls. The mean layer thickness for the fovea and parafovea and the 95% confidence intervals (CI) are shown. The X-axis represents the distance from the fovea in the nasal and temporal directions (in mm). The Y-axis represents the layer thickness in microns.*

Table 7.3: Summary of parafoveal measurements in patients with *FRMD7* mutations in comparison to controls

Thickness measurement (μm)	Control group Mean (μm)	*FRMD7* group Mean (μm)	Difference (μm)	*P*-value
Nerve Fibre Layer	25.2	19.4	5.8	<0.0001
GCL+IPL Complex	73.5	75.3	-1.8	0.0185
Inner Nuclear Layer	35.7	40.5	-4.8	<0.0001
Outer Plexiform Layer	20.5	16.3	4.2	<0.0001
Outer Nuclear Layer	66.4	65.8	0.6	0.9343
Inner Segment	25.8	24.3	1.5	0.0001
Outer Segment	21.6	21.1	0.5	0.5687
Retinal Pigment Epithelium	23.5	24.5	-1.0	0.1587
Retinal Thickness	271.0	266.3	4.7	0.2631

7.3.1.3 OPTIC NERVE HEAD ABNORMALITIES ASSOCIATED WITH *FRMD7* MUTATIONS

Example of optic disc abnormalities associated with *FRMD7* mutations are shown in figure 7.6. The average peripapillary NFL thickness was significantly decreased in patients with *FRMD7* mutations in comparison to controls. The cup depth, cup and disc diameter and cup:disc ratio was also significantly decreased in patients with *FRMD7* mutations in comparison to controls (figure 7.6 and table 7.4). The RT surrounding the optic disc was not significantly different between the two groups. The diamond plots are shown in section 7.3.5.

(A) Example of Normal Optic Nerve Head — Hypoplastic Optic Nerve Head associated with FRMD7 mutations

(B) Worsening Morphological Appearance of the Optic Nerve Head

c.58-1G>A — c.1003C>T — c.47T>C

Figure 7.6: *Optic nerve head abnormalities associated with FRMD7 mutations. Example of a normal OCT is shown alongside the abnormal FRMD7 optic nerve head (A). The phenotypic spectrum based on morphological appearance of the cup size and depth is also shown in (B).*

Table 7.4: Summary of peripapillary nerve fibre layer, cup and optic disc measurements in patients with *FRMD7* mutations in comparison to controls

Measurement (μm or ratio)	Control group Mean (μm or ratio)	*FRMD7* group Mean (μm or ratio)	Difference (μm or ratio)	*P*-value
Peripapillary NFL	71.1	59.3	11.8	<0.0001
Retinal Thickness	296.5	302.6	-6.1	0.1988
Cup Depth	517.9	417.8	100.1	0.0035
Disc Diameter	1593.6	1423.8	169.8	<0.0001
Cup Diameter	842.8	578.2	264.6	0.0002
Cup:Disc Ratio	0.52	0.40	0.12	0.0045

NFL = Nerve Fibre Layer

7.3.2 *PAX6* MUTATIONS

7.3.2.1 OVERVIEW OF FAMILIES AND SINGLETONS WITH *PAX6* MUTATIONS

We identified a total of 8 mutations in six families and two singletons. Family P2 and singleton PS2 had the same mutation. Four out of the seven mutations were novel. The pedigrees, mutations and domains affected are shown in table 7.5. Most mutations affected the paired domain and the structural effects of the mutations are shown in figure 7.7. Five of the eight mutations were missense mutations within identical blocks of residues between different species suggesting that the affected regions are critical to the functioning of the PAX6 protein (figure 7.7). The nonsense mutation identified (c. 325G>T) was predicted to result in translation of a smaller polypeptide which is approximately 25.5% of its normal size. We also identified a novel anti-termination mutation which is predicted to create a longer transcript. Therefore the c.1269A>T mutation obliterates the original translation termination site and this results in a new translation termination site 14 residues downstream from the original termination site

Only family P6 had the typical phenotype of aniridia which was detected on both anterior segment photography and OCT. The remaining families had varying degrees of iris involvement ranging from sectorial hypoplasia to subtle transillumination defects of the iris. Examples of the iridial phenotypic variability associated with *PAX6* mutations have been shown in figure 7.8.

(A)

| Species | R38G | S74G; P76R | R208W |
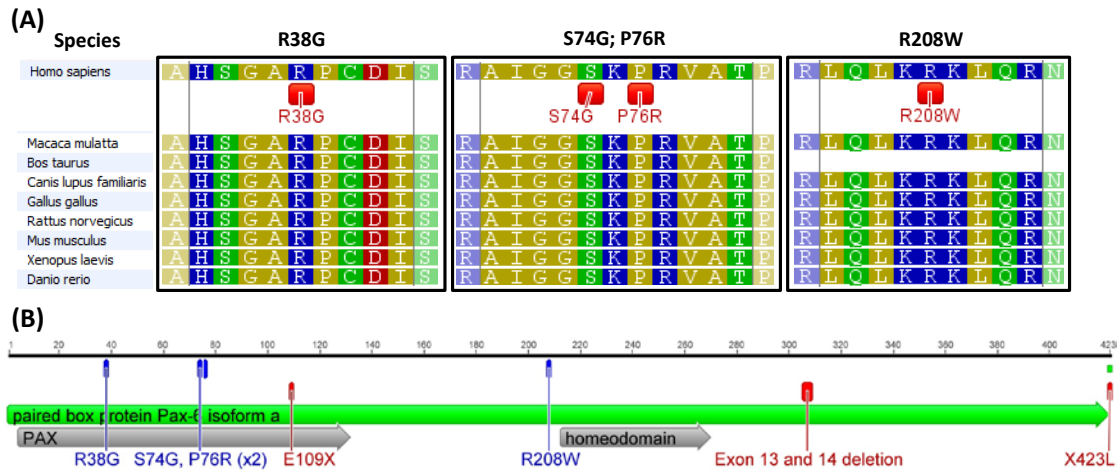
Figure 7.7: Alignment of PAX6 mutations, which were located within invariant blocks of residues among different species (A). Location of PAX6 mutations in relation to the functional domains (B).

Table 7.5: The families and singletons with *PAX6* mutations. The domain affected, electropherogram and previous report of the mutation are also shown.

Family ID	Pedigree	Mutation	Domain affected	Electropherogram	Previous reports
P1		c.474C>G; p.R38G	Paired box domain		Novel
P2		c.622C>T; p.R208W	Flanking the 5' end of homeodomain		Hanson et al. 1993
P3		c.227C>G; p. P76R	Paired box domain		Novel
P4		c.220A>G; p.S74G	Paired box domain		Dansault et al. 2007
P5		c.1269A>T; p.X423L	Stop codon		Novel
P6		c.917_1184del	Flanking the 3' end of homeodomain	NA	Novel
PS1	Singleton 1	c.325G>T; p. E109X	Paired box domain		Robinson et al. 2008
PS2	Singleton 2	c.227C>G; p. P76R	Paired box domain		Novel
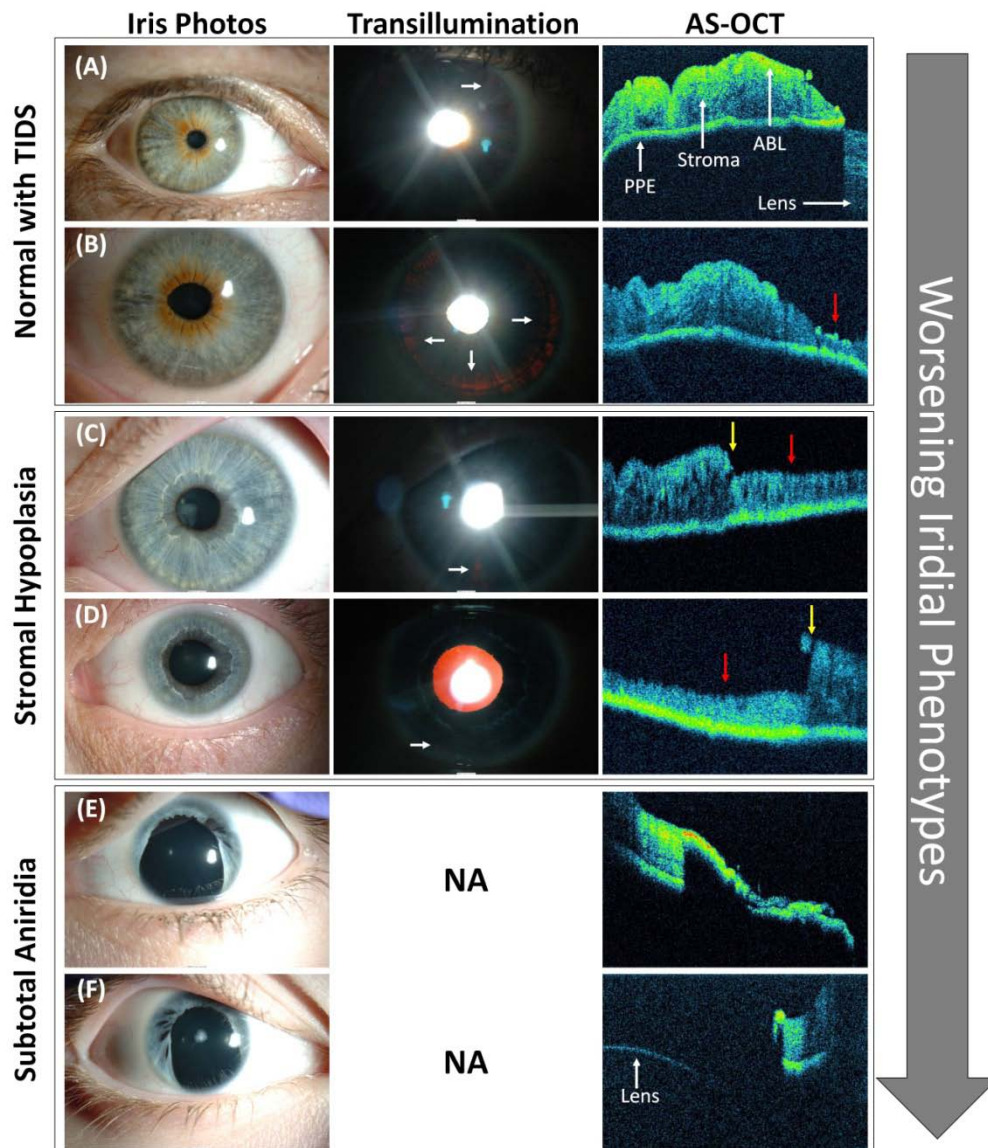
Figure 7.8: *Iridial phenotypes associated with PAX6 mutations. Images were ordered based on increasing severity of iris involvement. Iris photos, iridial trans-illumination images and anterior segment-OCT images are shown. (A&B) In this patient there is no obvious iridial lesion on the iris photos however on retro-illumination, we observe subtle trans-illumination defects (white arrows). (A) The AS-OCT shows the normal iris structure near the pupillary border. (B) The AS-OCT over the trans-illumination defect shows a thinner iris (red arrows). (C&D) Iris pictures show abnormal iris structure and iris hypoplasia at the pupillary border with inferior iris trans-illumination. Stromal hypoplasia is clearly visible in the AS-OCT (red arrow). The border between hypoplastic and normal iris is shown with the yellow arrow on AS-OCT. (E&F) In this patient the iris photos show subtotal aniridia where there is loss of most of the iris tissue with preservation of some of the peripheral parts. (E) AS-OCT some remnant tissue at the pupillary border, however in certain regions there is only an iris stump (F). PPE = Posterior Pigment Epithelium; ABL = Anterior Border Layers; AS-OCT = Anterior Segment Optical Coherence Tomography.*

203

7.3.2.2 FOVEAL ABNORMALITIES ASSOCIATED WITH *PAX6* MUTATIONS

In 3/15 patients with *PAX6* mutations the OCT quality was poor due to corneal/media opacity. The mutations in these patients were: c.220A>G, c.227C>G, and c.325G>T. One of the patient with the c.622C>T mutation also had a cataract; therefore we were not able to obtain OCT images from one of the eyes in this affected family member (Family ID:P2, Individual: II:2) (figure 7.9).
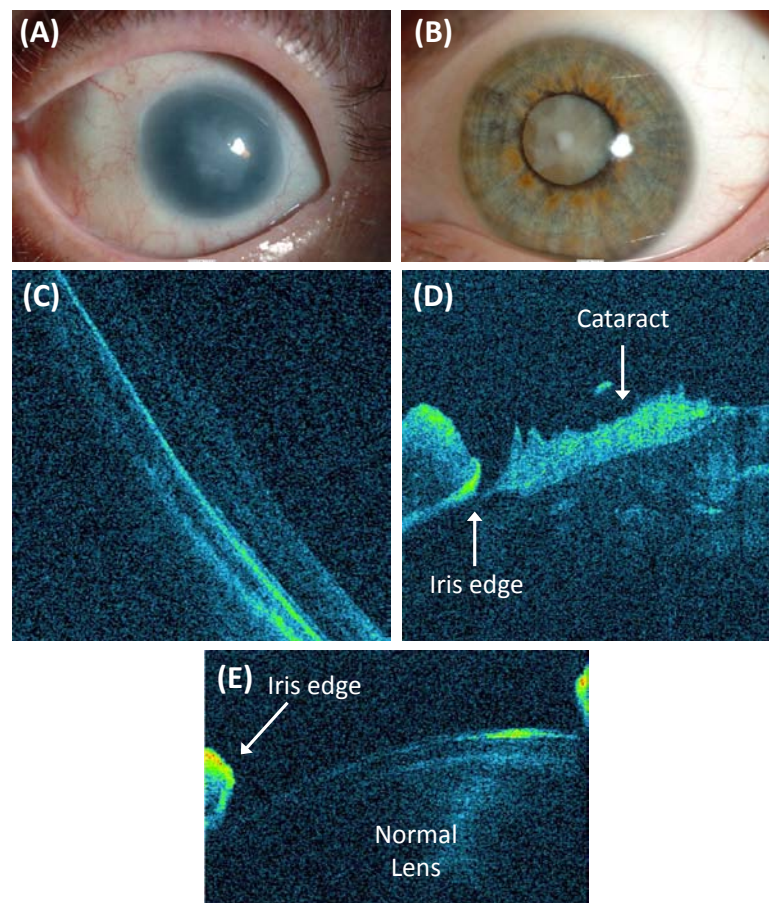
Figure 7.9: Corneal opacity (A) as a result of the PAX6 mutation (c. 325G>T). Cataract involving the anterior capsule and affecting the left eye resulting from mutation c.622C>T is shown (B). Corneal opacity results in a poor quality posterior foveal scan which cannot be segmented (C). The corresponding anterior segment scan shows the cataract (D). The normal lens is shown in figure (E). Photographs and tomograms from (A) and (C) are from (Patient ID: PS1). Photos and tomograms from B and D are from (Family ID: P2, Individual: II:2).

All the remaining patients examined had foveal hypoplasia. In the patients with foveal hypoplasia 7/12 had a rudimentary foveal pit and 5/12 had fovea plana (i.e.

no discernable foveal pit). One patient had IS/OS junction abnormalities. Examples of OCTs from patients with foveal hypoplasia and *PAX6* mutations are shown in figure 7.10. Patients with *PAX6* mutations had significantly: (1) shallower foveal pit, (2) thinner OS, (3) thicker ONL and (4) increased CMT in comparison to controls. These results are summarised in table 7.6 and figure 7.11. The diamond plots are shown in section 7.3.5.
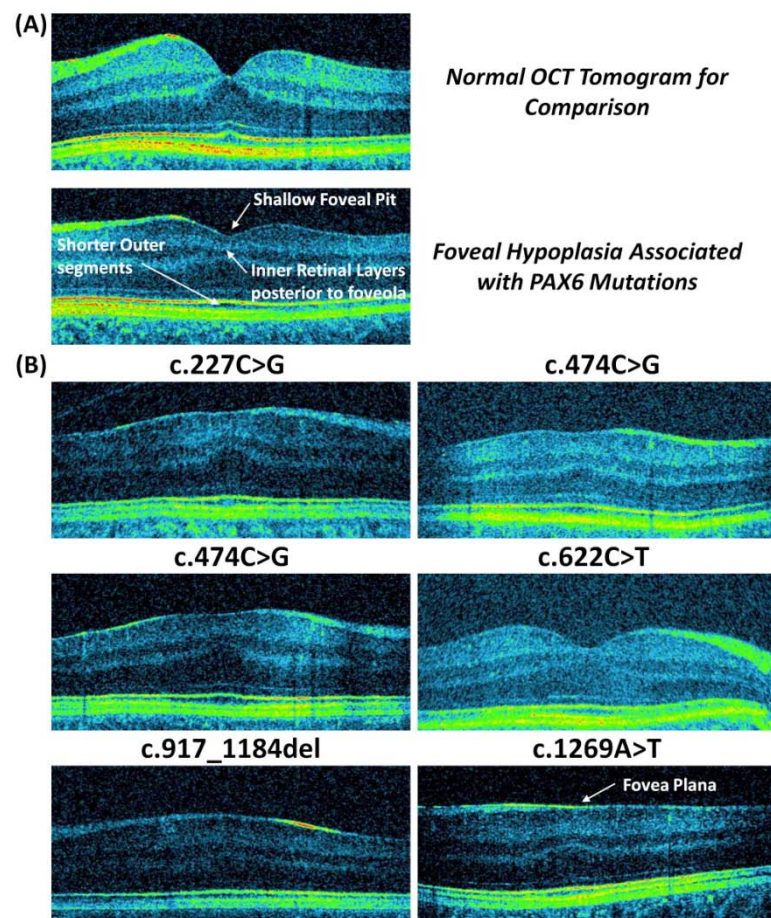
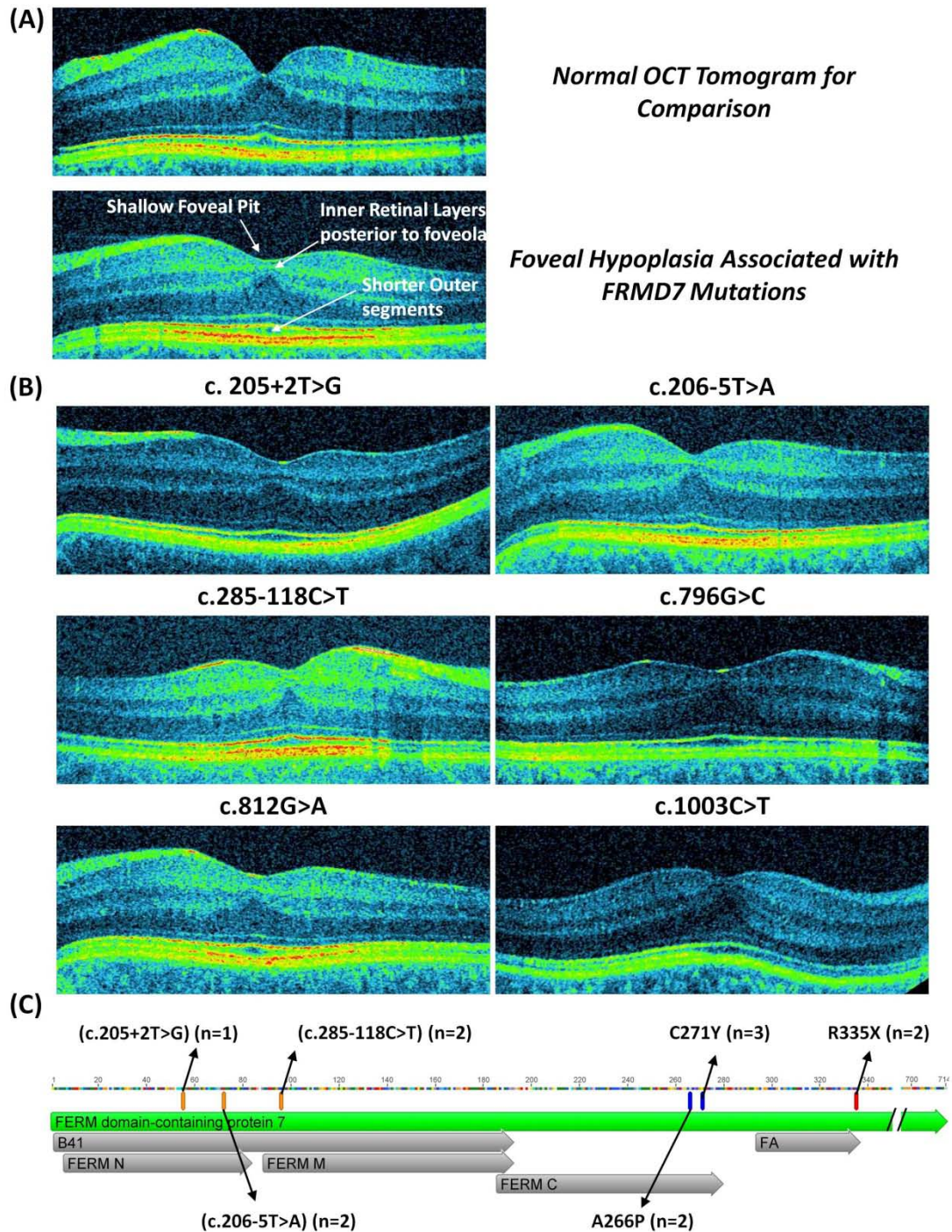*Figure 7.10:* *The morphological abnormalities associated with foveal hypoplasia and PAX6 mutations are shown in (A). Patients had: a rudimentary pit or no foveal pit (fovea plana), continuation of the inner retinal layer posterior to the foveola and shorter outer segments (A & B). Examples of foveal hypoplasia associated with each mutation are shown in (B). The mutations are shown above the tomograms.*

Table 7.6: Summary of foveal measurements in patients with *PAX6* mutations in comparison to controls

Thickness measurement (μm)	Control group mean (μm)	*PAX6* group mean (μm)	Difference (μm)	*P*-value
Foveal Depth	133.8	32.7	101.1	<0.0001
Outer Nuclear Layer	102.9	117.0	-14.1	0.0050
Inner Segment	33.5	32.4	1.1	0.1800
Outer Segment	50.2	36.9	13.3	<0.0001
Retinal Pigment Epithelium	18.2	21.2	-3.0	0.0012
Central Macular Thickness	190.8	280.5	-89.7	<0.0001

7.3.2.3 PARAFOVEAL ABNORMALITIES ASSOCIATED WITH *PAX6* MUTATIONS

The average parafoveal NFL, GCL+IPL complex, OPL and RT were significantly decreased in *PAX6* patients compared to controls. The INL was significantly thicker within the *PAX6* group in comparison to controls. These findings have been summarised in table 7.7 and figure 7.11. The average parafoveal ONL, IS, OS and RPE thicknesses were not significantly different (*p*>0.05) between the *PAX6* group and controls. The diamond plots are shown in section 7.3.5.
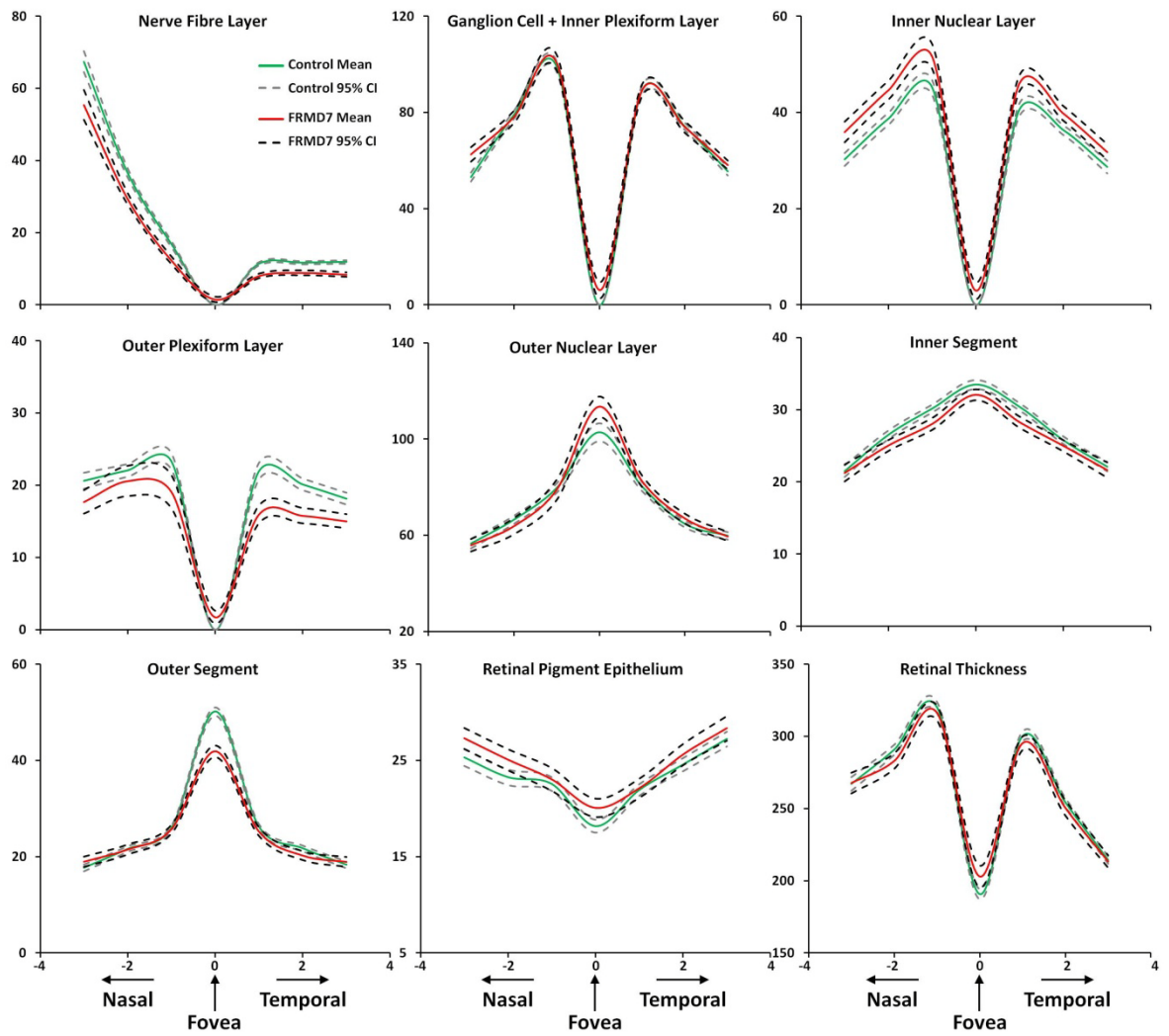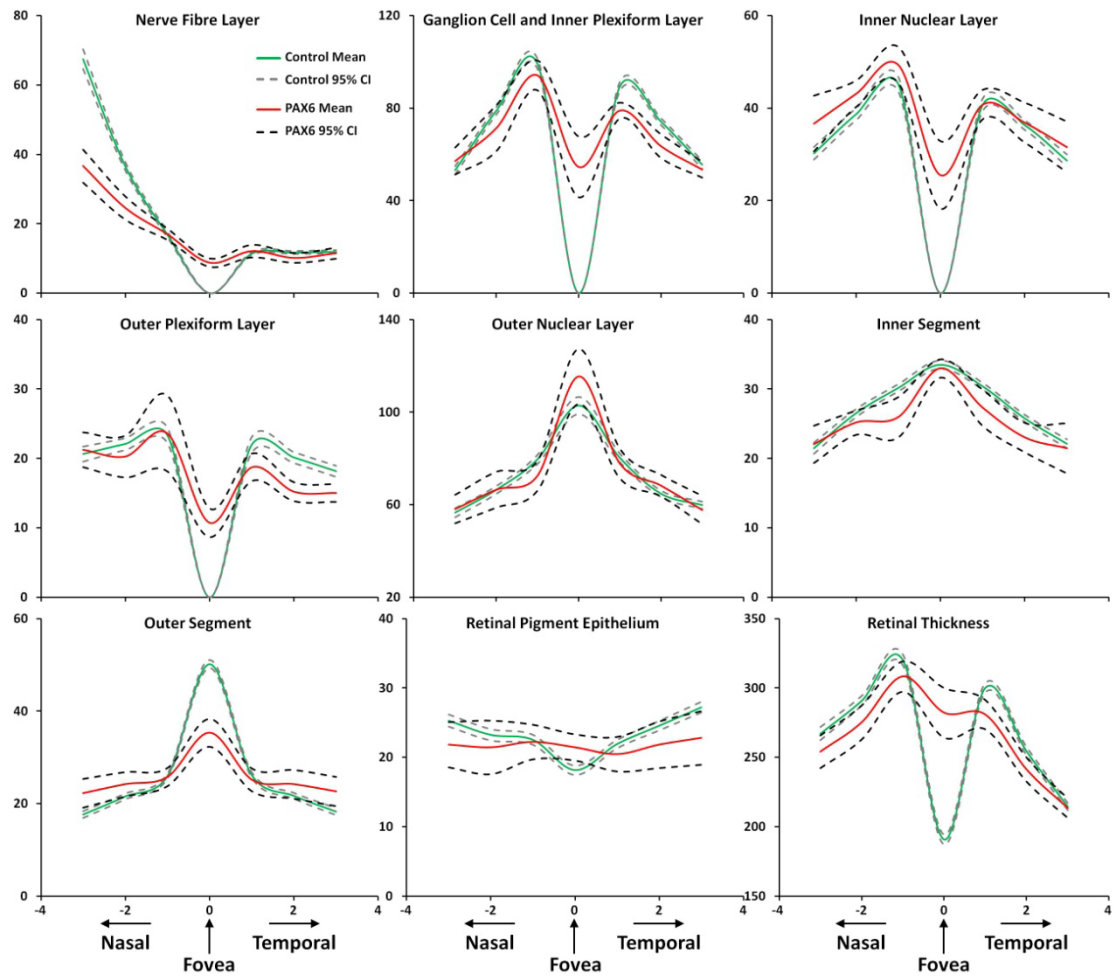
Figure 7.11: *Intra-retinal thickness measurements in patients with PAX6 mutations in comparison to controls. The mean layer thickness for the fovea and parafovea and the 95% confidence intervals (CI) are shown. The X-axis represents the distance from the fovea in the nasal and temporal directions (in mm). The Y-axis represents the layer thickness in microns.*

Table 7.7: Summary of parafoveal measurements in patients with *PAX6* mutations in comparison to controls

Thickness measurement (μm)	Control group Mean (μm)	*PAX6* group Mean (μm)	Difference (μm)	*P*-value
Nerve Fibre Layer	25.2	16.9	8.3	<0.0001
GCL+IPL complex	73.5	65.4	8.1	0.0072
Inner Nuclear Layer	35.7	37.5	-1.8	0.0064
Outer Plexiform Layer	20.5	17.1	3.4	0.0137
Outer Nuclear Layer	66.4	61.8	4.6	0.6397
Inner Segment	25.8	21.5	4.3	0.1250
Outer Segment	21.6	21.5	0.1	0.1000
Retinal Pigment Epithelium	23.5	18.5	5.0	0.1500
Retinal Thickness	271.0	254.3	16.7	0.0065

7.3.2.4 OPTIC NERVE HEAD ABNORMALITIES ASSOCIATED WITH *PAX6* MUTATIONS

Family P2 had an optic disc coloboma (figure 7.13). Optic disc analysis in the remaining families showed a significantly decreased peripapillary NFL. The cup depth, cup and disc diameter and cup:disc ratio was also significantly decreased in patients with *PAX6* mutations in comparison to controls (figure 7.12 and table 7.8). The RT surrounding the optic disc was not significantly different between the two groups (*p*>0.05). The diamond plots are shown in section 7.3.5.
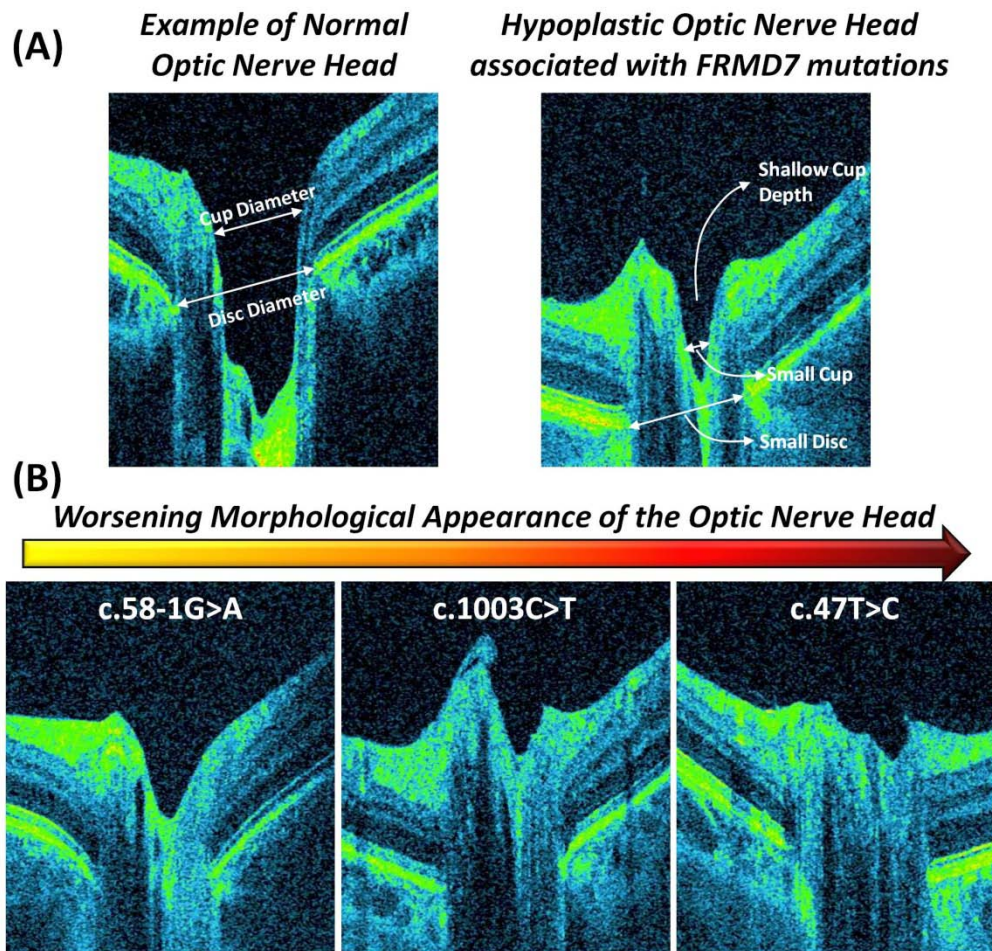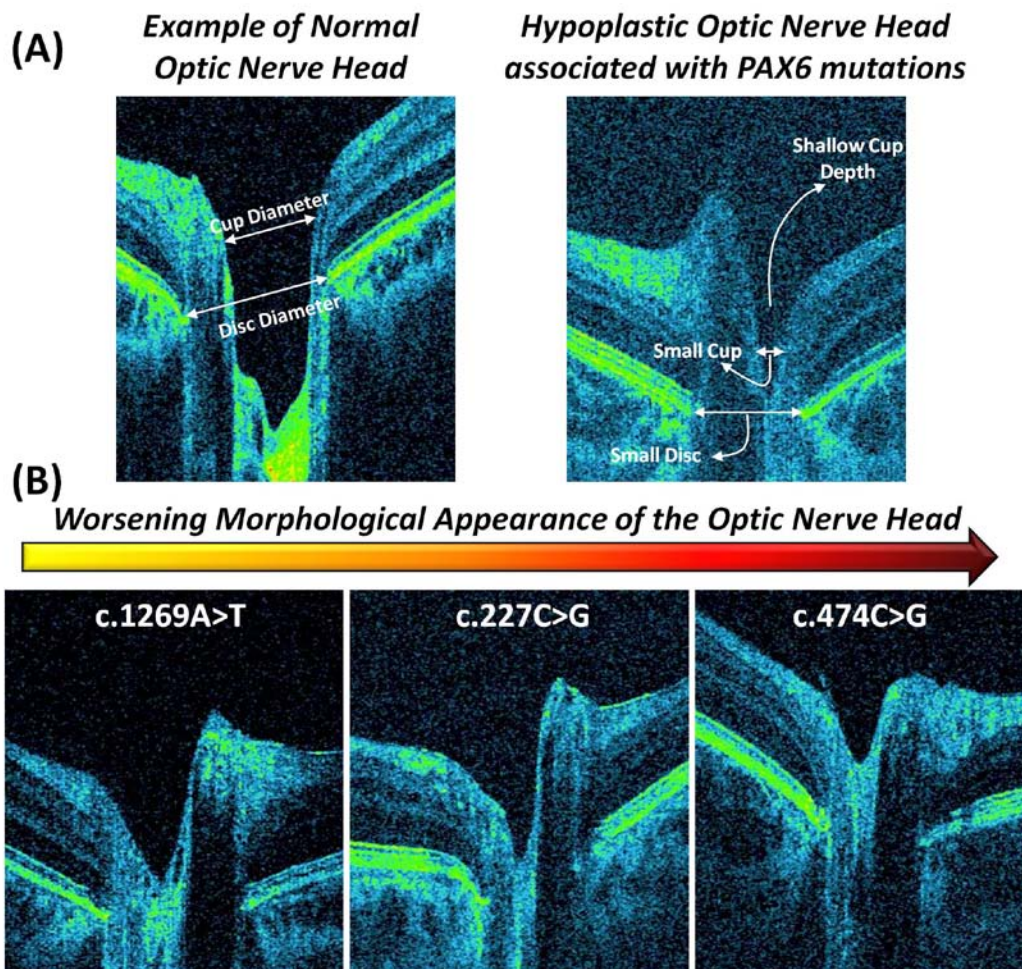
Figure 7.12: *Optic nerve head abnormalities associated with PAX6 mutations. Example of a normal OCT is shown alongside the abnormal PAX6 optic nerve head (A). The phenotypic spectrum based on morphological appearance of the cup size and depth is also shown in (B).*
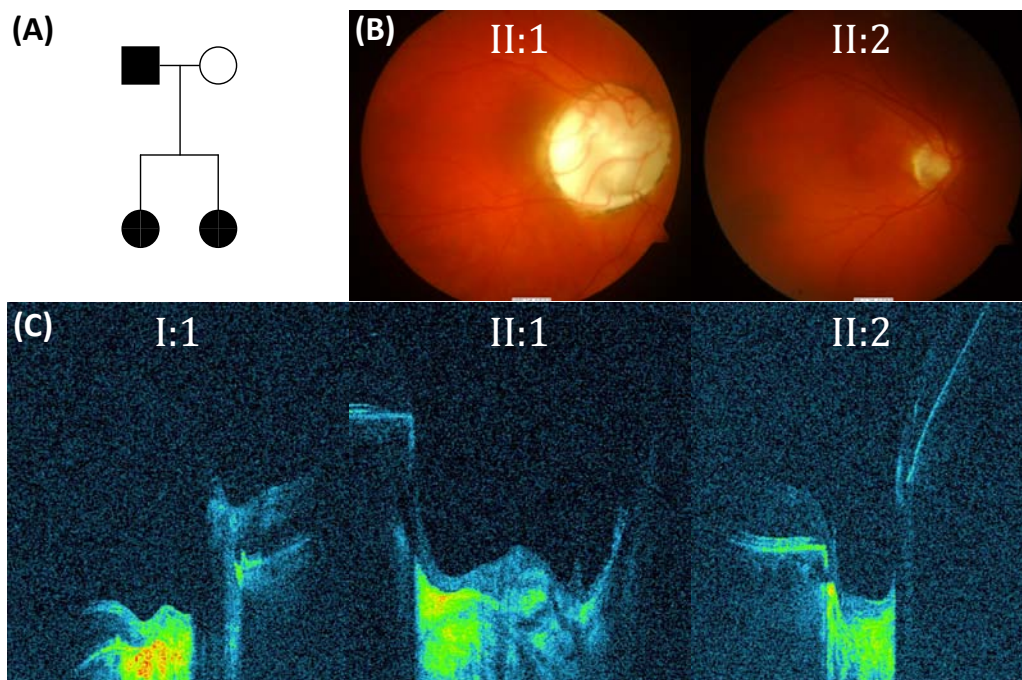
Figure 7.13: *Ocular phenotypes from family P2 with PAX6 mutation. The pedigree from the family (A) and fundus photos (B). OCT tomograms from affected individuals show optic disc coloboma (C). The OCT tomograms show regions of hyperreflectivity in the region of the coloboma at the level of the choroid. There is some phenotypic variation although all members have been identified to have the same mutation on segregation analysis. The individual IDs are shown at the top of each figure within the panel.*

Table 7.8: Summary of peripapillary nerve fibre layer, cup and optic disc measurements in patients with *PAX6* mutations in comparison to controls

Measurement (μm or ratio)	Control group Mean (μm or ratio)	*PAX6* group Mean (μm or ratio)	Difference (μm or ratio)	*P*-value
Peripapillary NFL	71.1	49.9	21.2	<0.0001
Retinal Thickness	296.5	305.3	-8.8	0.2169
Cup Depth	517.9	359.4	158.5	0.0029
Disc Diameter	1593.6	1347.1	246.5	<0.0001
Cup Diameter	842.8	525.8	317.0	0.0031
Cup:Disc Ratio	0.52	0.39	0.13	0.0338

NFL = Nerve Fibre Layer

7.3.3 ALBINISM

7.3.3.1 FOVEAL ABNORMALITIES ASSOCIATED WITH ALBINISM

Foveal hypoplasia was identified in all patients diagnosed with albinism. Examples of OCTs from patients with foveal hypoplasia are shown in figure 7.14. Patients with albinism had significantly: (1) shallower foveal pit, (2) thinner OS, (3) thicker RPE and (4) increased CMT in comparison to controls. These results are summarised in table 7.9 and figure 7.15. The diamond plots are shown in section 7.3.5.
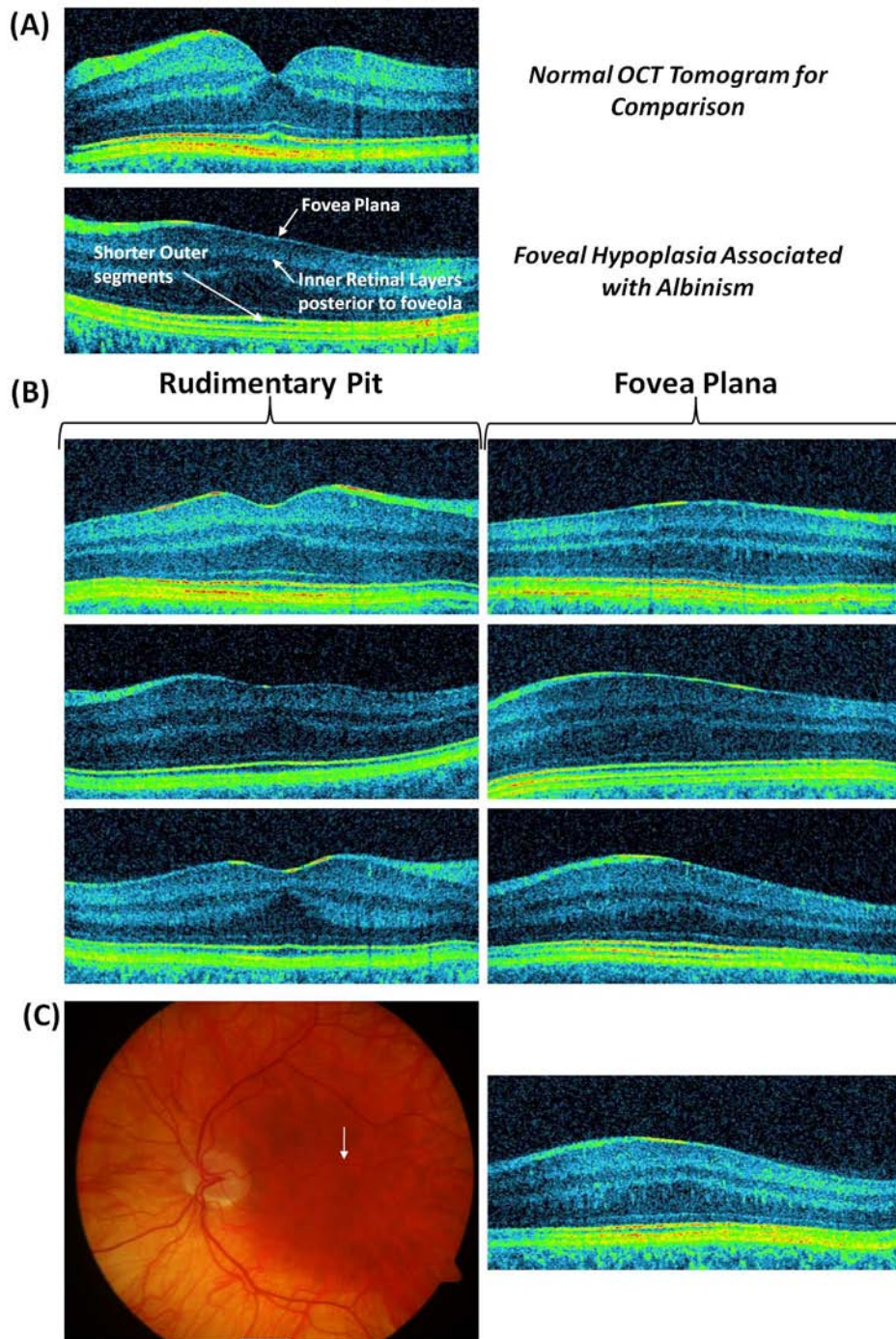
Figure 7.14: *The morphological abnormalities associated with foveal hypoplasia in albinism are shown in (A). Patients either had a rudimentary pit or no foveal pit (fovea plana), continuation of the inner retinal layer posterior to the foveola and shorter outer segments (A). Optical coherence tomograms show the spectrum of foveal development in patients with albinism (B). Fundus photo shows peripheral hypopigmentation and anomalous vasculature at the exit of the optic nerve, in the periphery, with abnormal and foveal hypoplasia and central abnormal vasculature (white arrow) which crosses the putative foveal zone. The optic nerve is small without cup and tilted (C).*

212

Table 7.9: Summary of foveal measurements in patients with albinism in comparison to controls

Thickness measurement (μm)	Control group mean (μm)	Albinism group mean (μm)	Difference (μm)	*P*-value
Foveal Depth	133.8	12.6	121.2	<0.0001
Outer Nuclear Layer	102.9	107.1	-4.2	0.2692
Inner Segment	33.5	33.0	0.5	0.4120
Outer Segment	50.2	33.2	17.0	<0.0001
Retinal Pigment Epithelium	18.2	20.4	-2.2	0.0031
Central Macular Thickness	190.8	287.4	-96.6	<0.0001

7.3.3.2 PARAFOVEAL ABNORMALITIES ASSOCIATED WITH ALBINISM

The average parafoveal NFL, GCL+IPL complex, OPL and RT were significantly decreased in patients with albinism compared to controls. The OS was significantly increased within the albinism group in comparison to controls. These findings have been summarised in table 7.10 and figure 7.15. The average parafoveal INL, ONL, IS and RPE thicknesses were not significantly different (*p*>0.05) between the albinism group and controls. The diamond plots are shown in section 7.3.5.
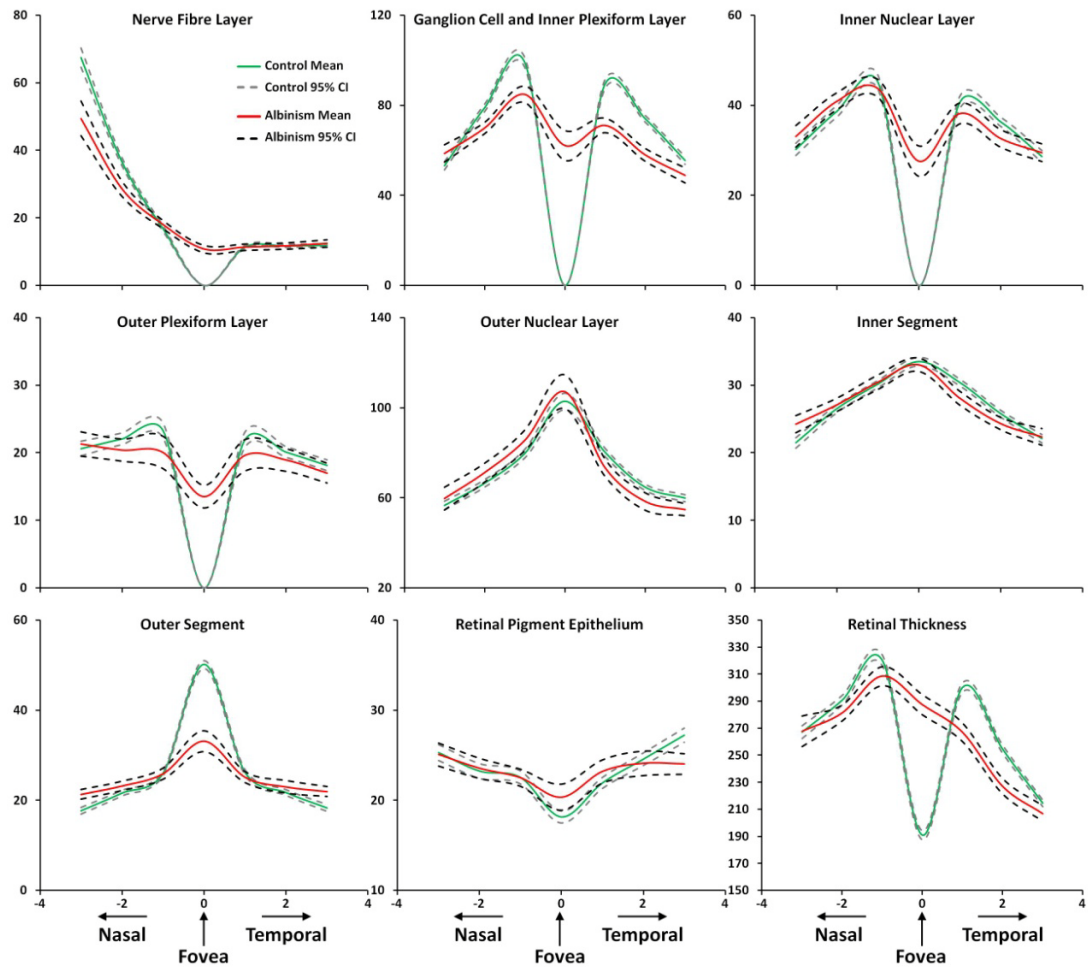
Figure 7.15: *Intra-retinal thickness measurements in patients with albinism mutations in comparison to controls. The mean layer thickness for the fovea and parafovea and the 95% confidence intervals (CI) are shown. The X-axis represents the distance from the fovea in the nasal and temporal directions (in mm). The Y-axis represents the layer thickness in microns.*

214

Table 7.10: Summary of parafoveal measurements in patients with albinism in comparison to controls

Thickness measurement (μm)	Control group Mean (μm)	Albinism group Mean (μm)	Difference (μm)	*P*-value
Nerve Fibre Layer	25.2	20.5	4.7	<0.0001
GCL+IPL Complex	73.5	62.8	10.7	<0.0001
Inner Nuclear Layer	35.7	34.9	0.8	0.6813
Outer Plexiform Layer	20.5	18.3	2.2	0.0001
Outer Nuclear Layer	66.4	64.9	1.5	0.8911
Inner Segment	25.8	25.4	0.4	0.9547
Outer Segment	21.6	22.7	-1.1	0.0003
Retinal Pigment Epithelium	23.5	22.9	0.6	0.4593
Retinal Thickness	271.0	253.7	17.3	<0.0001

7.3.3.3 OPTIC NERVE HEAD ABNORMALITIES ASSOCIATED WITH ALBINISM

Examples of optic disc abnormalities associated with albinism are shown in figure 7.16. The average peripapillary NFL thickness was significantly decreased in patients with albinism in comparison to controls. The cup depth, cup diameter and cup:disc ratio were also significantly decreased in patients with albinism in comparison to controls (figure 7.16 and table 7.11). The disc diameter and the RT surrounding the optic disc were not significantly different between the two groups (*p*>0.05). The diamond plots are shown in section 7.3.5.
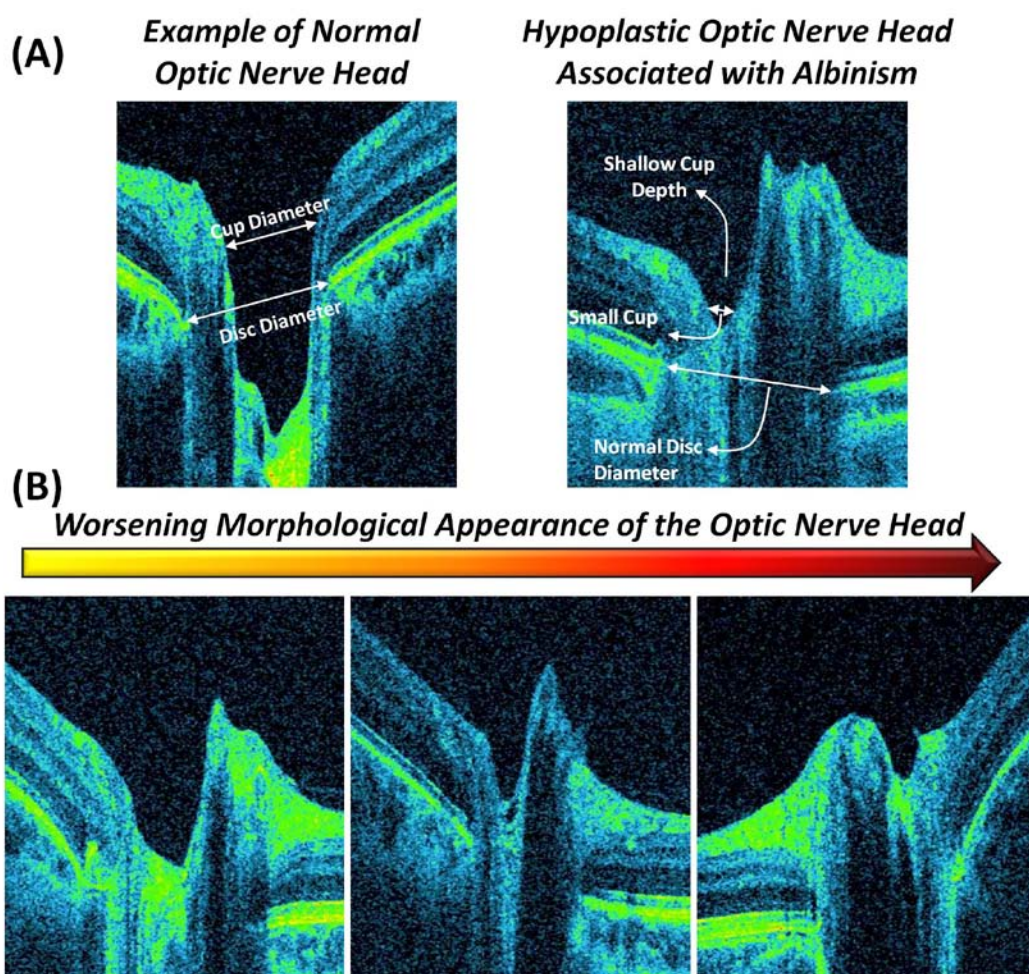
Figure 7.16: *Optic nerve head abnormalities associated with albinism. Example of a normal OCT is shown alongside the abnormal albinism optic nerve head (A). The phenotypic spectrum based on morphological appearance of the cup size and depth is also shown in (B).*

Table 7.11: Summary of peripapillary nerve fibre layer, cup and optic disc measurements in patients with albinism in comparison to controls

Measurement (μm or ratio)	Control group Mean (μm or ratio)	Albinism group Mean (μm or ratio)	Difference (μm or ratio)	*P*-value
Peripapillary NFL	71.1	60.3	10.8	<0.0001
Retinal Thickness	296.5	296.0	0.5	0.9254
Cup Depth	517.9	325.5	192.4	<0.0001
Disc Diameter	1593.6	1603.9	-10.3	0.8070
Cup Diameter	842.8	446.0	396.8	<0.0001
Cup:Disc Ratio	0.52	0.27	0.25	<0.0001

NFL = Nerve Fibre Layer

216

7.3.4 ACHROMATOPSIA

7.3.4.1 FOVEAL ABNORMALITIES ASSOCIATED WITH ACHROMATOPSIA

The foveal abnormalities in achromatopsia were associated with reflectivity changes; hence reflectance profiles will be used in this section to describe the results.

On gross visualization of the OCT tomograms, a spectrum of OCT changes was detected in patients with achromatopsia (figure 7.17). The most obvious changes included the so-called punched out lesion representing a hyporeflective zone (HRZ) at the foveola. This HRZ resulted in either complete disruption (figure 7.17Bii) or a discontinuous IS/OS junction reflectivity (figure 7.17Cii). Eight of 14 patients had the punched out lesion. Some patients showed only subtle discontinuities of the IS/OS junction in the foveal region (figure 7.17D). Using the reflectance profile, a loss of peak P3 corresponding to the IS/OS junction can be demonstrated (see reflectivity profiles in figure 7.17). Similarly, in 5 of 14 patients, there was a loss of the COST reflectivity typically in regions corresponding to the location of the HRZ or loss of IS/OS junction reflectivity. This also is detected on the reflectance profile with a loss of peak P4 (see reflectivity profiles in figure 7.17).

7.3.4.2 FEATURES OF THE HYPOREFLECTIVE ZONE

The mean area occupied by the HRZ was 1.6×10^4 μm^2 (range, $7.2 \times 10^3 - 2.8 \times 10^4$ μm^2). There was a statistically significant effect of age on the presence of this HRZ ($p = 0.001$). The HRZ was seen predominantly in the older patients with achromatopsia. The HRZ had an asymmetric location, with most of the area occupied in the nasal part of the fovea (figure 7.18). A line drawn from the centre

of the fovea was used to divide the area into 2 halves: a nasal HRZ and a temporal

HRZ. A paired *t*-test showed that the area of the nasal HRZ was significantly larger

than the area of the temporal HRZ (mean difference, 6.3 x 10^3 μm^2; *p* = 0.002; see

figure 7.18B).
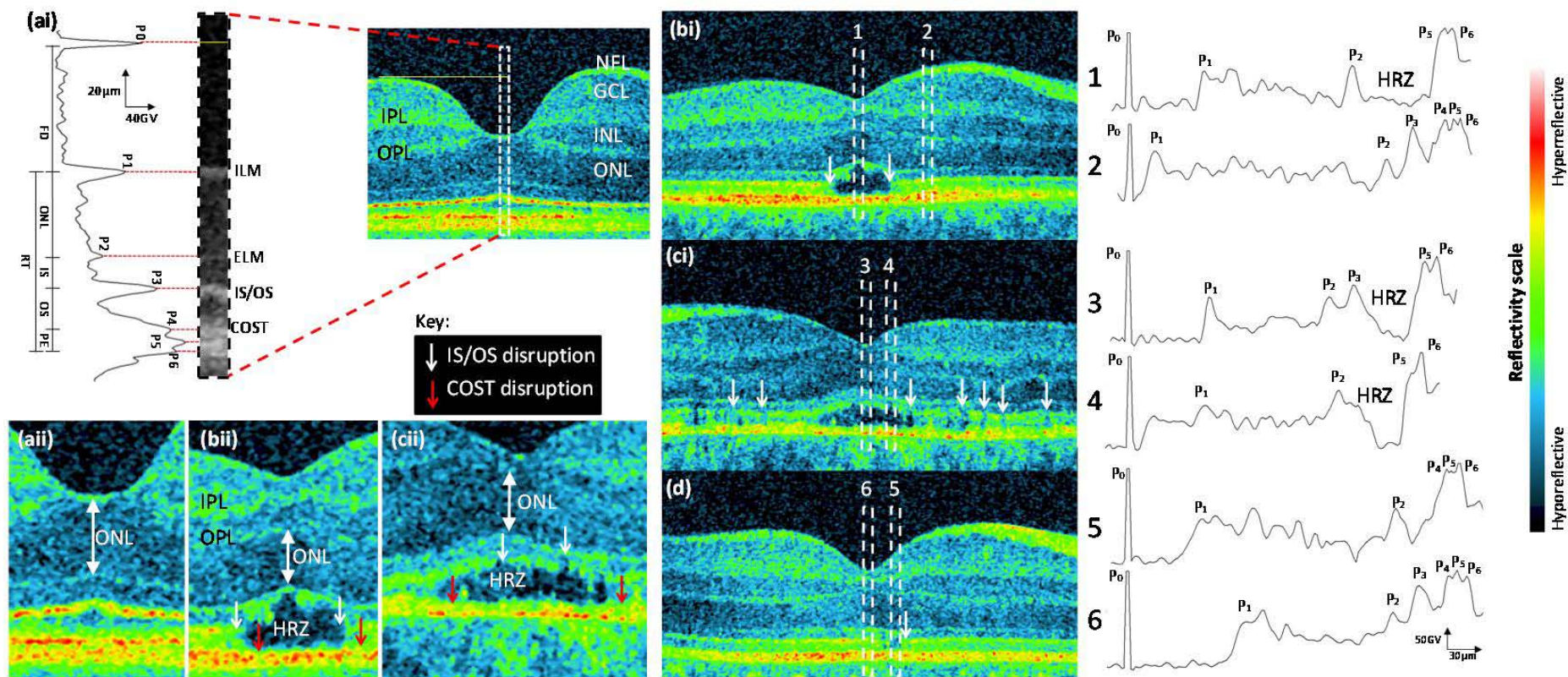
Figure 7.17: *Tomograms from achromats and a control. Ai, Normal tomograms with annotation of retinal layers and reflectance graph derived from the sampling window (white rectangle). Bi, Ci, Tomograms from achromats with hyporeflective zone (HRZ). Aii, Bii, Cii, Magnified images at (Bii, Cii) the fovea of achromats and (Aii) in the control. D, Younger patient without HRZ. B–D, Continuation of inner retinal layers a sign of foveal hypoplasia. Loss of inner segment–outer segment (IS/OS) junction and cone outer segment tip (COST) reflectance are shown with white and red arrows, respectively. This is seen as a loss of peaks P3 and P4, respectively, on the corresponding reflectivity profiles for sampling windows shown on the right. ELM = external limiting membrane; GCL= ganglion cell layer; ILM = internal limiting membrane; INL = inner nuclear layer; IPL = inner plexiform layer; ONL = outer nuclear layer; NFL = nerve fibre layer; OPL = outer plexiform layer.*

7.3.4.3 FOVEAL MALDEVELOPMENT AND THINNING OF THE OUTER NUCLEAR LAYER

Foveal maldevelopment was detected in patients with achromatopsia. This represents an atypical foveal hypolpasia since there is continuation of inner retinal layers posterior to the foveola with a thinner rather than a thicker central macula. This was noted in 10 of 14 patients with achromatopsia, which can be visualized grossly on the OCT and can be detected by the continuation of the OPL and IPL layers (figure 7.17B–D). The foveal depth (P0 –P1) was reduced significantly in patients with achromatopsia when compared with controls (mean difference, 52.6μm; p <0.0001). Similarly, the ONL thickness was reduced significantly in the achromats compared with controls (mean difference, 31.7μm; p <0.0001). A linear regression showed that the ONL thinning was age dependent (R^2 = 0.63; p = 0.0007), with older patients having much thinner ONL compared with younger patients. The achromat cohort also had a significantly thinner RT compared with controls (mean difference, 23.7μm; p<0.0001; see figure 7.18) (table 7.12). The diamond plots are shown in section 7.3.5.

Table 7.12: Summary of foveal measurements in patients with achromatopsia in comparison to controls

Thickness measurement (μm)	Control group mean (μm)	*FRMD7* group mean (μm)	Difference (μm)	*P*-value
Foveal Depth	133.8	81.2	52.6	<0.0001
Outer Nuclear Layer	102.9	71.1	31.8	<0.0001
Retinal Pigment Epithelium	18.2	8.9	9.3	<0.0001
Central Macular Thickness	190.8	167.1	23.7	<0.0001
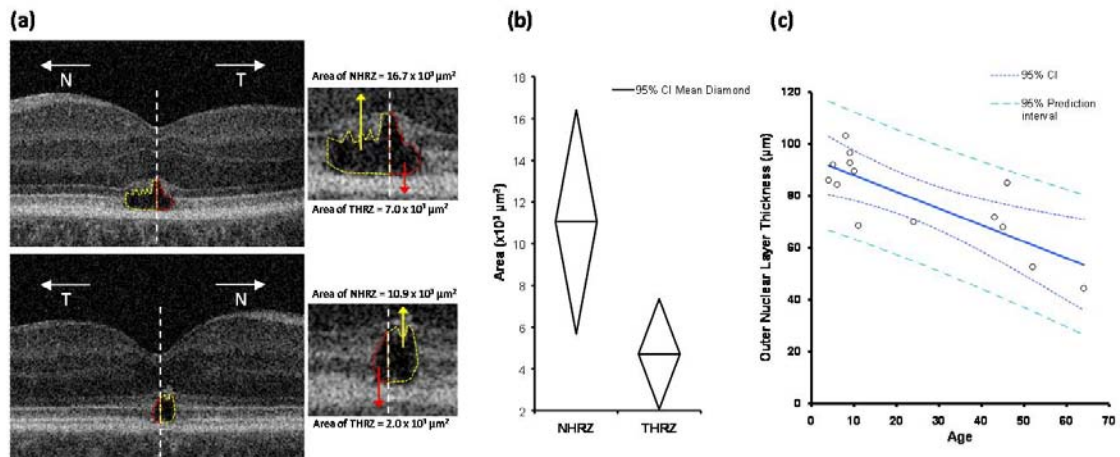
Figure 7.18: *Features of the hyporeflective zone (HRZ) and outer nuclear layer thinning. The asymmetric area distribution of the HRZ is shown in (a). The yellow and red outlined areas represent the areas of the HRZ located nasal (NHRZ) and temporal (THRZ) to the foveola respectively. The NHRZ was significantly larger than the THRZ (b). Linear regression of ONL thickness with age showed a significant relationship (c). The outer limits of the diamond plot (b) represent the 95% confidence intervals (CI) and the line bisecting the diamond is the mean.*

7.3.4.4 PARAFOVEAL ABNORMALITIES ASSOCIATED WITH ACHROMATOPSIA

The average parafoveal NFL, GCL+IPL complex, OPL, ONL, IS and RPE were significantly decreased in achromatopsia patients compared to controls. The OS was significantly thicker in achromatopsia compared to controls. The INL was not significantly different (p>0.05) between achromatopsia patients and controls. These findings have been summarised in table 7.13 and figure 7.19. The diamond plots are shown in section 7.3.5.
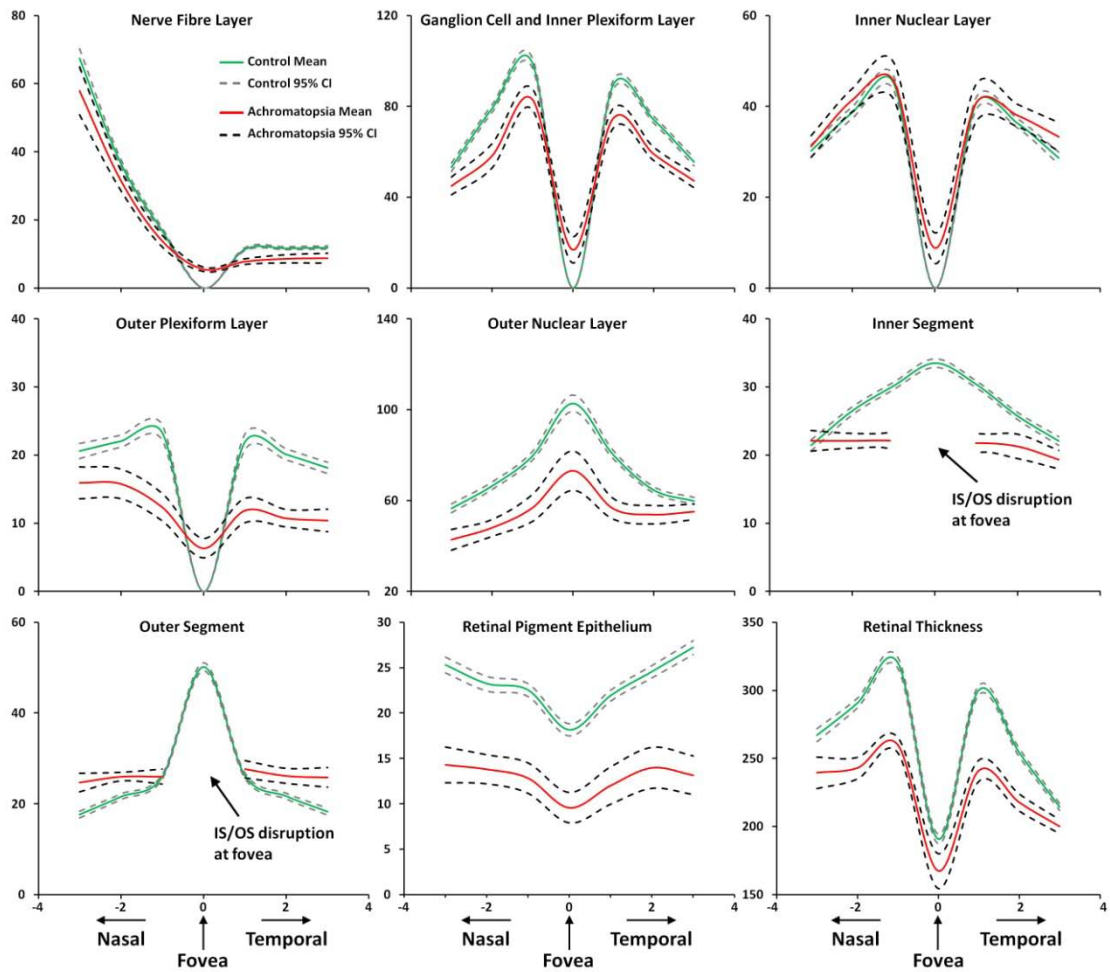
Figure 7.19: *Intra-retinal thickness measurements in patients with achromatopsia in comparison to controls. The mean layer thickness for the fovea and parafovea and the 95% confidence intervals (CI) are shown. The X-axis represents the distance from the fovea in the nasal and temporal directions (in mm). The Y-axis represents the layer thickness in microns. Due to the inner segment-outer segment junction disruption the inner segment and outer segment thickness cannot be determined at the fovea.*

Table 7.13: Summary of parafoveal measurements in patients with achromatopsia in comparison to controls

Thickness measurement (μm)	Control group Mean (μm)	Achromatopsia group Mean (μm)	Difference (μm)	*P*-value
Nerve Fibre Layer	25.2	19.4	5.8	<0.0001
GCL+IPL Complex	73.5	58.0	15.5	<0.0001
Inner Nuclear Layer	35.7	36.1	-0.4	0.0836
Outer Plexiform Layer	20.5	11.7	8.8	<0.0001
Outer Nuclear Layer	66.4	49.2	17.2	<0.0001
Inner Segment	25.8	20.7	5.1	<0.0001
Outer Segment	21.6	24.9	-3.3	<0.0001
Retinal Pigment Epithelium	23.5	11.6	11.9	<0.0001
Retinal Thickness	271.0	227.3	43.7	<0.0001

7.3.4.5 OPTIC NERVE HEAD ABNORMALITIES ASSOCIATED WITH ACHROMATOPSIA

Examples of optic disc OCTs from achromatopsia patients are shown in figure 7.20. The average peripapillary NFL thickness was significantly decreased in patients with achromatopsia in comparison to controls. The disc diameter and RT were significantly reduced in the achromats compared to controls. However the cup depth, cup diameter and cup:disc ratio were not significantly different between the two groups (*p*>0.05) (table 7.14). The diamond plots are shown in section 7.3.5.
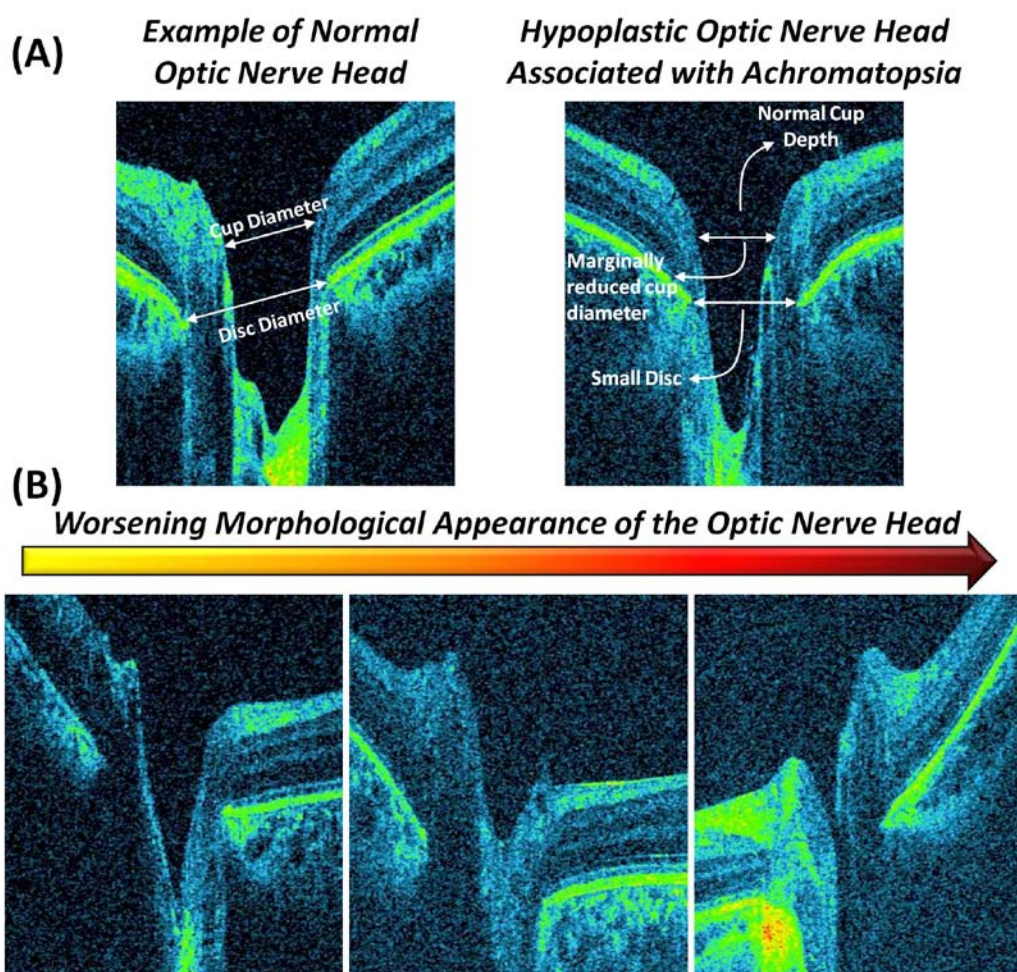
Figure 7.20: *Optic nerve head abnormalities associated with achromatopsia. Example of a normal OCT is shown alongside the abnormal achromatopsia optic nerve head (A). The phenotypic spectrum based on morphological appearance of the cup size and depth is also shown in (B).*

Table 7.14: Summary of peripapillary nerve fibre layer, cup and optic disc measurements in patients with achromatopsia in comparison to controls

Measurement (µm or ratio)	Control group Mean (µm or ratio)	Achromatopsia group Mean (µm or ratio)	Difference (µm or ratio)	*P*-value
Peripapillary NFL	71.1	55.7	15.4	<0.0001
Retinal Thickness	296.5	278.5	18.0	0.0183
Cup Depth	517.9	515.6	2.3	0.9668
Disc Diameter	1593.6	1398.4	195.2	<0.0001
Cup Diameter	842.8	634.6	208.2	0.0565
Cup:Disc Ratio	0.52	0.45	0.07	0.2364

NFL = Nerve Fibre Layer

224

The clinical and genetic features along with the follow up time of the patients

recruited for the longitudinal study are shown in table 7.15.

Sequence Analysis

Seven out of the eight patients had homozygous or compound-heterozygous

mutations in either *CNGA3* or *CNGB3* (Table 7.15). Sequence analysis of *CNGA3,*

CNGB3 and *GNAT2* did not identify any mutations for patient 4. In total, we

identified five different mutant alleles in *CNGA3*, and two in *CNGB3*. Of these, one

mutation in *CNGB3* (c.1426C>T) and one mutation in *CNGA3* (c.107_110del) were

novel and are to date unique to these patients. The nucleotide substitution

c.1426C>T in *CNGB3* represents a nonsense mutation and results in a premature

stop codon (PTC) after glutamine 476 (p.Q476X). The novel mutation in *CNGA3*

deletes four nucleotides (c.107_110del) creating a frame-shift after histidine 36,

and subsequently also results in PTC.

Table 7.15: Clinical, genetic and optical coherence tomography characteristics of patients with achromatopsia who had longitudinal examinations.

ACHM Patient ID	Age at visit 1	Age at visit 2	Follow up time	IS/OS change between visits	BCVA	Nystagmus	Gene	Allele 1		Allele 2	
								Nucleotide Alteration	Polypeptide Alteration	Nucleotide Alteration	Polypeptide Alteration
1	5y10m	6y9m	11 months	Yes	0.60	Present	*CNGA3*	c.1279C>T	p.R427C	c.107_110del	p.H36RfsX118
2	8y5m	9y10m	17 months	Yes	0.60	Present	*CNGA3*	c.1279C>T	p.R427C	c.107_110del	p.H36RfsX118
3	9y3m	10y7m	16 months	Yes	1.00	Present	*CNGA3*	c.1641C>A	p.F547L	c.1641C>A	p.F547L
4	8y10m	9y9m	11 months	Yes	1.00	Present	Unknown	-	-	-	-
5	9y2m	10y0m	10 months	Yes	0.80	Present	*CNGB3*	c.1148delC	p.T383IfsX13	c.1426C>T	p.Q476X
6	42y2m	44y3m	25 months	No	1.10	Present	*CNGA3*	c.1279C>T	p.R427C	c.1706G>A	p.R569H
7	45y0m	46y1m	13 months	No	1.00	Present	*CNGA3*	c.1279C>T	p.R427C	c.1706G>A	p.R569H
8	45y0m	46y11m	22 months	No	0.38	Present	*CNGB3*	c.1148delC	p.T383IfsX13	c.1148delC	p.T383IfsX13

Abbreviations: ACHM = achromatopsia; 5y10m = 5 years 10 months; IS/OS = inner segment outer segment junction; BCVA = Best Corrected Visual Acuity (binocular).

Temporal retinal changes and development of the hyporeflective zone

Among the eight patients we followed up, five of them (aged 5-9 years) showed altered foveal cone photoreceptor morphology on the second visit. In the remaining 3 patients (aged 42-45 years) there were no gross morphological changes between visit 1 and 2. These retinal changes are shown in figure 7.21.

In patients 5, 6, 7 and 8 we detected a HRZ on the tomograms obtained in visit 1. All of these patients had a disrupted IS/OS junction at the region of the HRZ. Among the older patients (patient 6-8) there were no gross morphological changes of the HRZ between visit 1 and 2. In the child patient 5, the size of the IS/OS disruption (visit 1 = 470µm; visit 2 = 667µm) was increased between the two visits although the HRZ appeared flatter between visit 1 and 2 (figure 7.21).

Interestingly patient 4 presented, during visit 1, only with a disrupted IS/OS junction and some hyperreflectivity surrounding the site of the lesion. However on visit 2 the size of the IS/OS disruption was increased (visit 1 = 157 µm; visit 2 = 363 µm) and this region also developed into a HRZ. There was an asymmetric distribution for both the initial IS/OS disruption and the subsequent HRZ. Unlike the distinct IS/OS disruption seen with patient 4, in patient 3 only a small lesion with hyperreflectivity changes at the fovea was evident on visit 1. On visit 2 an IS/OS disruption (size = 132 µm) was noted and early hyporeflective changes were also visible in patient 3.

During visit 1 for patient 2 we observed subtle reflectivity changes at the fovea. These reflectivity changes became more pronounced as seen from the tomograms generated during the second visit. Similarly patient 1 presented with slight IS/OS

discontinuities during visit 1, however a hyperreflective zone developed posterior

to the foveola. In both patient 1 and 2 there were no distinct IS/OS disruption.
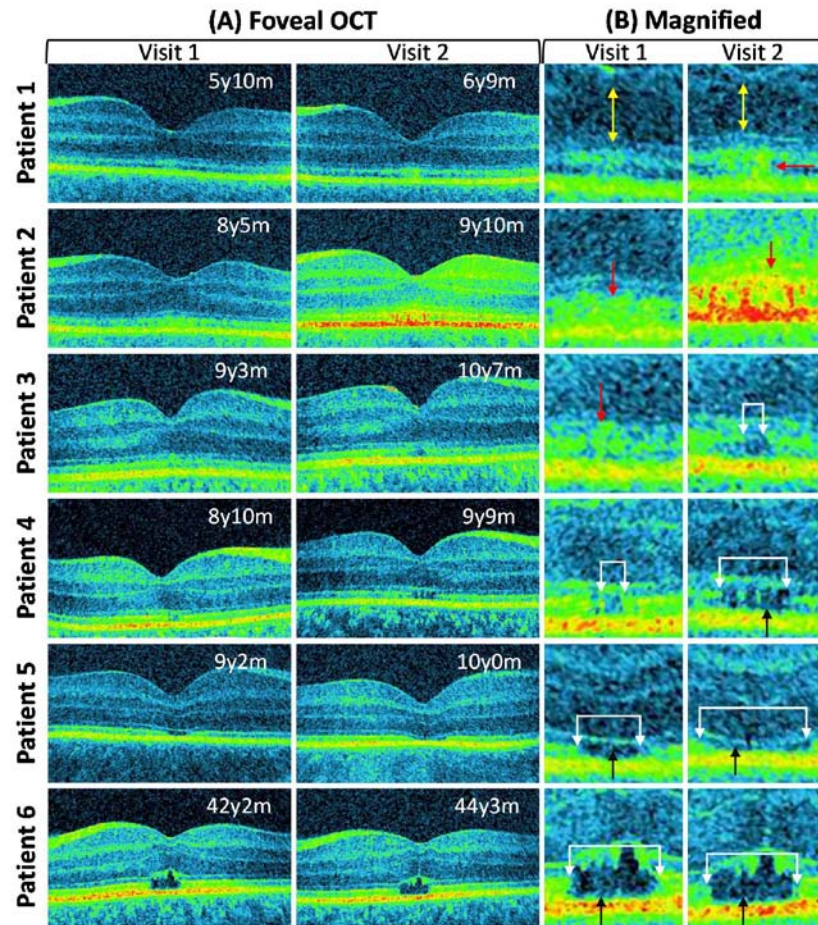
Figure 7.21: *Progressive retinal changes associated with achromatopsia. The foveal tomograms obtained during visit 1 and 2 are shown. In patients 1-5 the photoreceptor morphology changed from visit 1 to 2. These changes are shown in the magnified images. In patient 1 and 2 there was development of a hyper-reflective zone (shown by the red arrow). Patient 1 also showed outer nuclear thinning (yellow arrow). In patient 3 the hyperreflective region (red arrow) developed into a disrupted IS/OS junction (shown by the white arrows). In patient 4 the extent of the IS/OS disruption enlarged (white arrows) and a hyporeflective zone developed (black arrow). In patient 5 the extent of the hyporeflective zone and IS/OS disruption widened (white arrows). In patient 6 there was no difference in the extent of the IS/OS disruption or the hyporeflective zone (white arrows). The ages of the patients are shown on the top right side of the tomogram (y=year, m=months).*

Changes in Retinal Thickness Measurements

In addition to analysing the changes in the IS/OS junction disruption and reflectivity at the fovea we also performed CMT and ONL thickness measurements. Quantitative thickness measurements at the fovea showed that both the CMT and ONL thickness had changed in the younger patients (patient 1-5) between visit 1 and 2. However there was minimal variation in the thickness measurements for the older patients (patients 6-8) between visit 1 and 2. The difference plots showing the variation in both the ONL and CMT are shown in figure 7.22.
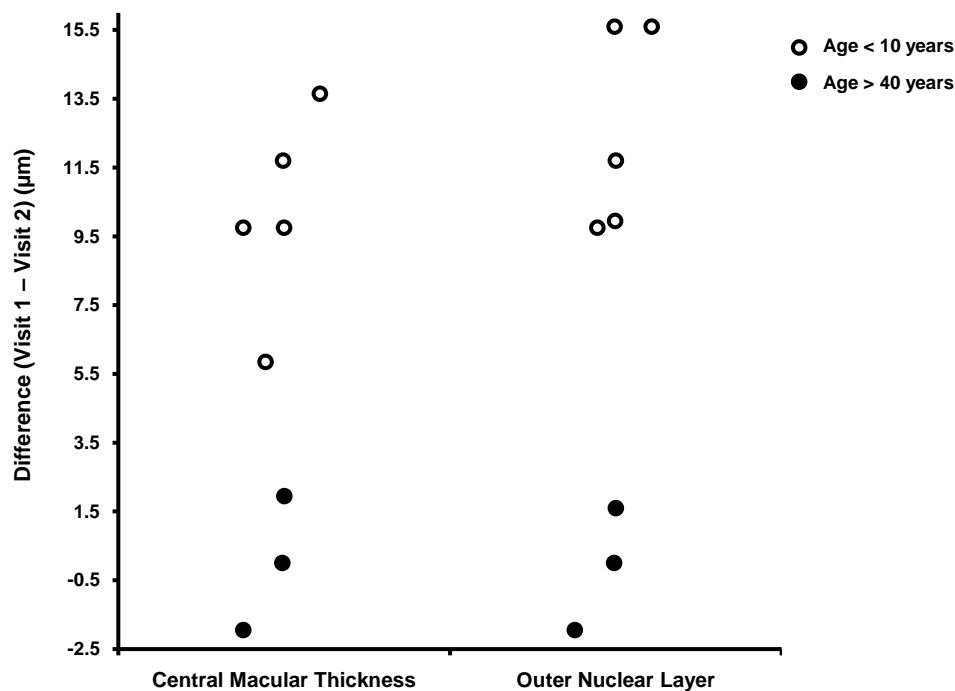
Figure 7.22: *The difference plots for the central macular and outer nuclear layer thickness measurements between visit 1 and visit 2. In the younger patients (age<10 years) there were larger changes in the measurements indicating a loss of photoreceptor cells. However in the older patients (age>40 years) the changes in thickness measurements were minimal.*
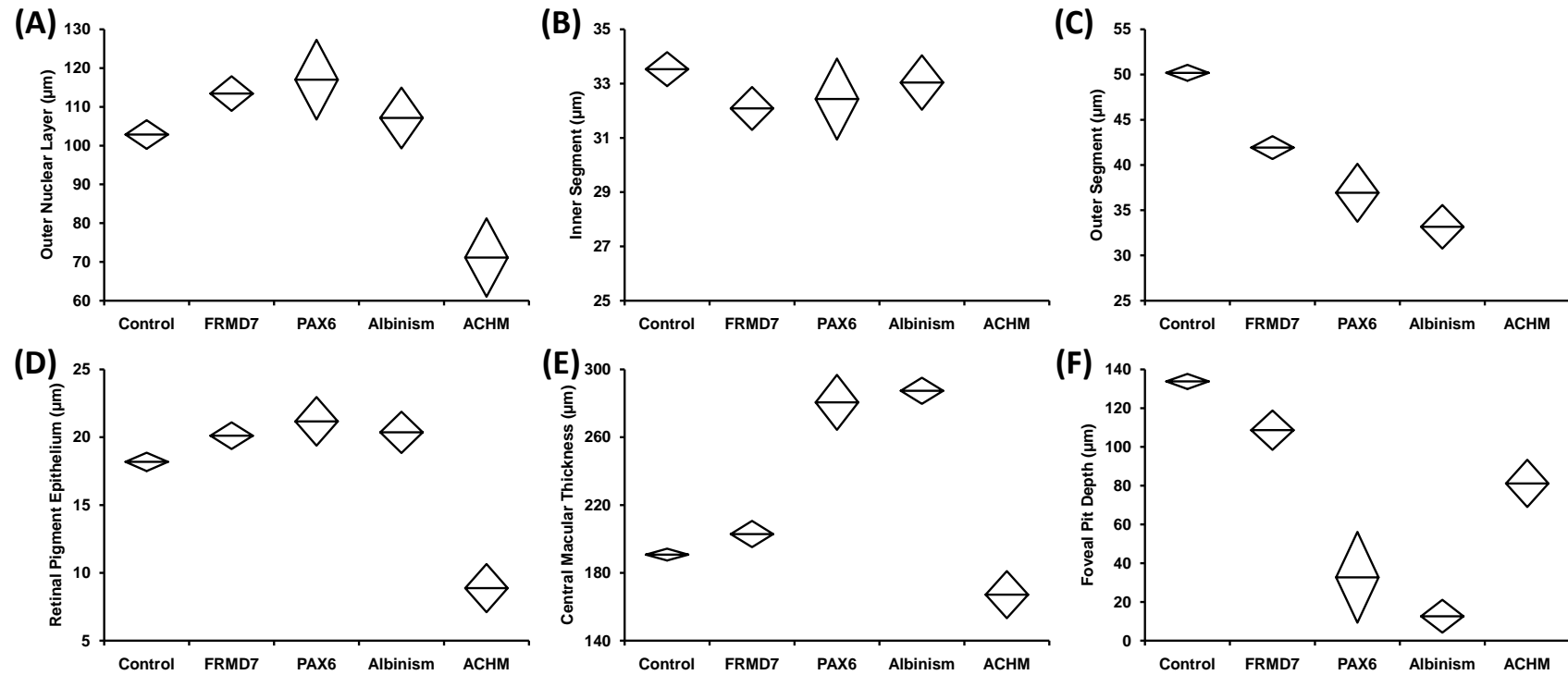
Figure 7.23: *Plots showing differences in foveal intra-retinal thickness measurements between controls and the patients (FRMD7, PAX6, albinism and achromatopsia (ACHM)). The measurements include: (A) outer nuclear layer, (B) inner segment, (C) outer segment, (D) retinal pigment epithelium, (E) central macular thickness and (F) foveal pit depth. The line bisecting the diamond plot represents the mean and the extent of the diamond plot represents the upper and lower 95% confidence intervals.*

229
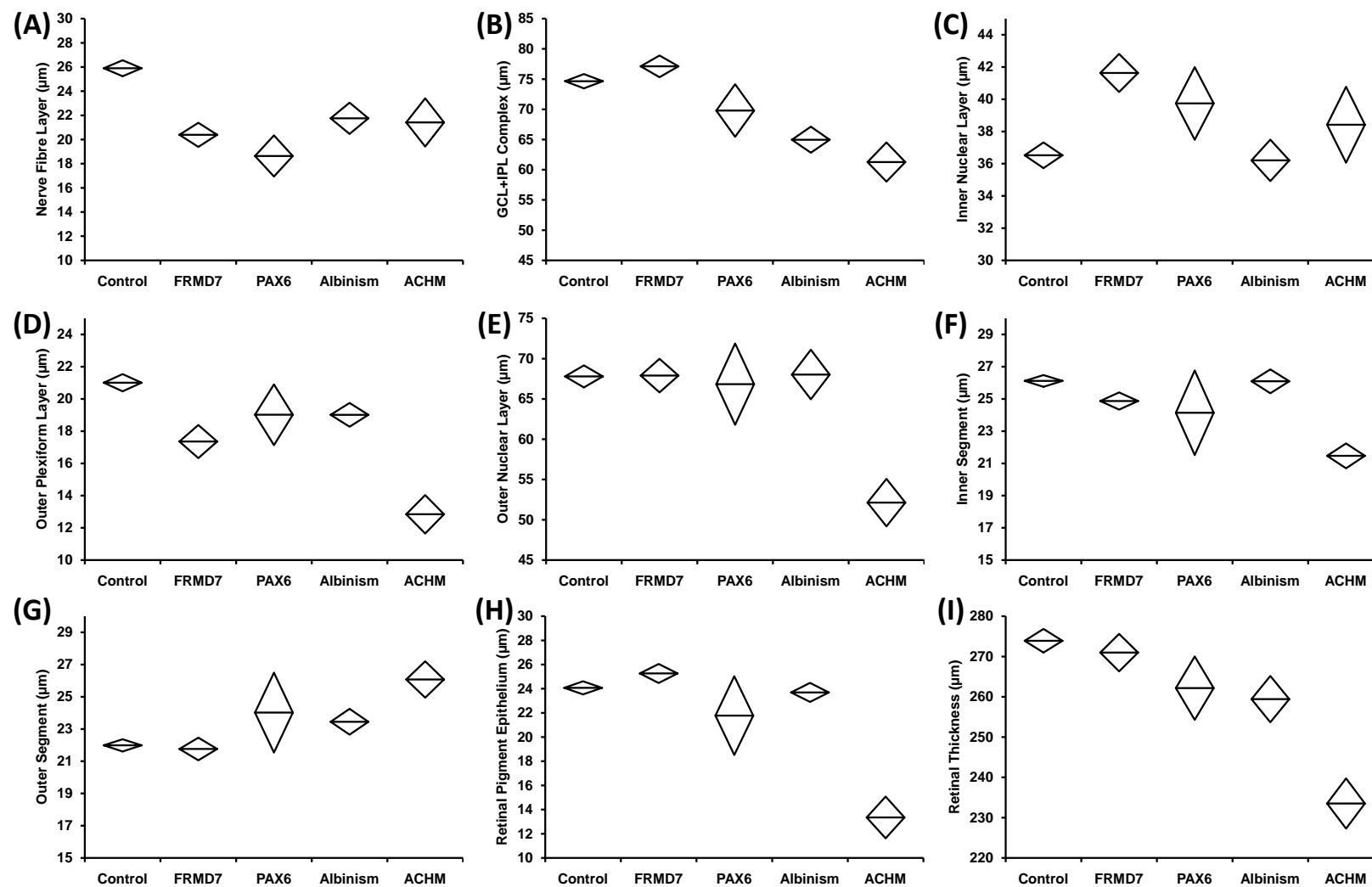
Figure 7.24: *Plots showing differences in parafoveal intra-retinal thickness measurements between controls and the patients (FRMD7, PAX6, albinism and achromatopsia (ACHM)). The measurements include: (A) nerve fibre layer, (B) ganglion cell layer and inner plexiform layer complex (GCL+IPL complex), (C) inner nuclear layer, (D) outer plexiform layer, (E) outer nuclear layer, (F) inner segment, (G) outer segment, (H) retinal pigment epithelium and (I) retinal thickness. The line bisecting the diamond plot represents the mean and the extent of the diamond plot represents the upper and lower 95% confidence intervals.*
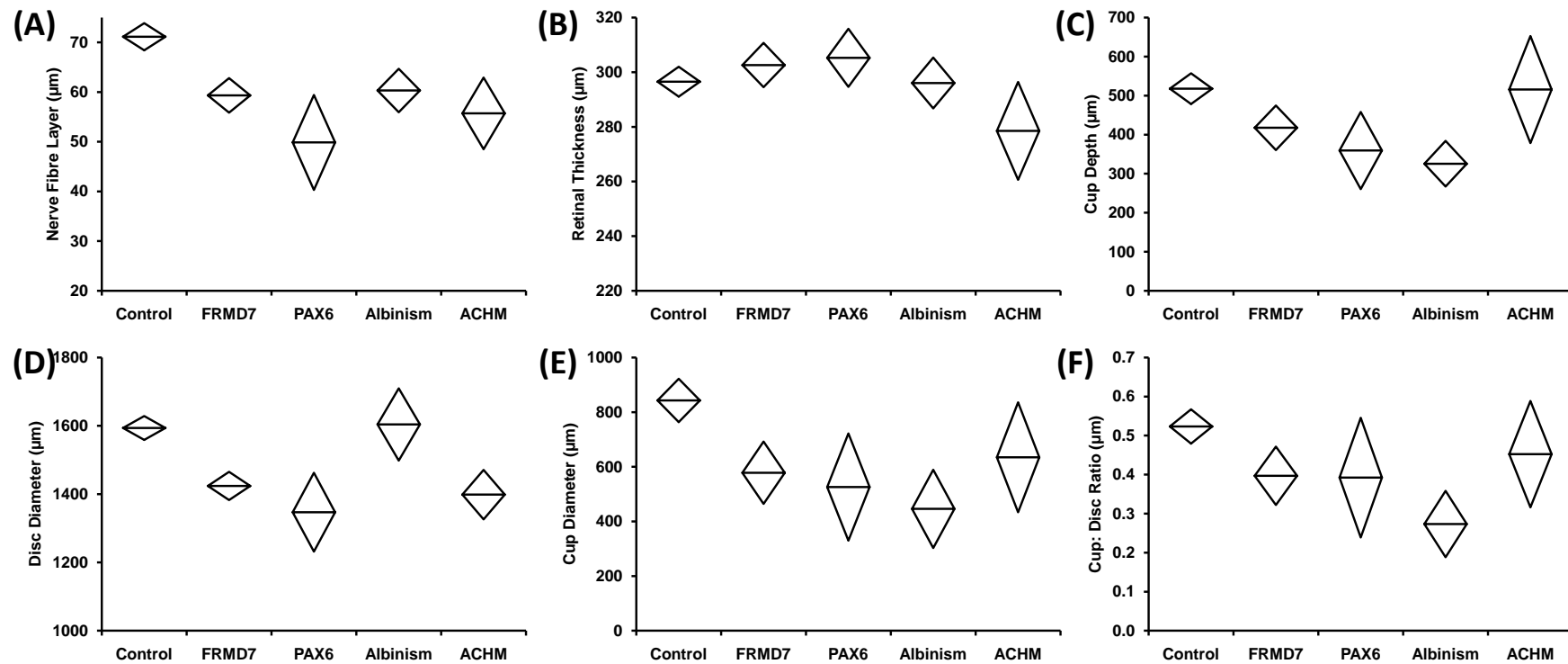
Figure 7.25: *Plots showing differences in optic disc measurements between controls and the patients (FRMD7, PAX6, albinism and achromatopsia (ACHM)). The measurements include: (A) peripapillary nerve fibre layer, (B) retinal thickness (C) cup depth (D) disc diameter, (E) cup diameter, (F) Cup:Disc ratio. The line bisecting the diamond plot represents the mean and the extent of the diamond plot represents the upper and lower 95% confidence intervals.*

7.3.6 EVIDENCE FOR ASYMMETRIC RETINAL DEVELOPMENT

7.3.6.1 PARAFOVEAL NERVE FIBRE LAYER

The nasal NFL was significantly decreased in all groups in comparison to controls. The temporal NFL was only decreased in the achromatopsia and FRMD7 group. These findings are reflected also in the NT-NFL ratio which is decreased in the PAX6 and albinism group, however the NT-NFL ratio is increased in the achromatopsia and FRMD7 groups.

7.3.6.2 PARAFOVEAL RETINAL THICKNESS

Both the nasal and temporal RT was significantly decreased in the PAX6 and achromatopsia groups in comparison to controls. However in the albinism group only the temporal RT is significantly decreased. In the FRMD7 group there are no significant differences in the both the nasal and temporal RT in comparison to controls. As a result the NT-RT ratio is significantly increased in the albinism group. However it is not significantly different in the other three groups when compared to controls.

7.3.6.3 PERIPAPILLARY NERVE FIBRE LAYER

The nasal NFL was significantly decreased in all groups in comparison to controls. Interestingly the temporal NFL was also decreased in all the groups except the albinism group. As a result the NT-NFL ratio in the albinism group is significantly decreased in comparison to controls. However in the achromatopsia group the NT-NFL ratio is significantly increased in comparison to controls.

These findings are summarised in table 7.16 and figure 7.26.

232

Table 7.16: The mean differences between controls and patients for nasal, temporal and nasal:temporal (NT) ratio for the following regions: (i) parafoveal nerve fibre layer, (ii) parafoveal retinal thickness and (iii) peripapillary nerve fibre layer. The significance values are shown below the mean differences.

Region / Diagnosis	Parafoveal Nerve Fibre Layer			Parafoveal Retinal Thickness			Peripapillary Nerve Fibre Layer		
	Nasal	Temporal*	NT ratio*	Nasal	Temporal	NT ratio	Nasal*	Temporal	NT ratio
FRMD7	8.51 (*p<0.0001*)	3.40 (*p<0.0001*)	-0.30 (*p=0.003*)	5.60 (*p=0.239*)	5.22 (*p=0.176*)	0.01 (*p=0.092*)	12.25 (*p=0.0002*)	12.19 (*p=0.0002*)	0.03 (*p=0.580*)
PAX6	15.75 (*p<0.0001*)	1.12 (*p=0.352*)	1.22 (*p<0.0001*)	22.14 (*p=0.013*)	17.12 (*p=0.006*)	0.05 (*p=0.155*)	19.55 (*p<0.0001*)	22.84 (*p<0.0001*)	-0.03 (*p=0.651*)
Albinism	8.83 (*p<0.0001*)	0.44 (*p=0.773*)	0.79 (*p<0.0001*)	9.67 (*p=0.614*)	25.79 (*p<0.0001*)	-0.07 (*p=0.0005*)	19.62 (*p<0.0001*)	1.92 (*p=0.619*)	0.23 (*p<0.0001*)
Achromatopsia	8.38 (*p=0.001*)	3.95 (*p<0.0001*)	-0.23 (*p=0.003*)	49.40 (*p<0.0001*)	40.13 (*p<0.0001*)	0.02 (*p=0.161*)	9.17 (*p=0.020*)	22.04 (*p<0.0001*)	-0.15 (*p=0.044*)

*In order to achieve normality the data was Log transformed. The results presented here are back-transformed.
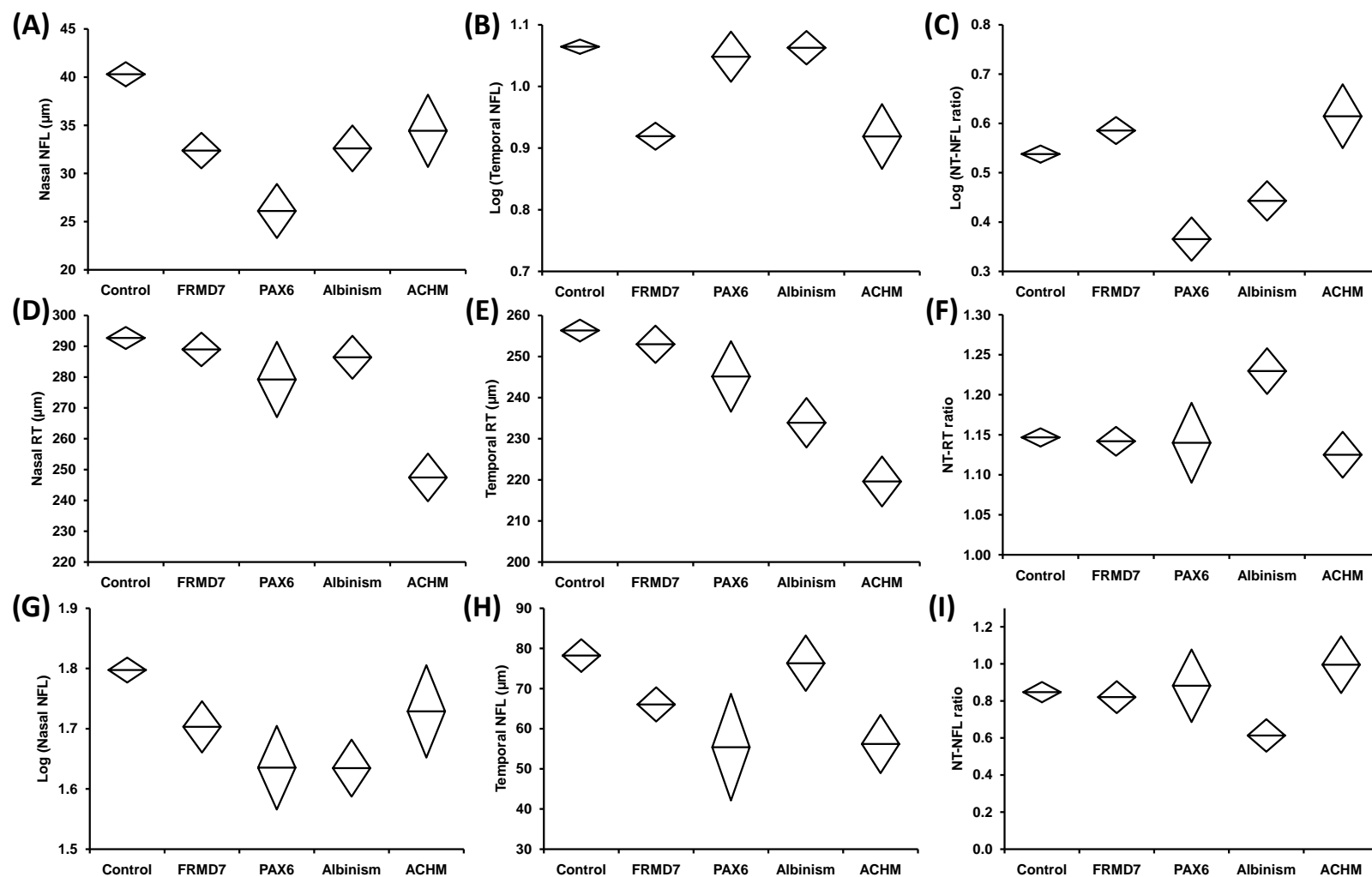
Figure 7.26: *Nasal and temporal differences in retinal nerve fibre layer and retinal thickness measurements. Parafoveal nerve fibre layer (NFL) and retinal thickness (RT) comparisons are show in (A-F). The peripapillary nerve fibre layer thickness comparisons are shown in (G-I). The ratio between nasal and temporal thicknesses (NT ratio) are shown in (C, F, I). Log transformation was performed in (B, C and G).*

7.4 DISCUSSION

7.4.1 SUMMARY OF RESULTS

Since there is some overlap in the retinal phenotypical characteristics between patients with *FRMD7* mutations, *PAX6* mutations and albinism this will be first discussed. Due to the unique findings associated with achromatopsia these will be discussed separately in relation to animal models. The summary of results is shown in table 7.17.

Table 7.17: Summary of foveal (A), parafoveal (B) and optic disc (C) measurements in patients with infantile nystagmus (FRMD7, PAX6, albinism and achromatopsia) in comparison to controls.

(A)

Diagnosis	FD	ONL	IS	OS	RPE	CMT
FRMD7	↓	↑	↓	↓	↑	↑
PAX6	↓	↑	↔	↓	↑	↑
Albinism	↓	↔	↔	↓	↑	↑
Achromatopsia	↓	↓	NA	NA	↓	↓

(B)

Diagnosis	NFL	GCL+IPL	INL	OPL	ONL	IS	OS	RPE	RT
FRMD7	↓	↑	↑	↓	↔	↓	↔	↔	↔
PAX6	↓	↓	↑	↓	↔	↔	↔	↔	↓
Albinism	↓	↓	↔	↓	↔	↔	↓	↔	↓
Achromatopsia	↓	↓	↔	↓	↓	↓	↑	↓	↓

(C)

Diagnosis	NFL	Cup Depth	Disc Diameter	Cup Diameter	C:D ratio	RT
FRMD7	↓	↓	↓	↓	↓	↔
PAX6	↓	↓	↓	↓	↓	↔
Albinism	↓	↓	↔	↓	↓	↔
Achromatopsia	↓	↔	↓	↔	↔	↔

↑ = Significantly increased compared to control
↓ = Significantly decreased compared to control
↔ = No significant difference compared to control
NA = Not applicable due to IS/OS disruption
Abbreviations: FD = foveal depth; ONL = Outer Nuclear Layer; IS = Inner Segment; OS = Outer Segment; RPE = Retinal Pigment Epithelium; CMT = Central Macular Thickness; NFL = Nerve Fibre Layer; GCL+IPL = Ganglion Cell Layer and Inner Plexiform Layer complex; OPL = Outer Plexiform Layer; C:D ratio = Cup to Disc ratio; RT = Retinal Thickness

7.4.2 FOVEAL HYPOPLASIA

It is well known that foveal hypoplasia can be associated with *PAX6* mutations and albinism. However IIN has been considered as a disorder without any afferent retinal abnormalities. This is the first study showing that foveal hypoplasia can be associated with *FRMD7* mutations. This is consistent with the extensive retinal expression we have observed in the earlier chapters. Taken together it suggests that *FRMD7* has an important role in retinal development and loss of function results in arrested retinal development. Therefore arrested or delayed retinal development could be a common aetiological factor in the development of infantile nystagmus.

The common signs of foveal hypoplasia seen in patients with *FRMD7* mutations, *PAX6* mutations and albinism include: (1) shallower foveal pit, (2) continuation of inner retinal layers posterior to the foveola, (3) increased CMT, (4) decreased OS thickness and (5) increased RPE thickness. We suspect the latter two signs are related to the cone photoreceptor specialisation.

7.4.2.1 FOVEAL PIT FORMATION

During foveal pit formation there is extrusion of the inner retinal layers posterior to the foveola as the foveal pit deepens. This results in a decrease in the CMT. Therefore the first three findings are inter-related and the shallower foveal pit has arisen as a result of lack of centrifugal migration of the inner retinal layers. Moreover, the persistence of inner retinal cells at the fovea has also caused an increase in the CMT compared to controls.

It is interesting to note that mutations of *PAX6* and the albinism genes can manifest with both a rudimentary foveal pit as well as foveal plana (no discernable foveal pit). However the foveal hypoplasia associated with mutations of *FRMD7* is more subtle and in all cases a rudimentary pit was present. This may also explain why the visual acuity associated with *FRMD7* mutations is better in comparison to albinism (234). There are a number of theories regarding the development of the foveal pit which ranges from active movement of inner retinal cells (235) to apoptosis of inner retinal cells (236). However since there is a lack of mitotic figures within the central retina after foetal week 14 it suggests that apoptosis is unlikely to play a role in the normal formation of the foveal pit (13). Springer and Hendrickson showed using a mathematical model that pit formation is likely to be a passive phenomenon which is dependent on the differential elasticity between the future foveal and peripheral retinal tissue (13). The future foveal tissue has increased elasticity in comparison to the surrounding tissue due to the avascular zone (AZ). Subsequently due to mechanical effects of intraocular pressure and retinal stretch during development, the malleable AZ forms a foveal pit (13). Indeed studies looking at the distribution of retinal vasculature in albinism have shown that the foveal avascular zone is perturbed (237-239) and we have also shown an example of a large noncilioretinal vessels that traverses through the putative foveal region (figure 7.14). Similarly using fluorescein angiography in a case of isolated foveal hypoplasia McGuire et al. demonstrated that the foveal avascular zone was disrupted (240). It has also been suggested that abnormal retinal

vasculature could also form as a result of *PAX6* mutations and this has been identified in patients with aniridia (146,198). Although we have not systematically analysed the retinal vasculature in the three groups of patients, previous literature and mathematical models suggest that a common mechanism related to abnormal retinal angiogenesis might be responsible for the retarded pit formation. Further imaging studies would be useful to: (1) confirm whether this could be a common link for the shallow/absent foveal pit and (2) test whether the degree of foveal AZ disruption is related to foveal pit depth. If the hypothesis proposed by Springer and Hendrickson were accurate then we would expect the foveal AZ disruption to be less severe in patients with *FRMD7* mutations in comparison to *PAX6* mutations and albinism. Or alternately a difference in the intraocular pressure/retinal stretch during development might explain the variable pit sizes observed between these groups.

7.4.2.2 OUTER NUCLEAR LAYER CHANGES

We find that the ONL thickness is increased in patients with *PAX6* and *FRMD7* mutations in comparison to controls. However in the patients with albinism there was no significant difference in the ONL compared to controls. This observation is novel and could be explained based on the developmental events that occur at the fovea. Previous histological studies have shown that there is a steady rise in the ONL thickness between 150 days post conception (dpc) up to 360 dpc, however between 360dpc -1500 dpc there is a decrease in the ONL thickness. At 1500 dpc the ONL thickness is decreased to the same amount of thickness as observed at 240dpc (241). Thus if the developmental

arrest occurs between 240dpc – 360dpc it could explain why the ONL thickness is increased. By 240 dpc the foveal avascular zone is already defined and an immature foveal pit should be formed (241,242). Hence the increased ONL thickness should be predominantly seen in patients with a rudimentary pit and not in cases of foveal plana. In retinopathy of prematurity (ROP) the foveal hypoplasia is subtle (i.e. a rudimentary pit is present in most cases), a previous OCT study in ROP found that the ONL thickness in ROP patients was increased in comparison to controls, however its significance was unclear (243). This hypothesis can be tested by grouping patients based on retinal developmental events (for e.g. patients with a foveal pit versus patients without a foveal pit).

The other possibility of why the ONL thickness is increased is possibly due to aberrant Henle fibres or disease specific effects to the outer nuclear layer. In the mature fovea the base of the pit is formed by the oblique Henle fibres (13,244), if orientations of the fibres are altered it could also appear in the OCT as an increase in the foveal ONL thickness. FRMD7 knockdown assays are associated with an increase in cell numbers and decrease in neurite length (86). Previously we showed that at carnegie stage 15 there was strong hybridisation signals from the outer neuroblastic layer (chapter 4). Studies into the timing and sequence of retinal cell genesis have shown that there are two phases of cell generation. The first sets of cells produced are: retinal ganglion cells, horizontal cells and cone photoreceptors (Phase1), after a gap the remaining cells are produced (Phase 2) (201,245,246). Carnegie stage 15 occurs within phase 1 of retinal cell generation (247). Similarly *PAX6*

expression is seen during phase 1, as ganglion and cone photoreceptor precursor cells undergo postmitotic differentiation (247-251). Electrophysiological studies in patients with *PAX6* mutations have shown that based on the genotype there are abnormalities in ERG responses suggestive of abnormal photoreceptor function (199,252). Hence it is possible that the morphology of the foveal ONL layer is altered in patients with *FRMD7* and *PAX6* mutations thus we observe the phenotypic differences on OCT studies. Previous studies have suggested that ERG findings in patients with *FRMD7* mutations are normal; in our cohort of patients also the ERG findings were normal. However, the ERGs currently performed represents the global retinal responses, thus it may explain why we are not observing focal abnormalities. It would be useful to evaluate the ERG responses within the central 5-10° using multifocal ERG in all three groups of patients (*FRMD7*, *PAX6* and albinism). This would provide evidence of how the morphological abnormalities correlate to the physiological/functional status of the cones.

7.4.2.3 CONE PHOTORECEPTOR SPECIALISATION

We find that there is decreased foveal OS length and increased RPE thickness in all three groups of patients (FRMD7, PAX6 and albinism). Previous histological studies have shown that the cone OS at the foveola in adults have a length of 50-65μm (7,246). In our control cohort we found that the mean OS length at the fovea was 50 μm. However in the FRMD7, PAX6 and albinism cohorts the mean OS lengths were 42, 37 and 33μm respectively. The shorter OS suggests that cone specialisation has not occurred to a full extent and the foveal photoreceptors in the three cohorts represent immature cones. This

finding of shortened OS length at the fovea has been previously reported with albinism (224,227); however we report this for the first time associated with *FRMD7* and *PAX6* mutations. Fulton et al. reported that the central cone density was significantly decreased after performing post-mortem analysis in a case with albinism (253). A multifocal ERG study by Kelly and Weiss reported that in albinism the responses representing cone function were reduced in amplitude within the central 5°. They suggested that the reduced ERG amplitudes represented a decrease in foveal cone density (254), thus cone packing is not optimal in albinism. Using adaptive optics, McAllister et al. also showed that the cone density was abnormal at the fovea in patients with albinism. However there was considerable variability in the cone density among different albino patients (227).

The variability in the cone OS length between the three different disorders (FRMD7>PAX6>Albinism) might be related to the timing at which the developmental arrest has occurred, or disease specific effects associated with different gene mutations. Since the OS length increases with age (7), the earlier the developmental arrest the shorter the OS. Hence as seen with foveal pit formation and ONL changes, it is possible that the developmental arrest associated with *FRMD7* and *PAX6* mutations occurs at a later time point in comparison to albinism. Immunocytochemistry studies of PAX6 localisation in chicken retina did not find any staining of the cone OS (255). Therefore PAX6 effects on OS development may be indirect through an interacting protein. Previous studies have shown an overlap in expression patterns and phenotype between *PAX6* and *OTX2* (256,257). Conditional

knockout of *OTX2* prevented photoreceptor differentiation and OS development (258) . Data from co-expression database (http://coxpresdb.jp/) also shows that as the expression of *OTX2* and *PAX6* are related and specific to the retina. Thus the interaction between OTX2 and PAX6 may explain the altered OS morphology observed with *PAX6* mutations.

The increase in RPE thickness in all three groups is also related to the immature foveal cones as described in the previous paragraph. In the normal foveal OCT the increase in OS length not only extends in the anterior direction but also there is an indentation within the RPE layer (see figure 7.1). There is loss of the indentation in the RPE layer in all three disorders. This occurs because the first RPE signal represents the COST/RPE microvilli complex. Hence if there are immature foveal cones this signal would be anterior compared to a fovea which contains only highly specialised cones that have attained full OS length. An additional possibility is that the rod free zone is disrupted and hence the RPE thickness at the fovea is comparable to the control parafoveal RPE thicknesses. Previous histological studies in albinism have reported that there is a lack of a rod free zone (253,259), so this is also a plausible explanation for the changes observed. In albino mice it has also been shown that the RPE cells have polyploidal features with large and fragmented nuclei (260). These morphological changes in the RPE cells may explain the difference in RPE morphology in albinos. It has also been suggested that the lack of melanin might be responsible for the RPE changes (261). However the findings observed are not only seen in albinos but also in patients with *FRMD7* and *PAX6* mutations. Furthermore the RPE changes

observed are confined to the fovea. However due to lack of histological studies in cases of *FRMD7* and *PAX6* mutations it is not possible to say whether rod free zone is disrupted or the RPE morphology is altered. With the advent of adaptive optics or *en-face* imaging it might be possible to resolve this question.

7.4.3 PARAFOVEAL ABNORMALITIES

In patients with *FRMD7* mutations, *PAX6* mutations and albinism, we find a significantly decreased thickness of the NFL in comparison to controls. Optic nerve hypoplasia has previously been described in albinism (239) and associated with *PAX6* mutations/aniridia (146,262). However this has not been previously documented using OCT and we also report it for the first time in patients with *FRMD7* mutations. By measuring the parafoveal and peripapillary NFL thicknesses we have been able to show that there is significant reduction in this layers thickness. Consistent with these findings we see that in the PAX6 and albinism groups the GCL+IPL complex is also significantly reduced. However interestingly in the FRMD7 group we find an increased thickness for the GCL+IPL complex. This suggests that different mechanisms could exist in the development of such variable laminar structure.

Histological analysis in a 20 week old aborted foetus diagnosed with OCA revealed decreased ganglion cell numbers and an "immature" NFL. In albino animals, an abnormal distribution (263) and reduction of cells (264) within the GCL was noted when compared to pigmented animals. However for INL and ONL there were no differences in cell density between albino and

pigmented mammals (263). In this study we also see similar translaminar deficits (i.e. decreased GCL+IPL, however no change in INL & ONL) in patients with albinism.

In PAX6 expression studies the most intense staining from the GCL has been observed during development (255,265). One of the critical genes required for retinal ganglion cell formation is *Math5*. The retinal ganglion cells and optic nerves failed to form in *Math5* mutant mice (266). It has also been shown that Math5 plays an important role in differentiation of progenitor cells into a stable population of RGC's (266,267). Recently it has been shown that PAX6 is not only important in initiation of the *Math5* mRNA expression but also PAX6 binds to the *Math5* retinal enhancer site to increase its expression (268). Moreover in *Pax6* KO mice, there was failure of initiation of *Math5* expression (269). Thus in mutations of *PAX6* leading to haploinsufficiency, as seen with our patients, one would expect Math5 downregulation, with subsequent effects on RGC development and competence.

In both albinism and PAX6 patients a decrease in the ganglion cell density could be responsible for the decrease in the NFL thickness. However, for FRMD7 patients a different mechanism could be responsible for the NFL thinning since there is an increase in GCL+IPL complex. In the post natal mice and rat retina we found immunostaining within most retinal layers, with the exception of the ONL (chapter 5). If we consider the results from the knockdown assays (86) and apply it to the retinal cell types showing expression, it could explain the parafoveal changes observed in patients with

FRMD7 mutations. The knockdown assays in Neuro2A cells showed an average reduction of neurite length and an increase in cell numbers (86). Therefore, the increases in GCL and INL thickness and the reduction in RNFL and OPL are likely to be as a result of loss of function of FRMD7. Jensen et al. identified the *moe* gene in zebrafish which encodes for a FERM protein, they showed that FERM motif is important in ensuring cell polarity and retinal lamination (270,271). Similarly the Moe protein cooperates with the CRB1 protein to ensure process of retinal lamination occurs correctly (270). Jacobson et al. performed an OCT study in patients with *CRB1* mutations and found that the retinal lamination was abnormal and that the retina was thicker in the parafoveal regions (272). Although we did not observe any retinal degeneration as seen with the *CRB1* mutations, the parafoveal morphology observed could be one which represents an immature lamination pattern as a result of lack of the normal developmental apoptosis. Moreover, defective arborisation within the retinal laminar structure could explain the thinning of the plexiform/axonal layers. Hence we do not observe an overall increase in parafoveal retinal thickness.

In patients with *PAX6* mutations we find an increase in the INL thickness. The INL consists of bipolar cells, amacrine cells and horizontal cells. As we have discussed previously, conditional inactivation of *PAX6* results in down regulation of a number of proneural genes (including *Math5* – hence the decrease in GCL thickness). However one proneural gene that was unaffected was *NeuroD*, which showed high levels of expression in spite of the PAX6 knockout (269). Interestingly, Morrow et al. showed that NeuroD promotes

245

amacrine cell genesis and differentiation (273). The retinal progenitor cells thus have a biased cell fate towards amacrine cell interneurons. Therefore an increase in INL in patients with *PAX6* mutations could be related to an increase in amacrine cells as a result of up regulation of *NeuroD* expression.

7.4.4 OPTIC NERVE HEAD ABNORMALITIES

In patients with *FRMD7* and *PAX6* mutations we find a significantly reduced peripapillary NFL, cup depth, disc diameter, cup diameter and cup:disc ratio in comparisons to controls. In albinism also we observe similar findings however interestingly the disc diameter is not significantly different from the controls.

The reduction in size of the peripapillary NFL mirrors the results observed with the parafoveal NFL. Therefore this could be attributed to either the reduction in GCL or decreased length of neurites (as previously discussed). Therefore it is plausible that a reduction in the optic nerve axons from the papillomacular nerve fibre bundle could also result in a decrease in the disc diameter. A unique finding confined to the albino group is the decreased NT ratio for the peripapillary NFL. This resulted from a significantly decreased nasal NFL while the temporal NFL was not significantly decreased. This has not been previously described and could also form the basis of the asymmetric VEP's detected in albinism patients. However we do not see a decrease in disc diameter in albinism. Based on ophthalmoscopic findings Schatz and Pollock showed that the albino optic disc diameter was smaller and there was an absence of a physiological optic cup (274). The reason we were not able to corroborate the ophthalmoscopic findings could be due to a

difference in the imaging modality. One of the limitations of this study was that we did not determine the mutations and genes involved in the albino cohort. The genotypic heterogeneity within the albino cohort could be the alternate reason we do not observe the significant difference in the optic disc diameter compared to controls. It is possible that allelic variation arising from mutations of certain albino genes predispose to alterations in disc diameter while others do not. This is also reflected in the literature where MRI studies have shown conflicting evidence regarding whether there is a significant reduction in optic nerve size (275,276). Thus genotypic stratification based on mutation type and genes involved would help establish the cause of the phenotypic heterogeneity. Another explanation is the current setup for disc diameter measurements are restricted in the horizontal direction. Therefore it is possible that this imaging setup does not capture all possible disc changes (for instance an alteration to the vertical disc diameter would be missed).

Previous studies in both albinism and aniridia have identified optic nerve hypoplasia clinically. A literature survey shows only one published OCT study in albinism which describes abnormal optic nerve head morphology (113). McCulley et al. identified that approximately 10% of patients with aniridia have optic nerve hypoplasia (262). Azuma et al. identified unique *PAX6* mutations associated with optic nerve malformations. They suggested that the regulatory circuit between PAX6 and PAX2 is likely to be responsible for the variety of optic nerve malformations ranging from coloboma to optic nerve hypoplasia (145). We identified the one family (P2) with *PAX6*

mutation resulting in the amino acid variation R208W with the phenotype of optic disc coloboma. The R208W variation has previously been identified by Hanson et al. and the predominant phenotype reported was aniridia (140). However interestingly in this family we did not detect any aniridia although we identified trans-illumination defects of the iris in addition to the optic disc coloboma.

The decrease in optic cup depth, cup diameter and cup to disc ratio is likely to be related to the hypoplastic peripapillary NFL and possible local miswiring. Netrin-1 has been identified as an axon-guidance molecule and has a role in the normal formation of the optic disc. Knockout mouse studies in Netrin-1 results in pathfinding errors at the level of the optic disc and optic nerve hypoplasia (277). In addition the mice also exhibited agenesis of the corpus callosum and mis-wiring at other brain centres (278). Furthermore, Netrin-1 belongs to the Semaphorin family of axon guidance molecules and is co-expressed with Sema5A within this region (279,280). Toyofuku et al. have shown that FARP2 also mediates its function by signalling a member of the semaphorin family and thus ensuring axonal guidance. Interestingly the FERM domain in FARP2 is also an essential part of triggering the signals for Sema-3A (88). Based on sequence homology to FARP2, it is possible that FRMD7 also has a role in pathfinding of RGCs. The mis-wiring at the level of the optic disc could be responsible for the decreased cup depth, cup diameter and cup to disc ratio. Whether FRMD7 also mediates its function by signalling members of the semaphorin family would need to be further investigated.

Although there is no evidence to suggest that patients with *PAX6* mutations might have axon guidance defects at the level of the retina or the optic disc. Evidence from *PAX6* knockout mouse models has identified axon pathfinding defects in the brain (200). Furthermore based the in situ expression results high resolution MRI studies were performed in patients with *PAX6* mutations which showed interhemispheric brain anomalies (143,281). Thus if similar pathfinding errors occur at the optic disc and retina it would help explain the retinal phenotypes seen. In albinism there is a decrease in the number of RGC axons that project ipsilaterally. On the other hand there is excessive crossing of retinofugal fibres at the optic chiasma. This forms the basis of the asymmetric visually evoked potentials detected in albinism (115). Thus the elevated optic nerve head/decreased optic cup depth seen in albinism could represent axons from the temporal retina destined to cross to the contralateral hemisphere at the optic chiasma. This is consistent with the changes we observe for the peripapillary NFL thickness measurements. We find that in albinism there is no reduction in the temporal peripapillary NFL thickness, however there is a significant reduction in the nasal peripapillary NFL. This is further reflected by the nasotemporal ratio for peripapillary NFL which is only decreased in albinism and no other disorder. In patients with *PAX6* mutations and *FRMD7* mutations we do not find any significant difference in NT ratio for peripapillary NFL when compared to controls.

7.4.5 ADDITIONAL OCULAR PHENOTYPES ASSOCIATED WITH PAX6 MUTATIONS

In our cohort of patients with *PAX6* mutations we only identified one family with aniridia. This may be due to type of clinic where mainly nystagmus patients with unclear diagnosis are referred and possibly less patients with aniridia since diagnosis is more obvious. The remaining families had a range of iridial phenotypes from sectorial hypoplasia to subtle iris transillumination defects. Detecting iris transillumination defects normally points towards a diagnosis of albinism, however here we also show that it could be part of the spectrum of iridial phenotypes encountered with *PAX6* mutations. Gronskov et al. developed a classification system for iris phenotypes for patients with *PAX6* mutations. They divided the phenotypes ranging from stromal hypoplasia to complete aniridia (147). However they did not identify any cases of iris transillumination defects hence it was not included in their classification system. Similarly Hingorani et al. also examined a large cohort of patients with *PAX6* mutations (n=43); however they did not detect any patients with iris transillumination defects (146). We suspect that the transillumination defects represent a milder phenotype in comparison to the stromal hypoplasia. It is possible also to distinguish these phenotypes based on anterior segment OCT, which will be a useful imaging modality in classifying the degree of iris involvement.

It is not clear whether the foveal phenotypes correlate to the iris phenotypes and/or the genotypes. Hingorani et al. suggested that missense mutations within the paired domain resulted in milder phenotypes and less incidence of foveal hypoplasia. Furthermore, they also suggested that the C-terminal

extension mutations were associated with severe anomalies such as exudative retinopathy. They also predicted that phenotype resulting from C-terminal extension mutation is similar to loss of function mutations (such as nonsense mutations) (146). In our cohort, family P5 had a C-terminal extension mutation. Although this family had fovea plana (figure 7.10) we did not identify any signs of an exudative retinopathy as described by Hingorani et al. This could be because it was a novel anti-termination mutation and hence could have variable effects to what has previously been described. It has also been shown that nonsense mediated decay surveillance is unlikely to detect such mutations and thus would allow translation of a larger polypeptide (282). We have shown the degenerative changes that can be encountered as a result of the *PAX6* mutation. This was however seen only in one case with a missense mutation rather than a C-terminal extension mutation.

7.4.3 ACHROMATOPSIA

7.4.3.1 FOVEAL FINDINGS

Herein for the first time a hyporeflective sign detectable on OCT is reported that may aid in the diagnosis of achromatopsia. The other novel findings in the achromatopsia cohort include thinning of the ONL, disruption of the COST reflectivity, and foveal maldevelopment. Also described for the first time are the relationship of age to ONL thickness and the presence of the HRZ. The findings of the previous 2 studies are corroborated (137,230), showing disruption of IS/OS junction. However, this study found that IS/OS junction disruption is not confined only to the fovea; rather, it also can be seen in the

parafoveal regions. Contrary to the findings of Barthelmes et al. (137) a significant reduction in RT was found, which is consistent with the report from Varsanyi et al. (230) .

The most striking finding in the present study was the presence of an HRZ located in the foveal region occupying an area where cone photoreceptor density is maximal. The HRZ occupied mostly the nasal part of the fovea compared with the temporal part of the fovea; this was seen consistently in all patients with the HRZ zone. This could be attributed to the asymmetric distribution of cone photoreceptors (244,283,284). Based on the longitudinal case studies we see that prior to the formation of the HRZ, the outer segment region becomes hyper-reflective which could be an indication of the dynamic degenerative processes that the retina is undergoing in this disorder.

The key to interpreting a number of findings in this study is related to the thinning of the ONL in the achromats. This is consistent with previous histopathologic reports in patients with achromatopsia in which thinning of the ONL was shown (285,286). It is suspected that the HRZ arises either because of cone OS autolysis or because of progressive extrusion of the nuclei from the ONL into the photoreceptor layer, therefore resulting in both thinning of the ONL and subsequent HRZ. Both ONL thinning and the presence of the HRZ are age dependent phenomena, which is an indication of the progressive nature of this disorder. Mouse models have shown progressive nuclear extrusion and ectopic localization of nuclei into the photoreceptor layer (287). Chang et al. (288) reported a progressive thinning of the ONL in GNAT2 knockout mouse models. Two further studies also

showed a progressive loss of cone photoreceptors with age in *CNGA3* knockout mouse models (289,290). Canine models exhibiting mutations for *CNGB3* showed that cone ERG function is intact in young pups, but becomes undetectable in mature dogs (291). Because of the afoveate retina in the canine model, it is not directly comparable with human achromatopsia; however, progressive reduction of ERG function gives additional support that achromatopsia associated with mutations in *CNGB3* represents a progressive disorder. Thiadens et al. (133) showed that regardless of the genetic cause, there was progression of cone dysfunction (progressive ERG changes were seen in 9% to 13% of patients with *CNGB3* mutations), worsening macular appearance, and deterioration of visual acuity. In light of these animal models, phenotypic studies in humans, and the findings in the present study, it is highly suggestive that achromatopsia represents a progressive retinal disorder (132,133).

Ten of 14 patients showed continuation of the OPL and IPL posterior to the foveola. This is one of the hallmarks of foveal hypoplasia, because it has been described in conditions such as albinism (227). However, this has been described as foveal maldevelopment (or atypical foveal hypoplasia) because in achromatopsia, it is associated with other atypical findings, such as reduction in retinal thickness, disruption of the IS/OS junction, and ONL thinning. The paradoxical reduction in RT is the result of ONL thinning. Hence, the actual foveal depth (P0 –P1) was measured, which was significantly reduced in achromats when compared with controls. During foveal pit formation, there is centrifugal displacement of the inner retinal

253

layers away from the location of the incipient fovea (244). It seems that this process has occurred only to a partial extent; hence, there is continuation of the plexiform layers posterior to the foveola. These findings are not reflected in animal models because they are afoveate.

The progressive nature of this disorder raises interesting questions regarding both pathogenesis and treatment. Disruption of the IS/OS junction was seen in all patients, which was more discontinuous and subtle in the younger patients, whereas the disruption was more discrete and confined to the location of the HRZ in the older patients. This suggests that the initial changes occur at the IS/OS junction, which becomes completely disrupted with time, and hence is linked to the appearance of the HRZ. Similarly, complete loss of cone function also is demonstrated by an alteration to the COST reflectivity, which can be resolved only on UHR OCT (231). The spectrum of morphologic changes suggests that it is likely that gene therapy would be most effective in patients at a younger age.

Foveal maldevelopment and progressive cone degeneration are likely to represent 2 phenomena. There is a critical developmental window for ensuring the normal foveal architecture (from approximately foetal week 25 to 15 months of age) (7,244). If cone degeneration is marked before or during this period, it may explain the arrested development of the incipient fovea. In addition, age dependent loss of ONL, presence of HRZ, IS/OS disruption, and COST disruption are likely to be manifestations of the apoptotic cascade in cones.

Previously Varsanyi et al. reported a decrease in parafoveal thickness in achromats (n=8) compared to controls however they were not able to segment and identify the layers that are likely to be affected (230). Similarly in oligocone trichromacy Andersen et al. also described a decreased parafoveal and perifoveal retinal thickness in comparison to controls (292). We have also seen significant reduction in parafoveal RT in comparison to controls. Furthermore this reduction in parafoveal retinal thickness is due to a significant decrease in NFL, GCL+IPL complex, OPL and ONL in comparison to controls. Similarly the peripapillary NFL was also consistently reduced in thickness. These findings suggest that the cone photoreceptor loss is not only confined to the foveal cones but it is more widespread and includes parafoveal cones. However we do not observe hyporeflective zones in the parafoveal region. This is possibly due to the decreased cone photoreceptor density as well as an increase in rod photoreceptors density. In the parafoveal region the rod photoreceptors also contribute to the IS/OS junction signal in addition to the outer segment tip signals (231). Since the rods are unaffected in this disorder the IS/OS signal remains intact. The loss of the parafoveal cone photoreceptors would explain the reduction in the ONL layer thickness. It is plausible that this could have a knock on effect to the inner retinal layers resulting in a loss of ganglion cells and NFL. Moreover, in *CNGB3*$^{-/-}$ mice mislocalisation of cone opsins to the outer nuclear layer and outer plexiform layers have been reported. Michalakis et al. report that in *CNGA3*$^{-/-}$ mice there is impaired migration of cone somata which results in aberrant localisation within the outer plexiform layer (289).

This could explain the decreased thickness/reflectivity observed in the plexiform layer. In *CNGA3-/- Rho-/-* double mutant mice degenerative changes within the IPL have been described (293). Interestingly the INL is not significantly different between achromats and controls. Haverkamp et al. have shown that the cone bipolar cells in the *CNGA3-/-* mutant mice do not always undergo degeneration since they sometimes form ectopic synapses with rods (294). Similar findings of ectopic synapse formation have also been described in *CNGA3-/-* and *Rho-/-* single knockout but not double knock out (293). This form of synaptic plasticity could help explain why we did not find a decrease in the INL thickness.

7.4.3.2 EARLY SIGNS OF PROGRESSIVE CONE PHOTORECEPTOR DEGENERATION

This is the first study showing progressive temporal retinal changes in patients with achromatopsia. By performing longitudinal studies in children with achromatopsia we show for the first time the development of the hyporeflective zone. In addition we also describe an interesting OCT sign, the hyperreflective zone, which appears to be a precursor to the development of the hyporeflective zone. To our knowledge, this transition phase of increased reflectivity of the foveal cone outer segments has not previously been described. Other signs that indicate the progressive retinal changes in the younger patients included an increase in the size of both the IS/OS disruption and hyporeflective zone. Furthermore quantitative changes such as outer nuclear layer thinning and reduction in central macular thickness also provide evidence towards cone photoreceptor death over time. These

256

dynamic changes were confined to the younger patients and were not seen in the older patients.

Interestingly the hyporeflective zone has not only been observed with achromatopsia but has also been described in patients with solar maculopathy, occult macular dystrophy, *KCNV2* mutations and Stargardt disease. (295-298) A further observation made by Comander et al. in patients with solar maculopathy was a hyperreflective ring surrounding the lesion. (295) The hyperreflective ring described by Comander et al. is sometimes seen in the older patients with achromatopsia (for example see figure 7.21, patient 6: note the hyperreflectivity at the top and outer edges). The significance of this is not clear although it has been suggested that it could represent cellular debris. (295) However this is different to the hyperreflective zone described in this study, since we observe this prior to the formation of the hyporeflective zone. Since the hyperreflective zone is a precursor to the development of the hyporeflective zone, it could represent one of the early signs of cone photoreceptor degeneration. In two patients (patient 1 and 2) we did not see the progression of this hyperreflective zone into a discrete IS/OS disruption, this could be because it represents the early stages of their disease. Further follow up over a longer time period may be required to observe the development of the hyporeflective zones in the aforementioned patients. A limitation in the study was that we were not able to perform statistical comparisons between visit 1 and 2 due to small sample numbers and the rareness of this disorder. Therefore further large scale studies with age and genotype stratification would be important to

understand the progressive nature of this disorder and whether it is confined to certain genotypes. As children in our study were between the ages of 5 and 9 years it would be also important to include a larger range of ages of children such as very young infants. A retrospective study by Thiadens et al. reported that 12% of patients with achromatopsia had visual acuity deterioration over time (mean follow up time was 15 years).(133) In contrast to the aforementioned study we have not found any decrease in VA in our patients. The stable VA in our patients could be due to a relatively short follow up period and smaller sample size. Recent cross sectional OCT studies have not been able to identify an age dependent deterioration of visual acuity or correlation of visual acuity to the development of the hyporeflective zone. (220,299)

Previous cross sectional studies have shown that there could be ONL thinning which is also noted as progressive reduction in central macular thickness. Using the longitudinal study design we are able to confirm the progressive loss of cone cells over time which is quantified by measuring both the outer nuclear layer and central macular thickness. This is consistent with animal models of achromatopsia which also describe ONL thinning with age. (289,290) With the advent of the spectral domain OCTs it is now possible to achieve faster scanning speeds and higher resolutions compared to the time domain instruments.

Interestingly patient 4, who had phenotypically all features of achromatopsia, did not have any mutations in the most commonly mutated genes associated with achromatopsia, *CNGB3* and *CNGA3*, or in *GNAT2*. This suggests that the

phenotype in this patient could arise from mutations of *PDE6C* or other achromatopsia associated genes which are yet to be identified. Evidence from gene therapy trials in mice suggest that early treatment is most likely to result in best outcome while intervention was less effective at older ages. This is probably due to the progressive cone photoreceptor degeneration. (300) We would also suspect similar results in possible future gene therapy trials in patients with achromatopsia in light of the mouse models and the findings presented in this study. Therefore the assessment of the structural and retinal thickness changes over time is not only helpful to document the progression of the disease but it could also be used as an objective measure to assess the most suitable patients and the effectiveness of gene therapy in the future.

In summary we detected for the first time retinal changes in FRMD7-related infantile nystagmus. Previously this disorder was thought to arise as a result of abnormalities within the brain rather than the retina, however the novel findings presented in this chapter suggests that abnormalities in retinal development could play a significant role in disease pathogenesis.

Foveal hypoplasia and optic nerve hypoplasia were also characterized in patients with PAX6 mutations, albinism and achromatopsia. The retinal changes in achromatopsia were progressive and atypical due to the cone photoreceptor degeneration.

Therefore arrested retinal development could be the common aetiological factor in the development of infantile nystagmus.

8. CHAPTER EIGHT: STRUCTURAL GRADING OF FOVEAL HYPOPLASIA

This chapter addresses the aim:

- To compare and classify foveal hypoplasia in albinism, achromatopsia, patients with *PAX6* mutations and isolated cases and to investigate whether morphological changes seen on OCT can help to predict visual acuity in foveal hypoplasia.

8.1 INTRODUCTION

Normal foveal development occurs in stages in which the pit formation for the incipient fovea starts at foetal week 25 and the excavation is complete 15 to 45 months after birth (244). Disruption of this developmental process leads to foveal hypoplasia, which is a characteristic morphologic abnormality associated with conditions such as albinism and *PAX6* mutations, or it may occur in isolation (146,211,227,301). With the advent of optical coherence tomography (OCT), it is now possible to document the varying degrees of foveal hypoplasia that are likely to represent the different stages of arrested development of the fovea. This has introduced various terms, such as *fovea plana*, *foveal dysgenesis*, and *foveal aplasia*, to describe the structural variability associated with arrested development of the fovea (224,262,302). Mietz et al. suggested that *foveal hypoplasia* is a more appropriate term rather than *aplasia* because hypoplasia encompasses both the partial and complete absence of a structure (303).

Recent studies have shown that OCT can be used as a diagnostic aid and prognostic indicator for the foveal hypoplasia (211,223,226). In addition, structural–functional correlation studies have been performed to document OCT findings in foveal hypoplasia, although most of them were disease specific for albinism. Harvey et al. showed a weak but significant correlation between CMT and visual acuity (VA) (222). In contrast, Holmstrom et al. did not find significant correlation between CMT and VA (226). Seo et al. proposed a grading system for foveal hypoplasia in albinism based on: (1) foveal hyporeflectivity, (2) choroidal transillumination, (3) tram tract sign, and (4) foveal depression (223). They showed in 13 patients that VA correlates well with degree of foveal hypoplasia, although subsequently they suggested that the role of foveal depression as prognostic indicator remains unclear because of the small sample size(225). Chong et al. also characterized the foveal morphologic abnormalities in 2 patients with ocular albinism and in 5 patients with suspected ocular albinism and reported that there were no foveal hyporeflectivity or tram tract signs in their study population(113). Marmor et al. noted a spectrum of different visual acuities in 4 patients who all lacked a foveal pit. Furthermore, they showed that foveal cone specialization, represented on OCT by the lengthening of the outer segment (OS) at the fovea, can be preserved even in the absence of a foveal pit (224).

However, it remains unclear how the morphologic variability associated with foveal hypoplasia relates to visual prognosis and what specific features at the fovea may be more important in determining visual performance.

This study sought to characterize the spectrum of foveal hypoplasia and to develop a structural grading system for foveal hypoplasia based on foveal development that can be applied to various disorders associated with foveal hypoplasia.

The purpose for establishing a grading system was 3-fold: (1) to document the stage at which foveal development was arrested, (2) to provide a prognostic indicator for visual acuity, and (3) to ensure applicability in a range of disorders associated with foveal hypoplasia.

Mohammad et al. showed that in albinism there is a good correlation between photoreceptor thickness and VA (R=-0.50). In addition a significant correlation between the photoreceptor thickness and inner retinal layer thickness was seen (216). Similarly, patients with diabetic macular oedema a significant and strong correlation was observed between VA and OS thickness (R between -0.61 and -0.81) (304). Linear regression analyses in retinitis pigmentosa patients have shown that CMT is a significant but poor predictor of VA (R^2=0.19), however interestingly the OS thickness was an excellent predictor of VA (R^2=0.89) (305). In order to investigate the quantitative relationships of the structural foveal elements to the grade of foveal hypoplasia and visual acuity a One-way ANOVA and a multiple regression model was used. Similarly based on the grades of foveal hypoplasia we investigated how closely the foveal developmental events were coupled.

8.2 METHODS

8.2.1 PATIENTS

The study population consisted of 69 patients with foveal hypoplasia
(defined as incursion or continuation of inner retinal layers) and 65 controls
with a mean age of 28.5 years (standard deviation, 15.7 years; range, 5–64
years) and 33.5 years (standard deviation, 14.3 years; range, 8–62 years),
respectively. The patient cohort consisted of 58 white persons (84%) and 11
Asians (16%); similarly, the control cohort consisted of 48 white persons
(74%) and 17 Asians (26%). In the patient group, there were 38 males (55%)
and 31 females (45%); in the control group, there were 31 males (48%) and
34 females (52%). All patients underwent an ophthalmologic examination
that included slit-lamp examination, fundus examination, and measurement
of binocular best-corrected visual acuity (BCVA) using standardized
logarithm of the minimum angle of resolution (logMAR) charts. The BCVA
with both eyes open was used for comparison with OCT grading because it
represents the best achievable VA and, for example, would reduce other
causes of decreased VA such as amblyopia or latent nystagmus. The patients
were diagnosed with albinism (n = 34), *PAX6* mutations (n = 10), isolated
foveal hypoplasia (n = 14), and achromatopsia (n = 11). The diagnostic
procedure has been elaborated in the chapter 2. Isolated foveal hypoplasia
includes IIN patients with and without *FRMD7* mutations. *PAX6* mutations
were detected in 10 patients, of whom 3 had aniridia. One patient with a
PAX6 mutation had to be excluded because of poor scan quality resulting
from corneal opacity. All patients in the study population had nystagmus.

There was no history of premature birth among the patients evaluated. All other patients and controls chosen for this study had clear media.

8.2.2 OPTICAL COHERENCE TOMOGRAPHY ACQUISITION AND ANALYSIS

The OCT acquisition and analysis protocol has been described in detail in chapter 6 and 7. Intra-retinal thickness measurements were obtained using reflectivity profiles. The thickness measurements derived from both eyes were averaged and analyzed subsequently, similar to a 1-eye study design as described by Ray and O'Day (306).

8.2.3 DEVELOPMENTAL BASIS OF GRADING FOVEAL HYPOPLASIA

The rationale behind the grading system that was adopted was based on the unique developmental processes occurring at the fovea (figure 1.3 and figure 8.1). During development of the fovea, there is (1) centrifugal displacement of cells of the inner retina toward the periphery, (2) centripetal migration of cone photoreceptors toward the location of the incipient fovea, and (3) cone specialization of the foveolar cones (7,244). Because of the centrifugal displacement of the inner retinal cells, the foveal depression continues to deepen until 15 months after birth, and this is seen as complete extrusion of the inner nuclear and plexiform layers posterior to the foveola (see example of normal OCT scan in figure 8.2) (13). The centripetal migration of the cone photoreceptors is represented by the outer nuclear layer (ONL) widening. The cone OS undergoes both a decrease in diameter and increase an in length (i.e., cone specialization); this allows an increase in foveolar cone packing density (7). The change in cone diameter continues up to 45 months after

265

birth. The cone specialization is represented on OCT by the OS lengthening

(224). The grading system used takes into account each of these

developmental steps.

Developmental event	Grade of foveal hypoplasia				OCT feature
	Grade 1	Grade 2	Grade 3	Grade 4	
Centrifugal displacement of inner retinal layers					Foveal pit and extrusion of inner retinal layers
Cone photoreceptor specialisation					Outer segment lengthening
Centripetal migration of cone photoreceptors					Outer nuclear layer widening

■ The developmental process has occurred at least to a partial extent
▢ The developmental process has not occurred

Figure 8.1: *The three developmental processes involved in formation of a structural and functional fovea. In grade 1 foveal hypoplasia all processes occurs to a certain extent. However in grade 4 none of these processes occur thus the retina resembles that of the parafovea. In grade 2 and 3 there is outer nuclear layer (ONL) widening but no foveal pit. The difference between grade 2 and 3 is occurrence of cone photoreceptor specialisation. Identifying these specific features on optical coherence tomography (OCT) enables us to understand whether or not the respective developmental process has occurred.*

8.2.4 STATISTICAL METHODS

Normality of the VA and intra-retinal thickness measurements data were

tested using the Shapiro-Wilk test. Nonparametric tests (Kruskal-Wallis)

were used (because of nonnormality) to test the difference in (1) logMAR VA

between the different grades of foveal hypoplasia, (2) retinal thickness, (3)

ONL thickness, and (4) foveal depth at the fovea between controls and

patients with typical and atypical forms of foveal hypoplasia. Multiple

comparisons were performed with Bonferroni correction. The Mann–

Whitney *U* test was used to test the differences in VA between typical and

atypical forms of foveal hypoplasia.

In order to assess the relationship of structural foveal elements to the grade of foveal hypoplasia and visual acuity an ANOVA and a multiple regression model was used respectively (the intra-retinal thickness were normally distributed when groups were divided based on foveal hypoplasia grade). The dependent variable was LogMAR visual acuity and the explanatory variables assessed were: (1) outer nuclear layer, (2) inner segment, (3) outer segment, (4) inner retinal layer thickness and (5) foveal pit depth. An adjusted R^2 value was used to take into account the number of explanatory variables. To assess whether developmental coupling occurs between the structural foveal elements a second order polynomial regression (due to non-linearity based on foveal hypoplasia grades) was used.

8.3 RESULTS

8.3.1 GROSS MORPHOLOGICAL FEATURES ASSOCIATED WITH FOVEAL HYPOPLASIA

Examples of the gross features of foveal hypoplasia detectable on ultra high-resolution spectral-domain OCT are shown in figure 8.2. The hallmark of foveal hypoplasia detectable on OCT is the incursion of the inner retinal layers posterior to the foveola. In addition to this, other features seen on OCT included: shallower or absent foveal pit, diminished ONL widening, decreased OS lengthening, and overall thickening of the retina. However, there is considerable phenotypic variability associated with foveal hypoplasia. Figure 8.2 shows examples of foveal hypoplasia and the degree of variability seen.
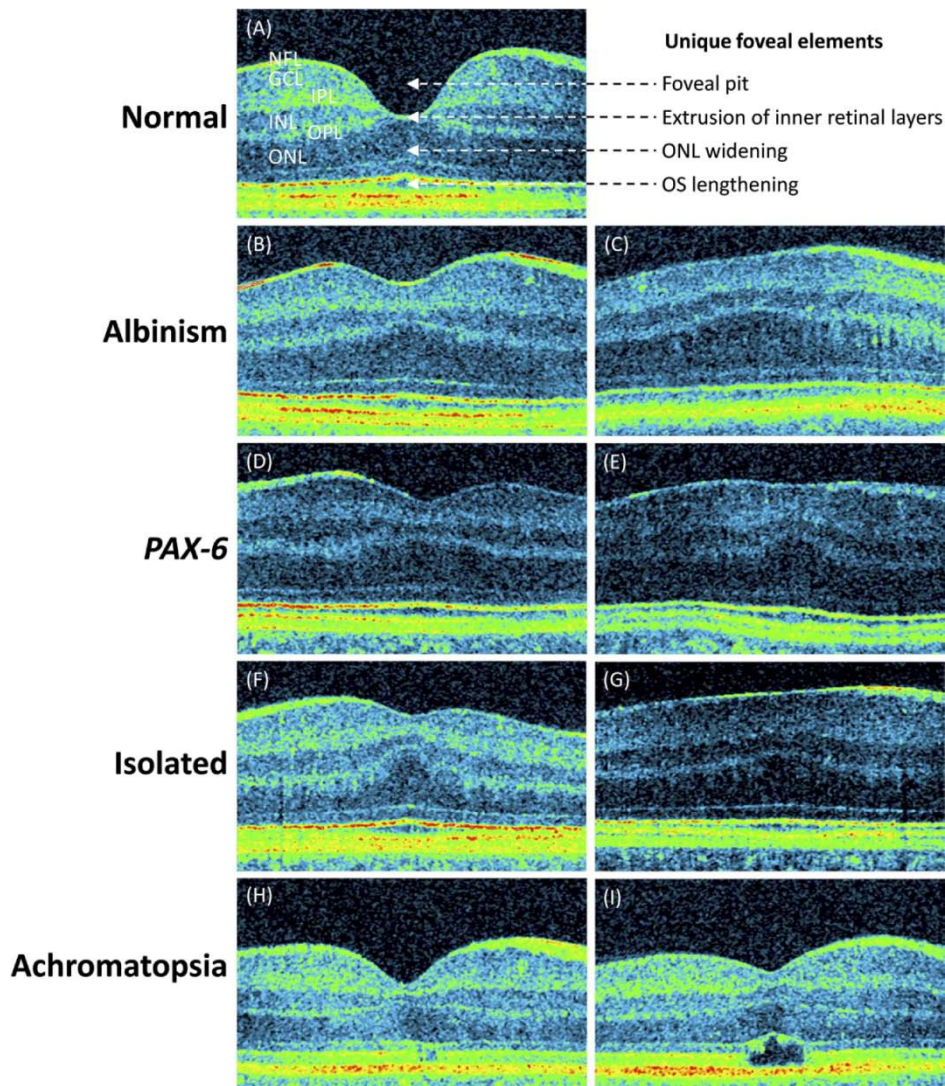
Figure 8.2: *(A) Optical coherence tomography scan showing a normal fovea with description of the normal foveal elements. Optical coherence tomography scans showing the spectrum of foveal hypoplasia seen in various conditions, including: (B, C) albinism, (D, E) associated with PAX6 mutations, (F, G) isolated cases, and (H, I) an atypical form of foveal hypoplasia seen in achromatopsia. A hyporeflective zone (cavitation) is also seen (I) that is a sign of cone photoreceptor degeneration. Both foveal hypoplasia and fovea plana were seen in all disorders except the achromatopsia, which results in an atypical form of foveal hypoplasia with a shallower pit, incursion of the plexiform layers, and disruption of the inner segment (IS)/outer segment (OS) junction. INL = inner nuclear layer; NFL = nerve fibre layer; ONL = outer nuclear layer.*

8.3.2 GRADING AND FUNCTIONAL IMPLICATIONS OF FOVEAL HYPOPLASIA

To derive a structural grading system for foveal hypoplasia, the foveal region was subdivided according to foveal development into the structural elements that represent the unique features of the fovea detectable using OCT (see figure 8.2 and figure 8.3A). Progressive loss of the foveal elements is represented as increasing grades (figure 8.3).
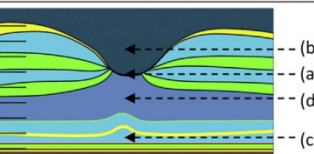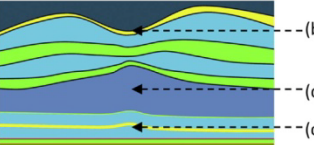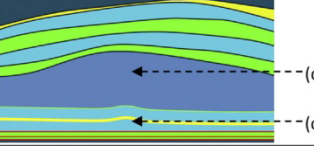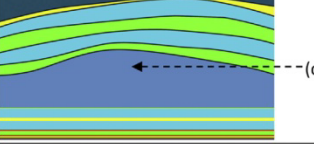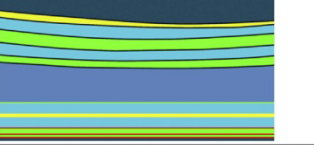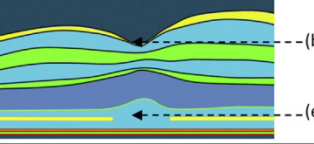
(A)

Normal foveal structural features detectable using optical coherence tomography	Illustration
(a) Extrusion of plexiform layers (b) Foveal pit (c) OS lengthening (d) ONL widening	RNFL — GCL IPL — INL OPL — ONL ELM — IS/OS RPE - - (b) - - (a) - - (d) - - (c)

(B)

Grade of foveal hypoplasia	Structural features detected on optical coherence tomography	Present or absent	Illustration
1	(a) Extrusion of plexiform layers (b) Foveal pit – Shallow (c) OS lengthening (d) ONL widening	(a) Absent (b) Present (c) Present (d) Present	- - (b) - - (d) - - (c)
2	(a) Extrusion of plexiform layers (b) Foveal pit (c) OS lengthening (d) ONL widening	(a) Absent (b) Absent (c) Present (d) Present	- - (d) - - (c)
3	(a) Extrusion of plexiform layers (b) Foveal pit (c) OS lengthening (d) ONL widening	(a) Absent (b) Absent (c) Absent (d) Present	- - (d)
4	(a) Extrusion of plexiform layers (b) Foveal pit (c) OS lengthening (d) ONL widening	(a) Absent (b) Absent (c) Absent (d) Absent	
Atypical	(a) Extrusion of plexiform layers (b) Foveal pit – Shallow (e) IS/OS disruption	(a) Absent (b) Present (e) Present	- - (b) - - (e)

Figure 8.3: *(A) Illustration showing the unique features of a normal fovea detectable on optical coherence tomography. (B) Illustration of typical and atypical grades of foveal hypoplasia. All grades of foveal hypoplasia had incursion of inner retinal layers. Atypical foveal hypoplasia also had incursion of the inner retinal layers. Grade 1 foveal hypoplasia is associated with a shallow foveal pit, outer nuclear layer (ONL) widening, and outer segment (OS) lengthening relative to the parafoveal ONL and OS length, respectively. In Grade 2 foveal hypoplasia, all features of grade 1 are present except the presence of a foveal pit. Grade 3 foveal hypoplasia consists of all features of grade 2 foveal hypoplasia except the widening of the cone outer segment. Grade 4 foveal hypoplasia represents all the features seen in grade 3 except there is no widening of the ONL at the fovea. Finally, an atypical form of foveal hypoplasia also is described in which there is a shallower pit with disruption of the inner segment/outer segment (IS/OS) junction, possibly a sign of photoreceptor degeneration. The atypical form of foveal hypoplasia is seen with achromatopsia, whereas grades 1 through 4 are seen with albinism, PAX6 mutations, and isolated cases. ELM=external limiting membrane; GCL= ganglion cell layer; INL=inner nuclear layer; IPL=inner plexiform layer; OPL=outer plexiform layer; RNFL=retinal nerve fibre layer; RPE=retinal pigment epithelium.*
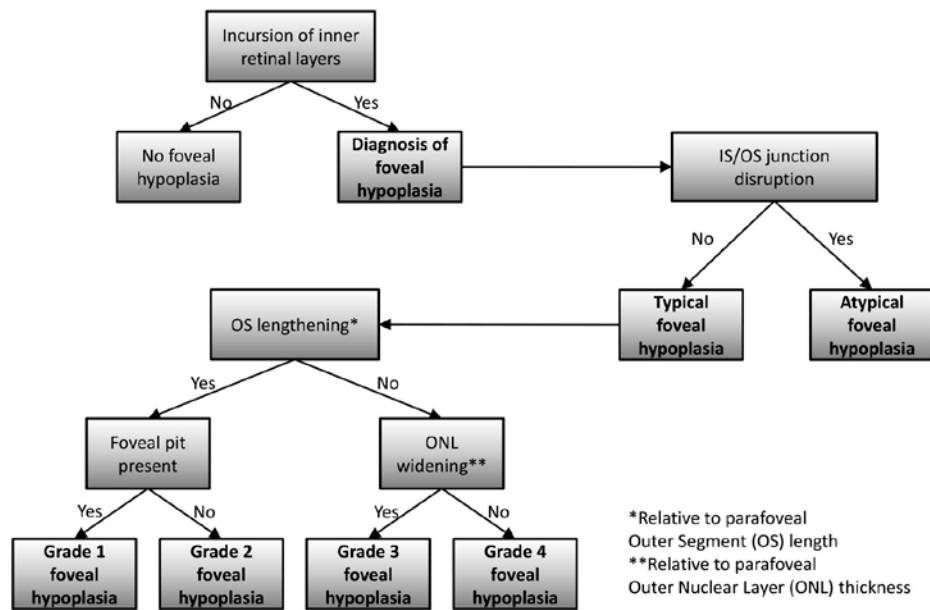
Figure 8.4: Algorithm used for grading foveal hypoplasia based on optical coherence tomography findings. The hallmark of foveal hypoplasia is incursion of the inner retinal layers. Based on disruption of the inner segment/outer segment (IS/OS) junction of the photoreceptor, the foveal hypoplasia is classified into either typical or atypical foveal hypoplasia. The grade of foveal hypoplasia can be determined based on whether the following features are present or absent: outer segment (OS) lengthening, foveal pit, and outer nuclear layer (ONL) widening.

Incursion of the plexiform layers was present in all types of foveal hypoplasia because it was the criteria used to diagnose foveal hypoplasia. Subsequently, the grading system gives most importance to the integrity of the OS (i.e., whether this region disrupted to rule out atypical forms of foveal hypoplasia).

Then, importance is given to the development of this region (detected on OCT by the lengthening of the OS; this feature is present in grades 1 and 2 but not in grades 3 and 4). Subsequently, the features of foveal development anterior to the inner segment (IS) and OS were assessed. Widening of the ONL differentiated between grades 3 and 4, and foveal pit formation differentiated between grades 1 and 2. The features of each grade are illustrated in figure

8.3. An algorithm was devised to grade foveal hypoplasia structurally (figure 8.4). Whether the grade of foveal hypoplasia significantly predicted the BCVA was assessed. There was a significant difference in BCVA between the grades of foveal hypoplasia ($p<0.0001$; see figure 8.5). Grade 1 foveal hypoplasia was associated with the best VA (median BCVA, 0.2 logMAR), whereas grades 2, 3, and 4 were associated with progressively poorer VA with a median BCVA of 0.44, 0.60, and 0.78 logMAR, respectively (figure 8.5). The results of the multiple comparisons of VA between the grades are shown in figure 8.5. A significant effect of gender, age, or ethnicity on the grade of foveal hypoplasia was not found.

8.3.3 COMPARISON OF TYPICAL AND ATYPICAL FOVEAL HYPOPLASIA

The number of patients within each grade and their diagnosis is shown in figure 8.5. Most patients with albinism had grade 3 foveal hypoplasia, whereas most isolated cases and *PAX6* patients had grade 1 foveal hypoplasia. Overall, patients with albinism were associated with the worst BCVA (median BCVA, 0.6 logMAR; interquartile range, 0.30), followed by patients with *PAX6* mutations (median BCVA, 0.4 logMAR; interquartile range, 0.35), and then isolated cases (median BCVA, 0.2 logMAR; standard deviation, 0.30). However, if the grade of foveal hypoplasia was considered, there was no significant difference in BCVA between the 3 disorders for grade 1 foveal hypoplasia ($p = 0.83$). (Only grade 1 had sufficient sample numbers within each diagnosis to make multiple comparisons.)

As shown in figure 8.2, achromatopsia is associated with disruption of the IS/OS junction; however, it also can be associated with a shallower pit and

incursion of the plexiform layers posterior to the foveola. This results in an atypical foveal hypoplasia because it is associated with photoreceptor degeneration. The other atypical features associated with achromatopsia that do not follow the pattern seen with the typical forms of foveal hypoplasia include: a significantly decreased retinal thickness and outer nuclear layer in comparison with both controls (p<0.0001) and the patients with typical foveal hypoplasia (p<0.0001; grades 1 through 4; figure 8.5). Although achromatopsia is associated with significantly shallower pit in comparison with the controls (p<0.0001), the foveal pit in achromatopsia is significantly deeper in comparison with the patients with grade 1 foveal hypoplasia (p = 0.005; only grade 1 foveal hypoplasia was used for this comparison because only these patients have a rudimentary foveal pit; see figure 8.5).
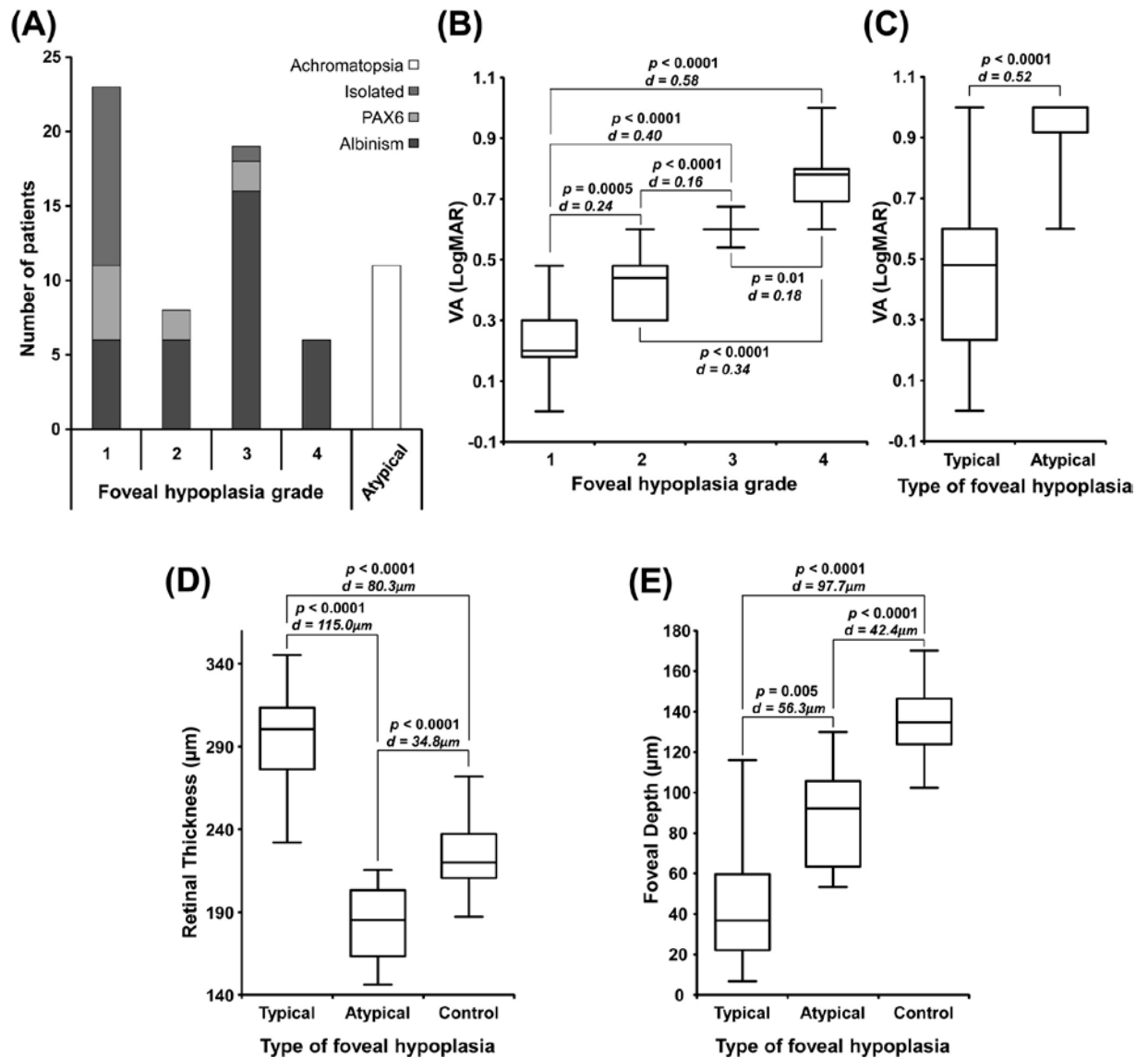
Figure 8.5: *(A) Bar graph showing the number of patients within each grade of foveal hypoplasia; the proportion of different disorders within each grade are shown with different shades. (B), Box plots of visual acuity (VA) for each grade of foveal hypoplasia. The results of multiple comparisons of how grade of foveal hypoplasia affects VA are shown with the respective P values and median difference (d) in VA measured in logarithm of the minimum angle of resolution (logMAR) units. (C), Box plot showing that similarly, there was a significant difference in visual acuity between the typical forms of foveal hypoplasia and atypical foveal hypoplasia. The other features that were significantly different between the controls and typical and atypical forms of foveal hypoplasia were: (D) retinal thickness at the fovea and (E) foveal depth. For all box plots, the whiskers represent the maximum and minimum range of observations, whereas the box represents the interquartile range and the line dividing the box represents the median. All multiple comparisons are shown with the box plots with the significance values and median differences (d), units for which are logMAR (for B and C) or micrometers (for D and E).*

275

8.3.4 RELATIONSHIP OF STRUCTURAL FOVEAL ELEMENTS TO THE GRADE OF FOVEAL HYPOPLASIA AND VISUAL ACUITY

With the exception of inner segment thickness, we found that the means of the remaining intra-retinal thickness measurements (ONL, OS, inner retinal layer thickness, total photoreceptor layer thickness and CMT) were significantly different ($p<0.05$) when the groups were classified based on the grade of foveal hypoplasia (table 8.1 and figure 8.6).

Multiple comparisons showed that grade 1 foveal hypoplasia had a significantly thicker ONL and total PRL when compared to grade 3 and 4 but not grade 2 (figure 8.6A and figure 8.7A). Similarly grade 2 foveal hypoplasia also had a significantly thicker ONL and total PRL when compared to grades 3 and 4. The thickness of the OS layer was significantly greater in grade 1 when compared to grade 2, 3 and 4 (figure 8.6C). Grade 2 foveal hypoplasia also had a significantly thicker OS when compared to grade 3 and 4, however there were no significant difference in OS thickness between grades 3 and 4. The inner retinal layers were significantly thinner in the grade 1 foveal hypoplasia when compared to grade 2, 3 and 4, however there were no significant difference in the IRL thickness between grades 2, 3 and 4 (figure 8.7B). The CMT was significantly thinner in the grade 1 group when compared to grade 2 and 3 but not grade 4 foveal hypoplasia (figure 8.7C). There were no significant difference in the CMT between foveal hypoplasia grades 2, 3 and 4.

Regression analyses showed that the following foveal elements were significant predictors ($p<0.05$) of visual acuity (table 8.2): (1) outer nuclear layer ($R^2 = 0.47$), (2) outer segment ($R^2 = 0.46$), (3) foveal pit depth ($R^2 = 0.18$) and (4) total inner retinal layer thickness ($R^2 = 0.54$). Using combined measurements such as total photoreceptor layer thickness ($R^2 = 0.53$) and central macular thickness ($R^2 = 0.17$) were also significant predictors of visual acuity. Inner segment thickness was not a significant ($p>0.05$) predictor of visual acuity. The strength of the relationships is shown in figure 8.6 and figure 8.7. The residuals show the degree of variation not accounted by the regression model (see table 8.2).

When using a multiple linear regression model (accounting for the combined effects of the each of the significant predictor (foveal pit depth, ONL, OS and total inner retinal layer thickness) a significantly stronger relationship is seen ($R^2 = 0.61$, $p<0.0001$) (figure 8.8). This also results in a substantial decrease in the residuals since the model takes into account the three main developmental events (figure 8.1) responsible for the formation of the area of high acuity.

Table 8.1: Results of the multiple comparisons for the means of the thickness measurements based on the grade of foveal hypoplasia.

Thickness measurement	Multiple Comparisons (grade)	Mean Difference (µm)	Std. Error	*p*-value	95% Confidence Interval	
					Lower	Upper
Outer Nuclear Layer	1 vs 2	5.1	4.75	1.00	-7.93	18.14
	1 vs 3	27.31	3.58	<0.0001	17.51	37.12
	1 vs 4	37.57	5.32	<0.0001	23	52.14
	2 vs 3	22.21	4.91	0.0002	8.76	35.66
	2 vs 4	32.47	6.29	<0.0001	15.23	49.71
	3 vs 4	10.26	5.45	0.3932	-4.69	25.2
Inner segment	1 vs 2	1.13	0.83	0.687	-1.21	3.47
	1 vs 3	-0.41	0.92	0.998	-2.94	2.11
	1 vs 4	2.57	1.41	0.418	-2.08	7.21
	2 vs 3	-1.54	0.74	0.247	-3.66	0.58
	2 vs 4	1.44	1.3	0.83	-3.23	6.11
	3 vs 4	2.98	1.36	0.267	-1.66	7.61
Outer Segment	1 vs 2	6.25	1.62	0.0019	1.8	10.69
	1 vs 3	12.23	1.22	<0.0001	8.89	15.58
	1 vs 4	12.61	1.81	<0.0001	7.64	17.58
	2 vs 3	5.99	1.67	0.0046	1.4	10.58
	2 vs 4	6.36	2.15	0.0272	0.48	12.25
	3 vs 4	0.38	1.86	1.00	-4.72	5.48
Total PRL	1 vs 2	12.48	5.56	0.1733	-2.75	27.71
	1 vs 3	39.16	4.18	<0.0001	27.7	50.61
	1 vs 4	52.74	6.21	<0.0001	35.71	69.76
	2 vs 3	26.68	5.74	0.0001	10.96	42.4
	2 vs 4	40.26	7.35	<0.0001	20.11	60.4
	3 vs 4	13.58	6.37	0.2264	-3.89	31.05
Total IRL	1 vs 2	-54.19	6.77	<0.0001	-73.31	-35.08
	1 vs 3	-65.44	6.08	<0.0001	-82.35	-48.53
	1 vs 4	-68.41	6.65	<0.0001	-87.41	-49.41
	2 vs 3	-11.25	5	0.203	-26.35	3.85
	2 vs 4	-14.22	5.68	0.142	-31.85	3.41
	3 vs 4	-2.97	4.84	0.987	-18.22	12.29
Central Macular Thickness	1 vs 2	-43.83	8.18	<0.0001	-66.25	-21.4
	1 vs 3	-28.02	6.15	0.0002	-44.89	-11.15
	1 vs 4	-17.46	9.15	0.3704	-42.53	7.61
	2 vs 3	15.81	8.45	0.4004	-7.34	38.96
	2 vs 4	26.37	10.82	0.1093	-3.29	56.04
	3 vs 4	10.56	9.38	1.00	-15.16	36.28

PRL = Photoreceptor Layer
IRL = Inner Retinal Layers

Table 8.2: Regression analyses of visual acuity against structural foveal elements

ID	Thickness measurement	R	R²	*P*-value	Source of Variation[a]		
					Model	Residual	Total
(a)	Outer Nuclear Layer	-0.69	0.47	<0.0001	1.19	1.33	2.52
(b)	Inner Segment	-0.07	0.01	0.58	0.01	2.51	2.52
(c)	Outer Segment	-0.68	0.46	<0.0001	1.16	1.36	2.52
(d)	Total PRL	-0.73	0.53	<0.0001	1.33	1.19	2.52
(e)	Foveal Depth	-0.43	0.18	0.02	0.12	0.53	0.65[b]
(f)	Total IRL	+0.74	0.54	<0.0001	1.37	1.15	2.52
(g)	Central Macular	+0.41	0.17	0.002	0.42	2.10	2.52
(h)	Combined (a,c,f)	+0.78	0.61	<0.0001	1.54	0.98	2.52

[a] Sum of squares (dependent variable: LogMAR visual acuity)
[b] The sum of squares is lower for the foveal depth measurement since it did not include patients with fovea plana.
PRL = Photoreceptor Layer (ONL+IS+OS); IRL = Inner retinal layers (all layers anterior to the outer nuclear layer).
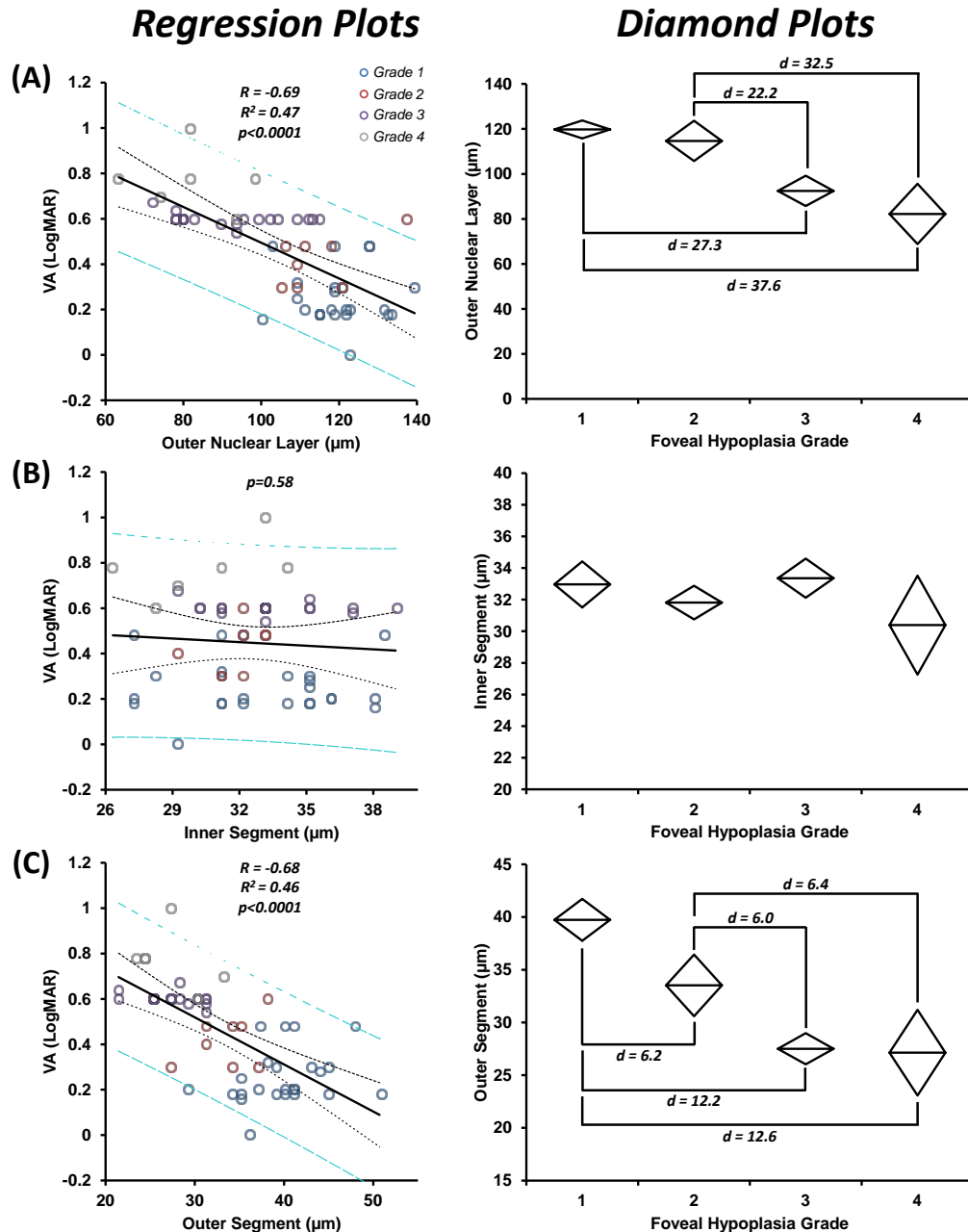
Figure 8.6: *Regression plots and diamond plots for: (A) outer nuclear layer, (B) inner segment and (C) outer segment thickness. The dependent variable in the regression plot is visual acuity (VA). The line of best fit (black line), 95% confidence intervals (dotted black lines) and 95% prediction intervals (dotted blue line) are shown in the regression graphs. Multiple comparisons between the different grades of foveal hypoplasia are shown. Significant differences of the mean (d) are shown. The outer limits of the diamond plot represent the 95% confidence intervals and the line bisecting the diamond is the mean.*
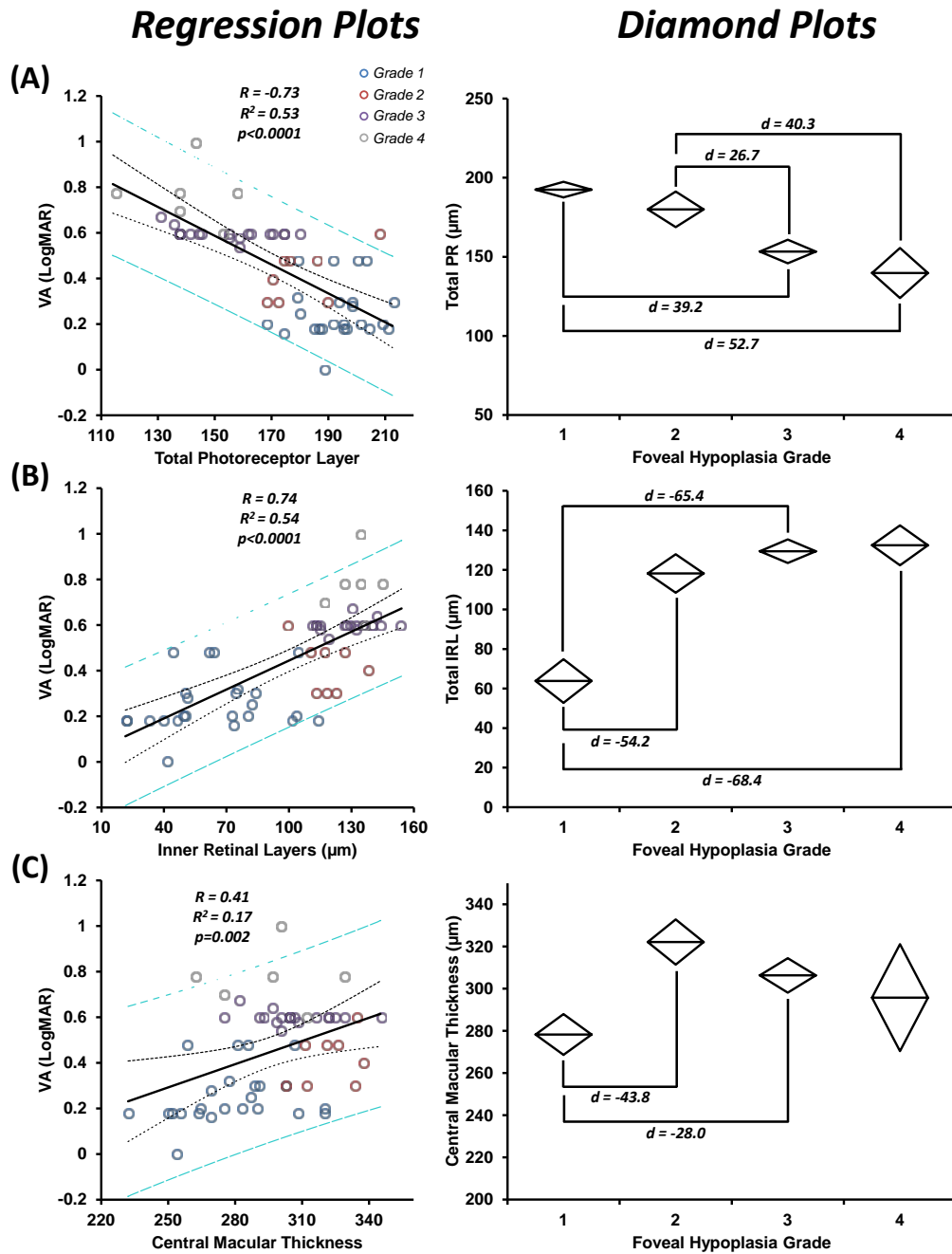
Figure 8.7: *Regression plots and diamond plots for: (A) total photoreceptor layer, (B) inner retinal layers and (C) central macular thickness. The dependent variable in the regression plot is visual acuity (VA). The line of best fit (black line), 95% confidence intervals (dotted black lines) and 95% prediction intervals (dotted blue line) are shown in the regression graphs. Multiple comparisons between the different grades of foveal hypoplasia are shown. Significant differences of the mean (d) are shown. The outer limits of the diamond plot represent the 95% confidence intervals and the line bisecting the diamond is the mean.*

281
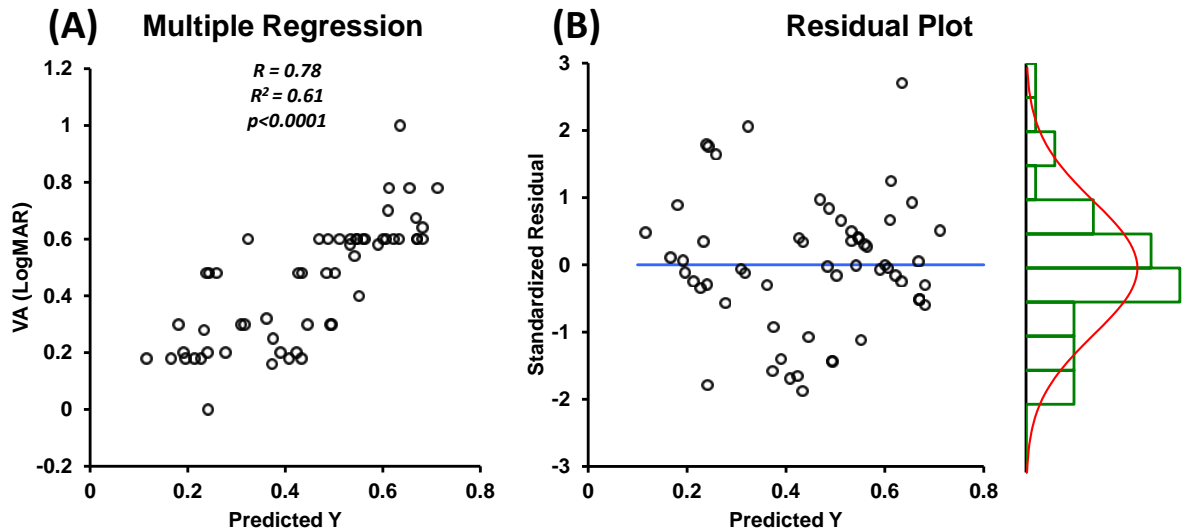
Figure 8.8: *(A) Scatter plot showing the relationship between visual acuity (LogMAR) and the predicted Y variables (based on the multiple regression predictors: inner retinal layer thickness, outer nuclear layer thickness and outer segment thickness)). (B) Residual plot showing distance of each observation from the fitted line. The standardized residuals lie within 2-3 standard deviations of zero. The histogram of the residuals with a normal curve overlay shows that the measurement errors in the response variable are normally distributed.*

8.3.5 DEVELOPMENTAL COUPLING OF STRUCTURAL FOVEAL ELEMENTS

8.3.5.1 CONE PHOTORECEPTOR SPECIALISATION, MIGRATION AND INNER RETINAL LAYERS EXTRUSION

In figure 8.9 the scatter plots show the relationship between widening of the outer nuclear layer and lengthening of the outer segments of cone photoreceptors at the fovea. We find that there is a significant correlation (R = 0.61, p<0.0001) between these two measurements in foveal hypoplasia grade 1 and 2, however no significant correlation was seen for grades 3 and 4 (p>0.05) (figure 8.9A). The ONL thickness and IRL thickness were also significantly correlated (R = 0.49, p=0.004) for foveal hypoplasia grades 1 and 2 however were not significantly correlated for grades 3 and 4 (p>0.05) (figure 8.9B). Similarly for grade 1 and 2 we find a significant correlation (R = 0.72, p<0.0001) between outer segment lengthening and inner retinal layer thickness, however for grades 3 and 4 there is no significant correlation (p>0.05) (figure 8.9C).

From the scatter plots it is evident that the xy values for the datasets (ONL vs OS, ONL vs IRL, OS vs IRL) as a whole are not linearly distributed. Hence a second order polynomial regression model was used to analyse the data. The results of the polynomial regression analyses are shown in figure 8.9. Using a polynomial regression model was associated with a lower residual variance compared to a linear regression.

Scatter Plots

Polynomial Regression
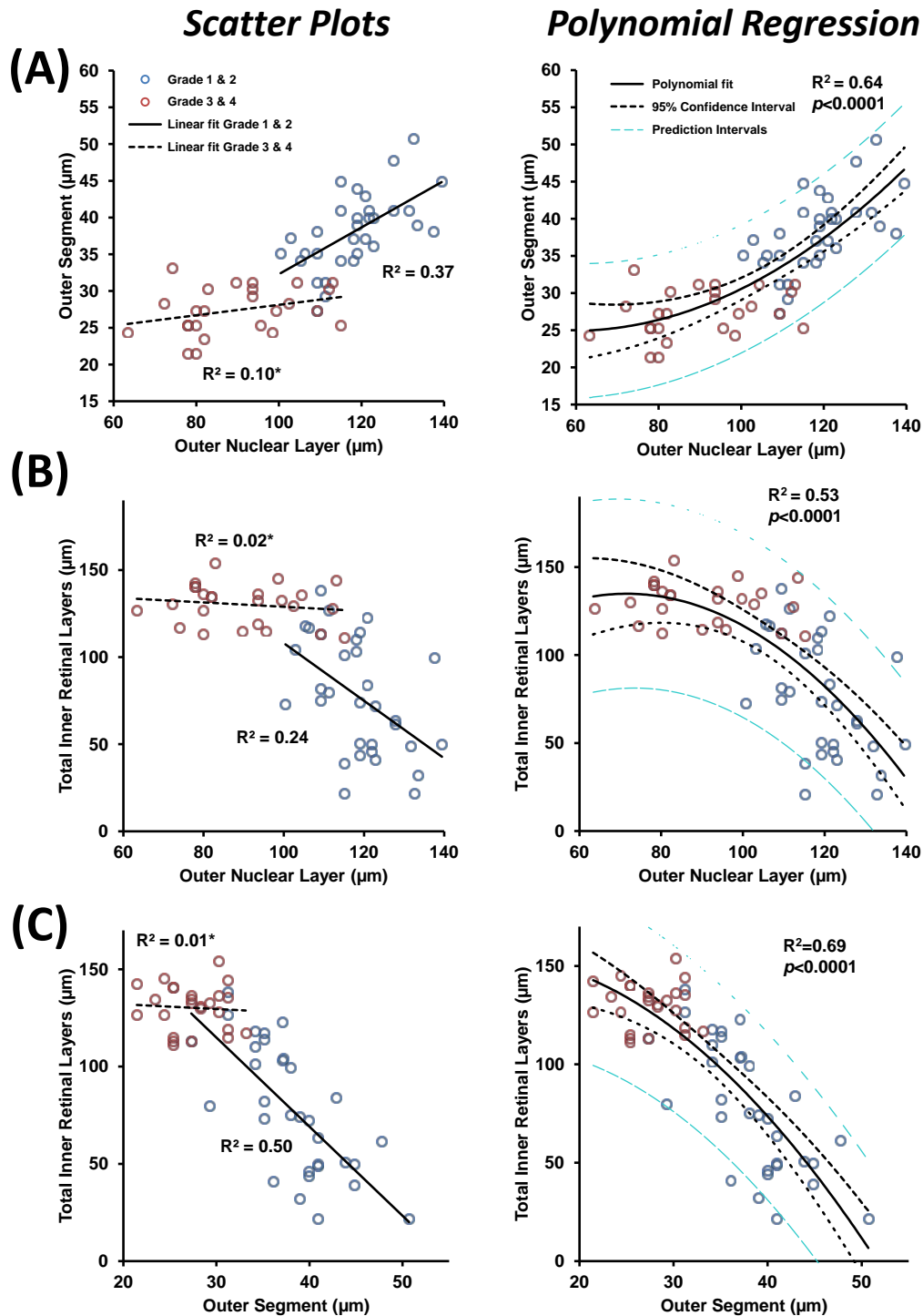
Figure 8.9: Developmental coupling of structural foveal elements based on the grade of foveal hypoplasia. The following scatter plots and polynomial regression plots are shown: (A) cone photoreceptor specialisation and migration of cone photoreceptors to the fovea; (B) centrifugal displacement of inner retinal layers and centripetal migration of cone photoreceptors and (C) centrifugal displacement of inner retinal layers and cone photoreceptor specialisation. The non-linear relationships between the variables are visible on the scatter plots. (* p>0.05; i.e. the relationship was not significant)

We found a significant relationship between the foveal pit depth and inner retinal layer thickness (R=-0.58, R^2 = 0.34, p = 0.003) (figure 8.10A). Similarly there was a significant relationship between foveal pit depth and central macular thickness (R=-0.62, R^2 = 0.38, p = 0.001) (figure 8.10B). However there was no significant relationship of foveal pit depth with outer nuclear layer and outer segment thickness (p>0.05) (figure 8.10C&D).
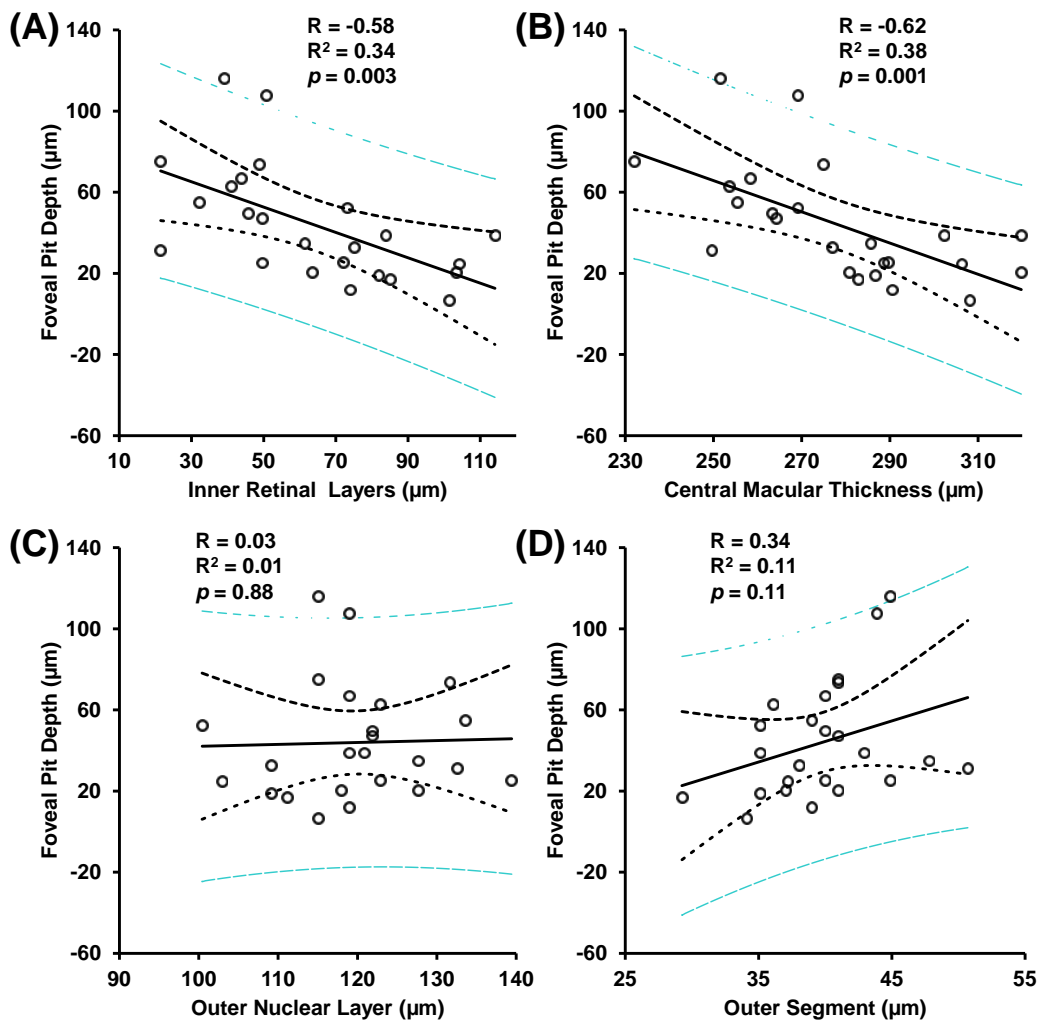
Figure 8.10: *Scatter plots showing the relationship of foveal pit formation with: (A) inner retinal layer, (B) central macular, (C) outer nuclear layer, and (D) outer segment thickness.*

8.4 DISCUSSION

This study proposed a structural grading system for foveal hypoplasia based on loss of unique elements that form the normal fovea that likely have been arrested during early development. The proposed grading system has 3 advantages: (1) it gives insight into the degree of development of the fovea, (2) it provides a prognostic indicator from a morphologic OCT scan, and (3) it can be applied to most disorders associated with foveal hypoplasia. The study also showed that achromatopsia can be associated with foveal hypoplasia, although it is associated with atypical features such as IS/OS disruption and ONL thinning, which are signs of photoreceptor degeneration, reduced retinal thickness (RT), and a deeper foveal pit in comparison with the typical forms of foveal hypoplasia.

From a developmental perspective, each grade suggests developmental arrest of the 3 key events to varying degrees, as shown in figure 8.1. All patients with foveal hypoplasia in this study had incursion of the plexiform layer posterior to the foveola, suggesting that pit formation was incomplete in all patients. A partial displacement of the inner retinal layers results in a rudimentary pit, as encountered with grade 1 foveal hypoplasia and atypical foveal hypoplasia. This process has failed to occur in grades 2, 3, and 4 of foveal hypoplasia. Lengthening of the OS is a sign of cone photoreceptor specialization, and this occurs to some extent in grades 1 and 2, but not grades 3 and 4. Lengthening of the OS can occur in the absence of a foveal pit, as seen in grade 2 foveal hypoplasia, and also as suggested by Marmor et al.(224). However, no cases where a foveal pit was present with no OS

lengthening (i.e., all patients with a foveal pit had OS lengthening) were encountered, suggesting that pit formation may be dependent partly on OS lengthening. Successful centripetal migration of cone photoreceptors is represented by ONL widening (seen in grades 1, 2, and 3). However, in grade 4 foveal hypoplasia, this developmental process is completely arrested and has failed to occur.

The quantitative data provides insight into the developmental coupling of the structural foveal elements and formation of the foveal pit. Both the ONL and the OS thickness increases progressively from grade 4 to grade 1. However we find from the regression plots that during grades 3 and 4 the ONL thickness changes significantly independent of the OS. However the regression plots show that for grades 1 and 2 there is a significant relationship between these two developmental processes. This suggests that during the early stages of development (grades 3 and 4) they occur independently however later on the processes get coupled. Using a polynomial regression we have been able to show that 64% of the total variance in foveal OS length is related to the centripetal migration of cone photoreceptors. Similarly we see that in grade 3 and 4 the ONL widening and outer segment lengthening does not have a significant effect on the centrifugal displacement of the inner retinal cells, however in grades 1 and 2 these developmental events become coupled. This suggests that after a certain developmental time point (grade 2 foveal hypoplasia onwards) as cone photoreceptor packing and specialization increase there is also an increase in the number of inner retinal cells displaced centrifugally. These

events subsequently lead to deepening of the foveal pit as suggested by the significant inverse relationship between foveal pit depth and displacement of inner retinal cells.

We have seen that the ONL thickness is greatest in patients with a rudimentary foveal pit (grade 1) as compared to patients with foveal plana. This strengthens the hypothesis put forward in the last chapter that the developmental arrest in grade 1 foveal hypoplasia patients occurs during a developmental window prior to reduction in ONL thickness however after the foveal avascular zone is defined. Furthermore since we observe a sequential rise in the ONL and central macular thickness between grades 2-4 this is consistent with histological studies which show that the maturity of the foveal ONL is progressive (241).

This grading system provides a prognostic visual function indicator by showing that the grade of foveal hypoplasia is significantly related to VA. It can be used easily in a clinical setting and does not require thickness measurements to predict and provide a likely visual prognosis for the patient with foveal hypoplasia. The grading system proposed accounts for the retinal structural basis for the decreased VA, but not for additional causes reducing VA, such as nystagmus, amblyopia, anterior segment disorder, or refractive error. Hence, morphologic grading of foveal hypoplasia can help in deciding whether further investigation or treatment are necessary to improve the patient's VA. For instance, if a patient has grade 1 foveal hypoplasia and a VA of 0.7 logMAR, factors other than the foveal hypoplasia are likely to be contributing to the poor VA. Similarly, if a patient has a VA of 0.6 logMAR and

has a grade 3 foveal hypoplasia, one would not expect the vision to improve past 0.5 logMAR because the structural development of the fovea is the limiting factor. An algorithm was also developed that is easy to follow and that can be used to derive the structural grade for foveal hypoplasia. Although 4 representative disorders associated with foveal hypoplasia were included, the grading system was not applied in patients with other forms of foveal hypoplasia, such as nanophthalmos(307) and retinopathy of prematurity (243). In this study population, VA correlated well with the grade of foveal hypoplasia; however, validation of the grading scheme in larger cohorts is necessary.

Harvey et al. showed a weak inverse correlation (R=-0.21) between CMT and VA, however two other studies in albinism have not found a significant correlation between CMT and VA (216,226). Previously in albinism a good negative correlation (R=-0.50) was seen for total photoreceptor thickness and VA, however regression analyses were not performed (216). Using a linear regression model we have been able to provide quantitative evidence to further strengthen the validity of the grading system. We have been able to show that each of the developmental events used in the grading system were significant predictors of visual acuity. Interestingly we found that ONL and OS thicknesses were able to account for 46-47% of the total variance of VA. Although CMT and FD were significant predictors of VA they were only able to account for 17-18% of the total variance of VA, thus CMT and FD were considered as poor predictors of VA. Subsequently we used a multiple regression model which takes into account the three developmental events

(centrifugal displacement of the inner retinal layers, cone photoreceptor specialization and centripetal migration of cone photoreceptor) which forms the basis of the grading system. When these developmental events were combined we observed the highest correlation coefficient (R = 0.78) and also this model was able to account for 61% of the total variance of VA. Although all the patients were refracted appropriately and the best corrected visual acuity was recorded the residual variance could be accounted for by non-retinal features such as (1) nystagmus characteristics such as intensity, NAFX and (2) disease specific characteristics such as abnormal electrodiagnostic tests, anterior segment abnormalities, photophobia, strabismus etc. Therefore further studies documenting these additional parameters would be useful to see how the residual variance is affected.

The previous study by Seo et al. (223) used OCT signs in albinism, which are dependent on reflectivity of structures in the tomogram such as foveal hyporeflectivity, choroidal transillumination, and tram tract sign. Presence or absence of foveal depression also was used to grade the foveal hypoplasia. Determining reflectivity features can be subjective, especially when using spectral-domain OCT, because they are associated with a sensitivity roll off, that is, the decrease in reflectivity values as the image moves away from the zero delay line. Hence, foveal hyporeflectivity may be difficult to interpret between an image that is close to the 0 delay line (which would be associated with higher reflectivity) and one that is further away (which would be less reflective) (217). This study avoided using reflectivity values because of the inherent difficulty in standardizing these values with spectral-domain OCT

and because these signs may be specific for albinism. This study also showed that atypical foveal hypoplasia (seen in achromatopsia) is associated with worse visual prognosis in comparison with the typical disorders associated with foveal hypoplasia; this is because of the photoreceptor degeneration, visualized on OCT as IS/OS disruption. Interestingly, in achromatopsia there is also a reduction in RT, whereas in typical foveal hypoplasia, there is an increase in RT compared with controls. This paradoxical reduction in RT in achromats is because of the ONL thinning resulting from photoreceptor degeneration. However in achromatopsia, there is still a significantly shallower foveal pit compared with that in controls and incursion of the inner retinal layers. This suggests that the centrifugal displacement of the inner retinal layers is not complete in some patients with achromatopsia.

In summary, a structural grading system for foveal hypoplasia that relates to developmental stages and visual prognosis was developed.

Atypical forms of foveal hypoplasia seen with achromatopsia that is associated with worse visual prognosis resulting from photoreceptor degeneration.

This grading is especially suitable for clinical use because it is qualitative and fast, does not need measurements or specialized analytical software, and hence can be used just by visualizing the OCT.

9. CHAPTER NINE: FINAL DISCUSSION

9.1 THESIS SUMMARY AND IMPLICATIONS

The results presented in this thesis have contributed towards expanding and understanding the genotypic and phenotypic spectrum associated with infantile nystagmus. The first step involved characterising the genotype of the largest reported cohort of patients with IIN. Using the allelic frequency data presented in this thesis along with all previous reports of *FRMD7* mutations we were able to identify mutation hotspots within the *FRMD7* gene, this has implications when developing a genetic test. Based on the data generated and methodology used (such as primer details) for *FRMD7* sequencing, the author contributed towards developing the first clinical genetics test for *FRMD7* mutations worldwide. This was done according to the guidelines stipulated by the United Kingdom Genetic Testing Network (UKGTN) (308) in collaboration with the Regional Genetics Centre based at Nottingham. Thus now patients on the National Health Service have access to a clinical genetics test, which will not only provide the patients with a definitive diagnosis but also help clinical geneticists in giving appropriate genetic counselling and family planning advice.

Previously *FRMD7* sequencing studies (with the exception of the Tarpey et al. study (47)) have had relatively small number of families which has restricted investigators to identify what could be responsible for the variable penetrance in female carriers. Compiling the penetrance results presented in this thesis along with the retrospective cases reported in the literature provided a large series (75 *FRMD7* family pedigrees). Contrary to reports

from Self et al. (62) we did not find any significant effect of mutation type on penetrance. However we found that the mutation location has a significant effect on the penetrance. This again will have implications when giving genetic counselling for families and estimating the risk a daughter is likely to have nystagmus if one of the parents has an *FRMD7* mutation. The author has also presented an overview of the risk of family members developing nystagmus in different scenarios in the following GeneReview: *FRMD7-Related Infantile Nystagmus* (46). The GeneReviews is an international resource funded by the National Institute of Health (NIH) which is freely available and provides physicians, healthcare providers and researcher's up to date medical genetics information.

The genetic basis of idiopathic infantile periodic alternating nystagmus (II-PAN) has been unknown. At the start of my PhD a separate nystagmus locus had been reserved (NYS 5) for this phenotype according to the OMIM records (309). Performing a detailed genotype-phenotype study in patients with II-PAN has provided conclusive evidence that mutations of *FRMD7* are responsible for II-PAN (310). Currently the OMIM records have been corrected and II-PAN is grouped under the NYS1 records (OMIM 310700). Furthermore phenotypic data in patients with II-PAN suggest that the optokinetic reflex arc is affected. This is consistent with *FRMD7* expression within the developing optokinetic and vestibulo-ocular reflex arcs. The phenotypic data presented in this thesis has also contributed to a study comparing the oculomotor abnormalities in *FRMD7* with albinism (234). The clinical implications of the results presented are multi-fold. A patient

presenting to a clinic with II-PAN is a good candidate for genetic testing for *FRMD7* mutations. Furthermore if *FRMD7* mutations are detected additional family members should also be assessed for segregation of both the mutation and the phenotype since we have described for the first time that sibship clustering occurs with this phenotype. The additional clinical implications if a patient is diagnosed with II-PAN are that surgery for correcting head posture is managed differently (177). Thus diagnosing II-PAN prior to performing surgery is pertinent.

In 56 days post ovulation human embryos Tarpey et al. noted *FRMD7* mRNA expression within the retina (47). Similarly while investigating the II-PAN phenotype we showed some retinal expression (310). We expanded on these preliminary finding and showed in a systematic manner that there is indeed both *FRMD7* mRNA and protein expression within the developing retina in not only humans but in mice, rat and zebrafish. Thus in this thesis we present for the first time the detailed spatiotemporal retinal expression profile across different species. This raised an interesting question of whether the retina could be involved in *FRMD7*-related infantile nystagmus.

Prior to investigating the retinal phenotype by optical coherence tomography imaging it was important to assess whether reliable thickness measurements can be derived from patients with infantile nystagmus. We developed a segmentation methodology and showed that there was good agreement of measurements between separate examinations. Furthermore the analytical methods developed during the course of this PhD formed the basis of a number of papers (215,216,220,311).

The retinal expression studies suggest that FRMD7 has a role in migration of retinal cells. Loss of function of FRMD7 can lead to foveal hypoplasia which represents a failure of the centrifugal migration of the inner retinal cells away from the fovea. The findings reported in this thesis suggest that a developmental abnormality within the retina could be the aetiological factor which is responsible for patients developing nystagmus. Betts-Henderson et al. showed using an in-vitro knockdown assay that loss of FRMD7 resulted in shorter neurites with increase in cell number, possibly indicating a sign of immature neuronal cells (86). Herein, we report for the first time the translaminar defects in the parafovea of patients with *FRMD7* mutations. The nuclear and cellular layers were thicker while the nerve fibre layer and plexiform layers were thinner than controls. Based on the results of the in-vitro model it is possible that the translaminar defects represent immature retinal neurons with shorter neurites but with increased cell numbers. The only layer that was unaffected in the parafovea was the outer nuclear layer; this was consistent with findings of *FRMD7* expression within the rod dominated rat retinal tissue which was devoid of expression within the developing outer nuclear layer. This could mean that the rod photoreceptors are unaffected in patients with *FRMD7* mutations, however all other layers anterior to this are affected.

Foveal and parafoveal analysis of patients with *PAX6* mutations, albinism and achromatopsia also showed arrested retinal development. However patients with achromatopsia had atypical features. In albinism and *PAX6* mutations the patients could either have a rudimentary foveal pit or fovea plana;

however in patients with *FRMD7* mutations and achromatopsia a rudimentary foveal pit was always present. This indicated that developmental arrest of the retina can occur before or after the fovea pit formation begins in patients with *PAX6* mutations and albinism however in patients with *FRMD7* mutations and achromatopsia the developmental arrest occurs only after the foveal pit formation begins which suggests that it occurs at a later time point. The translaminar defects associated with albinism and *PAX6* mutations were similar. Retinal nerve fibre layer hypoplasia was a common feature for all disorders; this was observed both in the parafovea and at the optic nerve head. Interestingly in albinism we describe for the first time an asymmetry between the nasal and temporal peripapillary nerve fibre layer. This is likely to be the basis of the VEP asymmetry described in the literature (115,116). This asymmetry was not observed in any other infantile nystagmus forms and thus could potentially be a useful diagnostic indicator.

A number of novel and interesting findings were identified on OCT imaging in patients with achromatopsia. A striking clinical sign detectable on OCT is the hyporeflective zone and disruption of the IS/OS junction which are signs of cone photoreceptor degeneration (220). Previously achromatopsia was considered as a stationary disease; however data presented in this thesis from both the cross sectional study and longitudinal study design show that there are progressive retinal changes which have not previously been described in humans. There is a progressive thinning of the outer nuclear layer with age (220), similarly there is also an increase in the size of the IS/OS junction disruption. The progressive ONL thinning has previously been

reported in knockout mouse studies (288-290). This has clinical implications from both and diagnostic and therapeutic perspective. From a therapeutic perspective it is likely to be useful in the future when gene therapy becomes available; the findings presented in this thesis suggest that early intervention in achromatopsia will probably be more beneficial. Evidence from a phase 1 gene therapy trial in Lebers Congenital Amaurosis showed that the greatest improvement in vision was noted in children compared to adults (312).

The last part of the thesis investigated the relationship between foveal hypoplasia and visual acuity. The aim was to develop a grading system based on the developmental events that were responsible to form the fovea. Four grades of foveal hypoplasia were distinguished grade 1 was associated with the best visual acuity while grade 4 was associated with the worst visual acuity. This was further modelled using a multiple regression and shown that the approximately 61% of the variation in the visual acuity can be accounted for by the OCT grading system. The remainder of the variation in the visual acuity is probably due to the nystagmus, optic nerve malformations or other sources. This has clinical implications because if a patient has foveal hypoplasia it provides information to the clinician regarding their best achievable visual acuity and how much of it is due to the foveal hypoplasia rather than other factors. The effects of foveal hypoplasia on vision are currently irreversible therefore any improvement in vision is likely to arise from correcting other abnormalities such as anterior segment abnormalities or altering the nystagmus characteristics.

9.2 FUTURE WORK

9.2.1 GENETICS

The work presented in this thesis has opened multiple avenues for both molecular genetics and clinical research. There still remain some families (34%) and a large proportion of singletons (86%) with IIN who do not have mutations of the *FRMD7* gene. Thus the genetic basis of their nystagmus is yet to be determined. As highlighted in the thesis we were able to detect a number of intronic mutations due to the unique design of the primer set, however there still remains a large proportion of the introns which have not been sequenced. Linkage analysis in a few families presented by both Tarpey et al. and Self et al. showed linkage to the Xq26.2 (*FRMD7* locus) yet no mutations were detected on sequence analysis (47,79). This suggests that there are mutations within this genomic interval possibly within regulatory domains or the promoter which are yet to be identified. Therefore the next step would be to sequence the entire *FRMD7* gene and flanking bases to determine whether the phenotypes could be arising from unidentified parts of the *FRMD7* gene or other *cis*-acting elements. In families that are negative for mutations within the entire *FRMD7* genomic region whole exome sequencing to identify other nystagmus genes would be important. The preliminary steps for an exome project are already underway this includes developing a control dataset to identify non-pathogenic polymorphisms; a large portion of this data will be available from previous sequencing projects and international initiatives such as the 1000 genomes project. However in

addition to this a number of control samples (without nystagmus) are currently being sequenced.

9.2.2 MOLECULAR BIOLOGY

It still remains unclear whether the *FRMD7* mutation type (truncating vs non-truncating) has varying effects on the mRNA expression and protein localisation. In the Tarpey et al. study it was assumed that all the mutations (missense, splice and nonsense) resulted in a loss of function. Recently Pu et al. showed that missense mutations (c.781C>G and c.886G>C) co-localised in a similar fashion to the wild type, however nonsense mutation c.1003C>T had a nuclear localisation pattern and unlike the wild type did not co-localise in the cytoplasm with F-actin (313). This suggests that the C-terminus could have an important role in trafficking of the FRMD7 protein. In chapter 4 we showed that certain mutations are associated with PAN phenotype, however the reason for why some mutations may cause PAN while others not is unclear. Investigating the expression patterns based on the mutation location and mutation type would provide evidence whether missense mutations could be associated with a dominant negative effect. In order to investigate if there are varying expression patterns the author has collected RNA saliva samples from patients based on which domains have been affected and the mutation type (missense, nonsense and splice). This is currently being investigated in collaboration with Dr. Watkins and Dr. Shackleton (Department of Biochemistry, University of Leicester). Similarly mutant FRMD7 constructs are being developed to investigate the subcellular localisation pattern based on mutation location and mutation type.

The Knockout Mouse Project (KOMP) repository has the largest collection of targeted knockout embryonic stem (ES) cells (http://www.komp.org/). In 2007, FRMD7 was nominated for priority targeting and development of ES cells. Currently the ES cells are available via the KOMP repository for generation of KO FRMD7 mice. Since the hemizygous mutations in humans are not associated with any lethal effects it is unlikely that the generation of the KO mice would result in lethality. Furthermore, histological analysis of retinal and brain sections can also be performed to visualise aberrant neural circuitry or translaminar defects as described in the parafoveal retina of humans. In addition optical coherence tomography would allow high resolution *in vivo* imaging of retina in animals including KO mice.

Recently it has been shown that achiasmatic fish exhibit spontaneous nystagmus with the nystagmus waveforms matching what has been observed in patients with infantile nystagmus syndrome (187,314). Hence performing an *FRMD7* knockdown experiment in zebrafish could potentially be a lot more useful. The preliminary steps towards creating a knockdown assay have been undertaken. In this thesis the author has already characterised the expression pattern for both *FRMD7a* and *FRMD7b*. The morpholinos required to perform the knockdown assays have also been designed in collaboration with Dr. Gesemann and Professor Neuhauss (University of Zurich). The morpholinos have been acquired from Gene Tools (http://www.gene-tools.com/).

9.2.3 CLINICAL PHENOTYPING

At each patient visit eye movement recordings were also obtained from patients undergoing OCT examinations. Therefore the Ophthalmology Group in Leicester has been able to collate a large dataset of eye movement recordings from the different patient groups (*FRMD7*, *PAX6*, albinism and achromatopsia). To date there have been no comparative analysis of null zone characteristics between these 4 groups. The CEMAS classification suggests that all conditions grouped under the infantile nystagmus syndrome group have similar oculomotor characteristics. Interestingly the preliminary analysis of the null zone dataset shows some interesting trends, with no discernable null zone in the achromatopsia group (figure 9.1). However in the albinism group there is a distinct null zone in most patients. The *PAX6* and *FRMD7* groups tend to be more heterogeneous. This suggests that there could be oculomotor distinctions within the INS group. Recent evidence from Kumar et al. also suggests that there are differences in oculomotor and clinical characteristics between albinism and patients with *FRMD7* mutations (234). The null zone characteristics could be further evaluated along with the nystagmus waveform in relation to the genotypes and retinal phenotypes.
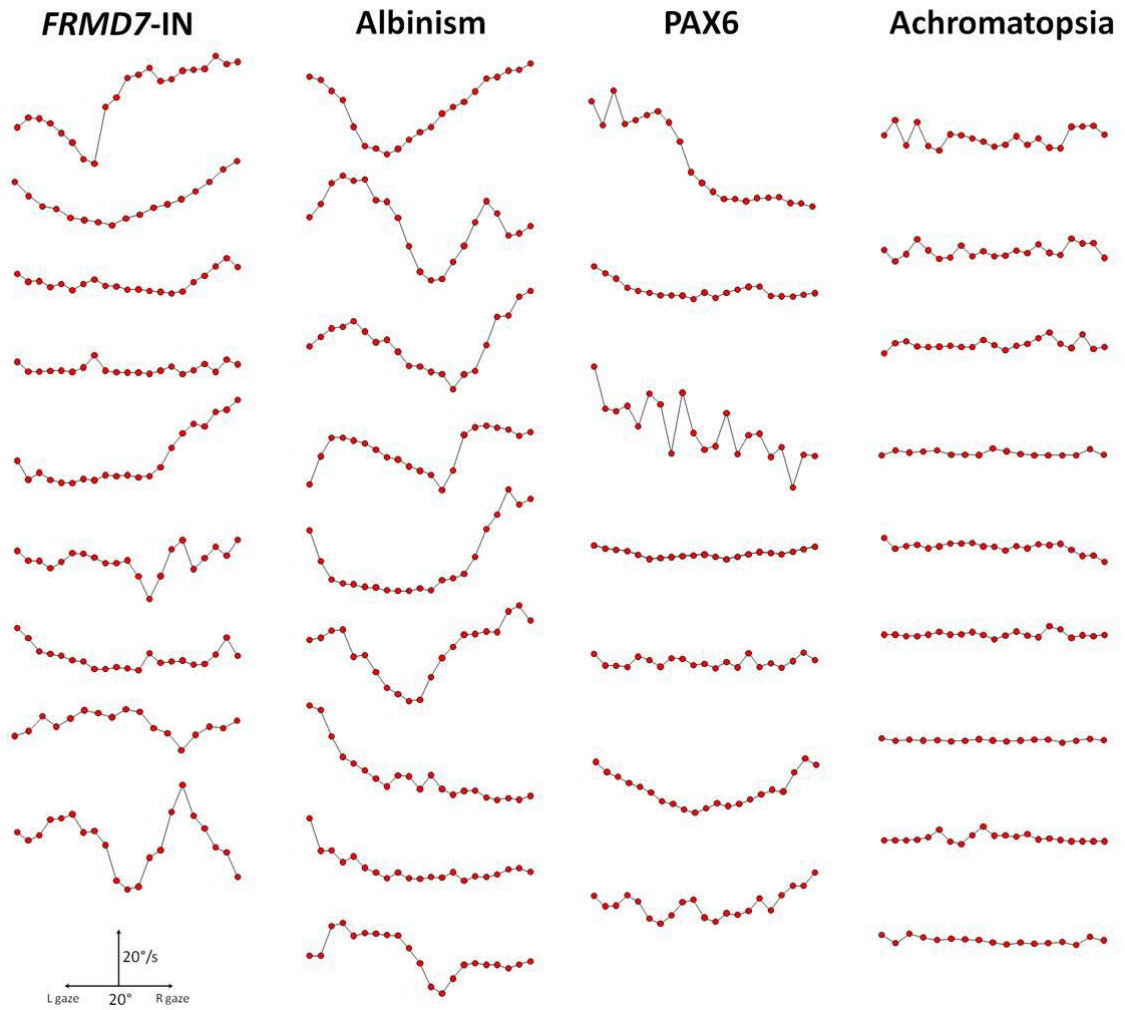
Figure 9.1: *Examples of intensity versus gaze position plots in patients with FRMD7 mutations, PAX6 mutations, albinism and achromatopsia.*

In patients with achromatopsia there has been one study showing age related changes in nystagmus waveform (315). This is an interesting observation and it would be useful to assess if there was any relationship between the age dependent changes in the retinal phenotypes obtained using OCT and the age dependent changes of nystagmus. If there is a relationship this would provide further evidence that the nystagmus is closely related to the retinal pathology.

From the cross sectional dataset obtained in chapter 8 we could not find any relationship between age and the degree of foveal hypoplasia. However we were not able to obtain OCT images from very young patients who could have progressive retinal changes. The recent procurement of the hand-held OCT by the Ophthalmology Group will give us the opportunity to obtain OCT from infants and very young children; this will allow to see whether there are any dynamic changes to the intra retinal layers during the early stages of postnatal foveal development. Characterising these changes will be essential since it would give an idea whether therapeutic strategies could influence the foveal development.

An important future study will involve expanding on the current regression model developed for predicting visual acuity in patients with infantile nystagmus. As previously mentioned eye movement recordings have also been acquired during the patient visit, therefore including oculomotor characteristics such as amplitude, frequency and foveation (for e.g. the eXpanded Nystagmus Acuity Function (NAFX)) in the model is likely to further reduce the residual variation. Therefore the model would be able to account for both the effects of foveal hypoplasia and nystagmus on the variation of visual acuity.

The aim of this PhD was to produce translational research, which has bench to bedside implications and ultimately benefits patients with infantile nystagmus. This has been achieved by exploring the genotypic characteristics combined with relevant cellular phenotypic studies and finally applying the results to clinical phenotyping studies.

10. CHAPTER TEN: BIBLIOGRAPHY

(1) Du Laurens A, Surflet R. A discourse of the preseruation of the sight: of melancholike diseases; of rheumes, and of old age. Composed by M. Andreas Laurentius, ordinarie phisition to the King, and publike professor of phisicke in the Vniuersitie of Mompelier. Translated out of French into English, according to the last edition, by Richard Surphlet, practitioner in phisicke. At London: Imprinted by Felix Kingston, for Ralph Iacson, dwelling in Paules Church yard at the signe of the Swan; 1599.

(2) Rossi EA, Roorda A. The relationship between visual resolution and cone spacing in the human fovea. Nat Neurosci 2010 Feb;13(2):156-157.

(3) Martinez-Conde S, Macknik SL, Hubel DH. The role of fixational eye movements in visual perception. Nat Rev Neurosci 2004 Mar;5(3):229-240.

(4) Long GM, Homolka JL. Contrast sensitivity during horizontal visual pursuit: dynamic sensitivity functions. Perception 1992;21(6):753-764.

(5) Leigh RJ. The neurology of eye movements. 4th ed. Oxford: Oxford University Press; 2006.

(6) American Academy of Ophthalmology. Fundamentals and principles of ophthalmology, 2005-2006. San Francisco, CA: American Academy of Ophthalmology; 2005.

(7) Yuodelis C, Hendrickson A. A qualitative and quantitative analysis of the human fovea during development. Vision Res 1986;26(6):847-855.

(8) Kandel ER, Schwartz JH, Jessell TM. Principles of neural science. 4th ed. New York ; London: McGraw-Hill; 2000.

(9) Wolburg H, Willbold E, Layer PG. Muller glia endfeet, a basal lamina and the polarity of retinal layers form properly in vitro only in the presence of marginal pigmented epithelium. Cell Tissue Res 1991 Jun;264(3):437-451.

(10) Prada C, Puelles L, Genis-Galvez JM. A golgi study on the early sequence of differentiation of ganglion cells in the chick embryo retina. Anat Embryol (Berl) 1981;161(3):305-317.

(11) Prada C, Puelles L, Genis-Galvez JM, Ramirez G. Two modes of free migration of amacrine cell neuroblasts in the chick retina. Anat Embryol (Berl) 1987;175(3):281-287.

(12) Gray H, Standring S, Ellis H, Berkovitz BKB. Gray's anatomy : the anatomical basis of clinical practice. . 39th ed. Edinburgh: Elsevier Churchill Livingstone; 2005. p. 1321-1361.

(13) Springer AD, Hendrickson AE. Development of the primate area of high acuity. 1. Use of finite element analysis models to identify mechanical variables affecting pit formation. Vis Neurosci 2004 Jan-Feb;21(1):53-62.

(14) Dorland WAN, Anderson DM. Dorland's illustrated medical dictionary [chief lexicographer Douglas M. Anderson]. 30th ed. Philadelphia, Pa. ; London: W.B. Saunders; 2003.

(15) Michel J. Historical research on the discovery of nystagmus and its physiopathologic significance | Recherches historiques sur la découverte du nystagmus et de sa signification physio-pathologique. Revue du Praticien 1990;40(23):2163-2166.

(16) Casteels I, Harris CM, Shawkat F, Taylor D. Nystagmus in infancy. Br J Ophthalmol 1992;76(7):434-437.

(17) McLean R, Proudlock F, Thomas S, Degg C, Gottlob I. Congenital nystagmus: randomized, controlled, double-masked trial of memantine/gabapentin. Ann Neurol 2007 Feb;61(2):130-138.

(18) Dell'Osso LF, Daroff RB. Congenital nystagmus waveforms and foveation strategy. Documenta Ophthalmologica 1975;39(1):155-182.

(19) Averbuch-Heller L, Dell'Osso LF, Leigh RJ, Jacobs JB, Stahl JS. The torsional component of "horizontal" congenital nystagmus. Journal of Neuro-Ophthalmology 2002;22(1):22-32.

(20) Serra A, Dell'Osso LF, Jacobs JB, Burnstine RA. Combined gaze-angle and vergence variation in infantile nystagmus: two therapies that improve the high-visual-acuity field and methods to measure it. Invest Ophthalmol 2006;47(6):2451-2460.

(21) Tkalcevic LA, Abel LA. The effects of increased visual task demand on foveation in congenital nystagmus. Vision Res 2005;45(9):1139-1146.

(22) Shibasaki H, Yamashita Y, Motomura S. Suppression of congenital nystagmus. Journal of Neurology Neurosurgery and Psychiatry 1978;41(12):1078-1083.

(23) Dickinson CM. The elucidation and use of the effect of near fixation in congenital nystagmus. Ophthalmic and Physiological Optics 1986;6(3):303-311.

(24) Thomas MG, Gottlob I, McLean RJ, Maconachie G, Kumar A, Proudlock FA. Reading strategies in infantile nystagmus syndrome. Invest Ophthalmol Vis Sci 2011 Oct 17;52(11):8156-8165.

(25) Levin LA, Albert DM. Ocular Disease: Mechanisms and Management: Expert Consult - Online and Print. : Elsevier Health Sciences; 2010.

(26) Chung ST, Bedell HE. Velocity criteria for "foveation periods" determined from image motions simulating congenital nystagmus. Optom Vis Sci 1996 Feb;73(2):92-103.

(27) Carpenter RHS. Movements of the eyes. 2nd ed.: Pion; 1988.

(28) Cogan DG. Congenital nystagmus. Can J Ophthalmol 1967 Jan;2(1):4-10.

(29) Dell'osso LF, Hertle RW, Daroff RB. "Sensory" and "motor" nystagmus: erroneous and misleading terminology based on misinterpretation of David Cogan's observations. Arch Ophthalmol 2007 Nov;125(11):1559-1561.

(30) Hertle RW, Bedell HE, Dell'Osso LF, Leigh RJ, Avallone J, Birch EE, et al. A Classification of Eye Movement Abnormalities and Strabismus (CEMAS). 2001; Available at: http://www.nei.nih.gov/news/statements/cemas.pdf. Accessed 01/23, 2008.

(31) Chao LY, Mishra R, Strong LC, Saunders GF. Missense mutations in the DNA-binding region and termination codon in PAX6. Hum Mutat 2003 Feb;21(2):138-145.

(32) Kupersmith MJ. Practical classification of nystagmus in the clinic. Arch Ophthalmol 2008 Jun;126(6):871-2; author reply 872.

(33) Dell'Osso LF, Hertle RW, Daroff RB. Practical classification of nystagmus in the clinic - Reply. Arch Ophthalmol 2008;126(6):872.

(34) Jacobs JB, Dell'Osso LF. Congenital nystagmus: hypotheses for its genesis and complex waveforms within a behavioral ocular motor system model. J Vis 2004 Jul 27;4(7):604-625.

(35) Optican LM, Zee DS. A hypothetical explanation of congenital nystagmus. Biol Cybern 1984;50(2):119-134.

(36) Barreiro AK, Bronski JC, Anastasio TJ. Bifurcation theory explains waveform variability in a congenital eye movement disorder. J Comput Neurosci 2009 Apr;26(2):321-329.

(37) Leigh RJ, Khanna S. What can acquired nystagmus tell us about congenital forms of nystagmus? Semin Ophthalmol 2006 Apr-Jun;21(2):83-86.

(38) SWANZY HR, Sir. A Handbook of the Diseases of the Eye and their treatment ... Fifth edition ... Edited ... by L. Werner. pp. xviii. 582. H. K. Lewis: London; 1895.

(39) Harris C, Berry D. A developmental model of infantile nystagmus. Semin Ophthalmol 2006 Apr-Jun;21(2):63-69.

(40) Sarvananthan N, Surendran M, Roberts E, Jain S, Thomas S, Shah N, et al. The prevalence of nystagmus: The Leicestershire nystagmus survey. Invest Ophthalmol Vis Sci 2009 May 20.

(41) Pilling RF, Thompson JR, Gottlob I. Social and visual function in nystagmus. Br J Ophthalmol 2005;89(10):1278-1281.

(42) Bury M. Chronic illness as biographical disruption. Sociology of Health and Illness 1982;4(2):167-182.

(43) Green G, Todd J, Pevalin D. Biographical disruption associated with multiple sclerosis: Using propensity scoring to assess the impact. Social Science and Medicine 2007;65(3):524-535.

(44) Goffman E. Stigma and social identity. Stigma: notes on the management of spoiled identity 1963:1-19.

(45) Goffman E. Stigma: Notes on the Management of Spoiled Identity. Harmondsworth: Penguin 1968.

(46) Thomas MG, Thomas S, Kumar A, Proudlock FA, Gottlob I. *FRMD7*-Related Infantile Nystagmus. In: Pagon RA, editor. GeneReviews at GeneTests Seattle: University of Washington; 2009.

(47) Tarpey P, Thomas S, Sarvananthan N, Mallya U, Lisgo S, Talbot CJ, et al. Mutations in FRMD7, a newly identified member of the FERM family, cause X-linked idiopathic congenital nystagmus. Nat Genet 2006 Nov;38(11):1242-1244.

(48) Kerrison JB, Arnould VJ, Barmada MM, Koenekoop RK, Schmeckpeper BJ, Maumenee IH. A gene for autosomal dominant congenital nystagmus localizes to 6p12. Genomics 1996 May 1;33(3):523-526.

(49) Klein C, Vieregge P, Heide W, Kemper B, Hagedorn-Greiwe M, Hagenah J, et al. Exclusion of chromosome regions 6p12 and 15q11, but not chromosome region 7p11, in a German family with autosomal dominant congenital nystagmus. Genomics 1998 Nov 15;54(1):176-177.

(50) Ragge NK, Hartley C, Dearlove AM, Walker J, Russell-Eggitt I, Harris CM. Familial vestibulocerebellar disorder maps to chromosome 13q31-q33: a new nystagmus locus. J Med Genet 2003 Jan;40(1):37-41.

(51) Cabot A, Rozet JM, Gerber S, Perrault I, Ducroq D, Smahi A, et al. A gene for X-linked idiopathic congenital nystagmus (NYS1) maps to chromosome Xp11.4-p11.3. Am J Hum Genet 1999 Apr;64(4):1141-1146.

(52) Hertle RW, Yang D, Kelly K, Hill VM, Atkin J, Seward A. X-linked infantile periodic alternating nystagmus. Ophthalmic Genet 2005 Jun;26(2):77-84.

(53) Dell'Osso LF, Weissman BM, Leigh RJ, Abel LA, Sheth NV. Hereditary congenital nystagmus and gaze-holding failure: the role of the neural integrator. Neurology 1993 Sep;43(9):1741-1749.

(54) Hayasaka S. Hereditary congenital nystagmus. A Japanese pedigree. Ophthalmic Paediatr Genet 1986;7(1):73-76.

(55) Forssman B. Hereditary studies of congenital nystagmus in a Swedish population. Ann Hum Genet 1971;35(2):119-138.

(56) Harcourt B. Hereditary nystagmus in early childhood. J Med Genet 1970;7(3):253-256.

(57) Burton-Fanning FW. HEREDITARY CONGENITAL NYSTAGMUS. The Lancet 1895;146(3772):1497.

(58) Patton MA, Jeffery S, Lee N, Hogg C. Congenital nystagmus cosegregating with a balanced 7;15 translocation. J Med Genet 1993 Jun;30(6):526-528.

(59) Kerrison JB, Koenekoop RK, Arnould VJ, Zee D, Maumenee IH. Clinical features of autosomal dominant congenital nystagmus linked to chromosome 6p12. Am J Ophthalmol 1998 Jan;125(1):64-70.

(60) Harris CM, Walker J, Shawkat F, Wilson J, Russell-Eggitt I. Eye movements in a familial vestibulocerebellar disorder. Neuropediatrics 1993 Jun;24(3):117-122.

(61) WAARDENBURG PJ. Genetics and Ophthalmology. Blackwell Scientific Publications: Oxford; Assen printed; 1961.

(62) Self J, Lotery A. A review of the molecular genetics of congenital Idiopathic Nystagmus (CIN). Ophthalmic Genet 2007 Dec;28(4):187-191.

(63) Kerrison JB, Vagefi MR, Barmada MM, Maumenee IH. Congenital motor nystagmus linked to Xq26-q27. American Journal of Human Genetics 1999;64(2):600-607.

(64) Forssman B, Ringnér B. Prevalence and inheritance of congenital nystagmus in a Swedish population. Ann Hum Genet 1971;35(2):139-147.

(65) Schneiderman LJ, Bartnof HS, Worthen DM. X-linked congenital nystagmus: A problem in genetic counseling. Ann Ophthalmol 1976;8(4):444-446.

(66) Huygen PLM, Verhagen WIM, Cruysberg JRM, Koch PAM. Familial congenital periodic alternating nystagmus with presumably X-linked dominant inheritance. Neuro-Ophthalmology 1995;15(3):149-155.

(67) Matton MT, Dewachter A, De Bie S, De Laey JJ. Genetic counseling for congenital nystagmus. Ophthalmic Paediatr Genet 1982;1(2):107-112.

(68) Kerrison JB, Giorda R, Lenart TD, Drack AV, Maumenee IH. Clinical and genetic analysis of a family with X-linked congenital nystagmus (NYS1). Ophthalmic Genetics 2001;22(4):241-248.

(69) Oetting WS, Armstrong CM, Holleschau AM, DeWan AT, Summers CG. Evidence for genetic heterogeneity in families with congenital motor nystagmus (CN). Ophthalmic Genet 2000;21(4):227-233.

(70) Mellott ML, Brown Jr. J, Fingert JH, Taylor CM, Keech RV, Sheffield VC, et al. Clinical characterization and linkage analysis of a family with congenital X-linked nystagmus and deuteranomaly. Arch Ophthalmol 1999;117(12):1630-1633.

(71) Liu ZR, Zhang BR, Ding MP, Xia K, Hu ZM, Deng H, et al. Mapping of a pedigree with congenital nystagmus. Yi chuan = Hereditas / Zhongguo yi chuan xue hui bian ji. 2004;26(4):437-440.

(72) Zhang B, Xia K, Ding M, Liang D, Liu Z, Pan Q, et al. Confirmation and refinement of a genetic locus of congenital motor nystagmus in Xq26.3-q27.1 in a Chinese family. Hum Genet 2005 Jan;116(1-2):128-131.

(73) Guo X, Li S, Jia X, Xiao X, Wang P, Zhang Q. Linkage analysis of two families with X-linked recessive congenital motor nystagmus. J Hum Genet 2006;51(1):76-80.

(74) Self JE, Ennis S, Collins A, Shawkat F, Harris CM, Mackey DA, et al. Fine mapping of the X-linked recessive congenital idiopathic nystagmus locus at Xq24-q26.3. Molecular Vision 2006;12.

(75) Schorderet DF, Tiab L, Gaillard MC, Lorenz B, Klainguti G, Kerrison JB, et al. Novel mutations in FRMD7 in X-linked congenital nystagmus. Mutation in brief #963. Online. Hum Mutat 2007 May;28(5):525.

(76) Zhang Q, Xiao X, Li S, Guo X. FRMD7 mutations in Chinese families with X-linked congenital motor nystagmus. Mol Vis 2007 Aug 3;13:1375-1378.

(77) Zhang B, Liu Z, Zhao G, Xie X, Yin X, Hu Z, et al. Novel mutations of the FRMD7 gene in X-linked congenital motor nystagmus. Mol Vis 2007 Sep 13;13:1674-1679.

(78) Shiels A, Bennett TM, Prince JB, Tychsen L. X-linked idiopathic infantile nystagmus associated with a missense mutation in FRMD7. Mol Vis 2007 Nov 29;13:2233-2241.

(79) Self JE, Shawkat F, Malpas CT, Thomas NS, Harris CM, Hodgkins PR, et al. Allelic variation of the FRMD7 gene in congenital idiopathic nystagmus. Arch Ophthalmol 2007 Sep;125(9):1255-1263.

(80) Li N, Wang L, Cui L, Zhang L, Dai S, Li H, et al. Five novel mutations of the FRMD7 gene in Chinese families with X-linked infantile nystagmus. Mol Vis 2008 Apr 18;14:733-738.

(81) Kaplan Y, Vargel I, Kansu T, Akin B, Rohmann E, Kamaci S, et al. Skewed X inactivation in an X linked nystagmus family resulted from a novel, p.R229G, missense mutation in the FRMD7 gene. Br J Ophthalmol 2008 Jan;92(1):135-141.

(82) He X, Gu F, Wang Y, Yan J, Zhang M, Huang S, et al. A novel mutation in FRMD7 causing X-linked idiopathic congenital nystagmus in a large family. Mol Vis 2008 Jan 11;14:56-60.

(83) Li N, Wang X, Wang Y, Wang L, Ying M, Han R, et al. Investigation of the gene mutations in two Chinese families with X-linked infantile nystagmus. Mol Vis 2011 Feb 11;17:461-468.

(84) Fingert JH, Roos B, Eyestone ME, Pham JD, Mellot ML, Stone E. Novel intragenic FRMD7 deletion in a pedigree with congenital X-linked nystagmus. Ophthalmic Genet 2010 Jun;31(2):77-80.

(85) He X, Gu F, Wang Z, Wang C, Tong Y, Wang Y, et al. A novel frameshift mutation in FRMD7 causing X-linked idiopathic congenital nystagmus. Genet Test 2008 Dec;12(4):607-613.

(86) Betts-Henderson J, Bartesaghi S, Crosier M, Lindsay S, Chen HL, Salomoni P, et al. The nystagmus-associated FRMD7 gene regulates neuronal outgrowth and development. Hum Mol Genet 2009 Nov 5;19(2):342-351.

(87) Kubo T, Yamashita T, Yamaguchi A, Sumimoto H, Hosokawa K, Tohyama M. A novel FERM domain including guanine nucleotide exchange factor is involved in Rac

signaling and regulates neurite remodeling. Journal of Neuroscience 2002;22(19):8504-8513.

(88) Toyofuku T, Yoshida J, Sugimoto T, Zhang H, Kumanogoh A, Hori M, et al. FARP2 triggers signals for Sema3A-mediated axonal repulsion. Nat Neurosci 2005 Dec;8(12):1712-1719.

(89) Gottlob I. Infantile nystagmus. Development documented by eye movement recordings. Invest Ophthalmol Vis Sci 1997 Mar;38(3):767-773.

(90) Hertle RW, Maldanado VK, Maybodi M, Yang D. Clinical and ocular motor analysis of the infantile nystagmus syndrome in the first 6 months of life. Br J Ophthalmol 2002 Jun;86(6):670-675.

(91) Thomas S, Proudlock FA, Sarvananthan N, Roberts EO, Awan M, McLean R, et al. Phenotypical characteristics of idiopathic infantile nystagmus with and without mutations in FRMD7. Brain 2008 Mar 27;131(5):1259-1267.

(92) Hertle RW, Dell'Osso LF. Clinical and ocular motor analysis of congenital nystagmus in infancy. J AAPOS 1999;3(2):70-79.

(93) Ukwade MT, Bedell HE. Stereothresholds in persons with congenital nystagmus and in normal observers during comparable retinal image motion. Vision Res 1999;39(17):2963-2973.

(94) Brodsky MC, Fray KJ. The prevalence of strabismus in congenital nystagmus: the influence of anterior visual pathway disease. J AAPOS 1997 Mar;1(1):16-19.

(95) Abadi RV, Bjerre A. Motor and sensory characteristics of infantile nystagmus. Br J Ophthalmol 2002;86(10):1152-1160.

(96) Hertle RW, Zhu X. Oculographic and clinical characterization of thirty-seven children with anomalous head postures, nystagmus, and strabismus: the basis of a clinical algorithm. J AAPOS 2000;4(1):25-32.

(97) Stevens DJ, Hertle RW. Relationships between visual acuity and anomalous head posture in patients with congenital nystagmus. J Pediatr Ophthalmol Strabismus 2003;40(5):259-264.

(98) Cesarelli M, Bifulco P, Loffredo L, Bracale M. Relationship between visual acuity and eye position variability during foveations in congenital nystagmus. Documenta Ophthalmologica 2000;101(1):59-72.

(99) Gottlob I. Nystagmus. Curr Opin Ophthalmol 2000 Oct;11(5):330-335.

(100) Oetting WS, King RA. Molecular basis of albinism: Mutations and polymorphisms of pigmentation genes associated with albinism. Hum Mutat 1999;13(2):99-115.

(101) King RA, Jackson OJ, Oetting WS. Molecular genetics of inherited eye disorders. In: Wright AF, Jay B, editors. Modern genetics ; vol.2 Switzerland ; Great Britain: Harwood Academic; 1994. p. 89-122.

(102) American Academy of Ophthalmology. Neuro-ophthalmology, 2005-2006. San Francisco, CA: American Academy of Ophthalmology; 2005.

(103) Oetting WS. New insights into ocular albinism type 1 (OA1): Mutations and polymorphisms of the OA1 gene. Hum Mutat 2002 Feb;19(2):85-92.

(104) Oetting WS, Fryer JP, Shriram S, King RA. Oculocutaneous albinism type 1: the last 100 years. Pigment Cell Res 2003 Jun;16(3):307-311.

(105) Okulicz JF, Shah RS, Schwartz RA, Janniger CK. Oculocutaneous albinism. J Eur Acad Dermatol Venereol 2003 May;17(3):251-256.

(106) Tomita Y, Takeda A, Okinaga S, Tagami H, Shibahara S. Human oculocutaneous albinism caused by single base insertion in the tyrosinase gene. Biochem Biophys Res Commun 1989 Nov 15;164(3):990-996.

(107) Durham-Pierre D, Gardner JM, Nakatsu Y, King RA, Francke U, Ching A, et al. African origin of an intragenic deletion of the human P gene in tyrosinase positive oculocutaneous albinism. Nat Genet 1994 Jun;7(2):176-179.

(108) Boissy RE, Zhao H, Oetting WS, Austin LM, Wildenberg SC, Boissy YL, et al. Mutation in and lack of expression of tyrosinase-related protein-1 (TRP-1) in melanocytes from an individual with brown oculocutaneous albinism: a new subtype of albinism classified as "OCA3". Am J Hum Genet 1996 Jun;58(6):1145-1156.

(109) Newton JM, Cohen-Barak O, Hagiwara N, Gardner JM, Davisson MT, King RA, et al. Mutations in the human orthologue of the mouse underwhite gene (uw) underlie a new form of oculocutaneous albinism, OCA4. Am J Hum Genet 2001 Nov;69(5):981-988.

(110) Bassi MT, Schiaffino MV, Renieri A, De Nigris F, Galli L, Bruttini M, et al. Cloning of the gene for ocular albinism type 1 from the distal short arm of the X chromosome. Nat Genet 1995 May;10(1):13-19.

(111) Collewijn H, Apkarian P, Spekreijse H. The oculomotor behaviour of human albinos. Brain 1985;108(1):1-28.

(112) Guyton AC, Hall JE. Textbook of medical physiology. . 11th ed. Philadelphia, Pa.: Elsevier Saunders; 2006. p. 626-650.

(113) Chong GT, Farsiu S, Freedman SF, Sarin N, Koreishi AF, Izatt JA, et al. Abnormal foveal morphology in ocular albinism imaged with spectral-domain optical coherence tomography. Arch Ophthalmol 2009 Jan;127(1):37-44.

(114) Russell-Eggitt I, Kriss A, Taylor DS. Albinism in childhood: a flash VEP and ERG study. Br J Ophthalmol 1990 Mar;74(3):136-140.

(115) Apkarian P, Reits D, Spekreijse H, Van Dorp D. A decisive electrophysiological test for human albinism. Electroencephalogr Clin Neurophysiol 1983 May;55(5):513-531.

(116) Apkarian P, Shallo-Hoffmann J. VEP projections in congenital nystagmus; VEP asymmetry in albinism: a comparison study. Invest Ophthalmol Vis Sci 1991 Aug;32(9):2653-2661.

(117) King RA, Pietsch J, Fryer JP, Savage S, Brott MJ, Russell-Eggitt I, et al. Tyrosinase gene mutations in oculocutaneous albinism 1 (OCA1): definition of the phenotype. Hum Genet 2003 Nov;113(6):502-513.

(118) Fryer JP, Oetting WS, King RA. Identification and characterization of a DNase hypersensitive region of the human tyrosinase gene. Pigment Cell Res 2003 Dec;16(6):679-684.

(119) Kedda MA, Stevens G, Manga P, Viljoen C, Jenkins T, Ramsay M. The tyrosinase-positive oculocutaneous albinism gene shows locus homogeneity on chromosome 15q11-q13 and evidence of multiple mutations in southern African negroids. Am J Hum Genet 1994 Jun;54(6):1078-1084.

(120) Manga P, Kromberg JG, Box NF, Sturm RA, Jenkins T, Ramsay M. Rufous oculocutaneous albinism in southern African Blacks is caused by mutations in the TYRP1 gene. Am J Hum Genet 1997 Nov;61(5):1095-1101.

(121) Inagaki K, Suzuki T, Shimizu H, Ishii N, Umezawa Y, Tada J, et al. Oculocutaneous albinism type 4 is one of the most common types of albinism in Japan. Am J Hum Genet 2004 Mar;74(3):466-471.

(122) Hegde M, Lewis RA, Richards CS. Diagnostic DNA testing for X-linked ocular albinism (OA1) with a hierarchical mutation screening protocol. Genet Test 2002 Spring;6(1):7-14.

(123) University of Colorado Denver. Denver Genetics, Tests. Available at: http://www.ucdenver.edu/ACADEMICS/COLLEGES/MEDICALSCHOOL/PROGRAMS/GENETICS/DIAGNOSTICTESTS/Pages/default.aspx#tab-2. Accessed 08/12, 2010.

(124) Sundin OH, Yang JM, Li Y, Zhu D, Hurd JN, Mitchell TN, et al. Genetic basis of total colourblindness among the Pingelapese islanders. Nat Genet 2000 Jul;25(3):289-293.

(125) Kohl S, Marx T, Giddings I, Jagle H, Jacobson SG, Apfelstedt-Sylla E, et al. Total colourblindness is caused by mutations in the gene encoding the alpha-subunit of the cone photoreceptor cGMP-gated cation channel. Nat Genet 1998 Jul;19(3):257-259.

(126) Wissinger B, Gamer D, Jagle H, Giorda R, Marx T, Mayer S, et al. CNGA3 mutations in hereditary cone photoreceptor disorders. Am J Hum Genet 2001 Oct;69(4):722-737.

(127) Kohl S, Baumann B, Rosenberg T, Kellner U, Lorenz B, Vadala M, et al. Mutations in the cone photoreceptor G-protein alpha-subunit gene GNAT2 in patients with achromatopsia. Am J Hum Genet 2002 Aug;71(2):422-425.

(128) Morton NE, Lew R, Hussels IE, Little GF. Pingelap and Mokil Atolls: historical genetics. Am J Hum Genet 1972 May;24(3):277-289.

(129) Thiadens AA, den Hollander AI, Roosing S, Nabuurs SB, Zekveld-Vroon RC, Collin RW, et al. Homozygosity mapping reveals PDE6C mutations in patients with early-onset cone photoreceptor disorders. Am J Hum Genet 2009 Aug;85(2):240-247.

(130) Kohl S, Varsanyi B, Antunes GA, Baumann B, Hoyng CB, Jagle H, et al. CNGB3 mutations account for 50% of all cases with autosomal recessive achromatopsia. Eur J Hum Genet 2005 Mar;13(3):302-308.

(131) Pediatric neuro-ophthalmology. 2nd ed. New York ; London: Springer; 2009.

(132) Thiadens AA, Roosing S, Collin RW, van Moll-Ramirez N, van Lith-Verhoeven JJ, van Schooneveld MJ, et al. Comprehensive analysis of the achromatopsia genes CNGA3 and CNGB3 in progressive cone dystrophy. Ophthalmology 2010 Apr;117(4):825-30.e1.

(133) Thiadens AA, Slingerland NW, Roosing S, van Schooneveld MJ, van Lith-Verhoeven JJ, van Moll-Ramirez N, et al. Genetic etiology and clinical consequences of complete and incomplete achromatopsia. Ophthalmology 2009 Oct;116(10):1984-9.e1.

(134) Sharpe LT, Stockman A, Jagle H, Nathans J. Opsin genes, cone photopigments, color vision, and color blindness. In: Gegenfurtner KR, Sharpe LT, editors. Color vision : from genes to perception Cambridge: Cambridge University Press; 1999. p. 3-52.

(135) Rosenberg T, Baumann B, Kohl S, Zrenner E, Jorgensen AL, Wissinger B. Variant phenotypes of incomplete achromatopsia in two cousins with GNAT2 gene mutations. Invest Ophthalmol Vis Sci 2004 Dec;45(12):4256-4262.

(136) Berson EL, Sandberg MA, Rosner B, Sullivan PL. Color plates to help identify patients with blue cone monochromatism. Am J Ophthalmol 1983 Jun;95(6):741-747.

(137) Barthelmes D, Sutter FK, Kurz-Levin MM, Bosch MM, Helbig H, Niemeyer G, et al. Quantitative analysis of OCT characteristics in patients with achromatopsia and blue-cone monochromatism. Invest Ophthalmol Vis Sci 2006 Mar;47(3):1161-1166.

(138) Lambert SR, Taylor D, Kriss A. The infant with nystagmus, normal appearing fundi, but an abnormal ERG. Surv Ophthalmol 1989 Nov-Dec;34(3):173-186.

(139) Jordan T, Hanson I, Zaletayev D, Hodgson S, Prosser J, Seawright A, et al. The human PAX6 gene is mutated in two patients with aniridia. Nat Genet 1992 Aug;1(5):328-332.

(140) Hanson IM, Seawright A, Hardman K, Hodgson S, Zaletayev D, Fekete G, et al. PAX6 mutations in aniridia. Hum Mol Genet 1993 Jul;2(7):915-920.

(141) Prosser J, van Heyningen V. PAX6 mutations reviewed. Hum Mutat 1998;11(2):93-108.

(142) van Heyningen V, Williamson KA. PAX6 in sensory development. Hum Mol Genet 2002 May 15;11(10):1161-1167.

(143) Sisodiya SM, Free SL, Williamson KA, Mitchell TN, Willis C, Stevens JM, et al. PAX6 haploinsufficiency causes cerebral malformation and olfactory dysfunction in humans. Nat Genet 2001 Jul;28(3):214-216.

(144) Glaser T, Jepeal L, Edwards JG, Young SR, Favor J, Maas RL. PAX6 gene dosage effect in a family with congenital cataracts, aniridia, anophthalmia and central nervous system defects. Nat Genet 1994 Aug;7(4):463-471.

(145) Azuma N, Yamaguchi Y, Handa H, Tadokoro K, Asaka A, Kawase E, et al. Mutations of the PAX6 gene detected in patients with a variety of optic-nerve malformations. Am J Hum Genet 2003 Jun;72(6):1565-1570.

(146) Hingorani M, Williamson KA, Moore AT, van Heyningen V. Detailed ophthalmologic evaluation of 43 individuals with PAX6 mutations. Invest Ophthalmol Vis Sci 2009 Jun;50(6):2581-2590.

(147) Gronskov K, Rosenberg T, Sand A, Brondum-Nielsen K. Mutational analysis of PAX6: 16 novel mutations including 5 missense mutations with a mild aniridia phenotype. Eur J Hum Genet 1999 Apr;7(3):274-286.

(148) Arroyave CP, Scott IU, Gedde SJ, Parrish RK,2nd, Feuer WJ. Use of glaucoma drainage devices in the management of glaucoma associated with aniridia. Am J Ophthalmol 2003 Feb;135(2):155-159.

(149) Hodgson SV, Saunders KE. A probable case of the homozygous condition of the aniridia gene. J Med Genet 1980 Dec;17(6):478-480.

(150) Robinson DO, Howarth RJ, Williamson KA, van Heyningen V, Beal SJ, Crolla JA. Genetic analysis of chromosome 11p13 and the PAX6 gene in a series of 125 cases referred with aniridia. Am J Med Genet A 2008 Mar 1;146A(5):558-569.

(151) Rosen S, Skaletsky HJ. Primer3 on the WWW for general users and for biologist programmers. In: Krawetz S, Misener S, editors. Bioinformatics Methods and Protocols: Methods in Molecular Biology Totowa, NJ: Humana Press; 2000. p. 365-386.

(152) Andreson R, Reppo E, Kaplinski L, Remm M. GENOMEMASKER package for designing unique genomic PCR primers. BMC Bioinformatics 2006 Mar 27;7:172.

(153) Garnier J, Osguthorpe DJ, Robson B. Analysis of the accuracy and implications of simple methods for predicting the secondary structure of globular proteins. J Mol Biol 1978 Mar 25;120(1):97-120.

(154) Capriotti E, Fariselli P, Casadio R. I-Mutant2.0: predicting stability changes upon mutation from the protein sequence or structure. Nucleic Acids Res 2005 Jul 1;33(Web Server issue):W306-10.

(155) Emsley P, Cowtan K. Coot: model-building tools for molecular graphics. Acta Crystallogr D Biol Crystallogr 2004 Dec;60(Pt 12 Pt 1):2126-2132.

(156) Wang M, Marín A. Characterization and prediction of alternative splice sites. Gene 2006;366(2):219-227.

(157) den Dunnen JT, Antonarakis SE. Mutation nomenclature extensions and suggestions to describe complex mutations: a discussion. Hum Mutat 2000;15(1):7-12.

(158) Lindsay S, Copp AJ. MRC-Wellcome Trust Human Developmental Biology Resource: enabling studies of human developmental gene expression. Trends Genet 2005 Nov;21(11):586-590.

(159) Odom JV, Bach M, Brigell M, Holder GE, McCulloch DL, Tormene AP, et al. ISCEV standard for clinical visual evoked potentials (2009 update). Doc Ophthalmol 2010 Feb;120(1):111-119.

(160) Adzhubei IA, Schmidt S, Peshkin L, Ramensky VE, Gerasimova A, Bork P, et al. A method and server for predicting damaging missense mutations. Nat Methods 2010 Apr;7(4):248-249.

(161) Mendell JT, Sharifi NA, Meyers JL, Martinez-Murillo F, Dietz HC. Nonsense surveillance regulates expression of diverse classes of mammalian transcripts and mutes genomic noise. Nat Genet 2004 Oct;36(10):1073-1078.

(162) Zhang B, Liu Z, Zhao G. Novel human pathological mutations. Gene symbol: FRMD7. Disease: congenital motor nystagmus. Hum Genet 2007 Nov;122(3-4):414.

(163) Desmet FO, Hamroun D, Lalande M, Collod-Beroud G, Claustres M, Beroud C. Human Splicing Finder: an online bioinformatics tool to predict splicing signals. Nucleic Acids Res 2009 May;37(9):e67.

(164) Query CC, Moore MJ, Sharp PA. Branch nucleophile selection in pre-mRNA splicing: evidence for the bulged duplex model. Genes Dev 1994 Mar 1;8(5):587-597.

(165) Khan SG, Yamanegi K, Zheng ZM, Boyle J, Imoto K, Oh KS, et al. XPC branch-point sequence mutations disrupt U2 snRNP binding, resulting in abnormal pre-mRNA splicing in xeroderma pigmentosum patients. Hum Mutat 2010 Feb;31(2):167-175.

(166) Khan SG, Metin A, Gozukara E, Inui H, Shahlavi T, Muniz-Medina V, et al. Two essential splice lariat branchpoint sequences in one intron in a xeroderma pigmentosum DNA repair gene: mutations result in reduced XPC mRNA levels that correlate with cancer risk. Hum Mol Genet 2004 Feb 1;13(3):343-352.

(167) Maslen C, Babcock D, Raghunath M, Steinmann B. A rare branch-point mutation is associated with missplicing of fibrillin-2 in a large family with congenital contractural arachnodactyly. Am J Hum Genet 1997 Jun;60(6):1389-1398.

(168) Li M, Pritchard PH. Characterization of the effects of mutations in the putative branchpoint sequence of intron 4 on the splicing within the human lecithin:cholesterol acyltransferase gene. J Biol Chem 2000 Jun 16;275(24):18079-18084.

(169) De Klein A, Riegman PH, Bijlsma EK, Heldoorn A, Muijtjens M, den Bakker MA, et al. A G-->A transition creates a branch point sequence and activation of a cryptic exon, resulting in the hereditary disorder neurofibromatosis 2. Hum Mol Genet 1998 Mar;7(3):393-398.

(170) Li ND, Cui LH, Wang LM, Ma HZ, Zhang LL, Yue YY, et al. The G990T mutation of the FRMD7 gene in a Chinese family with congenital idiopathic nystagmus]. Zhonghua Yi Xue Yi Chuan Xue Za Zhi 2008 Feb;25(1):11-14.

(171) Strachan T. Human molecular genetics. 4th ed. New York: Garland Science; 2010.

(172) Fearon ER, Winkelstein JA, Civin CI, Pardoll DM, Vogelstein B. Carrier detection in X-linked agammaglobulinemia by analysis of X-chromosome inactivation. N Engl J Med 1987 Feb 19;316(8):427-431.

(173) Leigh RJ, Robinson DA, Zee DS. A hypothetical explanation for periodic alternating nystagmus: instability in the optokinetic-vestibular system. Ann N Y Acad Sci 1981;374:619-635.

(174) Waespe W, Cohen B, Raphan T. Dynamic modification of the vestibulo-ocular reflex by the nodulus and uvula. Science 1985 Apr 12;228(4696):199-202.

(175) Baloh RW, Honrubia V, Konrad HR. Periodic alternating nystagmus. Brain 1976 Mar;99(1):11-26.

(176) Halmagyi GM, Rudge P, Gresty MA, Leigh RJ, Zee DS. Treatment of periodic alternating nystagmus. Ann Neurol 1980 Dec;8(6):609-611.

(177) Reinecke RD. Idiopathic infantile nystagmus: Diagnosis and treatment. Journal of AAPOS 1997;1(2):67-82.

(178) Shallo-Hoffmann J, Faldon M, Tusa RJ. The incidence and waveform characteristics of periodic alternating nystagmus in congenital nystagmus. Invest Ophthalmol Vis Sci 1999 Oct;40(11):2546-2553.

(179) Shallo-Hoffmann J, Dell'Osso LF, Dun S. Time-varying, slow-phase component interaction in congenital nystagmus. Vision Res 2004 Jan;44(2):209-220.

(180) Bullen P, Wilson DI. The Carnegie staging of human embryos: a practical guide. In: Strachan T, Lindsay S, Wilson DI, editors. Molecular Genetics of Early Human Development: Bios Scientific Publishers Limited; 1997.

(181) O'Rahilly R, Muller F. Developmental Stages in Human Embryos. Washington, DC.: Carnegie Institute Publication; 1987.

(182) Abadi RV, Pascal E. Periodic alternating nystagmus in humans with albinism. Invest Ophthalmol Vis Sci 1994 Nov;35(12):4080-4086.

(183) Gradstein L, Reinecke RD, Wizov SS, Goldstein HP. Congenital periodic alternating nystagmus. Diagnosis and Management. Ophthalmology 1997 Jun;104(6):918-28; discussion 928-9.

(184) Hertle RW, Reznick L, Yang D. Infantile aperiodic alternating nystagmus. J Pediatr Ophthalmol Strabismus 2009 Mar-Apr;46(2):93-103.

(185) Zhuang B, Su YS, Sockanathan S. FARP1 promotes the dendritic growth of spinal motor neuron subtypes through transmembrane Semaphorin6A and PlexinA4 signaling. Neuron 2009 Feb 12;61(3):359-372.

(186) Collewijn H, Winterson BJ, Dubois MFW. Optokinetic eye movements in albino rabbits: Inversion in anterior visual field. Science 1978;199(4335):1351-1353.

(187) Huang Y-, Rinner O, Hedinger P, Liu S-, Neuhauss SCF. Oculomotor instabilities in zebrafish mutant belladonna: A behavioral model for congenital nystagmus caused by axonal misrouting. Journal of Neuroscience 2006;26(39):9873-9880.

(188) Demer JL, Zee DS. Vestibulo-ocular and optokinetic deficits in albinos with congenital nystagmus. Invest Ophthalmol Vis Sci 1984 Jun;25(6):739-745.

(189) Yee RD, Baloh RW, Honrubia V. Study of congenital nystagmus: optokinetic nystagmus. Br J Ophthalmol 1980 Dec;64(12):926-932.

(190) Furman JM, Wall C,3rd, Pang DL. Vestibular function in periodic alternating nystagmus. Brain 1990 Oct;113 (Pt 5)(Pt 5):1425-1439.

(191) Hashimoto T, Sasaki O, Yoshida K, Takei Y, Ikeda S. Periodic alternating nystagmus and rebound nystagmus in spinocerebellar ataxia type 6. Mov Disord 2003 Oct;18(10):1201-1204.

(192) Matsumoto S, Ohyagi Y, Inoue I, Oishi A, Goto H, Nakagawa T, et al. Periodic alternating nystagmus in a patient with MS. Neurology 2001 Jan 23;56(2):276-277.

(193) Solomon D, Shepard N, Mishra A. Congenital periodic alternating nystagmus: response to baclofen. Ann N Y Acad Sci 2002 Apr;956:611-615.

(194) Comer RM, Dawson EL, Lee JP. Baclofen for patients with congenital periodic alternating nystagmus. Strabismus 2006 Dec;14(4):205-209.

(195) Self J, Haitchi HM, Griffiths H, Holgate ST, Davies DE, Lotery A. Frmd7 expression in developing mouse brain. Eye (Lond) 2010 Jan;24(1):165-169.

(196) Sabaliauskas NA, Foutz CA, Mest JR, Budgeon LR, Sidor AT, Gershenson JA, et al. High-throughput zebrafish histology. Methods 2006 Jul;39(3):246-254.

(197) Bradford Y, Conlin T, Dunn N, Fashena D, Frazer K, Howe DG, et al. ZFIN: enhancements and updates to the Zebrafish Model Organism Database. Nucleic Acids Res 2011 Jan;39(Database issue):D822-9.

(198) Azuma N, Nishina S, Yanagisawa H, Okuyama T, Yamada M. PAX6 missense mutation in isolated foveal hypoplasia. Nat Genet 1996 Jun;13(2):141-142.

(199) Tremblay F, Gupta SK, De Becker I, Guernsey DL, Neumann PE. Effects of PAX6 mutations on retinal function: An electroretinographic study. Am J Ophthalmol 1998;126(2):211-218.

(200) Mastick GS, Davis NM, Andrew GL, Easter SS,Jr. Pax-6 functions in boundary formation and axon guidance in the embryonic mouse forebrain. Development 1997 May;124(10):1985-1997.

(201) Rapaport DH, Wong LL, Wood ED, Yasumura D, LaVail MM. Timing and topography of cell genesis in the rat retina. J Comp Neurol 2004 Jun 21;474(2):304-324.

(202) Drager UC. Birth dates of retinal ganglion cells giving rise to the crossed and uncrossed optic projections in the mouse. Proc R Soc Lond B Biol Sci 1985 Mar 22;224(1234):57-77.

(203) Torres M, Gomez-Pardo E, Gruss P. Pax2 contributes to inner ear patterning and optic nerve trajectory. Development 1996 Nov;122(11):3381-3391.

(204) Leguire LE, Kashou NH, Fogt N, Smith MA, Lewis JR, Kulwin R, et al. Neural Circuit Involved in Idiopathic Infantile Nystagmus Syndrome Based on fMRI. J Pediatr Ophthalmol Strabismus 2011 Jan 25:1-10.

(205) Kashou NH, Mohsin AO, Smith MA, Leguire LE,IV. Tractography of Infantile Nystagmus Syndrome. Invest Ophthalmol Vis Sci 2011 April 22;52(6):4688.

(206) Kiernan DF, Mieler WF, Hariprasad SM. Spectral-domain optical coherence tomography: a comparison of modern high-resolution retinal imaging systems. Am J Ophthalmol 2010 Jan;149(1):18-31.

(207) Drexler W, Fujimoto JG. State-of-the-art retinal optical coherence tomography. Prog Retin Eye Res 2008 Jan;27(1):45-88.

(208) Drexler W. Cellular and functional optical coherence tomography of the human retina: the Cogan lecture. Invest Ophthalmol Vis Sci 2007 Dec;48(12):5339-5351.

(209) Leung CK, Cheung CY, Weinreb RN, Qiu Q, Liu S, Li H, et al. Retinal nerve fiber layer imaging with spectral-domain optical coherence tomography: a variability and diagnostic performance study. Ophthalmology 2009 Jul;116(7):1257-63, 1263.e1-2.

(210) Menke MN, Dabov S, Knecht P, Sturm V. Reproducibility of retinal thickness measurements in healthy subjects using spectralis optical coherence tomography. Am J Ophthalmol 2009 Mar;147(3):467-472.

(211) Cronin TH, Hertle RW, Ishikawa H, Schuman JS. Spectral domain optical coherence tomography for detection of foveal morphology in patients with nystagmus. J AAPOS 2009 Dec;13(6):563-566.

(212) Bainbridge JW, Smith AJ, Barker SS, Robbie S, Henderson R, Balaggan K, et al. Effect of gene therapy on visual function in Leber's congenital amaurosis. N Engl J Med 2008 May 22;358(21):2231-2239.

(213) Anger EM, Unterhuber A, Hermann B, Sattmann H, Schubert C, Morgan JE, et al. Ultrahigh resolution optical coherence tomography of the monkey fovea.

Identification of retinal sublayers by correlation with semithin histology sections. Exp Eye Res 2004 Jun;78(6):1117-1125.

(214) Huang Y, Cideciyan AV, Papastergiou GI, Banin E, Semple-Rowland SL, Milam AH, et al. Relation of optical coherence tomography to microanatomy in normal and rd chickens. Invest Ophthalmol Vis Sci 1998 Nov;39(12):2405-2416.

(215) Thomas MG, Kumar A, Mohammad S, Proudlock FA, Engle EC, Andrews C, et al. Structural Grading of Foveal Hypoplasia Using Spectral Domain Optical Coherence Tomography; A Predictor of Visual Acuity? Ophthalmology 2011.

(216) Mohammad S, Gottlob I, Kumar A, Thomas MG, Sheth V, Degg C, et al. The Functional Significance of Foveal Abnormalities in Albinism Measured Using Spectral-domain Optical Coherence Tomography. Ophthalmology 2011.

(217) Ho J, Castro DP, Castro LC, Chen Y, Liu J, Mattox C, et al. Clinical Assessment of Mirror Artifacts in Spectral Domain Optical Coherence Tomography. Invest Ophthalmol Vis Sci 2010 Feb 24;51(7):3714-3720.

(218) Bland JM, Altman DG. Statistical methods for assessing agreement between two methods of clinical measurement. Lancet 1986 Feb 8;1(8476):307-310.

(219) Ishikawa H, Stein DM, Wollstein G, Beaton S, Fujimoto JG, Schuman JS. Macular segmentation with optical coherence tomography. Invest Ophthalmol Vis Sci 2005 Jun;46(6):2012-2017.

(220) Thomas MG, Kumar A, Kohl S, Proudlock FA, Gottlob I. High-resolution in vivo imaging in achromatopsia. Ophthalmology 2011 May;118(5):882-887.

(221) Alexander JJ, Umino Y, Everhart D, Chang B, Min SH, Li Q, et al. Restoration of cone vision in a mouse model of achromatopsia. Nat Med 2007 Jun;13(6):685-687.

(222) Harvey PS, King RA, Summers CG. Spectrum of foveal development in albinism detected with optical coherence tomography. J AAPOS 2006 Jun;10(3):237-242.

(223) Seo JH, Yu YS, Kim JH, Choung HK, Heo JW, Kim SJ. Correlation of visual acuity with foveal hypoplasia grading by optical coherence tomography in albinism. Ophthalmology 2007 Aug;114(8):1547-1551.

(224) Marmor MF, Choi SS, Zawadzki RJ, Werner JS. Visual insignificance of the foveal pit: reassessment of foveal hypoplasia as fovea plana. Arch Ophthalmol 2008 Jul;126(7):907-913.

(225) Harvey PS, King RA, Summers CS. Foveal depression and albinism. Ophthalmology 2008 Apr;115(4):756; author reply 756-7.

(226) Holmstrom G, Eriksson U, Hellgren K, Larsson E. Optical coherence tomography is helpful in the diagnosis of foveal hypoplasia. Acta Ophthalmol 2009 Jun 2;88(4):439-442.

(227) McAllister JT, Dubis AM, Tait DM, Ostler S, Rha J, Stepien KE, et al. Arrested development: high-resolution imaging of foveal morphology in albinism. Vision Res 2010 Apr 7;50(8):810-817.

(228) Bredrup C, Knappskog PM, Rodahl E, Boman H. Clinical manifestation of a novel PAX6 mutation Arg128Pro. Arch Ophthalmol 2008 Mar;126(3):428-430.

(229) S. Mohammad. The Functional Significance of Foveal Abnormalities in Albinism Measured Using Spectral-domain Optical Coherence Tomography. University of Leicester: University of Leicester; 2010.

(230) Varsanyi B, Somfai GM, Lesch B, Vamos R, Farkas A. Optical coherence tomography of the macula in congenital achromatopsia. Invest Ophthalmol Vis Sci 2007 May;48(5):2249-2253.

(231) Srinivasan VJ, Monson BK, Wojtkowski M, Bilonick RA, Gorczynska I, Chen R, et al. Characterization of outer retinal morphology with high-speed, ultrahigh-resolution optical coherence tomography. Invest Ophthalmol Vis Sci 2008 Apr;49(4):1571-1579.

(232) Leung CK, Cheng AC, Chong KK, Leung KS, Mohamed S, Lau CS, et al. Optic disc measurements in myopia with optical coherence tomography and confocal scanning laser ophthalmoscopy. Invest Ophthalmol Vis Sci 2007 Jul;48(7):3178-3183.

(233) Leung CK, Chan WM, Hui YL, Yung WH, Woo J, Tsang MK, et al. Analysis of retinal nerve fiber layer and optic nerve head in glaucoma with different reference plane offsets, using optical coherence tomography. Invest Ophthalmol Vis Sci 2005 Mar;46(3):891-899.

(234) Kumar A, Gottlob I, Mclean RJ, Thomas S, Thomas MG, Proudlock FA. Clinical and oculomotor characteristics of albinism compared to FRMD7 associated infantile nystagmus. Invest Ophthalmol Visual Sci 2011;52(5):2306-2313.

(235) Provis JM, Diaz CM, Dreher B. Ontogeny of the primate fovea: A central issue in retinal development. Prog Neurobiol 1998;54(5):549-581.

(236) Georges P, Madigan MC, Provis JM. Apoptosis during development of the human retina: relationship to foveal development and retinal synaptogenesis. J Comp Neurol 1999 Oct 18;413(2):198-208.

(237) Abadi RV, Dickinson CM. Monochromatic fundus photography of human albinos. Arch Ophthalmol 1983 Nov;101(11):1706-1711.

(238) Charles SJ, Green JS, Grant JW, Yates JRW, Moore AT. Clinical features of affected males with X linked ocular albinism. Br J Ophthalmol 1993;77(4):222-227.

(239) Spedick MJ, Beauchamp GR. Retinal vascular and optic nerve abnormalities in albinism. J Pediatr Ophthalmol Strabismus 1986;23(2):58-63.

(240) McGuire DE, Weinreb RN, Goldbaum MH. Foveal hypoplasia demonstrated in vivo with optical coherence tomography. Am J Ophthalmol 2003 Jan;135(1):112-114.

(241) Springer AD, Hendrickson AE. Development of the primate area of high acuity. 2. Quantitative morphological changes associated with retinal and pars plana growth. Vis Neurosci 2004 Sep-Oct;21(5):775-790.

(242) Springer AD, Hendrickson AE. Development of the primate area of high acuity, 3: temporal relationships between pit formation, retinal elongation and cone packing. Vis Neurosci 2005 Mar-Apr;22(2):171-185.

(243) Hammer DX, Iftimia NV, Ferguson RD, Bigelow CE, Ustun TE, Barnaby AM, et al. Foveal fine structure in retinopathy of prematurity: an adaptive optics Fourier domain optical coherence tomography study. Invest Ophthalmol Vis Sci 2008 May;49(5):2061-2070.

(244) Hendrickson AE, Yuodelis C. The morphological development of the human fovea. Ophthalmology 1984;91(6):603-612.

(245) La Vail MM, Rapaport DH, Rakic P. Cytogenesis in the monkey retina. J Comp Neurol 1991 Jul 1;309(1):86-114.

(246) Retinal development. Cambridge: Cambridge University Press; 2006.

(247) Graw J. Eye development. Curr Top Dev Biol 2010;90:343-386.

(248) Graw J. Genetic aspects of embryonic eye development in vertebrates. Dev Genet 1996;18(3):181-197.

(249) Walther C, Gruss P. Pax-6, a murine paired box gene, is expressed in the developing CNS. Development 1991 Dec;113(4):1435-1449.

(250) Gruss P, Walther C. Pax in development. Cell 1992 May 29;69(5):719-722.

(251) Hirsch N, Harris WA. Xenopus Pax-6 and retinal development. J Neurobiol 1997;32(1):45-61.

(252) Gupta SK, De Becker I, Tremblay F, Guernsey DL, Neumann PE. Genotype/phenotype correlations in aniridia. Am J Ophthalmol 1998 Aug;126(2):203-210.

(253) Fulton AB, Albert DM, Craft JL. Human albinism. Light and electron microscopy study. Arch Ophthalmol 1978 Feb;96(2):305-310.

(254) Kelly JP, Weiss AH. Topographical retinal function in oculocutaneous albinism. Am J Ophthalmol 2006 Jun;141(6):1156-1158.

(255) Shin DH, Kwon BS, Chang YP, Bae SR, Kim J, Kim JW. Ultramicroscopical immunolocalization of PAX6 in the adult chicken retina. Acta Histochem 2003;105(3):267-272.

(256) Hever AM, Williamson KA, van Heyningen V. Developmental malformations of the eye: the role of PAX6, SOX2 and OTX2. Clin Genet 2006 Jun;69(6):459-470.

(257) Larsen KB, Lutterodt M, Rath MF, Moller M. Expression of the homeobox genes PAX6, OTX2, and OTX1 in the early human fetal retina. Int J Dev Neurosci 2009 Aug;27(5):485-492.

(258) Nishida A, Furukawa A, Koike C, Tano Y, Aizawa S, Matsuo I, et al. Otx2 homeobox gene controls retinal photoreceptor cell fate and pineal gland development. Nat Neurosci 2003 Dec;6(12):1255-1263.

(259) Naumann GOH, Lerche W, Schroeder W. Foveolar aplasia in tyrosinase positive oculocutaneous albinism. Albrecht von Graefes Archiv fur Klinische und Experimentelle Ophthalmologie 1976;200(1):39-50.

(260) Adams T, Shahabi G, Hoh-Kam J, Jeffery G. Held under arrest: Many mature albino RPE cells display polyploidal features consistent with abnormal cell cycle retention. Exp Eye Res 2010 Feb;90(2):368-372.

(261) Mohammad S, Gottlob I, Thomas MG, Kumar A, Proudlock FA. Evaluation of the Retinal Pigmented Epithelium Layer in Human Albinism. Invest Ophthalmol Vis Sci 2010 April 11;51(5):4407.

(262) McCulley TJ, Mayer K, Dahr SS, Simpson J, Holland EJ. Aniridia and optic nerve hypoplasia. Eye (Lond) 2005 Jul;19(7):762-764.

(263) Jeffery G, Kinsella B. Translaminar deficits in the retinae of albinos. J Comp Neurol 1992 Dec 22;326(4):637-644.

(264) Esteve JV, Jeffery G. Reduced retinal deficits in an albino mammal with a cone rich retina: a study of the ganglion cell layer at the area centralis of pigmented and albino grey squirrels. Vision Res 1998 Mar;38(6):937-940.

(265) Nishina S, Kohsaka S, Yamaguchi Y, Handa H, Kawakami A, Fujisawa H, et al. PAX6 expression in the developing human eye. Br J Ophthalmol 1999;83(6):723-727.

(266) Brown NL, Patel S, Brzezinski J, Glaser T. Math5 is required for retinal ganglion cell and optic nerve formation. Development 2001 Jul;128(13):2497-2508.

(267) Yang Z, Ding K, Pan L, Deng M, Gan L. Math5 determines the competence state of retinal ganglion cell progenitors. Dev Biol 2003 Dec 1;264(1):240-254.

(268) Riesenberg AN, Le TT, Willardsen MI, Blackburn DC, Vetter ML, Brown NL. Pax6 regulation of Math5 during mouse retinal neurogenesis. Genesis 2009 Mar;47(3):175-187.

(269) Marquardt T, Ashery-Padan R, Andrejewski N, Scardigli R, Guillemot F, Gruss P. Pax6 is required for the multipotent state of retinal progenitor cells. Cell 2001 Apr 6;105(1):43-55.

(270) Jensen AM, Westerfield M. Zebrafish mosaic eyes is a novel FERM protein required for retinal lamination and retinal pigmented epithelial tight junction formation. Curr Biol 2004 Apr 20;14(8):711-717.

(271) Jensen AM, Walker C, Westerfield M. Mosaic Eyes: a Zebrafish Gene Required in Pigmented Epithelium for Apical Localization of Retinal Cell Division and Lamination. Development 2001 Jan;128(1):95-105.

(272) Jacobson SG, Cideciyan AV, Aleman TS, Pianta MJ, Sumaroka A, Schwartz SB, et al. Crumbs homolog 1 (CRB1) mutations result in a thick human retina with abnormal lamination. Hum Mol Genet 2003 May 1;12(9):1073-1078.

(273) Morrow EM, Furukawa T, Lee JE, Cepko CL. NeuroD regulates multiple functions in the developing neural retina in rodent. Development 1999 Jan;126(1):23-36.

(274) Optic disc morphology in albinism. North American Neuro-Ophthalmology Society; February 27 - March 3; ; 1994.

(275) Schmitz B, Schaefer T, Krick CM, Reith W, Backens M, Kasmann-Kellner B. Configuration of the optic chiasm in humans with albinism as revealed by magnetic resonance imaging. Invest Ophthalmol Vis Sci 2003 Jan;44(1):16-21.

(276) Brodsky MC, Glasier CM, Creel DJ. Magnetic resonance imaging of the visual pathways in human albinos. J Pediatr Ophthalmol Strabismus 1993 Nov-Dec;30(6):382-385.

(277) Deiner MS, Kennedy TE, Fazeli A, Serafini T, Tessier-Lavigne M, Sretavan DW. Netrin-1 and DCC mediate axon guidance locally at the optic disc: loss of function leads to optic nerve hypoplasia. Neuron 1997 Sep;19(3):575-589.

(278) Deiner MS, Sretavan DW. Altered midline axon pathways and ectopic neurons in the developing hypothalamus of netrin-1- and DCC-deficient mice. J Neurosci 1999 Nov 15;19(22):9900-9912.

(279) Raper JA. Semaphorins and their receptors in vertebrates and invertebrates. Curr Opin Neurobiol 2000 Feb;10(1):88-94.

(280) Adams RH. Vascular patterning by Eph receptor tyrosine kinases and ephrins. Semin Cell Dev Biol 2002 Feb;13(1):55-60.

(281) Abouzeid H, Youssef MA, ElShakankiri N, Hauser P, Munier FL, Schorderet DF. PAX6 aniridia and interhemispheric brain anomalies. Mol Vis 2009 Oct 17;15:2074-2083.

(282) Khajavi M, Inoue K, Lupski JR. Nonsense-mediated mRNA decay modulates clinical outcome of genetic disease. Eur J Hum Genet 2006 Oct;14(10):1074-1081.

(283) Curcio CA, Sloan KR,Jr, Packer O, Hendrickson AE, Kalina RE. Distribution of cones in human and monkey retina: individual variability and radial asymmetry. Science 1987 May 1;236(4801):579-582.

(284) Curcio CA, Sloan KR, Kalina RE, Hendrickson AE. Human photoreceptor topography. J Comp Neurol 1990 Feb 22;292(4):497-523.

(285) Harrison R, Hoefnagel D, Hayward JN. Congenital total color blindness: a clincopathological report. Arch Ophthalmol 1960 Nov;64:685-692.

(286) Falls HF, Wolter JR, Alpern M. Typical total monochromacy. A histological and psychophysical study. Arch Ophthalmol 1965 Nov;74(5):610-616.

(287) Gropp KE, Szel A, Huang JC, Acland GM, Farber DB, Aguirre GD. Selective absence of cone outer segment beta 3-transducin immunoreactivity in hereditary cone degeneration (cd). Exp Eye Res 1996 Sep;63(3):285-296.

(288) Chang B, Dacey MS, Hawes NL, Hitchcock PF, Milam AH, Atmaca-Sonmez P, et al. Cone photoreceptor function loss-3, a novel mouse model of achromatopsia due to a mutation in Gnat2. Invest Ophthalmol Vis Sci 2006 Nov;47(11):5017-5021.

(289) Michalakis S, Geiger H, Haverkamp S, Hofmann F, Gerstner A, Biel M. Impaired opsin targeting and cone photoreceptor migration in the retina of mice lacking the cyclic nucleotide-gated channel CNGA3. Invest Ophthalmol Vis Sci 2005 Apr;46(4):1516-1524.

(290) Biel M, Seeliger M, Pfeifer A, Kohler K, Gerstner A, Ludwig A, et al. Selective loss of cone function in mice lacking the cyclic nucleotide-gated channel CNG3. Proc Natl Acad Sci U S A 1999 Jun 22;96(13):7553-7557.

(291) Sidjanin DJ, Lowe JK, McElwee JL, Milne BS, Phippen TM, Sargan DR, et al. Canine CNGB3 mutations establish cone degeneration as orthologous to the human achromatopsia locus ACHM3. Hum Mol Genet 2002 Aug 1;11(16):1823-1833.

(292) Andersen MK, Christoffersen NL, Sander B, Edmund C, Larsen M, Grau T, et al. Oligocone trichromacy: clinical and molecular genetic investigations. Invest Ophthalmol Vis Sci 2010 Jan;51(1):89-95.

(293) Claes E, Seeliger M, Michalakis S, Biel M, Humphries P, Haverkamp S. Morphological characterization of the retina of the CNGA3(-/-)Rho(-/-) mutant mouse lacking functional cones and rods. Invest Ophthalmol Vis Sci 2004 Jun;45(6):2039-2048.

(294) Haverkamp S, Michalakis S, Claes E, Seeliger MW, Humphries P, Biel M, et al. Synaptic plasticity in CNGA3(-/-) mice: cone bipolar cells react on the missing cone input and form ectopic synapses with rods. J Neurosci 2006 May 10;26(19):5248-5255.

(295) Comander J, Gardiner M, Loewenstein J. High-resolution optical coherence tomography findings in solar maculopathy and the differential diagnosis of outer retinal holes. Am J Ophthalmol 2011 Sep;152(3):413-419.e6.

(296) Sergouniotis PI, Holder GE, Robson AG, Michaelides M, Webster AR, Moore AT. High-resolution optical coherence tomography imaging in KCNV2 retinopathy. Br J Ophthalmol 2011 May 10.

(297) Gomes NL, Greenstein VC, Carlson JN, Tsang SH, Smith RT, Carr RE, et al. A comparison of fundus autofluorescence and retinal structure in patients with Stargardt disease. Invest Ophthalmol Vis Sci 2009 Aug;50(8):3953-3959.

(298) Sisk RA, Berrocal AM, Lam BL. Loss of Foveal Cone Photoreceptor Outer Segments in Occult Macular Dystrophy. Ophthalmic Surg Lasers Imaging 2010 Mar 9:1-3.

(299) Thiadens AA, Somervuo V, van den Born LI, Roosing S, van Schooneveld MJ, Kuijpers RW, et al. Progressive loss of cones in achromatopsia: an imaging study using spectral-domain optical coherence tomography. Invest Ophthalmol Vis Sci 2010 Nov;51(11):5952-5957.

(300) Carvalho LS, Xu J, Pearson RA, Smith AJ, Bainbridge JW, Morris LM, et al. Long-term and age-dependent restoration of visual function in a mouse model of CNGB3-associated achromatopsia following gene therapy. Hum Mol Genet 2011 Aug 15;20(16):3161-3175.

(301) Querques G, Bux AV, Iaculli C, Delle Noci N. Isolated foveal hypoplasia. Retina 2008 Nov-Dec;28(10):1552-1553.

(302) Recchia FM, Carvalho-Recchia CA, Trese MT. Optical coherence tomography in the diagnosis of foveal hypoplasia. Arch Ophthalmol 2002 Nov;120(11):1587-1588.

(303) Mietz H, Green WR, Wolff SM, Abundo GP. Foveal hypoplasia in complete oculocutaneous albinism. A histopathologic study. Retina 1992;12(3):254-260.

(304) Forooghian F, Stetson PF, Meyer SA, Chew EY, Wong WT, Cukras C, et al. Relationship between photoreceptor outer segment length and visual acuity in diabetic macular edema. Retina 2010 Jan;30(1):63-70.

(305) Witkin AJ, Ko TH, Fujimoto JG, Chan A, Drexler W, Schuman JS, et al. Ultra-high resolution optical coherence tomography assessment of photoreceptors in retinitis pigmentosa and related diseases. Am J Ophthalmol 2006 Dec;142(6):945-952.

(306) Ray WA, O'Day DM. Statistical analysis of multi-eye data in ophthalmic research. Invest Ophthalmol Vis Sci 1985 Aug;26(8):1186-1188.

(307) Bijlsma WR, van Schooneveld MJ, Van der Lelij A. Optical coherence tomography findings for nanophthalmic eyes. Retina 2008 Jul-Aug;28(7):1002-1007.

(308) Kroese M, Zimmern RL, Farndon P, Stewart F, Whittaker J. How can genetic tests be evaluated for clinical use? Experience of the UK Genetic Testing Network. Eur J Hum Genet 2007 Sep;15(9):917-921.

(309) McKusick-Nathans Institute of Genetic Medicine, Johns Hopkins University (Baltimore, MD). Online Mendelian Inheritance in Man, OMIM®. Available at: http://omim.org/. Accessed 02/04, 2008.

(310) Thomas MG, Crosier M, Lindsay S, Kumar A, Thomas S, Araki M, et al. The clinical and molecular genetic features of idiopathic infantile periodic alternating nystagmus. Brain 2011 Mar;134(Pt 3):892-902.

(311) Thomas MG, Kumar A, Thompson JR, Proudlock FA, Straatman K, Gottlob I. Is high-resolution spectral domain optical coherence tomography reliable in nystagmus? British Journal of Ophthalmology 2011 September 27.

(312) Maguire AM, High KA, Auricchio A, Wright JF, Pierce EA, Testa F, et al. Age-dependent effects of RPE65 gene therapy for Leber's congenital amaurosis: a phase 1 dose-escalation trial. Lancet 2009 Nov 7;374(9701):1597-1605.

(313) Pu J, Li Y, Liu Z, Yan Y, Tian J, Chen S, et al. Expression and localization of FRMD7 in human fetal brain, and a role for F-actin. Mol Vis 2011 Feb 24;17:591-597.

(314) Huang MY, Chen CC, Huber-Reggi SP, Neuhauss SC, Straumann D. Comparison of infantile nystagmus syndrome in achiasmatic zebrafish and humans. Ann N Y Acad Sci 2011 Sep;1233:285-291.

(315) Gottlob I, Reinecke RD. Eye and head movements in patients with achromatopsia. Graefes Arch Clin Exp Ophthalmol 1994 Jul;232(7):392-401.

ELECTRONIC APPENDIX

The DVD attached with this thesis contains the following files:

1) FOLDER: PUBLICATIONS ARISING FROM THIS WORK

1. File name: Thomas MG et al. PAN

Thomas MG, Crosier M, Lindsay S, Kumar A, Thomas S, Masasuke A, Talbot CJ, McLean RJ, Surendran M, Taylor K, Leroy BP, Moore AT, Hunter DG, Hertle RW, Tarpey P, Langmann A, Lindner S, Brandner M, Gottlob I. The clinical and molecular genetic features of idiopathic infantile periodic alternating nystagmus. *Brain* 2011 Mar;134(Pt 3):892-902.

2. Filename: Thomas MG et al. High Resolution In-vivo imaging in achromatopsia

Thomas MG, Kumar A, Kohl S, Proudlock FA, Gottlob I. High-resolution in vivo imaging in achromatopsia. *Ophthalmology* 2011 May;118(5):882-887.

3. Filename: Thomas MG et al. Structural Grading of foveal hypoplasia

Thomas MG, Kumar A, Mohammad S, Proudlock FA, Engle EC, Andrews C, Chan W, Thomas S, Gottlob I. Structural Grading of Foveal Hypoplasia Using Spectral Domain Optical Coherence Tomography; A Predictor of Visual Acuity? *Ophthalmology* 2011.

4. Filename: Thomas MG et al. *FRMD7*-Related Infantile Nystagmus

Thomas MG, Thomas S, Kumar A, Proudlock FA, Gottlob I. *FRMD7*-related infantile nystagmus. In: Pagon RA, ed. *GeneReviews* at GeneTests. Seattle: University of Washington; 2011.

5. Filename: Thomas MG et al. Reproducibility of OCT measurements

Thomas MG, Kumar A, Thompson JR, Proudlock FA, Straatman K, Gottlob I. Is high-resolution spectral domain optical coherence tomography reliable in nystagmus? *British Journal of Ophthalmology* 2011

2) FOLDER: VIDEOS

1. Filename: Child with IIN – Triangular Nystagmus Waveform

This is a video of a child with a large amplitude low frequency nystagmus. This is one of the early nystagmus waveforms seen during infancy and it is referred to as a triangular nystagmus waveform.

2. Filename: Adult with IIN – Jerk Nystagmus

This is a video of an adult with a central null position with a slow phase directed to the primary position while the quick phase is directed to the point of fixation

3. Filename: Anomalous Head Posture During Reading

This is a video of a young boy with an anomalous head posture during a reading task. This typically indicates an eccentric null position. An anomalous head posture is more commonly seen in patients with IIN without *FRMD7* mutations

4. Filename: FRMD7 - Gaze angle and Nystagmus

This video is an example of a patient with *FRMD7* mutation. He has a central null position, no anomalous head posture and the nystagmus intensity changes with gaze positions.

5. Filename: Albinism – Nystagmus and Strabismus

This video shows an example of nystagmus and strabismus in a patient with albinism

6. Filename: Vertical Nystagmus with PAX6 mutations

This video shows a patient with *PAX6* mutation and represents an example of nystagmus with a vertical component.

7. Filename: PAN with FRMD7 mutations

This is a video of a patient with *FRMD7* mutation and periodic alternating nystagmus.

8. Filename: Control subject reading

This video shows an example of a control subject (without nystagmus) reading text. The cyclopean gaze cursor (representing the point of fixation) is superimposed on the text.

9. Filename: Nystagmus patient reading

This video shows an example of a nystagmus patient (with left beat nystagmus) reading text. The nystagmus is worse on left gaze. The cyclopean gaze cursor (representing the point of fixation) is superimposed on the text.

10. Filename: Illustration of effects of nystagmus on reading

This video is an illustration of the effects of nystagmus on reading. The text was made to oscillate in the horizontal plane based on the nystagmus amplitude and frequency.

3) FOLDER: CONSENT FORMS AND INFORMATION LEAFLETS

1. Filename: Adult Invitation Letter
2. Filename: Adult Information Leaflet
3. Filename: Adult Consent Form
4. Filename: Child Invitation Letter
5. Filename: Child Information Leaflet
6. Filename: Parent Information Leaflet
7. Filename: Child Consent Form
8. Filename: 2009 Amendment Form to add Mervyn
9. Filename: Consent Assessment

4) FOLDER: SAMPLE SIZE CALCULATION

1. Filename: Sample Size Calculation – Chapter 7

This document shows the power curves generated based on the pilot study for determining the sample size in chapter 7.

5) FOLDER: DATASET

Files related to various experiments and datasets are in this folder.